CERN-ACC-Note-2020-0002
Version v1.0
Geneva, May 3, 2020

The Large Hadron-Electron Collider at the HL-LHC

LHeC Study Group

To be submitted to J.Phys. G

Instructions for LHeC editors

Thanks for contributing to the 2019 CDR for the LHeC experiment and accelerator. Here, we briefly provide instructions for the editors of the CDR document in order to facilitate editing.

Quick start with git

- Clone the git repository: `$ git clone ..`
- Go to the respective (sub)directory, e.g.: `$ cd lhec-cdr-2019/higgs`
- 'compile' the selected chapter, by typing `$ make`
  (which just calls `pdflatex` and `bibtex` consecutively)
- Open the resulting PDF file, e.g. `$ okular higgs.pdf`

For editing, just insert your contribution to the respective .tex-file (e.g. *higgs.tex*) (note: there may be a more distinct tex-substructure for individual chapters; therefore, please look out for further .tex-files in the directory).

Quick start with overleaf There exists a mirror at overleaf. Please ask for the link.

Compile the document To preview the manuscript, just navigate to a certain directory, i.e. type *cd ./higgs*, and then type *make*. This generates a PDF-file (e.g. *higgs.pdf*) which shows the selected chapter as written in the .tex-file (e.g. *higgs.tex*) together with the title page, this instructions page, table-of-content, and bibliography. **Important:** the latter pages disappear in the full document. The entire document is generated by calling *make* in the directory *main*.

Clean up Type *make clean* in a certain directory, which deletes all temporary latex files.

References Put BibTex-items in 'inspirehep'-format into the file *../lhec.bib*, and take care to not introduce duplicate entries (Example : [1]).

git repository The git repository is hosted by gitlab at CERN. For details see: `https://gitlab.cern.ch/lhec/lhec-cdr-2019`. Public checkout is possible, and the source is also available as a tar-ball (or .zip): `https://gitlab.cern.ch/lhec/lhec-cdr-2019/-/archive/master/lhec-cdr-2019-master.tar.gz` When committing changes, you need a CERN computing account, and authentication with ssh, krb5 or https is supported.

If you do not have a CERN account, please send your contribution to your chapter editor.

git commit

- synchronize with master: git pull
- compile: make
- (optional) list changes: git status
- (optional, but important) add new files: git add <new files >
- Commit changes: git commit -m ''your message'' [optional: select files]
- Push changes to our common repository: git push

Note: do not forget to add (commit and push) new files, e.g. figures. In case, there are problems when pushing to our main repository, send your changes to your chapter editor by mail.

No CERN account In case you do not have a CERN computing account: Clone/checkout the gitlab repository or download the source code as zip-file or tar-ball from[1] https://gitlab.cern.ch/lhec/lhec-cdr-2019. Then make your edits prompt, and send your contribution to the respective chapter editors by mail. Also, you can insert your contribution in overleaf.

[1] A direct download link would be https://gitlab.cern.ch/lhec/lhec-cdr-2019/-/archive/master/lhec-cdr-2019-master.tar.gz.

Remarks on the 'LHeC at HL-LHC' Paper (sent by mail, MK, 29.07.)

1. The paper should be an update of the CDR, may refer to that, but also be selfconsistent. It will have a few hundred pages, may be 400. There is no direct page limit, neither in total nor for any chapter. It will be published in JPhysG.

2. We will use PDFLaTeX and git such that all contributors may directly edit. In order to commit to the git repository, which is located at https://gitlab.cern.ch/lhec/lhec-cdr-2019, you will need write permissions. Please send a mail to Daniel (britzger@mpp.mpg.de)

3. For release in the fall, for presenting the results at the Chavannes workshop https://indico.cern.ch/event/835947, and for having a bit of time for editing, we have set a deadline of 11.10.2019 for all contributions. As all know, deadlines tend to slip, we yet will have to make a sincere effort to release the paper to the arXiv in November, for which 11.10. looks just about realistic. It is known to be tight, but we all write about things we have been working on for long.

4. There have been chapters created and chapter editors invited, who kindly agreed to help bringing the chapters together. Nothing is frozen, additional names/colleagues may be invited, headlines be changed as writing will dictate/suggest. This mail is to all of you, the authors of sections and editors who surely will find a good way to collaborate. The overall editing will be with Oliver and Max

5. We have agreed to write an update on LHeC at HL-LHC, not the FCC as its CDR just went out. Where reasonable a link to FCC as well as joint presentations or plots may be instructive. We thought it would be interesting, as an Appendix, to have a separate chapter on ep with what now is called LE FCC, a 20 TeV proton energy FCC.

6. We have put more emphasis than before on the relation to pp. Thus there is a separate chapter on HL-LHC and a separate chapter on the relation of ep with pp. We thought emphasis should also be clear to the importance of eA.

7. Further, the importance of energy recovery and the role and perspective of PERLE must be disussed, this is currently an appendix, but represents the base of the accelerator development to some extent.

8. Following the cost estimates and IR synchrotron radiation laod, we consider Ee=50 GeV in 1/4 U(LHC) as a new baseline [compared to 60 GeV, 1/3]. The 1/4 will allow upgrades to almost 60 GeV and we therefore shall not aim at redoing all analyses done with 60 GeV now with 50. If you do new ones, take in doubt 50 GeV please.

Contents

Chapter 1

Parton Distributions - Resolving the Substructure of the Proton

1.1 Introduction

Since the discovery of quarks in the famous $ep \to eX$ scattering experiment at Stanford [2, 3], the deep inelastic scattering process has been established as the most reliable method to resolve the substructure of protons, which was recognised, not least by Feynman [4], immediately. Since that time, a series of electron, muon and neutrino DIS experiments installed the Quark-Parton Model and supported the development of Quantum Chromodynamics. A new quality of this physics was realised with HERA, the first electron-proton collider built, which extended the kinematic range in momentum transfer squared to $Q^2_{max} = s \simeq 10^5\,\mathrm{GeV}^2$, for $s = 4E_eE_p$. Seen from today's perspective, largely influenced by the LHC, it is necessary to reach a further level in these investigations, with higher energy and much increased luminosity than HERA could achieve. This is a major motivation for building the LHeC, with an extension of the Q^2 and $1/x$ range by more than an order of magnitude and an increase of the luminosity by a factor of almost a thousand. QCD may break, be embedded in a higher gauge symmetry, free colour be observed: one may ask a series of fundamental questions on QCD [5] and grasp the importance of a precision DIS programme with the LHeC.

The subsequent chapter is mainly devoted to the exploration of the seminal potential of the LHeC to resolve the substructure of the proton in an unprecedented range, with the first ever complete and coherent measurement of the full set of parton distribution functions (PDFs) in one experiment. The precise determination of PDFs, consistently to high orders pQCD, is crucial for the interpretation of LHC physics, its precision electroweak and Higgs measurements as well as the exploration of the high mass region where new physics may occur when the HL-LHC operates. Extra constraints on PDFs arise also from pp scattering as is discussed in a later chapter. Conceptually, however, the LHeC provides the important opportunity to completely separate the PDF determination from proton-proton physics. This approach is not only more precise for the PDFs but it is theoretically more accurate and enables sincere tests of QCD, by confronting independent predictions with LHC (and later FCC) measurements, as well as providing an unambiguous base for reliable interpretations of searches for new physics.

While the resolution of the longitudinal, collinear structure of the proton is key to the physics programme of the LHeC (and the LHC), the ep collider provides further fundamental insight in the structure of the proton: semi-inclusive measurements of jets and vector mesons, and especially Deeply Virtual Compton Scattering, a process established at HERA, will shed light on also the transverse structure of the proton in a new kinematic range. This is presented at the end of the current chapter.

1.1.1 Partons in Deep Inelastic Scattering

Parton Distribution Functions $xf(x, Q^2)$ represent a probabilistic view on hadron substructure at a given distance, $1/\sqrt{Q^2}$. They depend on the parton type $f = (q_i,\ g)$, for quarks and gluons, and must be determined from experiment, most suitably DIS, as perturbative QCD is not prescribing the parton density at a given momentum fraction Bjorken x. PDFs are important also for they determine Drell-Yan, hadron-hadron scattering processes, supposedly universally through the QCD factorisation theorem [6] [1]. The PDF programme of the LHeC is of unprecedented reach for the following reasons:

- For the first time it will resolve the partonic structure of the proton (and nuclei) completely, i.e. determine the u_v, d_v, u, d, s, c, b, and gluon momentum distributions through neutral and charged current cross section as well as direct heavy quark PDF measurements, performed in a huge kinematic range of DIS, from $x = 10^{-6}$ to 0.9 and from Q^2 above 1 to $10^6\,\mathrm{GeV}^2$. The LHeC explores the strange density and the momentum fraction carried by top quarks [8] which was impossible at HERA.
- Very high luminosity and unprecedented precision, owing to both new detector technology and the redundant evaluation of the event kinematics from the leptonic and hadronic final states, will lead to extremely high PDF precision, and accuracy.
- Because of the high LHeC energy, the weak probes ($W,\ Z$) dominate the interaction at larger Q^2 which permits the up and down sea and valence quark distributions to be resolved in the full range of x. Thus no further data will be required [2]: that is, there is no influence from higher twists nor nuclear uncertainties or data inconsistencies, which are the main diseases of current so-called global PDF determinations.

While PDFs are nowadays often seen as merely a tool for interpreting LHC data, in fact what really is involved is a new understanding of strong interaction dynamics and the deeper resolution of substructure extending into hitherto uncovered phase space regions, in particular the small x region, by virtue of the very high energy s, and the very small spatial dimension ($1/\sqrt{Q^2}$) and the $x \to 1$ region, owing to the high luminosity and energy. The QPM is not tested well enough, despite decades of DIS and other experiments, and QCD is not developed fully either.

Examples of problems of fundamental interest for the LHeC to resolve are: i) the long awaited resolution of the behaviour of u/d near the kinematic limit ($x \to 1$); ii) the flavour democracy of the light quark sea (is $d \simeq u \simeq s$??); iii) the existence of quark-level charge-symmetry [9]; iv) the behaviour of the ratio $\bar{d}/\bar{u}$ at small x; v) the turn-on and the values of heavy quark PDFs; vi) the value of the strong coupling constant, or, vii) the question of the dynamics, linear or non-linear, at small x where the gluon and quark densities rise.

[1] In his referee report on the LHeC CDR, in 2012, Guido Altarelli noted on the factorisation theorem in QCD for hadron colliders that: "many people still advance doubts. Actually this question could be studied experimentally, in that the LHeC, with its improved precision, could put bounds on the allowed amount of possible factorisation violations (e.g. by measuring in DIS the gluon at large x and then comparing with jet production at large p_T in hadron colliders)." This question was addressed also in a previous LHeC paper [7].

[2] The LHeC may be operated at basically HERA energies and collect a fb^{-1} of luminosity for cross checks and maximising the high x, medium Q^2 acceptance, see Sect. 1.2.

Of special further interest is the gluon distribution, for the gluon self-interaction prescribes all visible mass, the gluon-gluon fusion process dominates Higgs production at hadron colliders, the LHC and the FCC, and because its large x behaviour, essentially unknown today, affects predictions of BSM cross sections at the LHC.

The LHeC may be understood as an extension of HERA to a considerable extent. It has the reach in $x \propto 1/s$ to resolve the question of new strong interaction dynamics at small x and it accesses with huge luminosity high Q^2, much larger than $M^2_{W,Z}$, to make accurate use of weak NC and CC cross sections in DIS PDF physics for the first time. QCD analyses of HERA data are still ongoing. For obvious reasons, there is no quantitative analysis of LHC related PDF physics possible without relying on the HERA data, and often on its QCD analyses. These are introduced briefly next. Albeit with certain assumptions and limited luminosity, HERA yet changed the field of PDF physics as compared to fixed target data completely, see Ref. [10], and it opened the era of physics of high parton densities at small x.

1.1.2 Fit Methodology and HERA PDFs

The methodology of PDF determinations with HERA data has been developed over decades by the H1 and ZEUS Collaborations [11–13], in close contact with many theorists. It has been essentially adopted with suitable modifications for the LHeC PDF prospect study as is detailed subsequently.

HERAPDF fits use information from both $e^{\pm}p$ neutral current and charged current scattering from exclusively the *ep* collider experiments, H1 and ZEUS, up to high $Q^2 = 30\ 000\,\mathrm{GeV}^2$ and down to about $x = 5 \cdot 10^{-5}$. The precision of the HERA combined data is below 1.5 % over the Q^2 range of $3 < Q^2 < 500\,\mathrm{GeV}^2$ and remains below 3% up to $Q^2 = 3000\,\mathrm{GeV}^2$. The precision for large $x > 0.5$ is rather poor due to limited luminosity and high-x acceptance limitations at medium Q^2.

The QCD analysis is performed at LO, NLO and NNLO within the *xFitter* framework [12, 14, 15], and the latest version is the HERAPDF2.0 family [13]. The DGLAP evolution of the PDFs, as well as the light-quark coefficient functions, are calculated using QCDNUM [16, 17]. The contributions of heavy quarks are calculated in the general-mass variable-flavour-number (GMVFN) scheme of Refs. [18,19]. Experimental uncertainties are determined using the Hessian method imposing a $\chi^2{+}1$ criterion. This is usually impossible in global fits over rather incoherent data sets originating from different processes and experiments, but has been a major advantage of the solely HERA based QCD analyses.

In the HERAPDF analysis, as well as subsequently in the LHeC study, the starting scale is chosen to be $Q^2_0 = 1.9\,\mathrm{GeV}^2$ such that it is below the charm mass threshold, m^2_c. The strong coupling constant is set to $\alpha_S(M_Z) = 0.118$ [3]. A minimum Q^2 cut, $Q^2_{min} \geq 3.5\,\mathrm{GeV}^2$, is imposed on the HERA data for staying in the DIS kinematic range. All these assumptions are varied in the evaluation of model uncertainties on the resulting fit. These variations will essentially have no significant effect with the LHeC as the sensitivity to the quark masses, for example, is hugely improved with respect to HERA, α_s known to $1-2$ per mille, and the kinematic range of the data is much extended.

[3] The strong coupling constant cannot be reliably determined from inclusive HERA data alone. DIS results, including fixed target data, have provided values which tend to be lower than the here chosen value, see for a discussion Ref. [20]. As is further presented in detail in Sect. 2.1 the LHeC reaches a sensitivity to α_s at the per mille level based on inclusive and jet data as well as their combination.

In HERAPDF fits, the quark distributions at the initial Q_0^2 are represented by the generic form

$$xq_i(x) = A_i x^{B_i}(1-x)^{C_i} P_i(x), \tag{1.1}$$

where i specifies the flavour of the quark distribution and $P_i(x) = (1+D_i x+E_i x^2)$. The inclusive NC and CC cross sections determine four independent quark distributions, essentially the sums of the up and down quark and anti-quark densities. These may be decomposed into any four other distributions of up and down quarks with an ad-hoc assumption on the fraction of strange to anti-down quarks which has no numeric effect on the PDFs, apart from that on xs itself. In HERAPDF2.0 the parameterised quark distributions, xq_i, are chosen to be the valence quark distributions (xu_v, xd_v) and the light anti-quark distributions ($x\bar{u}$, $x\bar{d}$). This has been adopted for the LHeC also.

The parameters A_{u_v} and A_{d_v} are fixed using the quark counting rule. The normalisation and slope parameters, A and B, of $\bar{u}$ and $\bar{d}$ are set equal such that $x\bar{u} = x\bar{d}$ at $x \to 0$, a crucial assumption which the LHeC can validate. The strange quark PDF $x\bar{s}$ is set as a fixed fraction $r_s = 0.67$ of $x\bar{d}$. This fraction is varied in the determination of model uncertainties. By default it is assumed that $xs = x\bar{s}$ and that u and d sea and anti-quarks have the same distributions also. These assumptions will be resolved by the LHeC and their uncertainties be eliminated, see Sect. 1.3.4. The D, E and F parameters in the polynomial $P_i(x)$ are used only if required by the data, following a χ^2 saturation procedure described in Ref. [12]. This leads for HERAPDF2.0 to two additional terms, $P_{u_v}(x) = 1 + E_{u_v}x^2$ and $P_{\bar{u}} = 1 + D_{\bar{u}}x$.

The gluon distribution is parameterised differently

$$xg(x) = A_g x^{B_g}(1-x)^{C_g} - A'_g x^{B'_g}(1-x)^{C'_g}. \tag{1.2}$$

The normalisation parameters A_g and A'_g are fixed using the momentum sum rule. Variations of the PDFs were also considered with $A'_g = 0$ which for all initial HERA data fits had been the default choice. The appearance of this negative second term may be understood as coming from a not-well constrained behaviour of $xg(x, Q^2)$ at small x. In fact, xg is resembling a valence-quark distribution at $Q^2 \simeq Q_0^2$. The much extended Q^2 range of the LHeC at a given small x and the access to much smaller x values than probed at HERA will quite certainly enable this behaviour to be clarified. Since also C'_g had been set to just a large value, there is negligible effect of that second term in Eq. (1.2) on the resulting PDF uncertainties. Consequently A'_g is set to zero in the LHeC study.

Alternative parameterisations are used in the evaluation of the parameterisation uncertainty. These variations include: introducing extra parameters D, E for each quark distribution; the removal of primed gluon parameters; and the relaxation of assumptions about the low-x sea. These fits provide alternative extracted PDFs with similar fit χ^2. The maximum deviation from the central PDF at each value of x is taken as an envelope and added in quadrature with the experimental and model uncertainties to give the total uncertainty. As for the model uncertainties, the extended range and improved precision of the LHeC data may well be expected to render such variations negligible.

The results of the HERA PDF analysis [13] are shown in Fig. 1.1 for the HERAPDF2.0NNLO PDF set, displaying experimental, model and parameterisation uncertainties separately. The structure of the proton is seen to depend on the resolution $\propto 1/\sqrt{Q^2}$, with which it is probed. At Q^2 of about $1-2\,\mathrm{GeV}^2$, corresponding to 0.2 fm, the parton contents may be decomposed as is shown in Figure 1.1 top. The gluon distribution at $Q^2 \simeq 1\,\mathrm{GeV}^2$ has a valence like shape, i.e. at very low x the momentum is carried by sea quarks, see Fig. 1.1 (top) . At medium $x \sim 0.05$ the gluon density dominates over all quark densities. At largest x, above 0.3, the

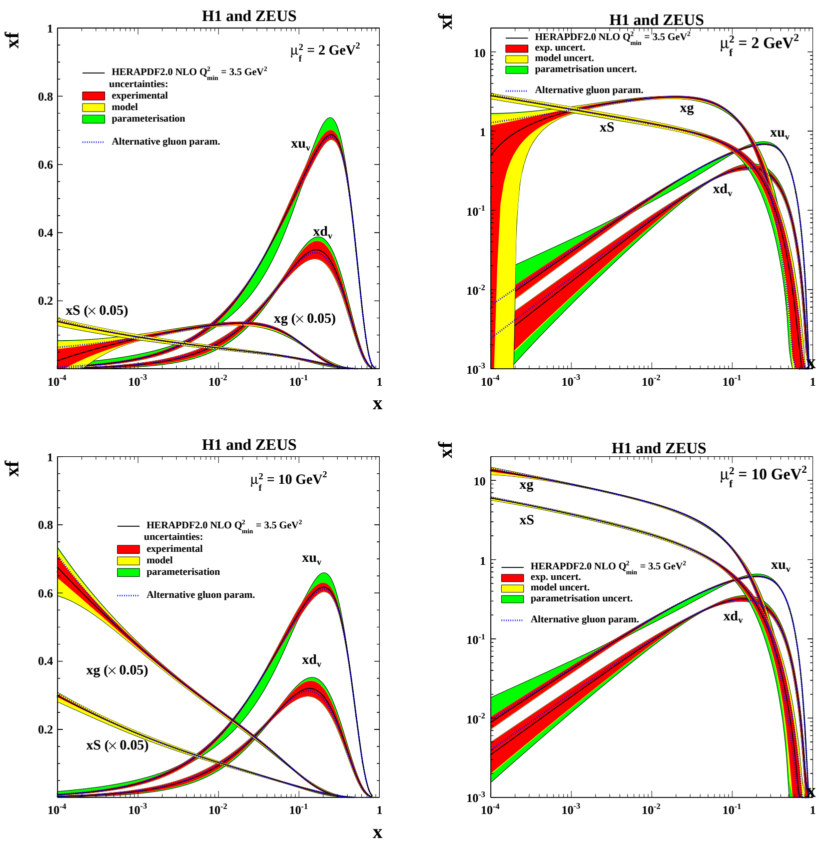

Figure 1.1: Parton distributions as determined by the QCD fit to the combined H1 and ZEUS data at $Q^2 = 1.9$ GeV^2 (top) and at $Q^2 = 10$ GeV^2 (bottom). The color coding represents the experimental, model and parameterisation uncertainties separately. Here $xS = 2x(\overline{U} + \overline{D})$ denotes the total sea quark density. Note that xg and xS are scaled by $1/20$ in the left side plots with a linear y scale.

proton structure is dominated by the up and down valence quarks. This picture evolves such that below 10^{-16} m, for $x \leq 0.1$, the gluon density dominates also over the sea quark density, see Figure 1.1 (bottom). The valence quark distributions are rather insensitive to the resolution which reflects their non-singlet transformation behaviour in QCD.

The HERAPDF set differs from other PDF sets in that: i) it represents a fit to a consistent data set with small correlated systematic uncertainties; ii) it uses data on solely a proton target such that no heavy target corrections are needed and the assumption of strong isospin invariance, $d_{\text{proton}} = u_{\text{neutron}}$, is not required; iii) a large x, Q^2 region is covered such that no regions where higher twist effects are important are included in the analysis.

The limitations of HERA PDFs are known as well: i) the data is limited in statistics such that the region $x > 0.5$ is poorly constrained; ii) the energy is limited such that the very low x region, below $x \simeq 10^{-4}$, is not or not reliably accessed; iii) limits of luminosity and energy implied that the potential of the flavour resolution through weak interactions, in NC and CC, while remarkable, could not be utilised accurately; iv) while the strange quark density was not accessed by H1 and ZEUS, only initial measurements of xc and xb could be performed. The strong success with respect to the fixed target PDF situation *ante* HERA has been most remarkable. The thorough clarification of parton dynamics and the establishment of a precision PDF base for the LHC and later hadron colliders, however, make a next generation, high energy and luminosity ep collider a necessity. The PDF potential of the LHeC is presented next.

1.2 Simulated LHeC Data

1.2.1 Inclusive Neutral and Charged Current Cross Sections

In order to estimate the uncertainties of PDFs from the LHeC, several sets of LHeC inclusive NC/CC DIS data with a full set of uncertainties have been simulated and are described in the following. The systematic uncertainties of the DIS cross sections have a number of sources, which can be classified as uncorrelated and correlated across bin boundaries. For the NC case, the uncorrelated sources, apart from event statistics, are a global efficiency uncertainty, due for example to tracking or electron identification errors, as well as uncertainties due to photo-production background, calorimeter noise and radiative corrections. The correlated uncertainties result from imperfect electromagnetic and hadronic energy scale and angle calibrations. In the classic *ep* kinematic reconstruction methods used here, the scattered electron energy E_e' and polar electron angle θ_e, complemented by the energy of the hadronic final state E_h, can be employed to determine Q^2 and x in a redundant way.

Briefly, Q^2 is best determined with the electron kinematics and x is calculated from $y = Q^2/sx$. At large y, the inelasticity is best measured using the electron energy, $y_e \simeq 1 - E_e'/E_e$. At low y, the relation $y_h = E_h \sin^2(\theta_h/2)/E_e$ can be used to provide a measurement of the inelasticity with the hadronic final state energy E_h and angle θ_h. This results in the uncertainty $\delta y_h/y_h \simeq \delta E_h/E_h$, which is determined by the E_h calibration uncertainty to good approximation.

There have been various refined methods proposed to determine the DIS kinematics, such as the double angle method [21], which is commonly used to calibrate the electromagnetic energy scale, or the so-called Σ method [22], which exhibits reduced sensitivity to QED radiative corrections, see a discussion in Ref. [23]. For the estimate of the cross section uncertainty the electron method (Q_e^2, y_e) is used at large y, while at low y we use Q_e^2, y_h, which is transparent and accurate to better than a factor of two. In much of the phase space, moreover, it is rather the uncorrelated efficiency or further specific errors than the kinematic correlations, which dominate the cross section measurement precision.

The assumptions used in the simulation of pseudodata are summarised in Tab. 1.1. The procedure was gauged with full H1 Monte Carlo simulations and the assumptions are corresponding to H1's achievements with an improvement by at most a factor of two. Using a numerical procedure developed in Ref. [24], the scale uncertainties are transformed to kinematics-dependent correlated cross-section uncertainties caused by imperfect measurements of E_e', θ_e and E_h. These

Source of uncertainty	Uncertainty
Scattered electron energy scale $\Delta E_e'/E_e'$	0.1 %
Scattered electron polar angle	0.1 mrad
Hadronic energy scale $\Delta E_h/E_h$	0.5 %
Radiative corrections	0.3 %
Photoproduction background (for $y > 0.5$)	1 %
Global efficiency error	0.5 %

Table 1.1: Assumptions used in the simulation of the NC cross sections on the size of uncertainties from various sources. The top three are uncertainties on the calibrations which are transported to provide correlated systematic cross section errors. The lower three values are uncertainties of the cross section caused by various sources.

data uncertainties were imposed for all data sets, NC and CC, as are subsequently listed and described.

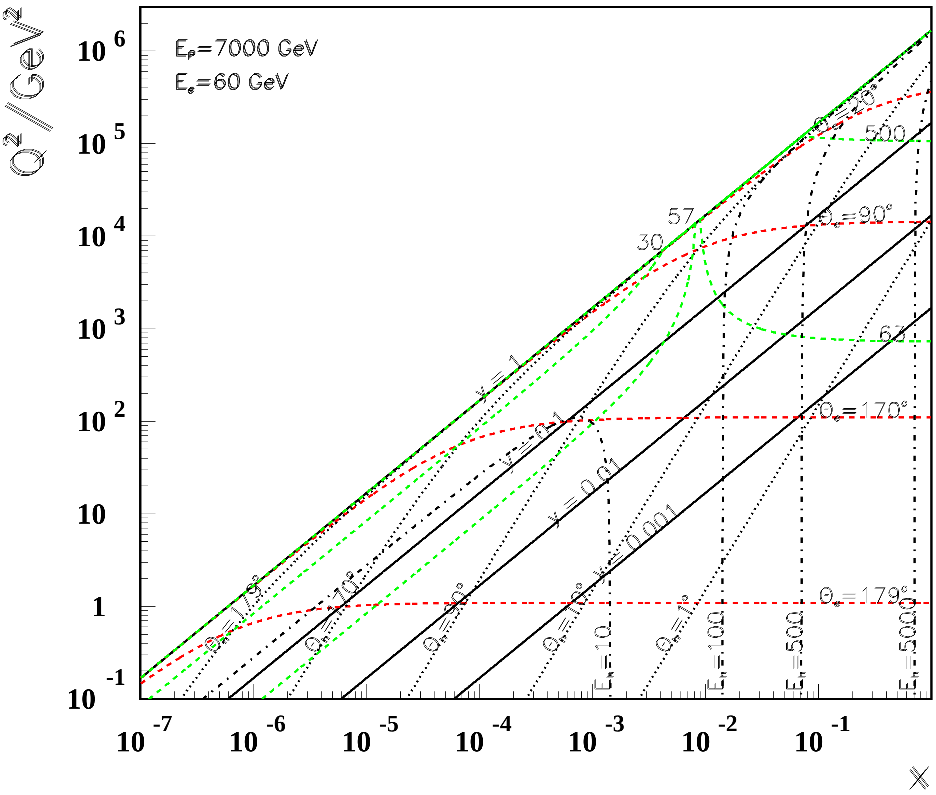

Figure 1.2: Kinematic plane covered with the maximum beam energies at the LHeC. Red dashed: Lines of constant scattered electron polar angle. Note that low Q^2 is measured with electrons scattered into the backward region, highest Q^2 is reached with Rutherford backscattering; Black dotted: lines of constant angle of the hadronic final state; Black solid: Lines of constant inelasticity $y = Q^2/sx$; Green dashed: Lines of constant scattered electron energy E_e'. Most of the central region is covered by what is termed the kinematic peak, where $E_e' \simeq E_e$. The small x region is accessed with small energies E_e' below E_e while the very forward, high Q^2 electrons carry TeV energies; Black dashed-dotted: lines of constant hadronic final state energy E_h. Note that the very forward, large x region sees very high hadronic energy deposits too.

The design of the LHeC assumes that it operates with the LHC in the high luminosity phase, following LS4 at the earliest. As detailed in Chapter 2, it is assumed there will be an initial phase, during which the LHeC may collect $50\,\text{fb}^{-1}$ of data. This may begin with a sample of $5\,\text{fb}^{-1}$. Such values are very high when compared with HERA, corresponding to the hundred(ten)-fold of luminosity which H1 collected in its lifetime of about 15 years. The total luminosity may come close to $1\,\text{ab}^{-1}$.

The bulk of the data is assumed to be taken with electrons, possibly at large negative helicity P_e, because this configuration maximises the number of Higgs bosons that one can produce at the LHeC: e^- couples to W^- which interacts primarily with an up-quark and the CC cross section is proportional to $(1 - P_e)$. However, for electroweak physics there is a strong interest to vary the polarisation and charge [4]. It was considered that the e^+p luminosity may reach $1\,\text{fb}^{-1}$ while the tenfold has been simulated for sensitivity studies. A dataset has also been produced

[4] With a linac source, the generation of an intense positron beam is very challenging and will not be able to compete with the electron intensity. This is discussed in the accelerator chapter.

with reduced proton beam energy as that enlarges the acceptance towards large x at smaller Q^2. Dedicated further sets have been generated for the F_L study (Sect. 2.2.3). The full list of simulated sets is provided in Tab. 1.2.

Parameter	Unit	Data set								
		D1	D2	D3	D4	D5	D6	D7	D8	D9
Proton beam energy	TeV	7	7	7	7	1	7	7	7	7
Lepton charge		-1	-1	-1	-1	-1	$+1$	$+1$	-1	-1
Longitudinal lepton polarisation		-0.8	-0.8	0	-0.8	0	0	0	$+0.8$	$+0.8$
Integrated luminosity	fb^{-1}	5	50	50	1000	1	1	10	10	50

Table 1.2: Summary of characteristic parameters of data sets used to simulate neutral and charged current $e^{\pm}$ cross section data, for a lepton beam energy of $E_e = 50$ GeV.

The highest energies obviously give access to the smallest x at a given Q^2, and to the maximum Q^2 at fixed x. This is illustrated with the kinematic plane and iso-energy and iso-angle lines, see Fig. 1.2. It is instructive to see how the variation of the proton beam energy changes the kinematics considerably and enables additional coverage of various regions. This is clear from Fig. 1.3 which shows the kinematic plane choosing the about minimum energies the LHeC could operate with. There are striking changes one may note which are related to kinematics

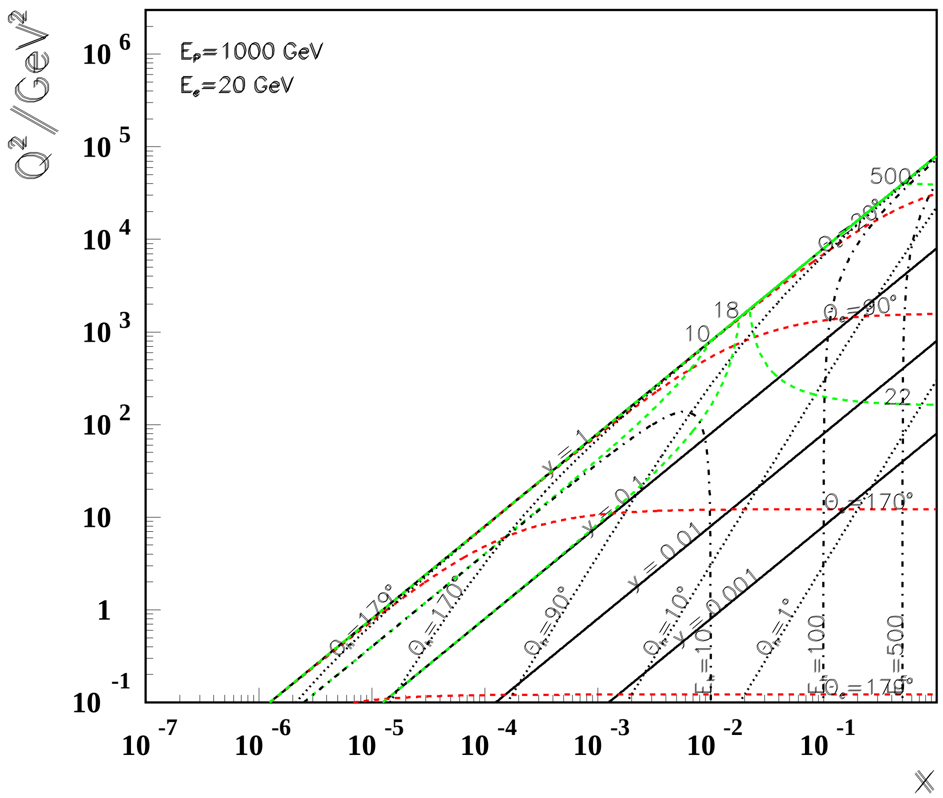

Figure 1.3: Kinematic plane covered with the minimum beam energies at LHeC. The meaning of the curves is the same as in the previous figure. This coverage is very similar to that by HERA as the energies are about the same.

(c.f. Ref. [24]). For example, one can see that the line of $\theta_e = 179°$ now corresponds to $Q^2 \simeq 0.1\,\mathrm{GeV}^2$ which is due to lowering E_e as compared to $1\,\mathrm{GeV}^2$ in the maximum energy case, cf. Fig. 1.2. Similarly, comparing the two figures one finds that the lower Q^2, larger x region becomes much easier accessible with lower energies, in this case solely owing to the reduction of E_p from 7 to 1 TeV. It is worthwhile to note that the LHeC, when operating at these low energies, would permit a complete repetition of the HERA programme, within a short period of special data taking.

The coverage of the kinematic plane is illustrated in the plot of the x, Q^2 bin centers of data points used in simulations, see Fig. 1.4 [25]. The full coverage at highest Bjorken-x, i.e. very close to $x = 1$, is enabled by the high luminosity of the LHeC. This was impossible to achieve for HERA as the NC/CC DIS cross sections decrease proportional to some power of $(1 - x)$ when x approaches 1, as has long been established with Regge counting [26–28].

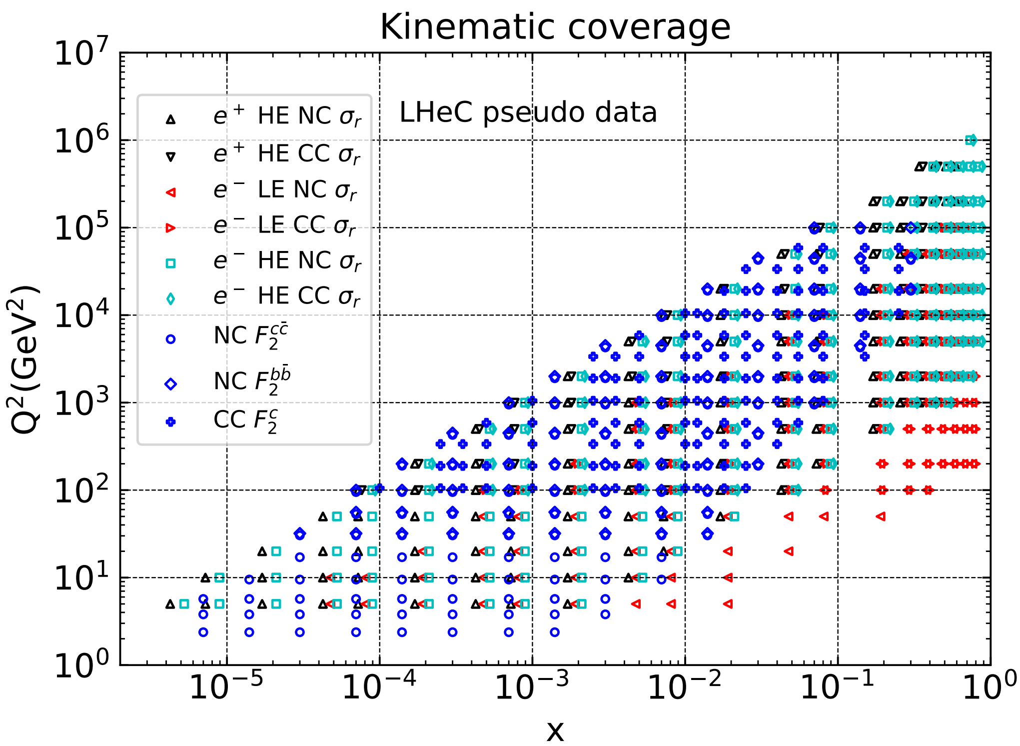

Figure 1.4: Illustration of the x, Q^2 values of simulated cross section and heavy quark density data used in LHeC studies. The red points illustrate the gain in acceptance towards large x at fixed Q^2 when E_p is lowered, see text.

It has been a prime goal, leading beyond previous PDF studies, to understand the importance of these varying data taking conditions for measuring PDFs with the LHeC. This holds especially for the question about what can be expected from an initial, lower luminosity LHeC operation period, which is of highest interest for the LHC analyses during the HL-LHC phase. Some special data sets of lowered electron energy have also been produced in order to evaluate the potential to measure F_L, see Sect. 2.2.3. These data sets have not been included in the bulk PDF analyses presented subsequently in this Chapter.

1.2.2 Heavy Quark Densities

The LHeC is the ideal environment for a determination of the strange, charm and bottom density distributions which is necessary for a comprehensive unfolding of the parton contents and dynamics in protons and nuclei. The principal technique is charm tagging (in CC for xs, in NC for xc) and bottom tagging (in NC for xb). The beam spot of the LHeC has a transverse extension of about $(7\,\mu\mathrm{m})^2$. The inner Silicon detectors has a resolution of typically 10 microns to be compared with decay lengths of charm and beauty particles of hundreds of μm. The experimental challenges then are the beam pipe radius, coping at the LHeC with strong synchrotron radiation effects, and the forward tagging acceptance, similar to the HL-LHC challenges albeit much easier through the absence of pile-up in ep. Very sophisticated techniques are being developed at the LHC in order to identify bottom production through jets [29] which are not touched upon here.

A simulation was made of the possible measurements of the anti-strange density (Fig. 1.5) using impact parameter tagging in ep CC scattering, and of the charm and beauty structure functions using $c$and b tagging in NC (Figs. 1.6, 1.7). The results served as input for the PDF study subsequently presented.

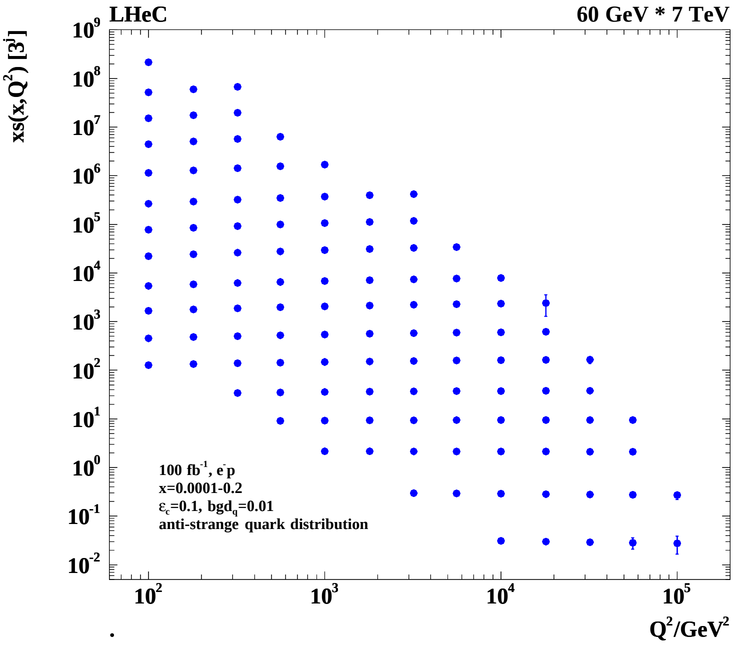

Figure 1.5: Simulation of the measurement of the (anti)-strange quark distribution, $x\bar{s}(x,Q^2)$, in charged current e^-p scattering through the t-channel reaction $W^-\bar{s} \to c$. The data are plotted with full systematic and statistical errors added in quadrature, mostly non-visible. The covered x range extends from 10^{-4} (top left bin), determined by the CC trigger threshold conservatively assumed to be at $Q^2 = 100\,\mathrm{GeV}^2$, to $x \simeq 0.2$ (bottom right) determined by the forward tagging acceptance limits, which could be further extended by lowering E_p.

Following experience on heavy flavour tagging at HERA and ATLAS, assumptions were made on the charm and beauty tagging efficiencies, to be 10 % and 60 %, respectively. The light-quark background in the charm analysis is assumed to be controllable to per cent level, while the charm background in the beauty tagging sample is assumed to be 10 %. The tagging efficiencies and background contaminations affect the statistical error which for the assumed $100\,\mathrm{fb}^{-1}$ is negligible, apart from edges of phase space as the figures illustrate for all three distribution.

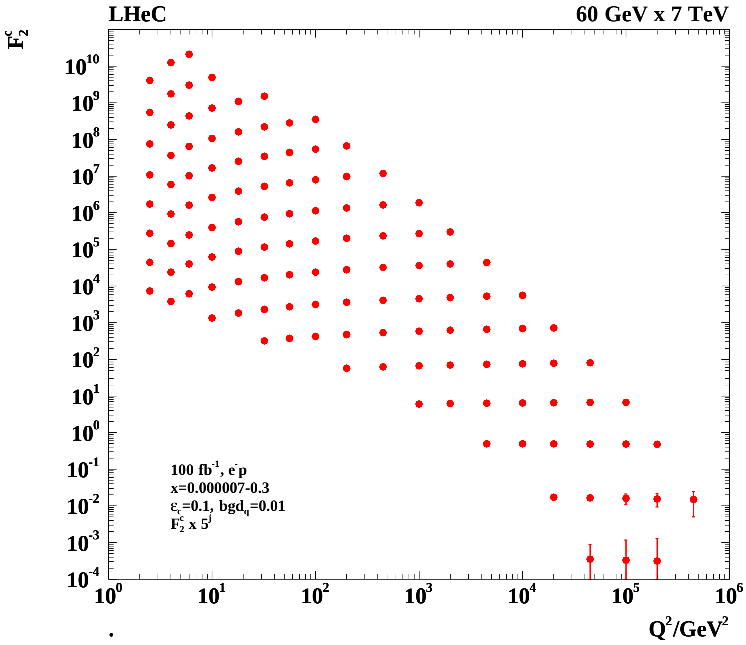

Figure 1.6: Simulation of the measurement of the charm quark distribution expressed as $F_2^c = e_c^2 x(c+\bar{c})$ in neutral current e^-p scattering. The data are plotted with full systematic and statistical errors added in quadrature, mostly invisible. The minimum x (left top bin) is at $7 \cdot 10^{-6}$, and the data extend to $x = 0.3$ (right bottom bin). The simulation uses a massless scheme and is only indicative near threshold albeit the uncertainties entering the QCD PDF analysis are estimated consistently.

An additional uncorrelated systematic error is assumed in the simulated strange and beauty quark measurements of 3 % while for charm a 2 % error is used. These errors determine the measurement uncertainties in almost the full kinematic range. At higher Q^2 and x, these increase, for example to 10, 5 and 7 % for xs, xc and xb, respectively, at $x \simeq 0.1$ and $Q^2 \simeq 10^5\,\text{GeV}^2$. As is specified in the figures, the x and Q^2 ranges of these measurements extend over 3, 5 and 4 orders of magnitude for s, c and b. The coverage of very high Q^2 values, much beyond M_Z^2, permits to determine the c and b densities probed in γZ interference interactions for the first time. At HERA, xs was not accessible while pioneering measurements of xc and xb could be performed [30], albeit in a smaller range and with lesser precision than shall be achieved with the LHeC. These measurements, as discussed below and in much detail in the 2012 LHeC CDR [1], are of vital importance for the development of QCD and for the interpretation of precision LHC data.

1.3 Parton Distributions from the LHeC

1.3.1 Procedure and Assumptions

In this section, PDF constraints from the simulation of LHeC inclusive NC and CC cross section measurements and heavy quark densities are investigated. The analysis closely follows the one for HERA as presented above.

The expectations on PDFs for the “LHeC inclusive” dataset, corresponding to the combination

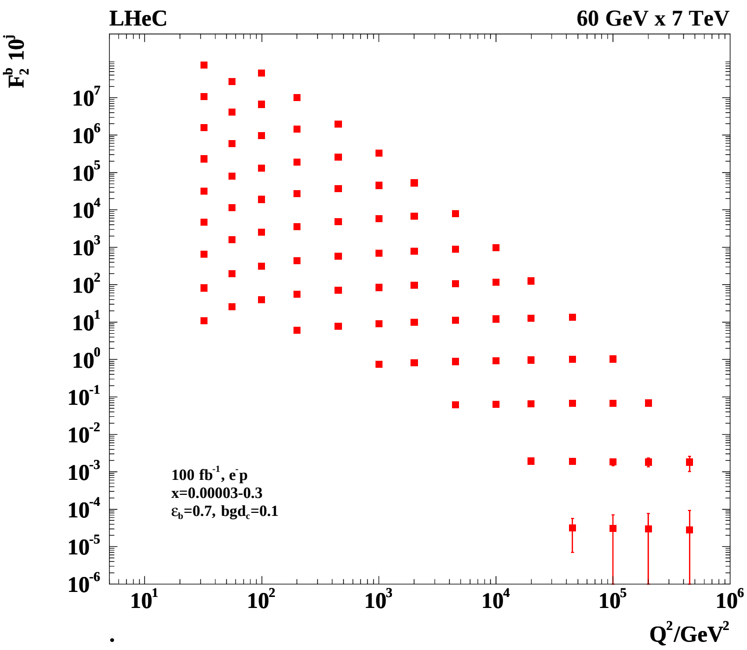

Figure 1.7: Simulation of the measurement of the bottom quark distribution expressed as $F_2^b = e_b^2 x(b+\bar{b})$ in neutral current e^-p scattering. The data are plotted with full systematic and statistical errors added in quadrature, mostly invisible. The minimum x (left top bin) is at $3 \cdot 10^{-5}$, and the data extend to $x = 0.3$ (right bottom bin). The simulation uses a massless scheme and is only indicative near threshold albeit the uncertainties entering the QCD PDF analysis are estimated consistently.

of datasets D4+D5+D6+D8, are presented, see Tab. 1.2. While this full combination is recorded concurrently to the HL-LHC operation, it will be available only after the end of the HL-LHC, and will become valuable for re-analysis or re-interpretation of (HL-)LHC data, and for further future hadron colliders.

Given the expected timeline for the HL-LHC, it is of high relevance that the LHeC can deliver PDFs of transformative precision already on a short timescale, in order to be useful during the lifetime of the HL-LHC. Therefore, in the present study particular attention is paid to PDF constraints that can be extracted from the first $50\,\text{fb}^{-1}$ of electron-proton data, which corresponds to the first three years of LHeC operation. The dataset is labelled D2 in Tab. 1.2 and also referred to as “LHeC 1st run” in the following.

Since even the initial instantaneous luminosity may exceed that of HERA significantly, and the kinematic range will largely be extended, the data recorded already during the initial weeks of data taking are highly valuable and will impose new PDF constraints, and these analyses will provide the starting point for the LHeC PDF programme. It may be recalled that the HERA I data period (1992-2000) provided just $0.1\,\text{fb}^{-1}$ of data which was ample for discovering the rise of F_2 and of xg towards small x at low Q^2. The sets in Tab. 1.2 comprise D1, with $5\,\text{fb}^{-1}$, still the tenfold of what H1 collected in 15 years, and D3, which resembles D2 but has the electron polarisation set to zero.

Additional dedicated studies of the impact of s, c, b data on the PDFs are then also presented, based on $10\,\text{fb}^{-1}$ of e^-p simulated data. Note, the precision measurements of s, c, b final states are not exploited in the PDF “LHeC 1st run” study, which considers only inclusive NC/CC DIS data, although such data will be available from the initial operation.

Further important PDF constraints that would be provided by measurements of F_L and jets are not considered in the present study. These remarks are significant in that they mean one has to be cautious when comparing the LHeC PDF potential with some global fits: F_L will resolve the low x non-linear parton interaction issue, see Sect. 2.2.3, and jets are important to pin down the gluon density behaviour at large x as well as providing a precision measurement of α_s, Sect. 2.1.

To assess the importance of different operating conditions, the impact of datasets with: differing amounts of integrated luminosity (D1 vs. D4); positrons (D6 vs. D7); and with different polarisation states for the leptons (D3 vs. D8) are also considered.

In order to study the effects of the LHeC data on the knowledge of PDFs, fits to the simulated input datasets, including their full systematic uncertainties as detailed above, are performed in NLO QCD. Fits in NNLO have been performed as a cross check. The present analysis follows closely the HERA QCD fit procedure as outlined above. The parameterised PDFs are the valence distributions xu_v and xd_v, the gluon distribution xg, and the $x\bar{U}$ and $x\bar{D}$ distributions, where $x\bar{U} = x\bar{u}$, $x\bar{D} = x\bar{d} + x\bar{s}$, where the parametric functions as in Eqs. (1.1) and (1.2) are used. The chosen fit parameters are similar, albeit to some extent more flexible, than for HERAPDF2.0 due to the stronger constraints from the LHeC. In total 14 parameters are free for the nominal fits. Specifically, the following parameters are set free: B_g, C_g, D_g, B_{uv}, C_{uv}, E_{uv}, B_{dv}, C_{dv}, $A_{\bar{U}}$, $B_{\bar{U}}$, $C_{\bar{U}}$, $A_{\bar{D}}$, $B_{\bar{D}}$, $C_{\bar{D}}$. Note, the B parameters for u_v and d_v, and the A and B parameters for $\bar{U}$ and $\bar{D}$ are fitted independently, such that the up and down valence and sea quark distributions are uncorrelated in the analysis, whereas for HERAPDF2.0 $x\bar{u} \to x\bar{d}$ as $x \to 0$ is imposed. The other main difference is that no negative gluon term has been included, i.e. $A'_g = 0$.

This ansatz is natural to the extent that the NC and CC inclusive cross sections determine the sums of up and down quark distributions, and their anti–quark distributions, as the four independent sets of PDFs, which may be transformed to the ones chosen if one assumes $u_v = U - \overline{U}$ and $d_v = D - \bar{D}$, i.e. the equality of anti– and sea–quark distributions of given flavour. For the majority of the QCD fits here presented, the strange quark distribution at Q_0^2 is assumed to be a constant fraction of $\bar{D}$, $x\bar{s} = f_s x\bar{D}$ with $f_s = 0.4$ as for HERAPDF, while this assumption is relaxed for the fits including simulated s, c, b data.

Note, that the prospects presented here are illustrations for a different era of PDF physics, which will be richer and deeper than one may be able to simulate now. For instance, without real data one cannot determine the actual parameterisation needed for the PDFs. In particular the low x kinematic region was so far unexplored and the simulated data relies on a simple extrapolation of nowadays PDFs, and no reliable data or model is available that provides constraints on this region[5]. The LHeC data explores new corners of phase space with high precision, and therefore it will have a great potential, much larger than HERA had, to determine the parameterisation. As another example, with LHeC data one can directly derive relations for how the valence quarks are determined with a set of NC and CC cross section data in a redundant way, since the gluon distribution at small x can be determined from the Q^2 derivative of F_2 and from a measurement of F_L. The question of the optimal gluon parameterisation may then be settled by analysing these constraints and not by assuming some specific behaviour of a given fit.

Furthermore, the precise direct determinations of s, c and b densities with measurements of the impact parameter of their decays, will put the treatment of heavy flavours in PDF analyses on a new level. The need for the phenomenological introduction of the f_s factor will disappear and

[5] It is expected that real LHeC data, and also the inclusion of further information such as F_{L}, will certainly lead to a quite different optimal parameterisation ansatz than was used in the present analysis. Though, it has been checked that with a more relaxed set of parameters, very similar results on the PDF uncertainties are obtained, which justifies the size of the prospected PDF uncertainties.

the debate on the value of fixed and variable heavy flavour schemes will be settled.

1.3.2 Valence Quarks

Since the first moments of DIS physics, it had been proposed to identify partons with quarks and to consider the proton to consist of valence quarks together with "an indefinite number of ($q\bar{q}$) pairs" [31]. 50 years later there are still basic questions unanswered about the behaviour of valence quarks, such as the d_v/u_v ratio at large x, and PDF fits struggle to resolve the flavour composition and interaction dynamics of the sea. The LHeC is the most suited machine to resolve these challenges.

The precision that can be expected for the valence quark distributions from the LHeC is illustrated in Fig. 1.8, and compared to a variety of modern PDF sets. Today, the knowledge of the valence quark distributions, particularly at large x, is fairly limited as it can be derived from the Figure. This is due to the limited HERA luminosity, challenging systematics that rise $\propto 1/(1-x)$, and to nuclear correction uncertainties. At low x the valence quark distributions are very small compared to the sea quarks and cannot be separated easily from these.

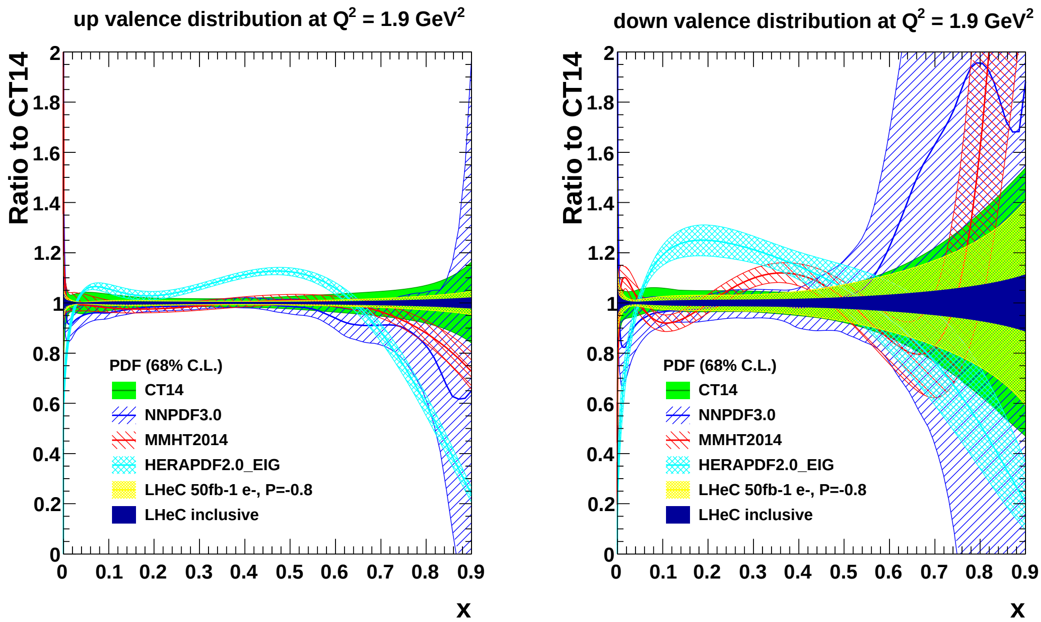

Figure 1.8: Valence quark distributions at $Q^2 = 1.9\,\mathrm{GeV}^2$ as a function of x, presented as the ratio to the CT14 [32] central values. The yellow band corresponds to the "LHeC 1st run" PDFs (D2), while the dark blue shows the final "LHeC inclusive" PDFs based on the data sets (D4+D5+D6+D8), as described in Sect. 1.3.1. For the purposes of illustrating the improvement to the uncertainties more clearly, the central value of the LHeC PDF has been scaled to the CT14 PDF, which itself is displayed by the green band. Note that the light blue HERAPDF2.0_EIG band corresponds to the experimental uncertainties only.

The u valence quark distribution is much better known than the d valence, since it enters with a four-fold weight in F_2 due to the electric quark charge ratio squared. Nevertheless, a substantial improvement in d_v by the LHeC is also visible, because the relative weight of d_v to u_v is changing favourably towards the down quark due to the influence of weak NC and CC interactions at high Q^2 where the LHeC is providing very accurate data. The strong constraints to the highest x

valence distributions at the LHeC are due to the very high integrated luminosity and large energy, and the corresponding extension in kinematic reach of the data in x (and Q^2) in comparison to HERA. At the LHC, in contrast, the highest x are only accessible as convolutions with partons at lower x, and those can therefore not be well constrained.

Note that the "LHeC 1st run" PDF, displayed by the yellow band in Fig. 1.8, includes only electron, i.e. no positron, data. In fact, from the $e^{\pm}p$ cross section differences access to valence quarks at low x can be obtained. As has already been illustrated in the CDR from 2012 [1] the sum of $2u_v + d_v$ may be measured directly with the NC γZ interference structure function $xF_3^{\gamma Z}$ down to $x \simeq 10^{-4}$ with very good precision. Thus the LHeC will have a direct access to the valence quarks at small x. This also tests the assumption of the equality of sea- and anti-quark densities which if different would cause $xF_3^{\gamma Z}$ to rise towards small x.

The precise determinations of the valence quark distributions at large x have strong implications for physics at the HL-LHC, in particular for BSM searches. The precise determinations of the valence quarks will resolve the long standing mystery of the behaviour of the d/u ratio at large x, see Fig. 1.9. As exemplarily shown in Fig. 1.9, there are currently conflicting theoretical pictures for the central value of the d/u ratio, albeit the large uncertainty bands of the different PDF sets mainly overlap. As of today, the constraints from data are inconclusive statistically and also suffer from large uncertainties from the use of DIS data on nuclear targets, which therefore

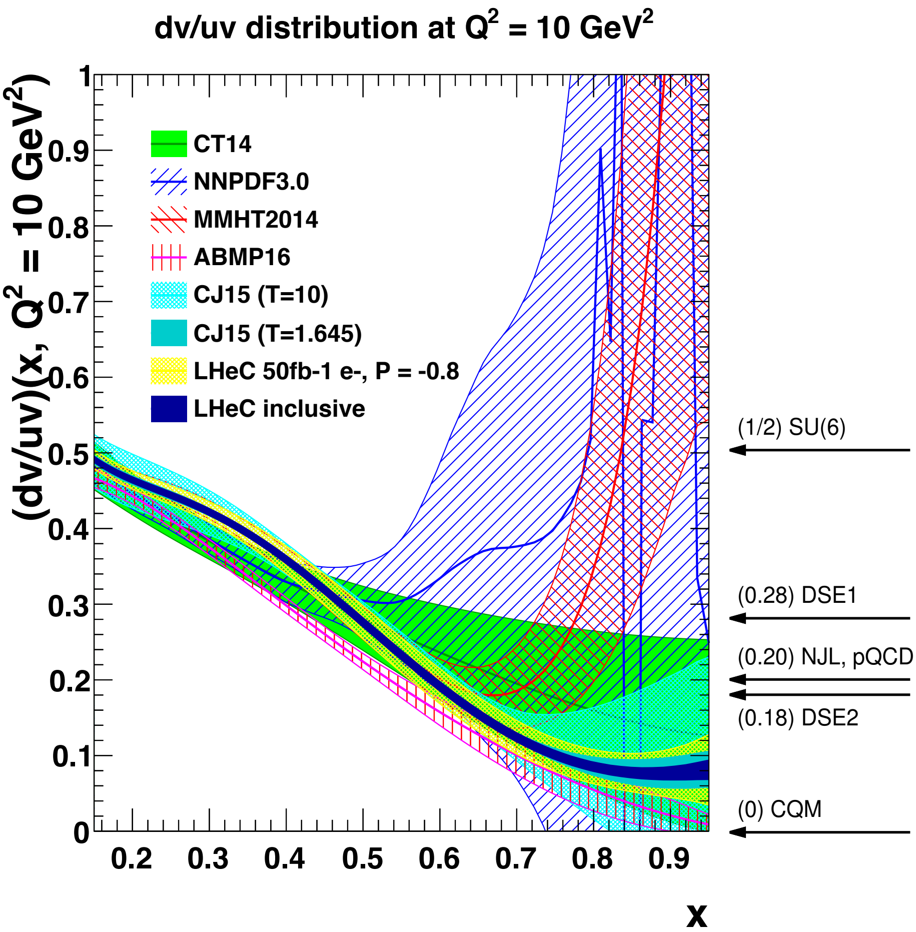

Figure 1.9: The d_v/u_v distribution at $Q^2 = 10\,\mathrm{GeV}^2$ as a function of x. The yellow band corresponds to the "LHeC 1st run" PDFs (D2), while the dark blue shows the final "LHeC inclusive" result. Both LHeC PDFs shown are scaled to the central value of CT14.

cause those large uncertainties.

1.3.3 Light Sea Quarks

Our knowledge today about the anti-quark distributions is fairly poor and uncertainties are very large at smaller values of x, and also at the highest x. In particular, at low x the size of the anti-quark PDFs are large and they contribute significantly to precision SM measurements at the HL-LHC. At high x, sea and valence need to be properly distinguished and accurately be measured for reliable BSM searches at high mass.

Our knowledge about the anti-quark PDFs will be changed completely with LHeC data. Precise constraints are obtained with inclusive NC/CC DIS data despite the relaxation of any assumptions in the fit ansatz that would force $\bar{u} \to \bar{d}$ as $x \to 0$, as it is present in other PDF determinations today. At smaller Q^2 in DIS one measures essentially $F_2 \propto 4\bar{U} + \bar{D}$. Thus, at HERA, with limited precision at high Q^2, one could not resolve the two parts, neither will that be possible at any other lower energy ep collider which is just not reaching small x. At the LHeC, in contrast, the CC DIS cross sections are measured very well down to x values even below 10^{-4}, and in addition there are strong weak current contributions to the NC cross section which probe the flavour composition differently than the photon exchange does. This enables this distinction of $\bar{U}$ and $\bar{D}$ at the LHeC.

The distributions of $\bar{U}$ and $\bar{D}$ for the PDFs from the 1st run and the "LHeC inclusive data" are shown in Figs. 1.10 and 1.11 for $Q^2 = 1.9\,\mathrm{GeV}^2$ and $Q^2 = 10^4\,\mathrm{GeV}^2$, respectively, and compared to present PDF analyses. One observes a striking increase in precision for both $\bar{U}$ and $\bar{D}$ which persists from the initial to the weak Q^2 scale. The relative uncertainty is large at high $x \geq 0.5$. However, in that region the sea-quark contributions are already very tiny. In the high x region one recognises the value of the full LHeC data sample fitted over the initial one while the uncertainties below $x \simeq 0.1$ of both the small and the full data sets are of comparable, very small size.

1.3.4 Strange Quark

The determination of the strange PDF has generated significant controversy in the literature for more than a decade. Fixed-target neutrino DIS measurements [33–37] typically prefer a strange PDF that is roughly half of the up and down sea distribution; $\kappa = (s + \bar{s})/(\bar{u} + \bar{d}) \sim 0.5$. The recent measurements from the LHC [38–41] and related studies [42, 43] suggest a larger strange quark distribution, that may potentially even be larger than the up and down sea quarks. The x dependence of xs is essentially unknown, and it may differ from that of $x\bar{d}$, or $x(\bar{u} + \bar{d})$, by more than a normalisation factor.

The precise knowledge of the strange quark PDF is of high relevance, since it provides a significant contribution to *standard candle* measurements at the HL-LHC, such as W/Z production, and it imposes a significant uncertainty on the W mass measurements at the LHC. The question of light-sea flavour 'democracy' is of principle relevance for QCD and the parton model. For the first time, as has been presented in Sect. 1.2.2, $x\bar{s}(x, Q^2)$ can be accurately measured, namely through the charm tagging $Ws \to c$ reaction in CC e^-p scattering at the LHeC. The inclusion of the CC charm data in the PDF analysis will settle the question of how strange the strange quark distribution really is [6]. This prospect has been analysed within the LHeC fit framework

[6] The provision of positron-proton data will enable very interesting tests of charge symmetry, i.e. permit to

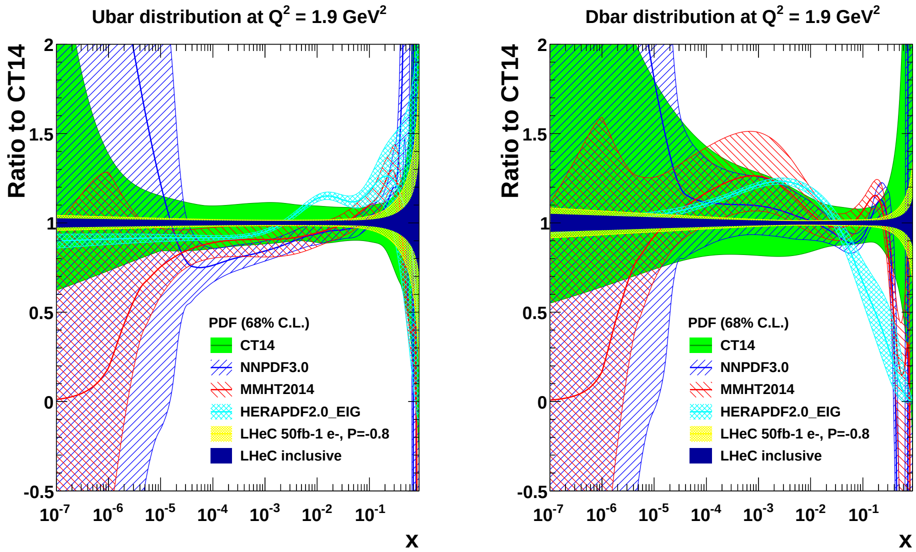

Figure 1.10: Sea quark distributions at $Q^2 = 1.9\,\mathrm{GeV}^2$ as a function of x, presented as the ratio to the CT14 central values. The yellow band corresponds to the "LHeC 1st run" PDFs (D2), while the dark blue shows the final "LHeC inclusive" PDFs (D4+D5+D6+D8), as described in the text. Both LHeC PDFs shown are scaled to the central value of CT14. Note that the HERAPDF2.0_EIG band corresponds to the experimental uncertainties only.

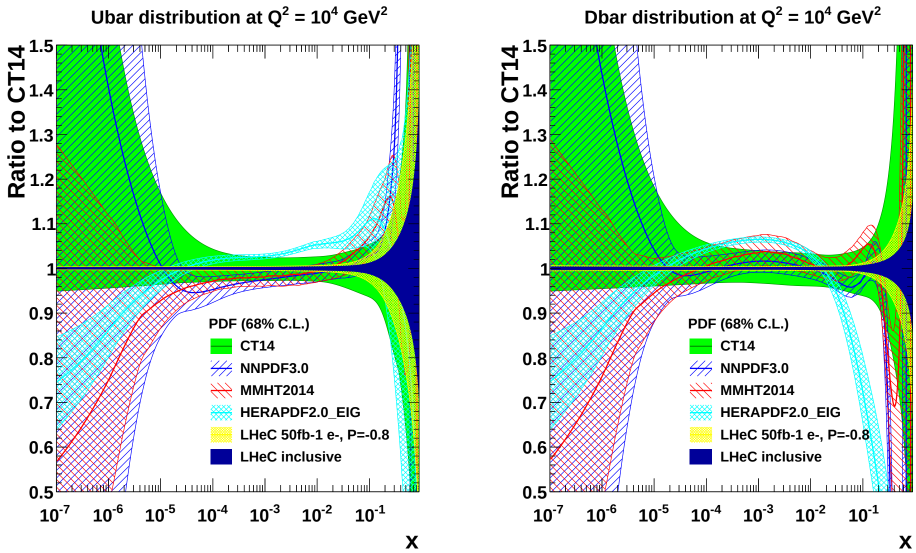

Figure 1.11: Sea quark distributions at $Q^2 = 10^4\,\mathrm{GeV}^2$ as a function of x, presented as the ratio to the CT14 central values. The yellow band corresponds to the "LHeC 1st run" PDFs (D2), while the dark blue shows the final "LHeC inclusive" PDFs (D4+D5+D6+D8), as described in the text. Both LHeC PDFs shown are scaled to the central value of CT14. Note that the HERAPDF2.0_EIG band corresponds to the experimental uncertainties only.

here introduced and as well studied in detail in a profiling analysis using *xFitter*. Both analyses yield rather compatible results and are presented in the following.

search for a difference between the strange and the anti-strange quark densities. This has not been studied in this paper.

In the standard LHeC fit studies, the parameterised PDFs are the four quark distributions xu_v, xd_v, $x\bar{U}$, $x\bar{D}$ and xg (constituting a 4+1 parameterisation), as the inclusive NC and CC data determine only the sums of the up and down quark and anti-quark distribution, as discussed previously. The strange quark PDF is then assumed to be a constant fraction of $x\bar{d}$.

With the strange quark data available, the LHeC PDF fit parameterisations can be extended to include $xs = x\bar{s}$, parameterised as $A_s x^{B_s}(1-x)^{C_s}$ [7]. For the fits presented in the following, the $\bar{d}$ and $\bar{s}$ are treated now separately, and therefore a total of five quark distributions are parameterised (xu_v, xd_v, $x\bar{U}$, $x\bar{d}$, $x\bar{s}$) as well as g. This provides a 5+1 parameterisation, and the total number of free parameters of the PDF fit then becomes 17.

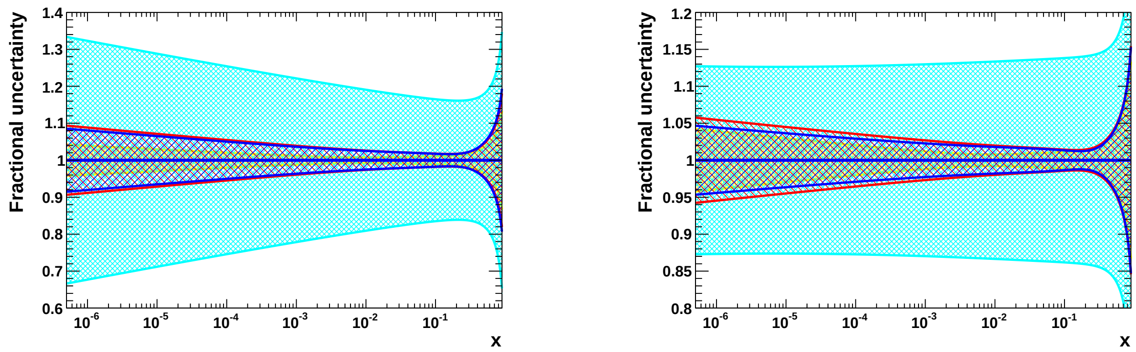

(a) $x\bar{d}$ quark distribution.

(b) $x\bar{s}$ quark distribution.

Figure 1.12: WILL PROBABLY BE REPLACED WITHOUT LIGHT BLUE PDF uncertainties at $Q^2 = 1.9\,\mathrm{GeV}^2$ as a function of x for the $\bar{d}$ and $\bar{s}$ distributions. The yellow band displays the uncertainties of the nominal "LHeC inclusive" PDF, which was obtained in a 4+1 PDF fit. From the same dataset, results of the more flexible 5+1 fit (see text) are displayed as a cyan band. The red band displays the results, when in addition an LHeC measurement of the $\bar{s}$ quark density is included. When even further including LHeC measurements of F_2^c and F_2^b, the PDF fits yields uncertainties as displayed by the blue band.

NEEDS CHAT WITH CLAIRE TO FINISH Results of the 5+1 PDF fits are shown in Fig. 1.12, where fits to inclusive NC/CC DIS data are displayed as reference (both for the 4+1 and 5+1 ansatz) and the fits where in addition strange density measurements and even further measurements of $F_2^{c,b}$ are considered. As expected, the uncertainties of the 5+1 fit to the inclusive DIS data, especially on the $\bar{d}$ and $\bar{s}$ distributions (c.f. Fig. 1.12), become substantially larger in comparison to the respective 4+1 fit, since the $\bar{d}$ and $\bar{s}$ distributions are treated now separately. This demonstrates that the inclusive DIS data alone does not have the flavour separating power to determine the individual distributions very precisely.

When including an LHeC measurement of the $\bar{s}$ quark density based on $10\,\mathrm{fb}^{-1}$ of e^-p data, the uncertainties on the $\bar{d}$ and $\bar{s}$ PDFs become significantly smaller. By chance, those uncertainties are then comparable to the 4+1 fit in which $x\bar{s}$ is linked to $x\bar{d}$ by a constant fraction.

The constraints from a measurement of charm quark production cross sections in charged current DIS have also been studied in a profiling analysis using *xFitter* [44]. The treatment of heavy quark production to higher orders in pQCD is discussed extensively in this paper. At leading-

[7] It is worth mentioning that the W, Z data [38] essentially determine only a moment of xs at $x \sim 0.02$, not the x dependence. Therefore, in analyses of HERA and ATLAS data such as Ref. [43], there is no determination attempted of the relevant parameter, B_s, which instead is set equal to $B_{\bar{d}}$. The kinematic dependence of xs is basically not determined by LHC data while the hint to the strange being unsuppressed has been persistent.

order QCD, the subprocess under consideration is $Ws \to c$, where the s represents an intrinsic strange quark. Fig. 1.13 displays the tight constraints obtained for the strange PDF when

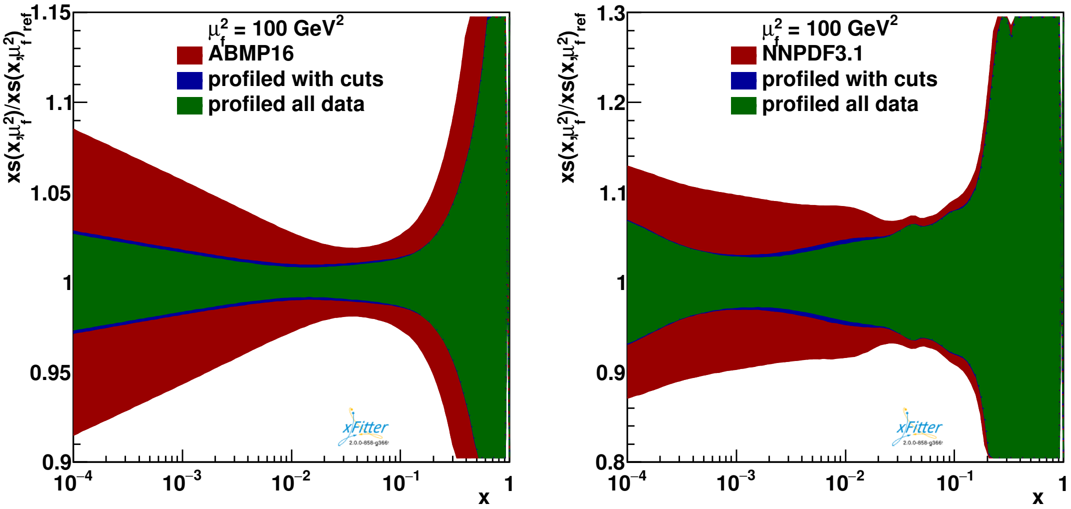

Figure 1.13: Constraints on the strange quark PDF xs using simulated data for charged-current production of charm quarks at the LHeC, from a profiling study [44] using the ABMP16 (left) and the NNPDF3.1 (right) PDF sets. The red band displays the nominal PDF uncertainties, and the green and blue bands the improved uncertainties due to the LHeC strange quark data.

using the LHeC pseudo-data for the CC charm production channel. The results of this profiling analysis, both when based on the ABM16 and the NNPDF3.1 PDF sets, and of the direct fit presented above, are very similar, reaching about $3-5\,\%$ precision for x below $\simeq 0.01$

In a variation of the study [44], a large reduction of uncertainties is already observed when restricting the input data to the kinematic range where the differences between the different heavy flavour schemes (VFNS and FFNS) are not larger than the present PDF uncertainties. This further indicates that the PDF constraints are stable and independent of the particular heavy-flavour scheme.

It may thus be concluded that the LHeC, through high luminosity, energy and precise kinematic reconstruction, will be able to solve a long standing question about the role of the strange-quark density in the proton, and its integration into a consistent QCD treatment of parton dynamics.

1.3.5 Heavy Quarks

One of the unsolved mysteries of the Standard Model is the existence of three generations of quarks and leptons. The strongly interacting fermion sector contains altogether six quarks with masses differing by up to five orders of magnitude. This hierarchy of masses is on one hand a challenge to explain, on the other hand it offers a unique opportunity to explore dynamics at a variety of different scales and thus develop different facets of the strong interaction. While the light quarks at low scales are non-perturbative and couple strongly, the heavier quarks charm, bottom and top are separated from the soft sea by their masses and thus can serve as a suitable additional probe for the soft part of QCD.

There are a number of deep and unresolved questions that can be posed in the context of the proton structure: what is the individual contribution of the different quark flavours to the structure functions?; are heavy quarks like charm and bottom radiatively generated or is there also an intrinsic heavy quark component in the proton?; to what extent do the universality and factorisation theorems work in the presence of heavy quarks? It is therefore imperative to be able to perform precise measurements of each individual quark flavour and their contribution to the proton structure. The LHeC is the ideal place for these investigations because it resolves the complete composition of the proton flavour by flavour. In particular, as shown in Sect. 1.2.2, the LHeC provides data on F_2^c and F_2^b extending over nearly 5 and 6 orders of magnitude in x, Q^2, respectively. These are obtained through charm and beauty tagging with high precision in NC *ep* scattering. A thorough PDF analysis of the LHeC data thus can be based on the inclusive NC/CC cross sections and tagged $s,\ c,\ b$ data. In addition, one may use DIS jets, here used for the α_s prospective study (Sect. 2.1) and low energy data, here analysed for resolving the low x dynamics with a precision measurement of F_L (Sect. 2.2.3). The current studies in this chapter therefore must be understood as indicative only as we have not performed a comprehensive analysis using all these data as yet [8].

The production of heavy quarks at HERA (charm and bottom) is an especially interesting process as the quark mass introduces a new scale ($m = m_{c,b}$) which was neither heavy or light (see e.g. reviews [45, 46]). Actually, the treatment of heavy quark mass effects is essential in PDF fits which include data from fixed target to collider energies and thus require the computation of physical cross sections over a large range of perturbative scales μ^2. With these scales passing through (or close to) the thresholds for charm, bottom and, eventually, top, precise computations demand the incorporation of heavy quark mass effects close to threshold, $\mu^2 \sim m^2$, and the resummation of collinear logarithms $\ln(\mu^2/m^2)$ at scales far above the threshold, $\mu^2 \gg m^2$. The first problem can be dealt with through the use of massive matrix elements for the generation of heavy quark-antiquark pairs but keeping a fixed number of parton densities (fixed flavour number schemes, FFNS). On the other hand, the proper consideration of resummation is achieved through the use of variable flavour number schemes (VFNS) which consider an increasing number of massless parton species, evolved through standard DGLAP, when the scale is increased above heavy quark mass thresholds. At present, calculations involving heavy quarks in DIS in different schemes (generalised mass VFNS) with different numbers of active flavours participating to DGLAP evolution are combined to derive an expression for the coefficient functions which is valid both close to threshold, and far above it. Such multi-scale problems are particularly difficult, and numerous techniques were developed to cope with this challenging problem [47–56]. Additional complications, see e.g. Ref. [57], arise when the possibility of a non-perturbative origin of heavy quark distributions is allowed above the heavy quark mass threshold - intrinsic heavy flavour. The ABMP16 analysis [58] underlines that the available DIS data are compatible with solely an FFNS treatment assuming that the heavy quarks are generated in the final state.

At the LHeC, as illustrated in Figs. 1.6, 1.7, the large polar angle acceptance and the high centre-of-mass energy allow heavy quark physics to be investigated from below threshold to almost $10^6\,\mathrm{GeV}^2$. The extended reach in comparison to HERA is dramatic. This permits to comprehensively explore the *asymptotic* high energy limit where $m_{c,b}^2/Q^2 \to 0$, as well as the low energy *decoupling* region $m_{c,b}^2/Q^2 \sim 1$.

For the PDF determination the obviously direct impact of the tagged charm and bottom data will be on the determination of xc and xb, and the clarification of their appropriate theoretical treatment. In addition, however, there is a remarkable improvement caused for the determination of the gluon density, see Fig. 1.14. The determination of xg will be discussed in much more detail in the following section.

[8] This is to be considered when one compares the precision of the inclusive PDF fits with so-called global analyses, for example regarding the behaviour of xg at large x.

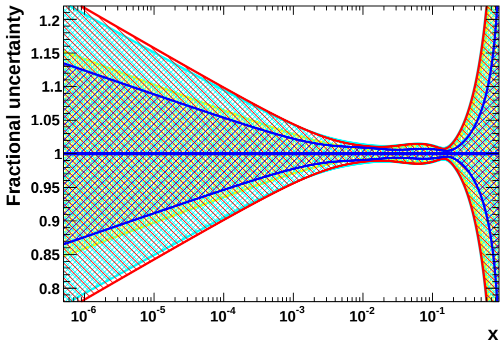

(a) Gluon distribution ($\log_{10} x$ scale)

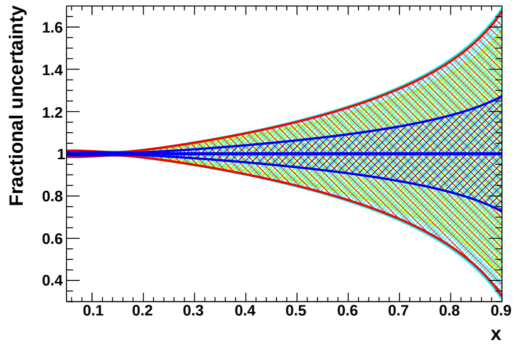

(b) Gluon distribution (linear x scale).

Figure 1.14: PDF uncertainties at $Q^2 = 1.9\,\mathrm{GeV}^2$ as a function of x to illustrate the constraints from additional heavy quark sensitive measurements at LHeC. Displayed is the gluon distribution on a logarithmic and linear scale. The yellow band illustrates the uncertainties of the nominal "LHeC inclusive" PDF, obtained in a 4+1 PDF fit. The red band displays the results, when in addition an LHeC measurement of the $x\bar{s}$ quark density is included which obviously is uncorrelated to xg. When further including LHeC measurements of F_2^c and F_2^b, the PDF fits yields uncertainties as displayed by the blue band.

These channels will also strongly improve the determination of the charm and bottom quark masses and bring these uncertainties down to about $\delta m_{c(b)} \simeq 3(10)\,\mathrm{MeV}$ [1] [9]. These accuracies are crucial for eliminating the corresponding model uncertainties in the PDF fit. Precision tagged charm and bottom data are also essential for the determination of the W-boson mass in pp, and the extraction of the Higgs $\to c\bar{c}$ and $b\bar{b}$ couplings in ep, as is discussed further below.

1.3.6 The Gluon PDF

The LHeC, with hugely increased precision and extended kinematic range of DIS, i.e. the most appropriate process to explore $xg(x, Q^2)$, can pin down the gluon distribution much more accurately than it is known today. This primarily comes from the extension of range and precision in the measurement of $\partial F_2/\partial \ln Q^2$, which at small x is a direct measure of xg. The precision determination of the quark distributions, discussed previously, also strongly constrains xg. Further sensitivity arises with the high-y part of the NC cross section which is controlled by the longitudinal structure function as is discussed in Sect. 2.2.3.

The result for the gluon distribution from the LHeC inclusive NC/CC data fits is presented in Fig. 1.15, and compared to several other PDF sets. On the left, the distribution is presented as a ratio to CT14, and is displayed on a log-x scale to highlight the small x region. On the right, the xg distribution is shown on a linear-x scale, accentuating the region of large x. The determination of xg will be radically improved with the LHeC NC and CC precision data, which provide constraints on $\partial F_2/\partial \ln Q^2$ down to very low x values, $\geq 10^{-5}$, and large $x \leq 0.8$.

Below $x \simeq 5 \cdot 10^{-4}$, the HERA data have almost vanishing constraining power due to kinematic range limitations, as one needs a lever arm to determine the Q^2 derivative, and so the gluon is simply not determined at lower x. This can be seen in all modern PDF sets. With the

[9] Such precision demands the availability of calculations with higher orders in pQCD, and those computations are already ongoing [59–61]. Note than in PDF fits the heavy quark mass is an effective parameter that has to be related with the pole mass, see e.g. Ref. [62] and refs. therein.

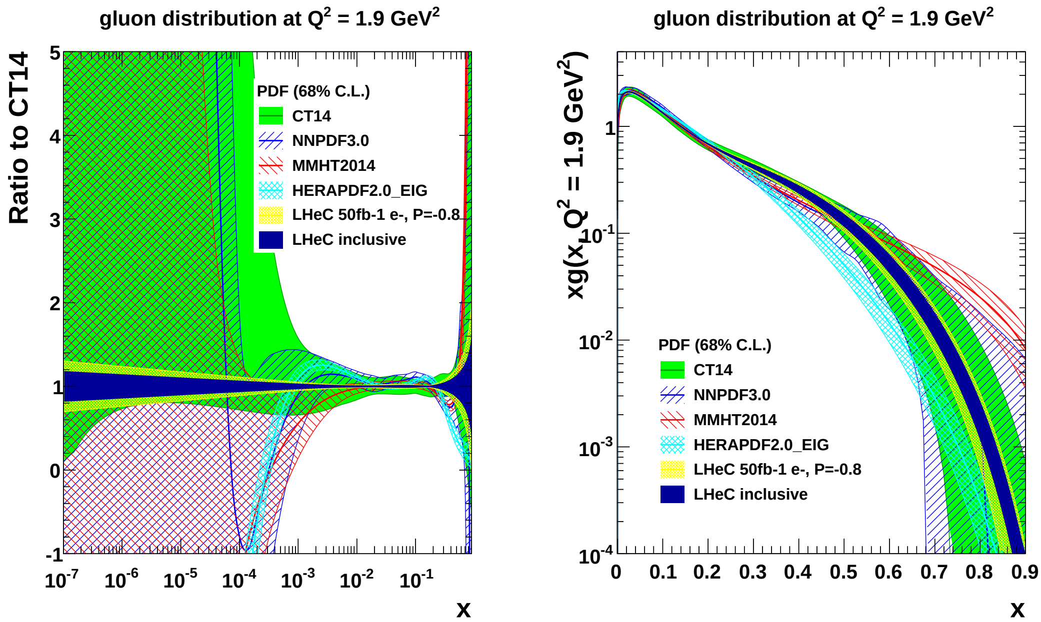

Figure 1.15: Gluon distribution at $Q^2 = 1.9\,\mathrm{GeV}^2$ as a function of x, highlighting (left) the low x and (right) the high x regions. The yellow band corresponds to the "LHeC 1st run" PDFs (D2), while the dark blue shows the "LHeC inclusive" PDFs (D4+D5+D6+D8), as described in the text. Both LHeC PDFs shown are scaled to the central value of CT14. The smooth extension of the LHeC xg uncertainty bands below $x \simeq 10^{-5}$ is an artefact of the parameterisation. Note that the HERAPDF2.0-EIG band corresponds to the experimental uncertainties only.

LHeC, a precision of a few per cent at small x becomes possible down to nearly 10^{-5}. This should resolve the question of non-linear parton interactions at small x (cf. Sect. 2.2). It also has direct implications for the LHC (and even stronger for the FCC): with the extension of the rapidity range to about 4 at the HL-LHC by ATLAS and CMS, Higgs physics will become small x physics for which xg must be known very accurately since $gg \to H$ is the dominant production mechanism.

At large $x \geq 0.3$, the gluon distribution becomes very small and large variations appear in its determination from several PDF groups, differing by orders of magnitude. That is related to uncertainties on jet measurements, theoretical uncertainties, and the fact that HERA did not have sufficient luminosity to cover the high x region where, moreover, the sensitivity to xg diminishes, since the valence quark evolution is insensitive to it. For the LHeC, the sensitivity at large x comes as part of the overall package: large luminosity allowing access to x values close to 1, fully constrained quark distributions and strong constraints at small x which feed through to large x via the momentum sum rule. The high precision illustrated will be crucial for BSM searches at high scales. It is also important for testing QCD factorisation and scale choices, as well as pinning down electroweak effects.

The analysis presented here has not made use of the additional information that can be provided at the LHeC in measurements of $F_2^{c,b}$ (see Sect. 1.3.5) or F_L. The large x situation can be expected to further improve by using LHeC jet data, providing further, direct constraints at large x which, however, have not yet been studied in comparable detail.

The LHeC is the ideal laboratory to resolve all unknowns of the gluon density, which is the origin for all visible mass, and one of the particular secrets of particle physics for the gluon cannot directly be observed but is confined inside hadrons. It is obvious that resolving this puzzle is an energy frontier DIS task and goal, including electron-ion scattering since the gluon inside heavy matter is known even much less. Therefore, the special importance of this part of high energy PDF physics is not primarily related to the smallness of uncertainties: it is about a consistent understanding and resolution of QCD at all regions of spatial and momentum dimensions which the LHeC will explore, and later the FCC-eh too.

1.3.7 Luminosity and Beam Charge Dependence of LHeC PDFs

It is informative to study the transition of the PDF uncertainties from the "LHeC 1st run" PDFs, which exploits only a single electron-proton dataset, D2, through to the "LHeC final inclusive" PDFs, which makes use of the full datasets D4+D5+D6+D8 as listed in Tab. 1.2, i.e. including high luminosity data (D4), small sets of low energy $E_p = 1\,\text{TeV}$ and positron data (D5 and D6) together with $10\,\text{fb}^{-}1$ of opposite helicity data. Various intermediate PDF fits are performed using subsets of the data in order to quantify the influence of the beam parameters on the precision of the various PDFs. All fits use the same, standard 4+1 fit parameterisation and exclude the use of $s,\ c,\ b$ data, the effect of which was evaluated before. The fits do neither include the low electron energy data sets generated for the F_L analysis, cf. Sect. 2.2.3, nor any jet ep data. The emphasis is on the development of the u_v, d_v, total sea and xg uncertainty, not the best possible value.

A first study, Fig. 1.16, shows the influence of the integrated luminosity. This compares four cases, three with evolving luminosity, from 5 over 50 to $1000\,\text{fb}^{-1}$. These assumptions, according to the luminosity scenarios presented elsewhere, correspond to year 1 (D1), the initial 3 years (D2) and to the maximum attainable integrated luminosity (D4). The fourth case is represented by what is denoted the LHeC inclusive fit. One observes a number of peculiarities. For example, the initial $5\,\text{fb}^{-1}$ (yellow in Fig. 1.16), i.e. the tenfold of what H1 collected over its lifetime (albeit with different beam parameters), leads i) to an extension of the HERA range to low and higher x, ii) to high precision at small x, for example of the sea quark density of 5 % below $x = 10^{-5}$ or iii) of also 5 % for u_v at very high $x = 0.8$. With $50\,\text{fb}^{-1}$ the down valence distribution is measured to within 20 % accuracy at $x = 0.8$, an improvement by about a factor of two as compared to the $5\,\text{fb}^{-1}$ case, and a major improvement to what is currently known about xd_v at large x, compare with Fig. 1.8. The very high luminosity, here taken to be $1\,\text{ab}^{-1}$, leads to a next level of high precision, for example of 2 % below $x = 10^{-5}$ for the total sea. The full data set further improves, especially the xd_v and the gluon at high x. The valence quark improvement is mostly linked to the positron data while the gluon improvement is related to the extension of the lever arm towards small values of Q^2 as the reduction of E_p extends the acceptance at large x. The visible improvement through the final inclusive fit is probably related to the increased precision at high x for there exists a momentum sum rule correlation over the full x range. In comparison to the analogous HERA fit, it becomes clear, that the vast majority of the gain comes already from the first $5 - 50\,\text{fb}^{-1}$.

The second study presented here regards the impact on the PDF uncertainties when adding additionally positron data of different luminosity to a baseline fit on $50\,\text{fb}^{-1}$ of $e^{-}p$ data, the "LHeC 1st run" dataset. The results are illustrated in Fig. 1.17. It is observed, that the addition of positron data does bring benefits, which, however, are not striking in their effect on the here considered PDFs. A prominent improvement is obtained for the d-valence PDF, primarily due to the sensitivity gained via the CC cross section of the positron data. The benefit of the precise access to NC and CC weak interactions by the LHeC is clearer when one studies the cross sections and their impact on PDFs. This is illustrated in the subsequent section.

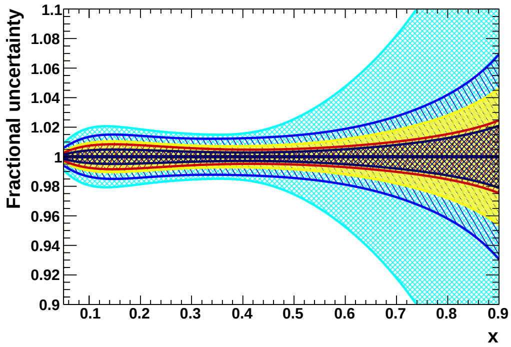

(a) u-valence distribution.

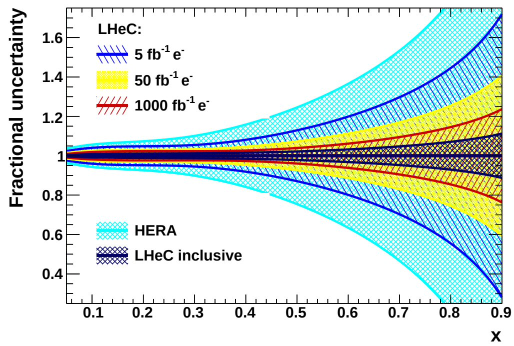

(b) d-valence distribution.

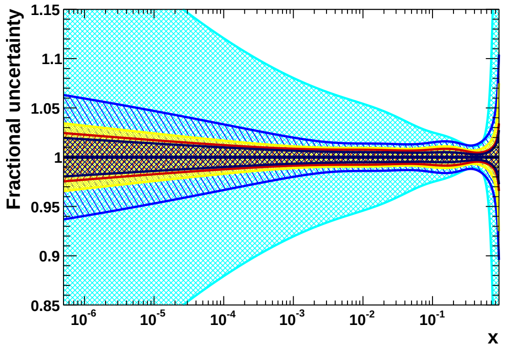

(c) Sea quark distribution ($\log_{10} x$ scale).

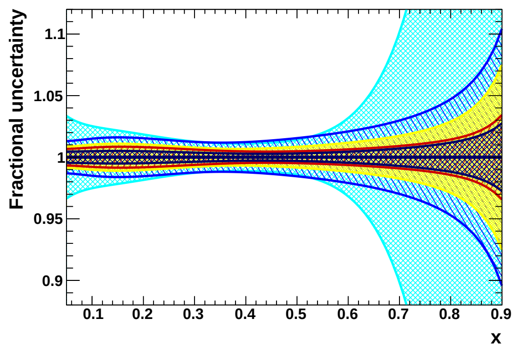

(d) Sea quark distribution (linear x scale).

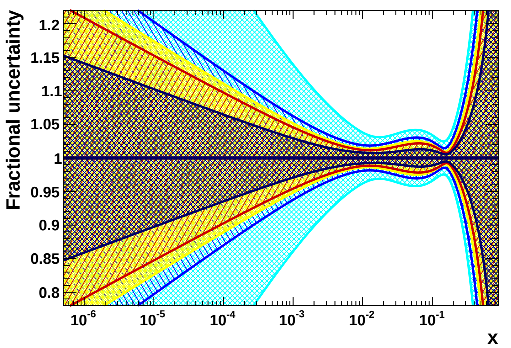

(e) Gluon distribution ($\log_{10} x$ scale).

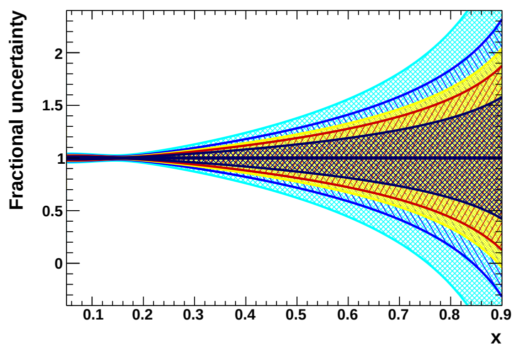

(f) Gluon distribution (linear x scale).

Figure 1.16: PDF distributions at $Q^2 = 1.9\,\mathrm{GeV}^2$ as a function of x, illustrating the impact of different amounts of integrated luminosity. The blue, yellow and red bands correspond to LHeC PDFs using electron-only NC and CC inclusive measurements with 5, 50 and $1000\,\mathrm{fb}^{-1}$ (datasets D1, D2 and D4), respectively. The yellow band is therefore equivalent to the “LHeC 1st run” PDF. For reference, the dark blue band shows the results of the final “LHeC inclusive” PDF. For comparison, the cyan band represents an identical PDF fit using HERA combined inclusive NC and CC data [13], restricted to solely the experimental uncertainties. Note that this, unlike the LHeC, extends everywhere beyond the narrow limits of the y scale of the plots.

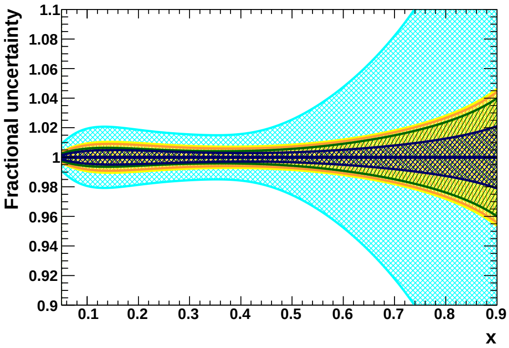

(a) u-valence distribution.

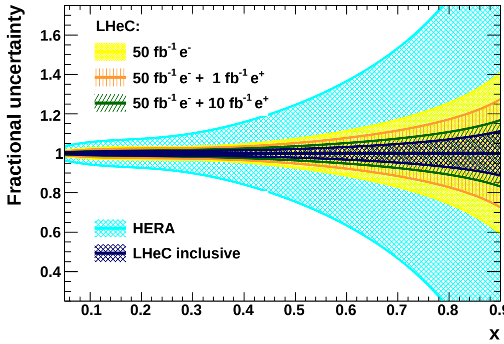

(b) d-valence distribution.

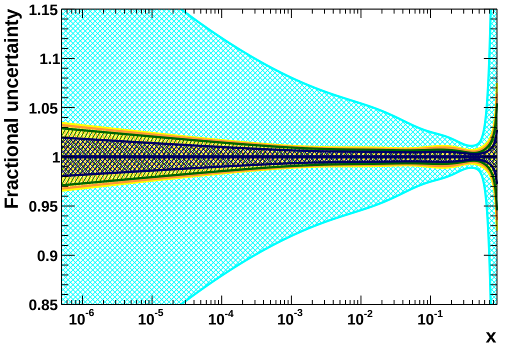

(c) Sea quark distribution ($\log_{10} x$ scale).

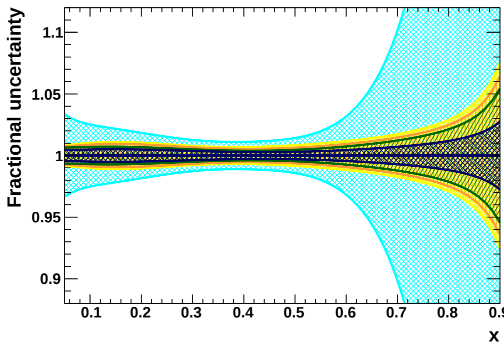

(d) Sea quark distribution (linear x scale).

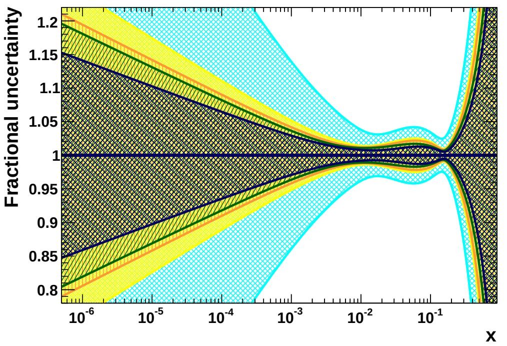

(e) Gluon distribution ($\log_{10} x$ scale).

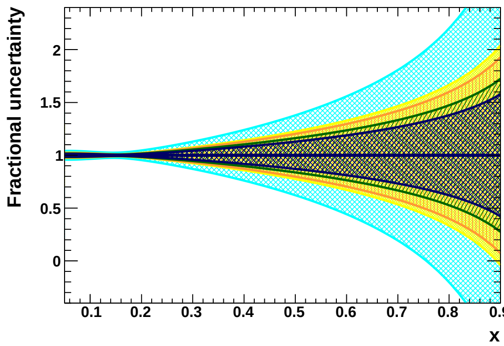

(f) Gluon distribution (linear x scale).

Figure 1.17: PDF distributions at $Q^2 = 1.9\,\mathrm{GeV}^2$ as a function of x, illustrating the impact of including positron data. The yellow ("LHeC 1st run") and dark blue ("LHeC final inclusive") and cyan bands (HERA data) are as in Fig. 1.16. The orange band corresponds to a fit with $1\,\mathrm{fb}^{-1}$ of inclusive NC and CC positron-proton data, in addition to $50\,\mathrm{fb}^{-1}$ of electron-proton data (D2+D6), while the green band is similar, but with $10\,\mathrm{fb}^{-1}$ of positron-proton data (D2+D7).

1.3.8 Weak Interactions Probing Proton Structure

It had long been considered to use the weak interactions to probe proton structure in deep inelastic scattering [63]. First important steps in this direction could be pursued with HERA, especially with the measurements of the polarisation and beam charge asymmetries in NC *ep* scattering by H1 and ZEUS [13]. This area of research will become a focus at the LHeC, and even more so at FCC-he, because the Q^2 range extends by 2-3 orders of magnitude beyond the weak scale $Q^2 \simeq M^2_{W,Z}$, with hugely increased luminosity. In Sect. 3.1 below, the emphasis is on accessing the electroweak theory parameters at a new level of sensitivity. Here we illustrate the importance of using the Z and also W exchange for pinning down the parton contents of the proton. This has been implicite for the QCD fits presented above, it yet emerges clearly only when one considers cross sections directly, their asymmetries with respect to beam charge and polarisation, and certain kinematic limits.

Parity violation is accessed in NC DIS through a variation of the lepton beam helicity, P, as can be deduced from [63]

$$\frac{\sigma^{\pm}_{r,NC}(P_R) - \sigma^{\pm}_{r,NC}(P_L)}{P_R - P_L} = \mp \varkappa_Z g^e_A F_2^{\gamma Z} - (\varkappa_Z g^e_A)^2 \frac{Y_-}{Y_+} x F_3^Z \tag{1.3}$$

where $\sigma_{r,NC}$ denotes the double differential NC scattering cross section scaled by $Q^4 x/2\pi\alpha^2 Y_+$. Here κ_Z is of the order of Q^2/M_Z^2, $F_2^{\gamma Z} = 2x \sum Q_q g_V^q (q - \bar{q})$ and the NC vector couplings are determined as $g_V^f = I^f_{3,L} - 2Q_f \sin^2\theta_W$, where Q_f is the electric charge and $I^f_{3,L}$ the left handed weak isospin charge of the fermion $f = e, q$, which also determines the axial vector couplings g_A^f, with $g_A^e = -1/2$. The second term in Eq. 1.3 is suppressed with respect to the first one as it results from pure Z exchange and because the Y factor is small, $\propto y$ since $Y_\mp = (1 \mp (1-y)^2)$.

For the approximate value of the weak mixing angle $\sin^2\theta_W = 1/4$ one obtains $g_V^e = 0$, $g_V^u = 1/6$ and $g_V^d = -1/3$. Consequently, one may write to good approximation

$$F_2^{\gamma Z}(x, Q^2) = 2x \sum_q Q_q g_V^q (q - \bar{q}) \simeq x \frac{2}{9}[U + \bar{U} + D + \bar{D}] \tag{1.4}$$

The beam helicity asymmetry therefore determines the total sea. A simulation is shown in Fig. 1.18 for integrated luminosities of $10\,\mathrm{fb}^{-1}$ and helicities of $P = \pm 0.8$. Apparently, this asymmetry will provide a very precise measurement of the total sea. The combination of up and down quarks accessed with $F_2^{\gamma Z}$ (Eq. 1.4) is different from that provided by the known function

$$F_2(x, Q^2) = 2x \sum_q Q_q^2 (q - \bar{q}) = x \frac{1}{9}[4(U + \bar{U}) + D + \bar{D}] \tag{1.5}$$

because of the difference of the photon and Z boson couplings to quarks. Following Eq. 1.3, the beam polarisation asymmetry

$$A^{\pm} = \frac{\sigma^{\pm}_{NC}(P_R) - \sigma^{\pm}_{NC}(P_L)}{\sigma^{\pm}_{NC}(P_R) + \sigma^{\pm}_{NC}(P_L)} \simeq \mp (P_L - P_R) \varkappa_Z g^e_A \frac{F_2^{\gamma Z}}{F_2}. \tag{1.6}$$

measures to a very good approximation the F_2 structure function ratio. The different composition of up and down quark contributions to $F_2^{\gamma Z}$ and F_2, see above, indicates that the weak neutral current interactions will assist to separate the up and down quark distributions which HERA had to link together by setting $B_d = B_u$.

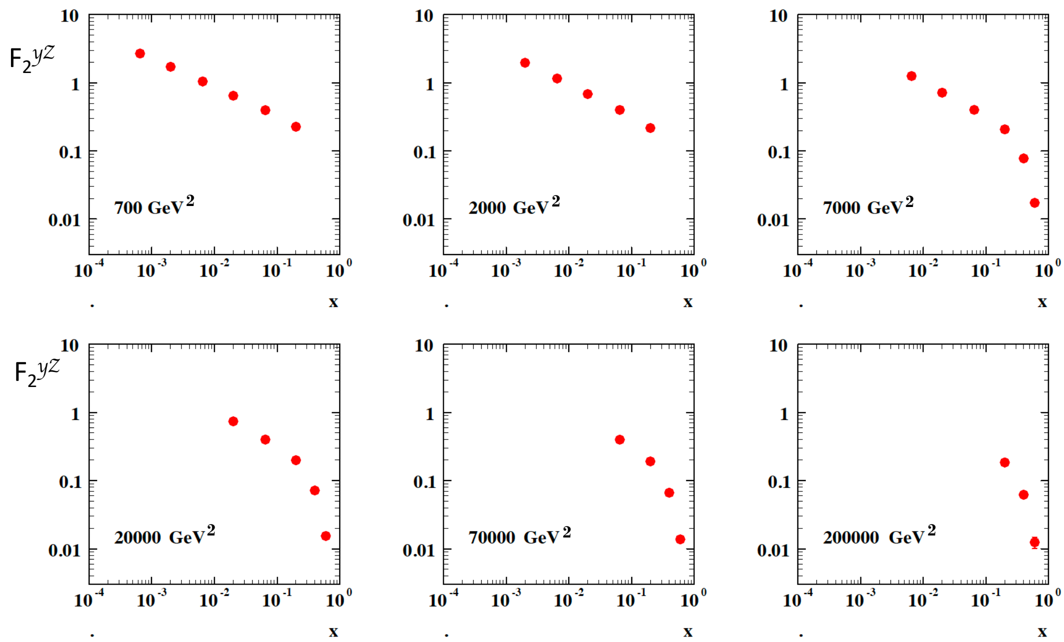

Figure 1.18: Prospective measurement of the photon-Z interference structure function $F_2^{\gamma Z}(x, Q^2)$ at the LHeC using polarised electron beams of helicity ± 0.8 and an integrated luminosity of $10\,\text{fb}^{-1}$ for each state. The uncertainties are only statistical.

Inserting $P_L = -P_R = -P$ and considering the large x limit, one observes that the asymmetry measures the d/u ratio of the valence quark distributions according to

$$A^{\pm} \simeq \pm \varkappa_Z P \frac{1 + d_v/u_v}{4 + d_v/u_v}. \tag{1.7}$$

This quantity will be accessible with very high precision, as Fig. 1.18 illustrates, which is one reason, besides the CC cross sections, why the d/u ratio comes out to be so highly constrained by the LHeC (see Fig. 1.9).

A further interesting quantity is the the lepton beam charge asymmetry, which is given as

$$\sigma^+_{r,NC}(P_1) - \sigma^-_{r,NC}(P_2) = \kappa_Z a_e[-(P_1 + P_2)F_2^{\gamma Z} - \frac{Y_-}{Y_+}(2xF_3^{\gamma Z} + \kappa_Z a_e(P_1 - P_2)xF_3^Z)] \tag{1.8}$$

neglecting terms $\propto g_V^e$. For zero polarisation this provides directly a parity conserving measurement of the structure function

$$xF_3^{\gamma Z}(x, Q^2) = 2x \sum_q Q_q g_A^q (q - \bar{q}) = \frac{2}{3}x(U - \bar{U}) + \frac{1}{3}x(D - \bar{D}). \tag{1.9}$$

The appearance of this function in weak NC DIS resembles that of xW^3 in CC, or fixed target neutrino-nucleon, scattering. It enables to resolve the flavour contents of the proton. The function $xF_3^{\gamma Z}$ was first measured by the BCDMS Collaboration in $\mu^{\pm}C$ scattering [64] at the SPS.

The HERA result is shown in Fig. 1.19. It covers the range from about $x = 0.05$ to $x = 0.6$ with typically 10 % statistical precision. Assuming that sea and anti-quark densities are equal, such as $u_s = \bar{u}$ or $d_s = \bar{d}$, $xF_3^{\gamma Z}$ is given as $x/3(2u_v + d_v)$. This function therefore accesses valence

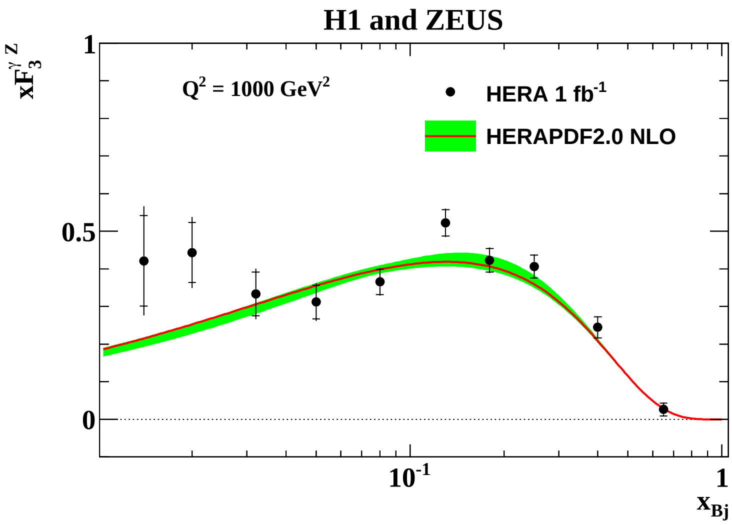

Figure 1.19: Combination of H1 and ZEUS measurement of the structure function $xF_3^{\gamma Z}(x, Q^2)$ as a function of x projected to a fixed Q^2 value of 2000 GeV^2, from [13]. The inner error bar represents the statistical uncertainty.

quarks down to small values of x where their densities become much smaller than that of the sea quarks. Since the Q^2 evolution of the non-singlet valence quark distributions is very weak, it has been customary to project the various charge asymmetry measurements to some lowish value of Q^2 and present the measurement as the x dependence of $xF_3^{\gamma Z}$.

If, however, there would be differences between the sea and anti-quarks, if for example $s \neq \bar{s}$, one expected a rise of $xF_3^{\gamma Z}$ towards low x. This may be a cause for the undershoot of the QCD fit below the HERA data near to $x \simeq 0.01$, see Fig. 1.19, which yet are not precise enough. However, it is apparent that, besides providing constraints on the valence quark densities, this measurement indeed has the the potential to discover a new anti-symmetry in the quark sea.

Such a discovery would be enabled by the LHeC as is illustrated in Fig. 1.20 with an extension of the kinematic range by an order of magnitude towards small x and a much increased precision in the medium x region. The simulation is performed for 10 and for 1 fb^{-1} of e^+p luminosity. Obviously it would be very desirable to reach high values of integrated luminosity in positron-proton scattering too.

It is finally of interest to consider the role of precisely measured cross sections in CC scattering. The coupling of the W boson to quarks is flavour dependent resulting in the relations

$$\sigma^+_{r,CC} = (1 + P)[x\bar{U} + (1 - y)^2 xD], \tag{1.10}$$

$$\sigma^-_{r,CC} = (1 - P)[xU + (1 - y)^2 x\bar{D}]. \tag{1.11}$$

Here $\sigma_{r,CC}$ is the double differential charged current DIS cross section scaled by a factor $2\pi x \cdot (M_W^2 + Q^2)^2/(G_F M_W^2)^2$ with the Fermi constant G_F and the W boson mass M_W. The positron beam at the LHeC is most likely unpolarised. Maximum rate in e^-p is achieved with large negative polarisation. In the valence-quark approximation, the e^+p CC cross section is proportional to $(1 - y)^2 xdv$ while $\sigma^-_{r,CC} \propto u_v$. This provides direct, independent measurements of d_v and u_v as had been illustrated already in the LHeC CDR [1].

Inclusive NC and CC DIS accesses four combinations of parton distributions, as is obvious from

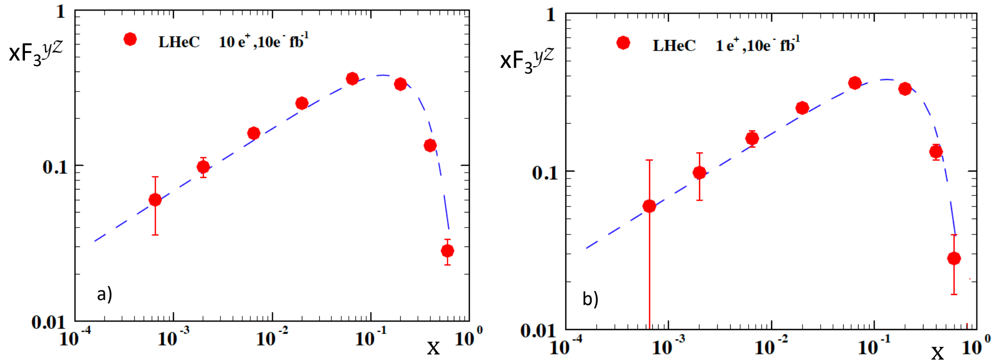

Figure 1.20: Prospective measurement of the photon-Z interference structure function $xF_3^{\gamma Z}(x, Q^2)$ at the LHeC projected to a fixed Q^2 value of 2000 GeV^2. The result corresponds to a cross section charge asymmetry for an unpolarised e^-p beam with 10 fb^{-1} luminosity combined with unpolarised e^+p beams of a) 10 fb^{-1} (left) and b) 1 fb^{-1} (right). The error bars represent the statistical uncertainty. The curve is drawn to guide the eye. It is possible that the measurement would discover a rise of $xF_3^{\gamma Z}$ towards low x should there exits so far unknown differences between sea and anti-quark densities, see text.

Eq. 1.10 for CC above and from the NC relation

$$\sigma^{\pm}_{r,NC} \simeq [c_u(U + \bar{U}) + c_d(D + \bar{D})] + \kappa_Z[d_u(U - \bar{U}) + d_d(D - \bar{D})]$$
$$\text{with } c_{u,d} = Q^2_{u,d} + \varkappa_Z(-g^e_V \mp Pg^e_A)Q_{u,d}g^{u,d}_V \text{ and } d_{u,d} = \pm g^e_A g^{u,d}_A Q_{u,d}, \qquad (1.12)$$

restricted to photon and γZ interference contributions. It is the high energy and high luminosity access to DIS, the high precision NC/CC and tagged heavy quark measurement programme, which makes the LHeC the uniquely suited environment to uncover the secrets of parton structure and dynamics. This will establish a new level with possible discoveries of strong interaction physics and also provide the necessary base for precision electroweak and Higgs measurements at the LHC, for massively extending the range of BSM searches and reliably interpreting new physics signals in hadron-hadron scattering at the LHC.

1.3.9 Parton-Parton Luminosities

The energy frontier in accelerator particle physics is the LHC, with a cms energy of $\sqrt{s} = 2E_p \simeq 14$ TeV, with the horizon of a future circular hadron collider, the FCC-hh, reaching energies up to $\sqrt{s} = 100$ TeV. Proton-proton collider reactions are characterised by the Drell-Yan scattering [65]. To leading order, the double differential Drell-Yan scattering cross section [66] for the neutral current reaction $pp \to (\gamma, Z)X \to e^+e^-X$ and the charged current (CC) reaction $pp \to W^{\pm}X \to e\nu X$, can be written as

$$\frac{d^2\sigma}{dMdy} = \frac{4\pi\alpha^2(M)}{9} \cdot 2M \cdot P(M) \cdot \Phi(x_1, x_2, M^2) \quad [\text{nb GeV}^{-1}]. \qquad (1.13)$$

Here M is the mass of the e^+e^- and $e^+\nu$ and $e^-\bar{\nu}$ systems for the NC and CC process, respectively, and y is the boson rapidity. The cross section implicitly depends on the Bjorken x values of the incoming quark q and its anti-quark $\overline{q}$, which are related to the rapidity y as

$$x_1 = \sqrt{\tau} e^{y} \quad x_2 = \sqrt{\tau} e^{-y} \quad \tau = \frac{M^2}{s}. \tag{1.14}$$

For the NC process, the cross section is a sum of a contribution from photon and Z exchange as well as an interference term. In the case of photon exchange, the propagator term $P(M)$ and the parton distribution term Φ are given by

$$P_\gamma(M) = \frac{1}{M^4} \qquad \Phi_\gamma = \sum_q Q_q^2 F_{q\bar{q}} \tag{1.15}$$

$$F_{q\bar{q}} = x_1 x_2 \cdot [q(x_1, M^2)\overline{q}(x_2, M^2) + \overline{q}(x_1, M^2) q(x_2, M^2)]. \tag{1.16}$$

Similar to DIS, the corresponding formulae for the γZ interference term read as

$$P_{\gamma Z} = \frac{\varkappa_Z g_V^e (M^2 - M_Z^2)}{M^2[(M^2 - M_Z^2)^2 + (\Gamma_Z M_Z)^2]} \qquad \Phi_{\gamma Z} = \sum_q 2 Q_q g_V^q F_{q\bar{q}} \tag{1.17}$$

The interference contribution is small being proportional to the vector coupling of the electron g_V^e. One also sees in Eq 1.17 that the interference cross section contribution changes sign from plus to minus as the mass increases and passes M_Z. The expressions of P and Φ for the pure Z exchange part are

$$P_Z = \frac{\varkappa_Z^2 (g_V^{e^2} + g_A^{e^2})}{(M^2 - M_Z^2)^2 + (\Gamma_Z M_Z)^2} \qquad \Phi_Z = \sum_q (g_V^{q^2} + g_A^{q^2}) F_{q\bar{q}}. \tag{1.18}$$

For the CC cross section the propagator term is

$$P_W = \frac{\kappa_W^2}{(M^2 - M_W^2)^2 + (\Gamma_W M_W)^2} \tag{1.19}$$

and the charge dependent parton distribution forms are

$$\Phi_{W^+} = x_1 x_2 [V_{ud}^2(u_1\overline{d}_2 + u_2\overline{d}_1) + V_{cs}^2(c_1\overline{s}_2 + c_2\overline{s}_1) + V_{us}^2(u_1\overline{s}_2 + u_2\overline{s}_1) + V_{cd}^2(c_1\overline{d}_2 + c_2\overline{d}_1)] \tag{1.20}$$

$$\Phi_{W^-} = x_1 x_2 [V_{ud}^2(\overline{u}_1 d_2 + \overline{u}_2 d_1) + V_{cs}^2(\overline{c}_1 s_2 + \overline{c}_2 s_1) + V_{us}^2(\overline{u}_1 s_2 + \overline{u}_2 s_1) + V_{cd}^2(\overline{c}_1 d_2 + \overline{c}_2 d_1)], \tag{1.21}$$

with $\kappa_W = 1/(4\sin^2\Theta)$ and $q_i = q_i(x, M^2)$ and the CKM matrix elements V_{ij}. The expressions given here are valid in the QPM. At higher order pQCD, Drell-Yan scattering comprises also quark-gluon and gluon-gluon contributions. Certain production channels are sensitive to specific parton-parton reactions, Higgs production, for example, originating predominantly from gluon-gluon fusion. Based on the factorisation theorem [6] one therefore opened a further testing ground for PDFs, and much of the current PDF analyses is about constraining parton distributions by Drell-Yan scattering measurements and semi-inclusive production processes, such as top, jet and charm production, at the LHC. An account of this field is provided below, including a study as to how LHeC would add to the "global" PDF knowledge at the time of the HL-LHC.

There are drawbacks to the use of Drell-Yan and other hadron collider data for the PDF determination and advantages for *ep* scattering: i) DIS has the ability to prescribe the reaction type and the kinematics (x, Q^2) through the reconstruction of solely the leptonic vertex; ii) there are no colour reconnection and, for the lepton vertex, no hadronisation effects disturbing the theoretical description; iii) the most precise LHC data, on W and Z production, are located at a fixed equivalent $Q^2 = M_{W,Z}^2$ and represent a snapshot at a fixed scale which in DIS at the LHeC varies by more than 5 orders of magnitude [10].

There are further difficulties inherent to the use of LHC data for PDF determinations, such as hadronisation corrections and incompatibility of data. For example, the most recent CT18 [67] global PDF analysis had to arrange for a separate set (CT18A) because the standard fit would not respond well to the most precise ATLAS W, Z data taken at 7 TeV cms. The intent to include all data can only be realised with the introduction of so-called χ^2 tolerance criteria which sincerely affect the meaning of the quoted PDF uncertainties.

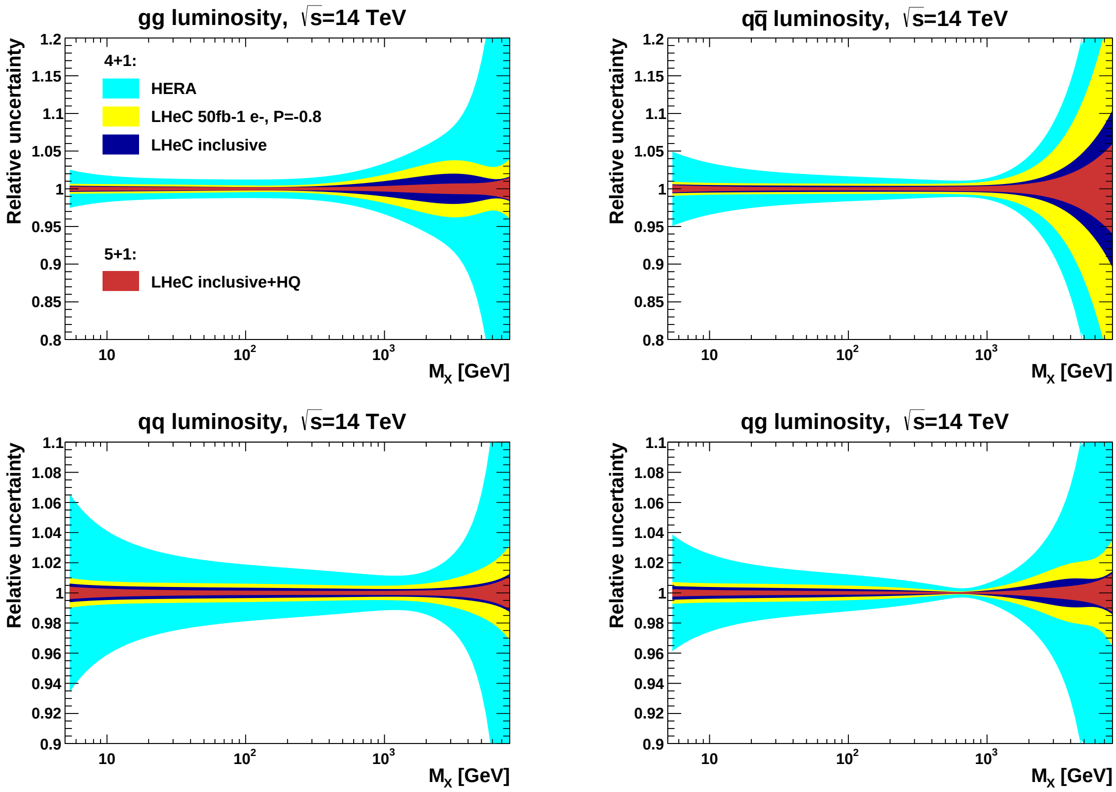

Figure 1.21: Uncertainty bands for parton luminosities as a function of the mass $M_X = \sqrt{sx_1x_2}$ for LHC energies. Light blue: HERA with only part of the uncertainties (EIG); yellow: expectation from the first run period of the LHeC with solely e^-p operation; dark blue: inclusive fit, based on the data sets (D4+D5+D6+D8) in Tab. 1.2; red: fit to the inclusive data adding simulated heavy flavour s, c, b data with a 5 quark distribution parameterisation as introduced above.

Conceptually, the LHeC enables to change this approach completely. Instead of trying to use all previous and current PDF sensitive data, to which currently one has no alternative, it replaces these by pure ep collider DIS data. Then one will bring order back into the PDF field: parton distributions, completely resolved, extending over nearly six orders of magnitude, calculated to all orders pQCD, then likely analysed from NLO to N^{4}LO pQCD (see Sect. 2.4.1), will be available for i) identifying new dynamics and symmetries; ii) testing factorisation; iii) confronting

[10]This is mitigated by measurements of Drell-Yan scattering at low masses, which are less precise, however. At high masses, $M = \sqrt{sx_1x_2} >> M_{W,Z}$, one soon reaches the region where new physics may occur, i.e. there arises the difficulty to separate unknown physics from the uncertainty of the quark and gluon densities at large x. High mass Drell Yan searches often are performed at the edge of the data statistics, i.e. they can not really be guided by data but miss a reliable guidance for the behaviour of the SM background around and beyond a (non-) resonant effect they would like to discover.

global fits at that time with precision PDFs from LHeC; iv) performing high precision Higgs and electroweak analyses and, not least, v) interpreting any peculiar signal for BSM, especially at high mass, using an independent and reliable PDF base. It has been customary, which is obvious from Eqs. 1.15, 1.20 and 1.21, to express the usefulness of various PDF determinations and prospects for the LHC, and similarly the FCC, with four so-called parton luminosities which are defined as

$$L_{ab}(M_X) = \int dx_a dx_b \sum_q F_{ab}\ \delta(M_X^2 - s x_a x_b) \tag{1.22}$$

where F_{ab} for $(a,b) = (q\bar{q})$ is defined in Eq. 1.15 and (a,b) could also be (g,q), $(g,\bar{q})$ and (gg), without a sum over quarks in the latter case. The expectations for the quark and gluon related four parton luminosities are presented in Fig. 1.21. The LHeC provides very precise parton luminosity predictions in the complete range of M_X up to the high mass edge of the search range at the LHC. This eliminates the currently sizeable PDF uncertainty of precision electroweak measurements at the LHC, as for example for the anticipated measurement of M_W to within 10^{-4} uncertainty, see below. One may also notice that the gluon-gluon luminosity (left top in Fig. 1.21) is at a per cent level for the Higgs mass $M_X = M_H \simeq 125\,\mathrm{GeV}$. This is evaluated further in the chapter on Higgs physics with the LHeC.

1.4 The 3D Structure of the Proton

As is evident from the discussion in the previous Sections, the LHeC machine will be able to measure the collinear parton distribution functions with unprecedented accuracy in its extended range of x and Q^2. Thus, it will provide a new insight into the details of the one-dimensional structure of the proton and nuclei, including novel phenomena at low x. In addition to collinear dynamics, the LHeC opens a new window into proton and nuclear structure by allowing a precise investigation of the partonic structure in more than just the one dimension of the longitudinal momentum. Precision DIS thus gives access to multidimensional aspects of hadron structure. This can be achieved by accurately measuring processes with more exclusive final states like production of jets, semi-inclusive production of hadrons and exclusive processes, in particular the elastic diffractive production of vector mesons and deeply virtual Compton (DVCS) scattering. These processes have the potential to provide information not only on the longitudinal distribution of partons in the proton or nucleus, but also on the dependence of the parton distribution on transverse momenta and momentum transfer. Therefore, future, high precision DIS machines like the LHeC or the Electron Ion Collider (EIC) in the US [68], open a unique window into the details of the 3D structure of hadrons.

The most general quantity that can be defined in QCD that would contain very detailed information about the partonic content of the hadron, is the Wigner distribution [69]. This function $W(x, \mathbf{k}, \mathbf{b})$ is a 1+4 dimensional function. One can think of it as the mother or master parton distribution, from which lower-dimensional distributions can be obtained. In the definition of the Wigner function, $\mathbf{k}$ is the transverse momentum of the parton and $\mathbf{b}$ is the 2-dimensional impact parameter, which can be defined as a Fourier conjugate to the momentum transfer of the process. The other, lower dimensional parton distributions can be obtained by integrating out different variables. Thus, transverse momentum dependent (TMD) parton distributions (or unintegrated parton distribution functions) $f_{\mathrm{TMD}}(x, \mathbf{k})$ can be obtained by integrating out the impact parameter $\mathbf{b}$ in the Wigner function, while the generalised parton densities (GPD), $f_{\mathrm{GPD}}(x, \mathbf{b})$, can be obtained from the Wigner function through the integration over the transverse momentum $\mathbf{k}$. In the regime of small x, or high energy, a suitable formalism is that of the dipole picture [70–75], where the fundamental quantity which contains the details of the partonic distribution is the dipole amplitude $N(x, \mathbf{r}, \mathbf{b})$. This object contains the dependence on the impact parameter $\mathbf{b}$ as well as another transverse size $\mathbf{r}$, the dipole size, which can be related to the transverse momentum of the parton $\mathbf{k}$ through a Fourier transform. The important feature of the dipole amplitude is that it should obey the unitarity limit $N \leq 1$. The dipole amplitude N within this formalism can be roughly interpreted as a Wigner function in the high energy limit, as it contains information about the spatial distribution of the partons in addition to the dependence on the longitudinal momentum fraction x.

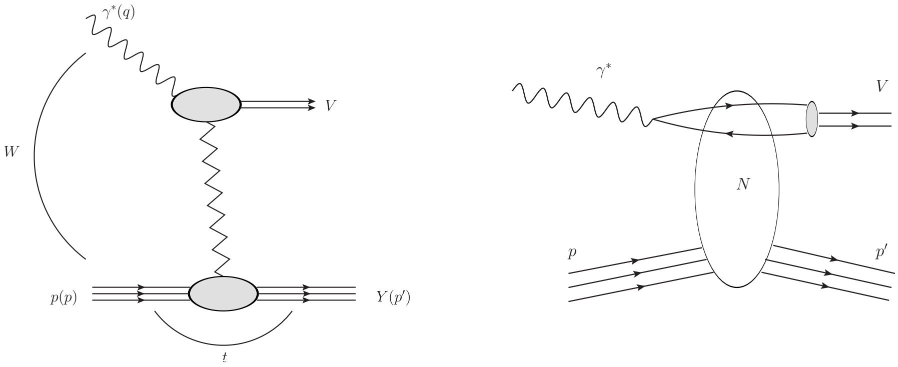

Figure 1.22: Left: diagram for the quasi-elastic production of the vector meson. Right: schematic illustration of the same process, quasi-elastic vector meson production, within the framework of the dipole picture. The initial virtual photon, fluctuates into a quark-antiquark pair which then scatters off the hadronic target and forms the vector meson. The details of the hadronic interaction of the dipole with the target are encoded in the dipole amplitude N.

Detailed simulations of elastic J/ψ vector meson production were performed for the LHeC kinematic region and beyond [1], using the formalism of the dipole picture. This particular process is shown in Fig. 1.22, left plot. The proton is scattered elastically with momentum transfer t, and the vector meson is produced, which is separated from the final state proton by a rapidity gap. Of particular importance is the measurement of the t slope of this process, since it can be related directly to the impact parameter distribution and is thus sensitive to the transverse variation of the partonic density in the target. The first type of analysis like this, in the context of elastic scattering, was performed by Amaldi and Schubert [76], where it was demonstrated that the Fourier transform of the elastic cross section yields access to the impact parameter profile of the scattering amplitude. This method can be used in the context of vector meson scattering in DIS, where the transverse distribution of partons, in the perturbative regime, can be extracted through the appropriate Fourier transform [77]. The additional advantage of studying diffractive vector meson production is the fact that the partonic distributions can be studied as a function of the hard scale in this process given by the mass of the vector meson M_V^2 in the photoproduction case or Q^2 (or more precisely a combination of Q^2 and M_V^2) in the case of the diffractive DIS production of vector mesons, as well as the energy W of the photon-proton system available in the process which is closely related to x.

The differential cross section for elastic vector meson production can be expressed in the following form:

$$\frac{d\sigma^{\gamma^* p \to J/\psi p}}{dt} = \frac{1}{16\pi} |\mathcal{A}(x, Q, \Delta)|^2 \,, \tag{1.23}$$

where the amplitude for the process of elastic diffractive vector meson production in the high energy limit, in the dipole picture, is given by

$$\mathcal{A}(x,Q,\Delta) \;=\; \sum_{h\bar{h}} \int d^2\mathbf{r} \int dz \Psi^*_{h\bar{h}}(z,\mathbf{r},Q)\, \mathcal{N}(x,\mathbf{r},\Delta)\, \Psi^V_{h\bar{h}}(z,\mathbf{r})\;. \tag{1.24}$$

In the above formula, $\Psi^*_{h\bar{h}}(z,\mathbf{r},Q)$ is the photon wave function which describes the splitting of the virtual photon γ^* into a $q\bar{q}$ pair. This wave funtion can be calculated in perturbative QCD. The function $\Psi^V_{h\bar{h}}(z,\mathbf{r})$ is the wave function of the vector meson. Finally, $\mathcal{N}(x,\mathbf{r},\Delta)$ is the dipole amplitude which contains all the information about the interaction of the quark-antiquark dipole with the target. The formula (1.24) can be interpreted as the process of fluctuation of the virtual photon into a $q\bar{q}$ pair, which subsequently interacts with the target through the dipole amplitude $\mathcal{N}$ and then forms the vector meson, given by the amplitude Ψ^V, see Fig. 1.22, right plot. The two integrals in the definition Eq. (1.24) are performed over the dipole size which is denoted by $\mathbf{r}$, and z which is the longitudinal momentum fraction of the photon carried by the quark. The scattering amplitude depends on the value of the momentum transfer Δ, which is related to the Mandelstam variable $t = -\Delta^2$. The sum is performed over the helicity states of the quark and antiquark.

The dipole amplitude $\mathcal{N}(x,\mathbf{r},\Delta)$ can be related to the dipole amplitude in coordinate space through the appropriate Fourier transform

$$N(x,\mathbf{r},\mathbf{b}) = \int d^2\Delta\, e^{i\Delta\cdot\mathbf{b}}\mathcal{N}(x,\mathbf{r},\Delta)\;. \tag{1.25}$$

We stress that $\mathbf{r}$ and $\mathbf{b}$ are two different transverse sizes here. The dipole size $\mathbf{r}$ is conjugate to the transverse momentum of the partons $\mathbf{k}$, whereas the impact parameter is roughly the distance between the centre of the scattering target to the centre-of-mass of the quark-antiquark dipole and is related to the Fourier conjugate variable, the momentum transfer Δ.

The dipole amplitude $N(x,\mathbf{r},\mathbf{b})$ contains rich information about the dynamics of the hadronic interaction. It is a 5-dimensional function and it depends on the longitudinal momentum fraction, and two two-dimensional coordinates. The dependence on the longitudinal momentum fraction is obviously related to the evolution with the centre-of-mass energy of the process, while the dependence on $\mathbf{b}$ provides information about the spatial distribution of the partons in the target. The dipole amplitude is related to the distribution of gluons in impact parameter space. The dipole amplitude has a nice property that its value should be bounded from above by the unitarity requirement $N \leq 1$. The complicated dependence on energy, dipole size and impact parameter of this amplitude can provide a unique insight into the dynamics of QCD, and on the approach to the dense partonic regime. Besides, from Eqs. (1.23),(1.24) and (1.25) it is evident that the information about the spatial distribution in impact parameter $\mathbf{b}$ is related through the Fourier transform to the dependence of the cross section on the momentum transfer $t = -\Delta^2$.

To see how the details of the distribution, and in particular the approach to unitarity, can be studied through the VM elastic production, calculations based on the dipole model were performed [78], and extended to energies which can be reached at the LHeC as well as the FCC-eh. The parameterisations used in the calculation were the so-called IP-Sat [79, 80] and b-CGC [81] models. In both cases the impact parameter dependence has to be modelled phenomenologically. In the IP-Sat model the dipole amplitude has the following form

$$N(x,\mathbf{r},\mathbf{b}) \;=\; 1-\exp\left[-\frac{\pi^2 r^2}{2N_c}\alpha_s(\mu^2)xg(x,\mu^2)T_G(b)\right]\;, \tag{1.26}$$

where $xg(x,\mu^2)$ is the collinear gluon density, evolved using LO DGLAP (without quarks), from an initial scale μ_0^2 up to the scale μ^2 set by the dipole size $\mu^2 = \frac{4}{r^2} + \mu_0^2$. $\alpha_s(\mu^2)$ is the strong coupling. The parameterisation of the gluon density at the initial scale μ_0^2 is given by

$$xg(x,\mu_0^2) = A_g x^{-\lambda_g}(1-x)^{5.6} \; , \tag{1.27}$$

and the impact parameter profile for the gluon by

$$T_G(b) \;=\; \frac{1}{2\pi B_G}\exp(-b^2/2B_G) \; . \tag{1.28}$$

An alternative parameterisation is given by the b-CGC model [81] which has the form

$$N(x,\mathbf{r},\mathbf{b}) \;=\; \begin{cases} N_0\left(\frac{rQ_s}{2}\right)^{2\gamma_{\rm eff}} & \text{for} \quad rQ_s \le 2 \; , \\ 1-\exp(-\mathcal{A}\ln^2(\mathcal{B}rQ_s)) & \text{for} \quad rQ_s > 2 \; . \end{cases} \tag{1.29}$$

Here the effective anomalous dimension $\gamma_{\rm eff}$ and the saturation scale Q_s of the proton explicitly depend on the impact parameter and are defined as

$$\begin{aligned} \gamma_]eff &= \gamma_s + \frac{1}{\kappa\lambda\ln 1/x}\ln\left(\frac{2}{rQ_s}\right) \; , \\ Q_s(x,b) &= \left(\frac{x_0}{x}\right)^{\lambda/2}\exp\left[-\frac{b^2}{4\gamma_s B_{\rm CGC}}\right] \; \text{GeV} \; , \end{aligned} \tag{1.30}$$

where $\kappa = \chi''(\gamma_s)/\chi'(\gamma_s)$, with $\chi(\gamma)$ being the leading-logarithmic BFKL kernel eigenvalue function [82]. The parameters $\mathcal{A}$ and $\mathcal{B}$ in Eq.(1.29) are determined uniquely from the matching of the dipole amplitude and its logarithmic derivatives at the limiting value of $rq_s = 2$. The b-CGC model is constructed by smoothly interpolating between two analytically known limiting cases [81], namely the solution of the BFKL equation in the vicinity of the saturation line for small dipole sizes $r < 2/Q_s$, and the solution of the BK equation deep inside the saturation region for large dipole sizes $r > 2/Q_s$.

The parameters μ_0, A_g, λ_g of the IP-Sat model and $N_0, \gamma_s, x_0\lambda$ of the b-CGC model were fitted to obtain the best description of the inclusive data for the structure function F_2 at HERA. The slope parameters B_g and $B_{\rm CGC}$, which control the b -dependence in both models, were fitted to obtain the best description of elastic diffractive J/ψ production, in particular its t-dependence, at small values of t.

In Figs. 1.23 and 1.24 we show the simulated differential cross section $d\sigma/dt$ as a function of $|t|$ and study its variation with energy and virtuality, and its model dependence. First, in Fig. 1.23 we show the differential cross section as a function of t for fixed energy $W = 1\,\text{TeV}$, in the case of the photoproduction of J/ψ (left plot) and for the case of DIS with $Q^2 = 10\,\text{GeV}^2$ (right plot). The energy W corresponds to the LHeC kinematics. There are three different calculations in each plot, using the IP-sat model, the b-CGC model and the 1-Pomeron approximation. The last one is obtained by keeping just the first non-trivial term in the expansion of the eikonalised formula of the IP-Sat amplitude (1.26). First, let us observe that all three models coincide for very low values of t, where the dependence on t is exponential. This is because for low $|t|$, relatively large values of impact parameter are probed in Eq. (1.24) where the amplitude is small, and therefore the tail in impact parameter is Gaussian in all three cases. Since the Fourier transform of the Gaussian in b is an exponential in t, the result at low t follows. On the other hand, the three scenarios differ significantly for large values of $|t|$. In the case of the

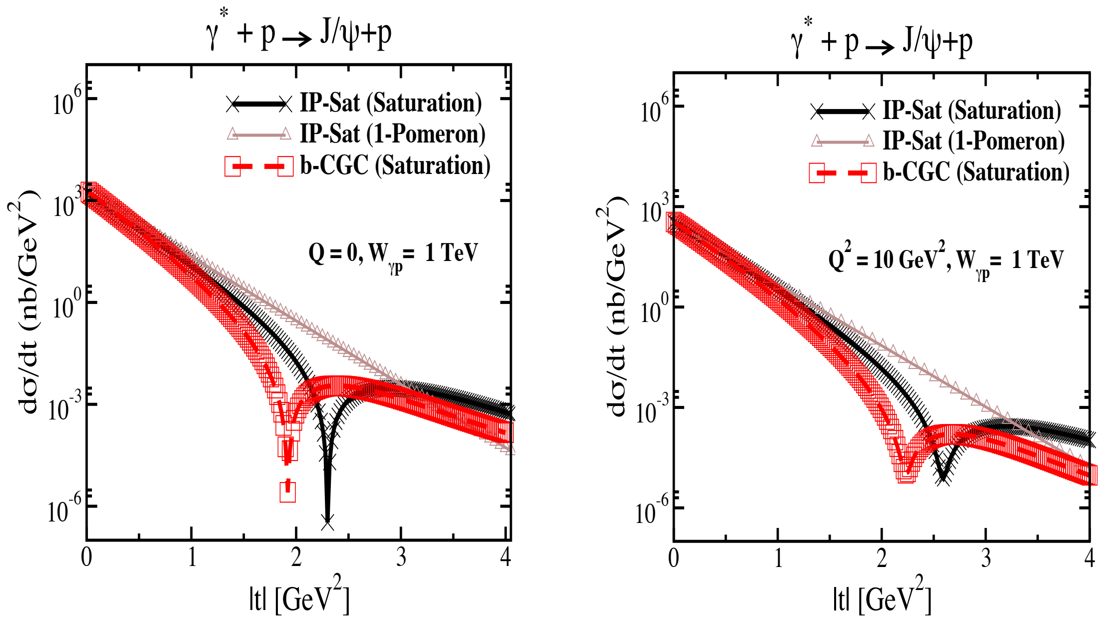

Figure 1.23: Differential cross section for the elastic J/ψ production as a function of $|t|$ within the IP-Sat (saturation), b-CGC and 1-Pomeron models at a fixed $W\gamma p = 1\,\text{TeV}$, which corresponds to the LHeC kinematics, and for two different values of photon virtuality $Q = 0$ and $Q^2 = 10$ GeV^2. The thickness of points includes the uncertainties associated with the freedom to choose different values for the charm quark mass within the range $m_c = 1.2 - 1.4$ GeV.

1-Pomeron approximation the dependence is still exponential, without any dips, which is easily understood since the impact parameter profile is perfectly Gaussian in this case. For the two other scenarios, dips in $d\sigma/dt$ as a function in t emerge. They signal the departure from the Gaussian profile in b for small values of b where the system is dense. A similar pattern can be observed when performing the Fourier transform of the Wood-Saxon distribution, which is the typical distribution used for the description of the matter density in nuclei. When Q^2 is increased the pattern of dips also changes. This is illustrated in Fig. 1.23. It is seen that the dips move to higher values of $|t|$ for DIS than for photoproduction. This can be understood from the dipole formula Eq. (1.24) which contains the integral over the dipole size. Larger values of Q^2 select smaller values of dipole size r, where the amplitude is smaller and thus in the dilute regime, where the profile in b is again Gaussian. On the other hand, small scales select large dipole sizes for which the dipole amplitude is larger and thus the saturation effects more prominent, leading to the distortion of the impact parameter profile and therefore to the emergence of dips in the differential cross section $d\sigma/dt$ when studied as a function of t.

In the next Fig. 1.24 we show the same calculation but for higher energy $W = 2.5\,\text{TeV}$, which could be explored in the FCC-eh. In this case we see that the dips move to lower values of $|t|$. This can be easily understood, as with increasing energy the dipole scattering amplitude increases, and thus the dilute-dense boundary shifts to larger values of b, meaning that the deviation from the exponential fall off occurs for smaller values of $|t|$. Similar studies [78] show also the change of the position of the dips with the mass of the vector meson: for lighter vector mesons like ρ, ω, ϕ the dips occur at smaller t than for the heavier vector mesons J/ψ or Υ. We note that, of course, the positions of the dips depend crucially on the details of the models, which are currently not constrained by the existing HERA data. We also note the sizeable uncertainties due to the charm quark mass (the fits to inclusive HERA data from which parameters of the models have been extracted are performed at each fixed value of the charm mass that is then

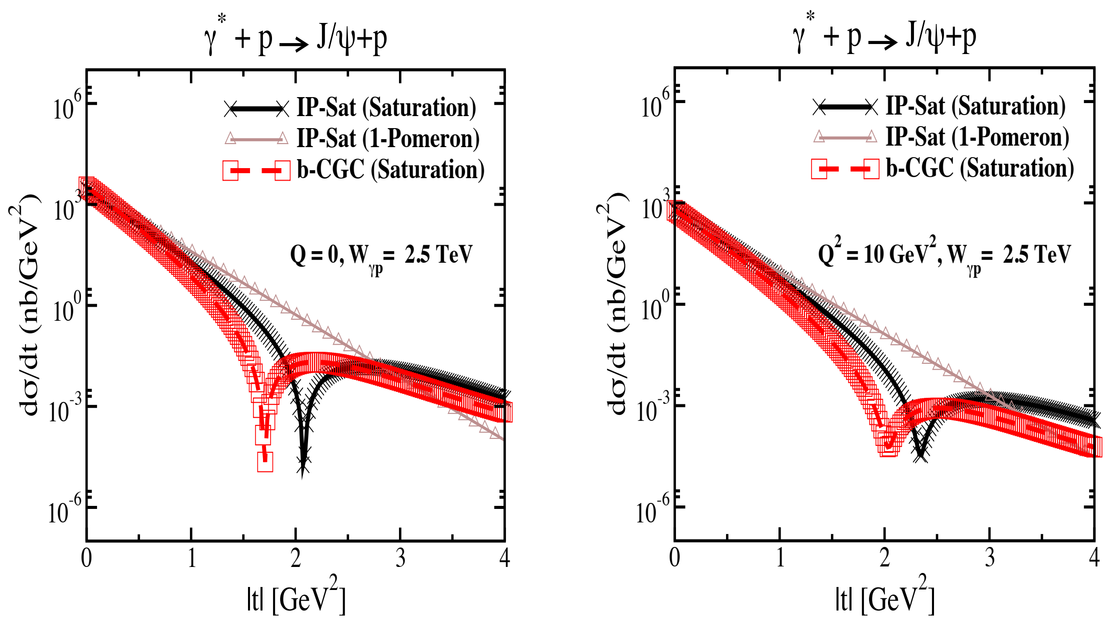

Figure 1.24: Differential cross section for elastic J/ψ production as a function of $|t|$ within the IP-Sat (saturation), b-CGC and 1-Pomeron models at a fixed $W\gamma p = 2.5\,\text{TeV}$, which corresponds to the region that can be explored by FCC-eh, and for two different values of photon virtuality $Q = 0$ (left plot) and $Q^2 = 10$ GeV^2 (right plot). The thickness of points includes the uncertainties associated with the freedom to choose different values for the charm quark mass within the range $m_c = 1.2 - 1.4$ GeV .

used to compute exclusive J/ψ production).

We thus see that the precise measurement of the t-slope in the elastic production of vector mesons at the LHeC, and its variation with x and scales, provide a unique opportunity to explore the transition between the dilute and dense partonic regimes. As mentioned earlier, elastic diffractive production is one among several different measurements which can be performed to explore the 3D structure of the hadron. Another one is Deeply Virtual Compton Scattering which is a process sensitive to the spatial distribution of quarks inside the hadron. Previous preliminary analyses [1] indicate a huge potential of LHeC for the measurement of DVCS. Another example of a process that could be studied at the LHeC, is diffractive exclusive dijet production. It has been suggested [83] that this process is sensitive to the Wigner function, and that the transverse momentum and spatial distribution of partons can be extracted by measuring this process. The transverse momentum of jets would be sensitive to the transverse momentum of the participating partons, whereas the momentum transfer of the elastically scattered proton would give a handle on the impact parameter distribution of the partons in the target [84–86], thus giving a possibility to extract information about the Wigner distribution.

So far we have referred to coherent diffraction, i.e. to a scenario in which the proton remains intact after the collision. There also exists incoherent diffraction, where the proton gets excited into some state with the quantum numbers of the proton and separated from the rest of the event by a large rapidity gap. In order to apply the dipole formalism to the incoherent case, see Sec. **??** where the formulae applicable for both protons and nuclei are shown. Here one must consider a more involved structure of the proton (e.g. as composed by a fixed [87–90] or a growing number with $1/x$ of hot spots [91–93]). As discussed in Sec. **??**, coherent diffraction is sensitive to the gluon distribution in transverse space, while incoherent diffraction is particularly sensitive to fluctuations of the gluon distribution. A prediction of the model with a growing number of hot spots, both in models where this increasing number is implemented by hand [91–93] and in those where it is dynamically generated [90] from a fixed number at larger x, is that the ratio of incoherent to coherent diffraction will decrease with W, and that this decrease is sensitive to the details of the distribution of hot spots. Thus, to the fluctuations of the gluon distribution in transverse space. In order to check these ideas, both the experimental capability to separate coherent from incoherent diffraction and a large lever arm in W, as available at the LHeC, are required.

Chapter 2

Exploration of Quantum Chromodynamics

The straightforward and strikingly simple formalism of Quantum Chromodynamics (QCD) provides a very successful description of strong interactions. Despite its undoubted success, the strong force remains one of the least known fundamental sectors of (particle) physics and many of its phenomena are known only with moderate or even poor precision, and several aspects still need to be explored, see the introductory Chapter **??**.

For an improved understanding of strong interactions and to answer a variety of those open questions additional measurements with highest precision have to be performed. At the LHeC, deep-inelastic electron-proton and lepton-nucleus reactions will extend tests of QCD phenomena to a new and yet unexplored domain up to the TeV scale and to x values as low as 10^{-6}, and QCD measurements can be performed with very high experimental precision. This is because the proton is a *strongly* bound system and in deep-inelastic scattering (DIS) the exchanged *colourless* photon (or Z) between the electron and the parton inside the proton acts as a neutral observer with respect to the phenomena of the strong force. In addition, the over-constrained kinematic system in DIS allows for precise (*in-situ*) calibrations of the detector to measure the kinematics of the scattered lepton, and, more importantly here, also the hadronic final state. In DIS, in many cases, the virtuality of the exchanged γ/Z boson often provides a reasonable scale to stabilise theoretical predictions.

In this Chapter, selected topics of QCD studies at the LHeC are discussed.

2.1 Determination of the strong coupling constant

Quantum Chromodynamics (QCD) [94, 95] has been established as the theory of strong interactions within the Standard Model of particle physics. While there are manifold aspects both from the theoretical and from the experimental point-of-view, by far the most important parameter of QCD is the coupling strength which is most commonly expressed at the mass of the Z boson, M_Z, as $\alpha_s(M_Z)$. Its (renormalisation) scale dependence is given by the QCD gauge group SU(3) [96, 97]. Predictions for numerous processes in e^+e^-, pp or ep collisions are then commonly performed in the framework of perturbative QCD, and (the lack of) higher-order QCD corrections often represent limiting aspects for precision physics. Therefore, the determination of the strong coupling constant $\alpha_s(M_Z)$ constitutes one of the most crucial tasks for future precision physics, while at the same time the study of the scale dependence of α_s provides an inevitable test of the validity of QCD as the theory of strong interactions and the portal for GUT theories.

Different processes and methodologies can be considered for a determination of $\alpha_s(M_Z)$ (see e.g. reviews [98–100]). Since QCD is an asymptotically free theory, with free behaviour at high scales but confinement at low scales, a high sensitivity to the value of $\alpha_s(M_Z)$ is naturally obtained from low-scale measurements. However, the high-scale behaviour must then be calculated by solving the renormalisation group equation, which implies the strict validity of the theory and an excellent understanding of all subleading effects, such as the behaviour around quark-mass thresholds.

Precision measurements at the LHeC offer the unique opportunity to exploit many of these aspects. Measurements of jet production cross sections or inclusive NC and CC DIS cross sections provide a high sensitivity to the value of $\alpha_s(M_Z)$, since these measurements can be performed at comparably low scales and with high experimental precision. At the same time, the LHeC provides the opportunity to test the running of the strong coupling constant over a large kinematic range. In this Section, the prospects for a determination of the strong coupling constant with inclusive jet cross sections and with inclusive NC/CC DIS cross sections are studied.

2.1.1 Strong coupling from inclusive jet cross sections

The measurement of inclusive jet or di-jet production cross sections in NC DIS provides a high sensitivity to the strong coupling constant and to the gluon PDF of the proton. This is because jet cross sections in NC DIS are measured in the Breit reference frame [101], where the virtual boson γ^* or Z collides head-on with the struck parton from the proton and the outgoing jets are required to have a non-zero transverse momentum in that reference frame. The leading order QCD diagrams are QCD Compton and boson-gluon fusion and are both $\mathcal{O}(\alpha_s)$, see Fig. 2.1.

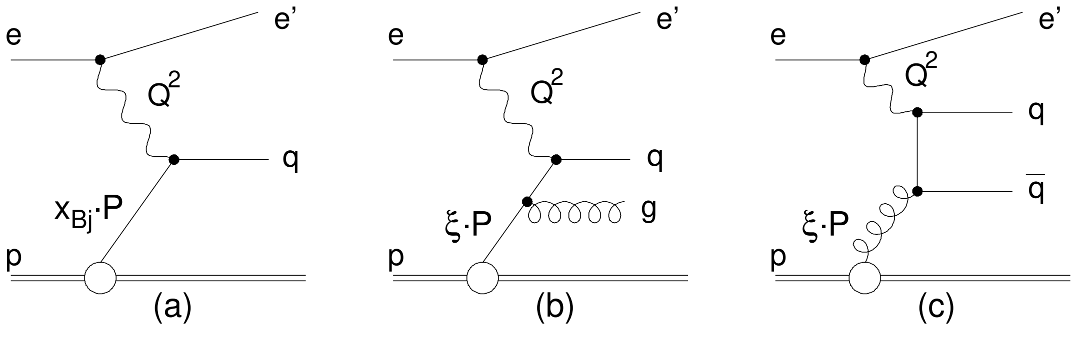

Figure 2.1: Leading order diagrams for inclusive DIS (a) and jet production (b,c) in the Breit frame (taken from Ref. [102]).

At HERA, jets are most commonly defined by the longitudinally invariant k_t jet algorithm [103] with a distance parameter $R = 1.0$ [102, 104–120]. This provides an infrared safe jet definition and the chosen distance parameter guarantees a small dependence on non-perturbative effects, such as hadronisation. Differently than in *pp* at the LHC [121–124], jet algorithms at the LHeC do not require any pile-up subtraction and any reduction of the dependence on minimum bias or underlying event, due to the absence of such effects. Therefore, for this study we adopt the choices made at HERA.

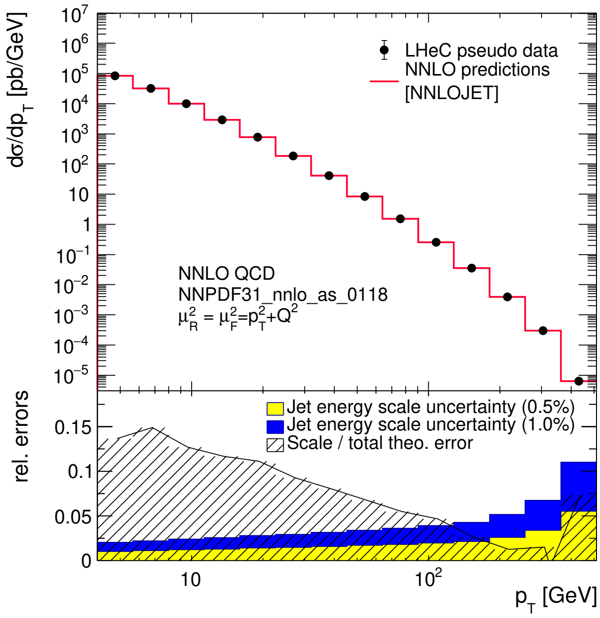

Figure 2.2: Inclusive jet cross sections calculated in NNLO QCD as a function of the jet transverse momentum in the Breit frame, p_{T}. The shaded area indicates NNLO scale uncertainties and the yellow band shows the estimated experimental jet energy scale uncertainty (JES) of 0.5 %. The blue band shows a very conservative assumption on the JES of 1 %.

In Fig. 2.2 the next-to-next-to-leading order QCD (NNLO) predictions [125, 126] for cross sections for inclusive jet production in NC DIS as a function of the transverse momentum of the jets in the Breit frame are displayed. The calculations are performed for an electron beam energy of $E_e = 60\,\mathrm{GeV}$ and include γ/Z and Z exchange terms and account for the electron polarisation $P_e = -0.8$. The NC DIS kinematic range is set to $Q^2 > 4\,\mathrm{GeV}^2$. The calculations are performed using the NNLOJET program [127] interfaced to the fastNLO (applfast) library [128–130].

The kinematically accessible range in jet-P_{T} ranges over two orders of magnitude, $4 < P_{\mathrm{T}} \lesssim 400\,\mathrm{GeV}$. The size of the cross section extends over many orders in magnitude, thus imposing challenging demands on LHeC experimental conditions, triggers and DAQ bandwidth, calibration, and data processing capabilities. The scale uncertainty of the NNLO predictions is about 10 % at low values of P_{T} and significantly decreases with increasing values of P_{T}. Future improved predictions will further reduce these theoretical uncertainties.

For the purpose of estimating the uncertainty of $\alpha_{\mathrm{s}}(M_{\mathrm{Z}})$ in a determination from inclusive jet cross sections at the LHeC, double-differential cross sections as a function of Q^2 and P_{T} with a full set of experimental uncertainties are generated. Altogether 509 cross section values are calculated in the kinematic range $8 < Q^2 < 500\,000\,\mathrm{GeV}^2$ and $4 < P_{\mathrm{T}} < 512\,\mathrm{GeV}$, and the bin grid is similar to the ones used by CMS, H1 or ZEUS [13, 121, 130, 131]. The various error sources considered are summarised in Tab. 2.1. The uncertainties related to the reconstruction of the NC DIS kinematic variables, Q^2, y and $x_{\mathrm{b}j}$, are similar to the estimates for the inclusive NC DIS cross sections (see section 1.2). For the reconstruction of hadronic final state particles which are the input to the jet algorithm, jet energy scale uncertainty (JES), calorimetric noise and the polar angle uncertainty are considered. The size of the uncertainties is gauged with achieved values by H1, ZEUS, ATLAS and CMS [111, 119, 132–134]. The size of the dominant JES one is assumed to be 0.5 % for reconstructed particles in the laboratory rest frame, yielding an uncertainty of 0.2–4.4 % on the cross section after the boost to the Breit frame. A JES uncertainty of 0.5 %

is well justified by improved calorimeters, since already H1 and ZEUS reported uncertainties of 1 % [111, 119, 132], and ATLAS and CMS achieved 1 % over a wide range in P_{T} [133, 134], albeit the presence of pile-up and the considerably more complicated definition of a reference object for the in-situ calibration. The size of the JES uncertainty is also displayed in Fig. 2.2. The calorimetric noise of ±20 MeV on every calorimeter cluster, as reported by H1, yields an uncertainty of up to 0.7 % on the jet cross sections. A minimum size of the statistical uncertainty of 0.15 % is imposed for each cross section bin. An overall normalisation uncertainty of 1.0 % is assumed, which will be mainly dominated by the luminosity uncertainty. In addition, an uncorrelated uncertainty component of 0.6 % collects various smaller error sources, such as for instance radiative corrections, unfolding or model uncertainties. Studies on the size and the correlation model of these uncertainties are performed below.

Exp. uncertainty	Shift	Size on σ [%]
Statistics with 1 ab^{-1}	min. 0.15 %	0.15 –5
Electron energy	0.1 %	0.02 –0.62
Polar angle	2 mrad	0.02 –0.48
Calorimeter noise	±20 MeV	0.01 –0.74
Jet energy scale (JES)	0.5 %	0.2 –4.4
Uncorrelated uncert.	0.6 %	0.6
Normalisation uncert.	1.0 %	1.0

Table 2.1: Anticipated uncertainties of inclusive jet cross section measurements at the LHeC.

The value and uncertainty of $\alpha_{\mathrm{s}}(M_{\mathrm{Z}})$ is obtained in a χ^2-fit of NNLO predictions [125, 126] to the simulated data with $\alpha_{\mathrm{s}}(M_{\mathrm{Z}})$ being a free fit parameter. The methodology follows closely analyses of HERA jet data [130,131] and the χ^2 quantity is calculated from relative uncertainties, i.e. those of the right column of Tab. 2.1. The predictions for the cross section σ account for both α_s-dependent terms in the NNLO calculations, i.e. in the DGLAP operator and the hard matrix elements, by using

$$\sigma = f_{\mu_0} \otimes P_{\mu_0 \to \mu_F}(\alpha_s(M_z)) \otimes \hat{\sigma}(\alpha_s(M_z), \mu)\,, \tag{2.1}$$

where f_{μ_0} are the PDFs at a scale of $\mu_0 = 30\,\mathrm{GeV}$, and $P_{\mu_0 \to \mu_F}$ denotes the DGLAP operator, which is dependent on the value of $\alpha_{\mathrm{s}}(M_{\mathrm{Z}})$. The α_s uncertainty is obtained by linear error propagation and is validated with a separate study of the $\Delta\chi^2 = 1$ criterion.

In the fit of NNLO QCD predictions to the simulated double-differential LHeC inclusive jet cross sections an uncertainty of

$$\Delta\alpha_{\mathrm{s}}(M_{\mathrm{Z}})(\mathrm{jets}) = \pm 0.00013_{(\mathrm{exp})} \pm 0.00010_{(\mathrm{PDF})} \tag{2.2}$$

is found. The PDF uncertainty is estimated from a PDF set obtained from LHeC inclusive DIS data (see Sec. 1.3). These uncertainties promise a determination of $\alpha_{\mathrm{s}}(M_{\mathrm{Z}})$ with the highest precision and would represent a considerable reduction of the current world average value with a present uncertainty of ±0.00110 [99].

The uncertainty of α_s is studied for different values of the experimental uncertainties for the inclusive jet cross section measurement and for different assumption on bin-to-bin correlations, expressed by the correlation coefficient ρ, of individual uncertainty sources, as shown in Fig. 2.3. It is observed that, even for quite conservative scenarios, $\alpha_s(M_Z)$ will be determined with an uncertainty smaller than 2 ‰. For this, it is important to keep the size of the uncorrelated uncertainty or the uncorrelated components of other systematic uncertainties under good control.

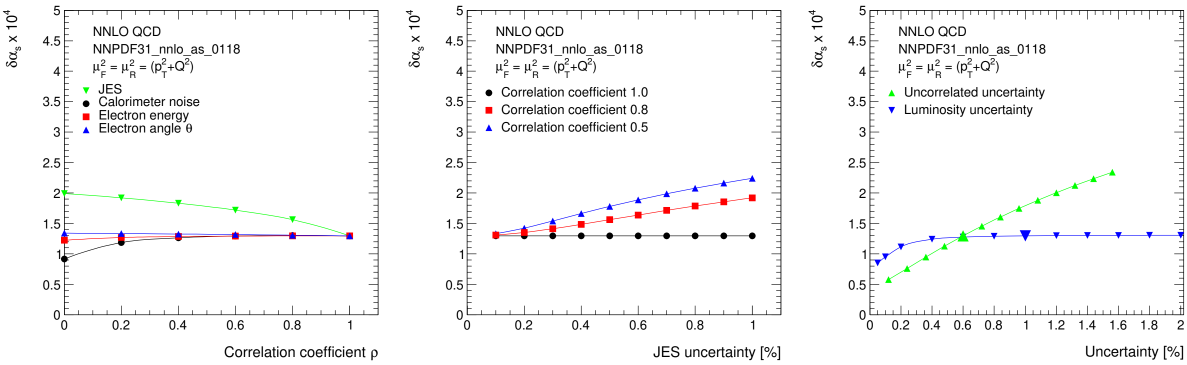

Figure 2.3: Studies of the size and correlations of experimental uncertainties impacting the uncertainty of $\alpha_s(M_Z)$. Left: Study of the value of the correlation coefficient ρ for different systematic uncertainties. Common systematic uncertainties are considered as fully correlated, $\rho = 1$. Middle: Size of the JES uncertainty for three different values of ρ_{JES}. Right: Impact of the uncorrelated and normalisation uncertainties on $\Delta\alpha_{\text{s}}(M_{\text{Z}})$.

In the present formalism theoretical uncertainties from scale variations of the NNLO predictions amount to about $\Delta\alpha_{\text{s}}(M_{\text{Z}}) = 0.0035\,(\text{NNLO})$. These can be reduced with suitable cuts in P_{T} or Q^2 to about $\Delta\alpha_{\text{s}}(M_{\text{Z}}) \approx 0.0010$. However, it is expected that improved predictions, e.g. with resummed contributions or N^{3}LO predictions will significantly reduce these uncertainties in the future. Uncertainties on non-perturbative hadronisation effects will have to be considered as well, but these will be under good control due to the measurements of charged particle spectra at the LHeC and improved phenomenological models.

2.1.2 Pinning Down α_s with Inclusive and Jet LHeC Data

The dependence of the coupling strength as a function of the renormalisation scale μ_{R} is predicted by QCD, which is often called the *running* of the strong coupling. Its study with experimental data represents an important consistency and validity test of QCD. Using inclusive jet cross sections the running of the strong coupling can be tested by determining the value of α_{s} at different values of μ_{R} by grouping data points with similar values of μ_{R} and determining the value of $\alpha_{\text{s}}(\mu_{\text{R}})$ from these subsets of data points. The assumptions on the running of $\alpha_{\text{s}}(\mu_{\text{R}})$ are then imposed only for the limited range of the chosen interval, and not to the full measured interval as in the previous study. Here we set $\mu_{\text{R}}^2 = Q^2 + P_{\text{T}}^2$ [1]. The experimental uncertainties from the fits to subsets of the inclusive jet pseudodata are displayed in Fig. 2.4. These results demonstrate a high sensitivity to α_s over two orders of magnitude in renormalisation scale up to values of about $\mu_{\text{R}} \approx 500\,\text{GeV}$. In the range $6 < \mu_{\text{R}} \lesssim 200\,\text{GeV}$ the experimental uncertainty is found to be smaller than the expectation from the world average value [142]. This region is of particular interest since it connects the precision determinations from lattice calculations [143]

[1] The choice of the scales follows a *conventional* scale setting procedure and uncertainties for the scale choice and for unknown higher order terms are estimated by varying the scales. Such variations are sensitive only to the terms which govern the behaviour of the running coupling, and may become unreliable due to renormalons [135]. An alternative way to fix the scales is provided by the Principle of Maximum Conformality (PMC) [136–140]. The PMC method was recently applied to predictions of event shape observables in $e^+e^- \to$ hadrons [141]. When applying the PMC method to observables in DIS, the alternative scale setting provides a profound alternative to verify the running of $\alpha_{\text{s}}(\mu_{\text{R}})$. Such a procedure could be particularly relevant for DIS event shape observables, where the leading-order terms are insensitive to α_{s} and conventional scale choices may not be adequately related to the α_s-sensitive higher order QCD corrections.

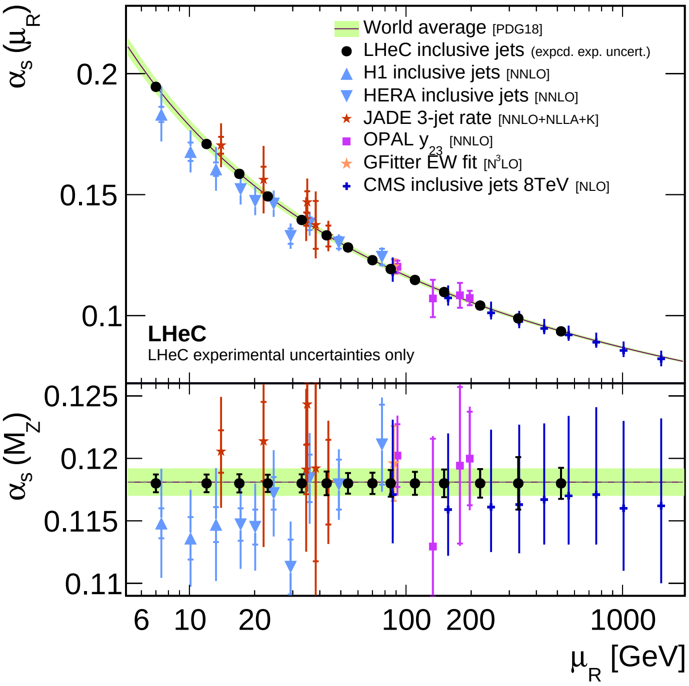

Figure 2.4: Uncertainties of $\alpha_s(M_Z)$ and corresponding $\alpha_s(\mu_R)$ in a determination of α_s using LHeC inclusive jet cross sections at different values of $\mu_R^2 = Q^2 + p_T^2$. Only experimental uncertainties are shown for LHeC and are compared with a number of presently available measurements and the world average value.

or τ decay measurements [144], which are at low scales $\mathcal{O}(\text{GeV})$, to the measurements at the Z pole [145] and to the applications to scales which are relevant for the LHC, e.g. for Higgs or top-quark physics or high-mass searches. This kinematic region of scales $\mathcal{O}(10\,\text{GeV})$ cannot be accessed by (HL-)LHC experiments because of limitations due to pile-up and underlying event [146].

Inclusive DIS cross sections are sensitive to $\alpha_s(M_Z)$ through higher-order QCD corrections, contributions from the F_L structure function and the scale dependence of the cross section at high x (*scaling violations*). The value of $\alpha_s(M_Z)$ can then be determined in a combined fit of the PDFs and $\alpha_s(M_Z)$ [131]. While a simultaneous determination of $\alpha_s(M_Z)$ and PDFs is not possible with HERA inclusive DIS data alone due to its limited precision and kinematic coverage [13, 131], the large kinematic coverage, high precision and the integrated luminosity of the LHeC data will allow for the first time such an α_s analysis.

For the purpose of the determination of $\alpha_s(M_Z)$ from inclusive NC/CC DIS data, a combined PDF+α_s fit to the simulated data is performed, similar to the studies in Sec. **??**. Other technical details are outlined in Ref. [131]. In this fit, however, the numbers of free parameters of the gluon parameterisation is increased, since the gluon PDF and $\alpha_s(M_Z)$ are highly correlated and LHeC data are sensitive to values down to $x < 10^{-5}$, which requires additional freedom for the gluon parameterisation. The inclusive data are restricted to $Q^2 > 3.5\,\text{GeV}^2$ in order to avoid a region where effects beyond fixed-order perturbation theory may become sizeable [13, 147].

Exploiting the full LHeC inclusive NC/CC DIS data with $E_e = 50\,\text{GeV}$, the value of $\alpha_s(M_Z)$ can be determined with an uncertainty $\Delta\alpha_s(M_Z) = \pm 0.00038$. With a more optimistic assumption on the dominant uncorrelated uncertainty of $\delta\sigma_{(\mathrm{uncor.})} = 0.25\,\%$, an uncertainty as small as

$$\Delta\alpha_s(M_Z)(\text{incl. DIS}) = \pm 0.00022_{(\mathrm{exp+PDF})} \tag{2.3}$$

is achieved. This would represent a considerable improvement over the present world average value. Given these small uncertainties, theoretical uncertainties from missing higher orders or heavy quark effects have to be considered in addition. In a dedicated study, the fit is repeated

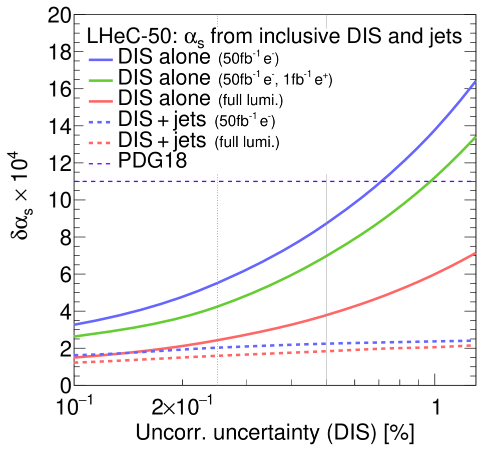

Figure 2.5: Uncertainties of $\alpha_s(M_Z)$ from simultaneous fits of $\alpha_s(M_Z)$ and PDFs to inclusive NC/CC DIS data as a function of the size of the uncorrelated uncertainty of the NC/CC DIS data. The full lines indicate the uncertainties obtained with different assumptions on the data taking scenario and integrated luminosity. The dashed lines indicate results where, additionally to the inclusive NC/CC DIS data, inclusive jet cross section data are considered.

with a reduced data set which can be accumulated already during a single year of operation [2], corresponding to about $\mathcal{L} \sim 50\,\mathrm{fb}^{-1}$. Already these data will be able to improve the world average value. These studies are displayed in Fig. 2.5.

The highest sensitivity to $\alpha_s(M_Z)$ and an optimal treatment of the PDFs is obtained by using inclusive jet data together with inclusive NC/CC DIS data in a combined determination of $\alpha_s(M_Z)$ and the PDFs. Jet data will provide an enhanced sensitivity to $\alpha_s(M_Z)$, while inclusive DIS data has the highest sensitivity to the determination of the PDFs. Furthermore, a consistent theoretical QCD framework can be employed.

For this study, the double-differential inclusive jet data as described above, and additionally the inclusive NC/CC DIS data with $E_e = 50\,\mathrm{GeV}$ as introduced in Sec. 1.2, are employed. Besides the normalisation uncertainty, all sources of systematic uncertainties are considered as uncorrelated between the two processes. A fit of NNLO QCD predictions to these data sets is then performed, and $\alpha_s(M_Z)$ and the parameters of the PDFs are determined. The methodology follows closely the methodology sketched in the previous study. Using inclusive jet and inclusive DIS data in a single analysis, the value of $\alpha_s(M_Z)$ is determined with an uncertainty of

$$\Delta\alpha_s(M_Z)(\text{incl. DIS \& jets}) = \pm 0.00018_{(\mathrm{exp+PDF})}\,. \tag{2.4}$$

This result will improve the world average value considerably. However, theoretical uncertainties are not included and new mathematical tools and an improved understanding of QCD will

[2] Two different assumptions are made. One fit is performed with only electron data corresponding to $\mathcal{L} \sim 50\,\mathrm{fb}^{-1}$, and an alternative scenario considers further positron data corresponding to $\mathcal{L} \sim 1\,\mathrm{fb}^{-1}$.

be needed in order to achieve small values similar to the experimental ones. The dominant sensitivity in this study arises from the jet data. This can be seen from Fig. 2.5, where $\Delta\alpha_s(M_Z)$ changes only moderately with different assumptions imposed on the inclusive NC/CC DIS data. Assumptions made for the uncertainties of the inclusive jet data have been studied above, and these results can be translated easily to this PDF+α_s fit.

The expected values for $\alpha_s(M_Z)$ obtained from inclusive jets or from inclusive NC/CC DIS data are compared in Fig. 2.6 with present determinations from global fits based on DIS data (called *PDF fits*) and the world average value [99]. It is observed that LHeC will have the potential

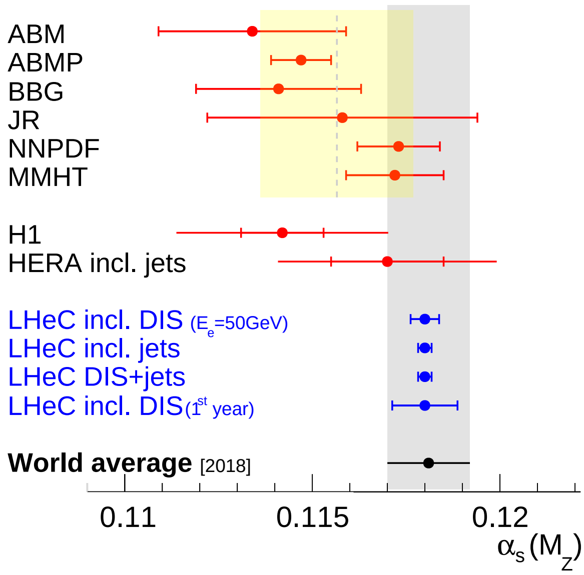

Figure 2.6: Summary of $\alpha_s(M_Z)$ values in comparison with present values.

to improve considerably the world average value. Already after one year of data taking, the experimental uncertainties of the NC/CC DIS data are competitive with the world average value. The measurement of jet cross sections will further improve that value (not shown).

Furthermore, LHeC will be able to address a long standing puzzle. All α_s determinations from global fits based on NC/CC DIS data find a lower value of $\alpha_s(M_Z)$ than determinations in the lattice QCD framework, from τ decays or in a global electroweak fit. With the expected precision from LHeC this discrepancy will be resolved.

2.1.3 Strong coupling from other processes

A detailed study for the determination of $\alpha_s(M_Z)$ from NC/CC DIS and from inclusive jet data was presented in the previous paragraphs. However, a large number of additional processes and observables that are measured at the LHeC can also be considered for a determination of $\alpha_s(M_Z)$. Suitable observables or processes are di-jet and multi-jet production, heavy flavour production, jets in photoproduction or event shape observables. These processes all exploit the α_s dependence of the hard interaction. Using suitable predictions, also *softer* processes can be exploited for an α_s determination. Examples could be jet shapes or other substructure observables, or charged particle multiplicities.

Since $\alpha_s(M_Z)$ is a parameter of a phenomenological model, the total uncertainty of $\alpha_s(M_Z)$ is always a sum of experimental and theoretical uncertainties which are related to the definition of the observable and to the applied model, e.g. hadronisation uncertainties, diagram removal/subtraction uncertainties or uncertainties from missing higher orders. Therefore, credible prospects for the total uncertainty of $\alpha_s(M_Z)$ from other observables or processes are altogether difficult to predict, even more since LHeC will explore a new kinematic regime that was previously unmeasured.

In a first approximation, for any process the sensitivity to $\alpha_s(M_Z)$ scales with the order n of α_s in the leading-order diagram, α_s^n. The higher the power n the higher the sensitivity to $\alpha_s(M_Z)$. Consequently, the experimental uncertainty of an α_s fit may reduce with increasing power n. Already at HERA three-jet cross section were proven to have a high sensitivity to $\alpha_s(M_Z)$ albeit their sizeable statistical uncertainties [102, 112]. At the LHeC, due to the higher $\sqrt{s}$ and huge integrated luminosity, as well as the larger acceptance of the detector, three-, four- or five-jet cross sections represent highly sensitive observables for a precise determination of $\alpha_s(M_Z)$, and high experimental precision can be achieved. In these cases, fixed order pQCD predictions may become limiting factors, since they are more complicated for large n.

Di-jet observables are expected to yield a fairly similar experimental uncertainty than inclusive jet cross sections, as studied in the previous paragraphs, since both have $n = 1$ at LO. However, their theoretical uncertainties may be smaller, since di-jet observables are less sensitive to additional higher-order radiation, in particular at lower scales where $\alpha_s(\mu_R)$ is larger.

Event shape observables in DIS exploit additional radiation in DIS events (see e.g. review [148] or HERA measurements [149, 150]). Consequently, once measured at the LHeC the experimental uncertainties of $\alpha_s(M_Z)$ from these observables are expected to become very similar to that in Eq. (2.4), since both the event sample and the process is similar to the inclusive jet cross sections [3]. However, different reconstruction techniques of the observables may yield reduced experimental uncertainties, and the calculation of event shape observables allow for the resummation of large logarithms, and steady theoretical advances promise small theoretical uncertainties [151–157].

Jet production cross sections in photoproduction represents a unique opportunity for another precision determination of $\alpha_s(M_Z)$. Such measurements have been performed at HERA [158–161]. The sizeable photoproduction cross section provides a huge event sample, which is statistically independent from NC DIS events, and already the leading-order predictions are sensitive to $\alpha_s(M_Z)$ [162]. Also its running can be largely measured since the scale of the process is well estimated by the transverse momentum of the jets $\mu_R \sim P_T^{\rm jet}$. Limiting theoretical aspects are due to the presence of a quasi-real photon and the poorly known photon PDF [163, 164].

A different class of observables represent heavy flavour (HF) cross sections, which are discussed in Sec. 1.3.5. Due to flavour conservation, these are commonly proportional to $\mathcal{O}(\alpha_s^1)$ at leading-order. However, when considering inclusive HF cross sections above the heavy quark mass threshold heavy quarks can be factorised into the PDFs, and the leading structure functions $F_2^{c,b}$ are sensitive to α_s only beyond the LO approximation (see reviews [45, 46], recent HERA measurements [30, 165] and references therein). The presence of the heavy quark mass as an additional scale stabilises perturbative calculations, and reduced theoretical uncertainties are expected.

At the LHeC the structure of jets and the formation of hadrons can be studied with unprece-

[3] It shall be noted, that event shape observables in NC DIS can be defined in the laboratory rest frame or the Breit frame.

dented precision. This is so because of the presence of a single hadron in the initial state. Therefore, limiting effects like the underlying event or pile-up are absent or greatly diminished. Precise measurements of jet shape observables, or the study of jet substructure observables [166], are highly sensitive to the value of $\alpha_s(M_Z)$, because parton shower and hadronisation take place at lower scales where the strong coupling becomes large and an increased sensitivity to $\alpha_s(M_Z)$ is attained [167, 168].

Finally, also the determination of $\alpha_s(M_Z)$ from inclusive NC DIS cross sections can be improved. For NC DIS the dominant sensitivity to α_s arises from the F_L structure function and from scaling violations of F_2 at lower values of Q^2 but at very high values of x. Dedicated measurements of these kinematic regions will further improve the experimental uncertainties from the estimated values in Eq. (2.3).

2.2 Discovery of New Strong Interaction Dynamics at Small x

The LHeC machine will offer access to a completely novel kinematic regime of DIS characterised by very small values of x. From the kinematical plane in (x, Q^2) depicted in Fig. **??**, it is clear that the LHeC will be able to probe Bjorken-x values as low as 10^{-6} for perturbative values of Q^2. At low values of x various phenomena may occur which go beyond the standard collinear perturbative description based on DGLAP evolution. Since the seminal works of Balitsky, Fadin, Kuraev and Lipatov [82,169,170] it has been known that, at large values of centre-of-mass energy $\sqrt{s}$ or, to be more precise, in the Regge limit, there are large logarithms of energy which need to be resummed. Thus, even at low values of the strong coupling α_s, logarithms of energy $\ln s$ may be sufficiently large, such that terms like $(\alpha_s \ln s)^n$ will start to dominate the cross section.

In addition, other novel effects may appear in the low x regime, which are related to the high gluon densities. At large gluon densities a recombination of the gluons may become important in addition to the gluon splitting. This is known as the parton saturation phenomenon in QCD, and is deeply related to the restoration of the unitarity in QCD. As a result, the linear evolution equations will need to be modified by the additional nonlinear terms in the gluon density. In the next two subsections we shall explore the potential and sensitivity of the LHeC to these small x phenomena.

2.2.1 Resummation at small x

The calculation of scattering amplitudes in the high-energy limit and the resummation of $(\alpha_s \ln s)^n$ series in the leading logarithmic order was performed in [82,169,170] and it resulted in the famous BFKL evolution equation. This small x evolution equation, written for the so-called gluon Green's function or the unintegrated gluon density, is a differential equation in $\ln 1/x$. An important property of this equation is that it keeps the transverse momenta unordered along the gluon cascade. This has to be contrasted with DGLAP evolution which is differential in the hard scale Q^2 and relies on the strong ordering in the transverse momenta of the exchanged partons in the parton cascade. The solution to the BFKL equation is a gluon density which grows sharply with decreasing x, as a power i.e. $\sim x^{-\omega_{IP}}$, where ω_{IP} is the hard Pomeron intercept, and in the leading logarithmic approximation equals $\frac{N_c \alpha_s}{\pi} 4 \ln 2$, which gives a value of about 0.5 for typical values of the strong coupling. The leading logarithmic (LLx) result yielded a growth of the gluon density which was too steep for the experimental data at HERA. The next-to-leading logarithmic (NLLx) calculation performed in the late 90s [171, 172] resulted in large negative corrections to the LLx value of the hard Pomeron intercept and yielded some instabilities in the cross section [173–177].

The appearance of the large negative corrections at NLLx motivated the search for the appropriate resummation which would stabilize the result. It was understood very early that the large corrections which appear in BFKL at NLLx are mostly due to the kinematics [178–180] as well as DGLAP terms and the running of the strong coupling. First attempts at combining the BFKL and DGLAP dynamics together with the proper kinematics [181] yielded encouraging results, and allowed a description of HERA data on structure functions with good accuracy. The complete resummation program was developed in a series of works [182–195]. In these works the resummation for the gluon Green's function and the splitting functions was developed.

The low-x resummation was recently applied to the description of structure function data at HERA using the methodology of NNPDF [196]. It was demonstrated that the resummed fits provide a better description of the structure function data than the pure DGLAP based fits at fixed NNL order. In particular, it was shown that the χ^2 of the fits does not vary appreciably when more small x data are included in the case of the fits which include the effects of the small-x resummation. On the other hand, the fits based on NNLO DGLAP evolution exhibit a worsening of their quality in the region of low x and low to moderate values of Q^2. This indicates that there is some tension in the fixed order fits based on DGLAP, and that resummation alleviates it. In addition, it was shown that the description of the longitudinal structure function F_L from HERA data is improved in the fits with the small x resummation. This analysis suggests that the small x resummation effects are indeed visible in the HERA kinematic region. Such effects will be strongly magnified at the LHeC, which probes values of x more than one order of magnitude lower than HERA. The NNPDF group also performed simulation of the structure functions F_2 and F_L with and without resummation in the LHeC range as well as for the next generation electron-hadron collider FCC-eh [196]. The predictions for the structure functions as a function of x for fixed values of Q^2 are shown in Figs. 2.7.

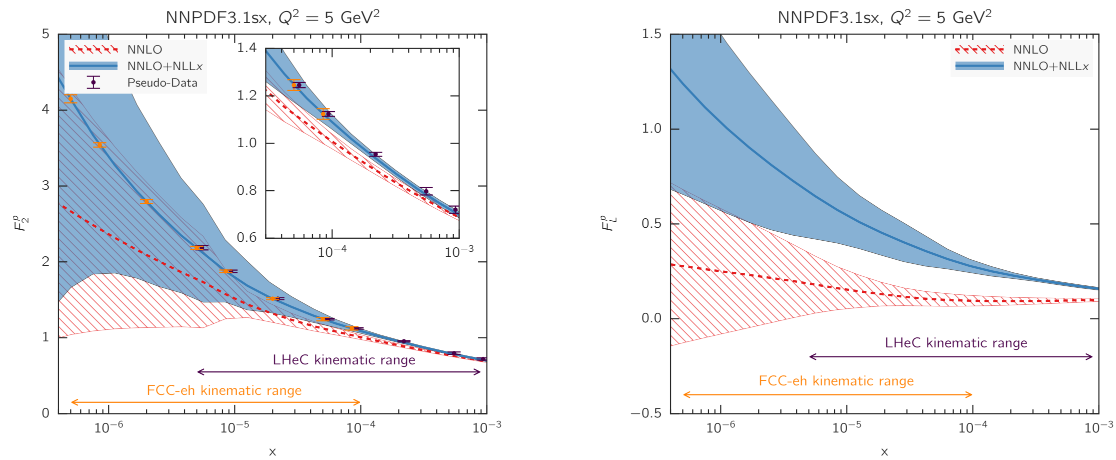

Figure 2.7: Predictions for the F_2 and F_L structure functions using the NNPDF3.1sx NNLO and NNLO+NLLx fits at $Q^2 = 5\,\mathrm{GeV}^2$ for the kinematics of the LHeC and FCC-eh. In the case of F_2, we also show the expected total experimental uncertainties based on the simulated pseudodata, assuming the NNLO+NLLx values as the central prediction. A small offset has been applied to the LHeC pseudodata as some of the values of x overlap with the FCC-eh pseudodata points. The inset in the left plot shows a magnified view in the kinematic region $x > 3 \times 10^{-5}$, corresponding to the reach of HERA data. Figure taken from Ref. [196].

The simulations were done using APFEL [197] together with the HELL package [198] which implements the small x resummation. From Fig. 2.7 it is clear that LHeC will have much higher sensitivity to discriminate between fixed order and resummed scenarios than the HERA collider, with even better discrimination at the FCC-eh. The differences between the central values for the two predictions are of the order of 15% for the case of F_2 and this is much larger than the projected error bar on the reduced cross section or structure function F_2 which could be measured at LHeC. For comparison, the simulated pseudodata for F_2 are shown together with the expected experimental uncertainties. The total uncertainties of the simulated pseudodata are at the few percent level at most, and are therefore much smaller than the uncertainties coming from the PDFs in most of the kinematic range.

It is evident that fits to the LHeC data will have power to discriminate between the different frameworks. In the right plot in Fig. 2.7, the predictions for the longitudinal structure function are shown. We see that in the case of the F_L structure function, the differences between the fixed order and resummed predictions are even larger, consistently over the entire range of x. This indicates the importance of the measurement of the longitudinal structure function F_L which can provide further vital constraints on the QCD dynamics in the low x region due to its sensitivity to the gluon density in the proton.

To further illustrate the power of a high energy DIS collider like the LHeC in exploring the dynamics at low x, fits which include the simulated data were performed. The NNLO+NLLx resummed calculation was used to obtain the simulated pseudodata, both for the LHeC, in a scenario of a 60 GeV electron beam on a 7 TeV proton beam as well as in the case of the FCC-eh scenario with a 50 TeV proton beam. All the experimental uncertainties for the pseudodata have been added in quadrature. Next, fits were performed to the DIS HERA as well as LHeC and FCC-eh pseudodata using the theory with and without the resummation at low x. Hadronic data like jet, Drell-Yan or top, were not included for this analysis but, as demonstrated in [196], these data do not have much of the constraining power at low x, and therefore the results of the analysis at low x are independent of the additional non-DIS data sets. The quality of the fits characterised by the χ^2 was markedly worse when the NNLO DGLAP framework was used to fit the HERA data and the pseudodata from LHeC and/or FCC-eh than was the case with resummation. To be precise, the χ^2 per degree of freedom for the HERA data set was equal to 1.22 for the NNLO fit, and 1.07 for the resummed fit. For the case of the LHeC/FCC-eh the χ^2 per degree of freedom was equal to 1.71/2.72 and 1.22/1.34 for NNLO and NNLO+resummation fits, respectively. These results demonstrate the huge discriminatory power of the new DIS machines between the DGLAP and resummed frameworks, and the large sensitivity to the low x region while simultaneously probing low to moderate Q^2 values.

In Fig. 2.8 the comparison of the gluon and quark distributions from the NNLO + NLLx fits is shown at $Q = 100$ GeV as a function of x, with and without including the simulated pseudodata from LHeC as well as FCC-eh. The large differences at large x are due to the fact that only DIS data were included in the fits, and not the hadronic data. The central values of the extracted PDFs using only HERA or using HERA and the simulated pseudodata coincide with each other, but a large reduction in uncertainty is visible when the new data are included. The uncertainties from the fits based on the HERA data only increase sharply already at $x \sim 10^{-4}$. On the other hand, including the pseudodata from LHeC and/or FCC-eh can extend this regime by order(s) of magnitude down in x. Furthermore, fits without resummation, based only on NNLO DGLAP, were performed to the HERA data and the pseudodata. We see that in this case the extracted gluon and singlet quark densities differ significantly from the fits using the NNLO+NLLx. Already at $x = 10^{-4}$ the central values of the gluon differ by 10% and at $x = 10^{-5}$, which is the LHeC regime, the central values for the gluon differ by 15%. This

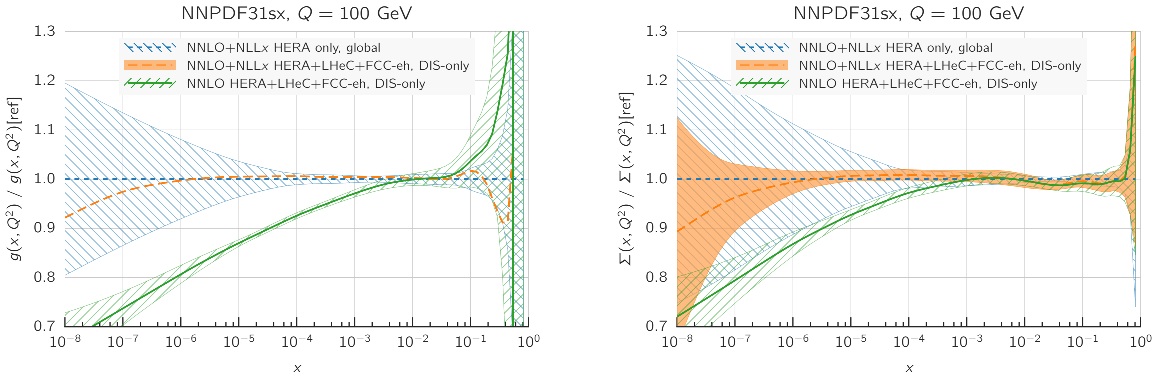

Figure 2.8: Comparison between the gluon (left plot) and the quark singlet (right plot) PDFs in the NNPDF3.1sx NNLO+NNLx fits without (blue hatched band) and with the LHeC+FCC-eh pseudodata (orange band) on inclusive structure functions. For completeness, we also show the results of the corresponding NNPDF3.1sx NNLO fit with LHeC+FCC-eh pseudodata (green hatched band). Figure taken from Ref. [196].

difference is much larger than the precision with which the gluon can be extracted from the DIS data, which is of the order of $\sim 1\%$.

The presented analysis demonstrates that the fixed order prediction based on the DGLAP evolution would likely fail to describe accurately the structure function data in the new DIS machines and that in that regime new dynamics including resummation are mandatory for quantitative predictions. Therefore, the LHeC machine has an unprecedented potential to pin down the details of the QCD dynamics at low values of Bjorken x.

2.2.2 Disentangling non-linear QCD dynamics at the LHeC

As mentioned previously the kinematic extension of the LHeC will allow unprecedented tests of the strong interaction in the extremely low x region, and allow for the tests of the novel QCD dynamics at low x. The second effect that may be expected is the parton saturation phenomenon, which may manifest itself as the deviation from the linear DGLAP evolution.

In particular, it has been argued that the strong growth of the gluon PDF at small-x should eventually lead to gluon recombination [199] to avoid violating the unitary bounds. The onset of such non-linear dynamics, also known as saturation, has been extensively searched but so far there is no conclusive evidence of its presence, at least within the HERA inclusive structure function measurements. In this context, the extended kinematic range of the LHeC provides unique avenues to explore the possible onset of non-linear QCD dynamics at small-x. The discovery of saturation, a radically new regime of QCD, would then represent an important milestone in our understanding of the strong interactions.

The main challenge in disentangling saturation lies in the fact that non-linear corrections are expected to be moderate even at the LHeC, since they are small (if present at all) in the region covered by HERA. Therefore, great care needs to be employed in order to separate such effects from those of standard DGLAP linear evolution. Indeed, it is well known that HERA data at small-x in the perturbative region can be equally well described, at least at the qualitative level, both by PDF fits based on the DGLAP framework as well as by saturation-inspired models. However, rapid progress both in theory calculations and methodological developments have pushed QCD fits to a new level of sophistication, and recently it has been shown that subtle but clear evidence of BFKL resummation at small-x is present in HERA data, both for inclusive and for heavy quark structure functions [200, 201]. Such studies highlight how it should be possible to tell apart non-linear from linear dynamics using state-of-the-art fitting methods even if these are moderate, provided that they are within the LHeC reach.

Here we want to assess the sensitivity of the LHeC to detect the possible onset of non-linear saturation dynamics. This study will be carried out by generalising a recent analysis [25] that quantified the impact of LHeC inclusive and semi-inclusive measurements on the PDF4LHC15 PDFs [202,203] by means of Hessian profiling [204]. There, the LHeC pseudodata was generated assuming that linear DGLAP evolution was valid in the entire LHeC kinematic range using the PDF4LHC15 set as input. To ascertain the possibility of pinning down saturation at the LHeC, here we have revisited this study but now generating the LHeC pseudodata by means of a saturation-inspired calculation. By monitoring the statistical significance of the tension that will be introduced (by construction) between the saturation pseudodata and the DGLAP theory assumed in the PDF fit, we aim to determine the likelihood of disentangling non-linear from linear evolution effects at the LHeC. See also [205] for previous related studies along the same direction.

Analysis settings

In this study we adopt the settings of [25, 206], to which we refer the interested reader for further details. In Ref. [25] the impact on the proton PDFs of inclusive and semi-inclusive neutral-current (NC) and charged current (CC) DIS structure functions from the LHeC was quantified. These results were then compared with the corresponding projections for the PDF sensitivity of the High-Luminosity upgrade of the LHC (HL-LHC). In the left panel of Fig. 2.9 we display the kinematic range in the (x, Q^2) plane of the LHeC pseudodata employed in that analysis, which illustrated how the LHeC can provide unique constraints on the behaviour of the quark and gluon PDFs in the very small-x region.

Since non-linear dynamics are known to become sizeable only at small-x, for the present analysis it is sufficient to consider the NC e^-p inclusive scattering cross sections from proton beam energies of $E_p = 7\,\mathrm{TeV}$ and $E_p = 1\,\mathrm{TeV}$. In the right panel in Fig. 2.9 we show the bins in (x, Q^2) for which LHeC pseudodata for inclusive structure functions has been generated according to a saturation-based calculation. Specifically, we have adopted here the DGLAP-improved saturation model of Ref. [207], in which the scattering matrix is modelled through eikonal iteration of two gluon exchanges. This model was further extended to include heavy flavour in [208]. The specific parameters that we use were taken from Fit 2 in [209], where parameterisations are provided that can be used for $x < 0.01$ and $Q^2 < 700\,\mathrm{GeV}^2$. These parameters were extracted from a fit to the HERA legacy inclusive structure function measurements [13] restricted to $x < 0.01$ and $0.045 < Q^2 < 650\,\mathrm{GeV}^2$. In contrast to other saturation models, the one we assume here [209] provides a reasonable description for large Q^2 in the small x region, where it ensure a smooth transition to standard fixed-order perturbative results.

Note that the above discussion refers only to the generated LHeC pseudodata: all other aspects of the QCD analysis of [25] are left unchanged. In particular, the PDF profiling will be carried out using theory calculations obtained by means of DGLAP evolution with the NNLO PDF4LHC15 set (see also [210]), with heavy quark structure functions evaluated by means of the FONLL-B general-mass variable flavour number scheme [54]. In order to ensure consistency with the PDF4LHC15 prior, here we will replace the DGLAP pseudodata by the saturation calculation

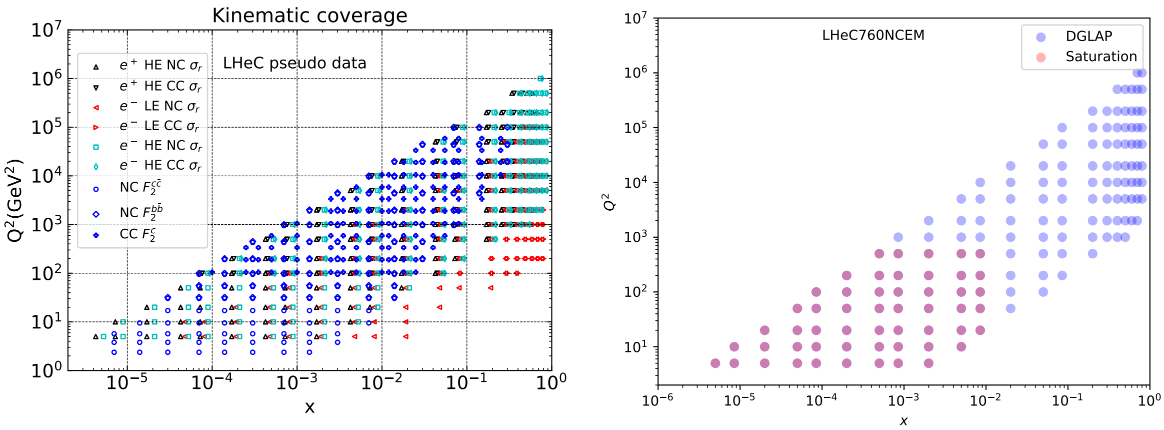

Figure 2.9: Left: the kinematic range in the (x, Q^2) plane of the LHeC pseudodata on inclusive and semi-inclusive DIS structure functions used in the PDF projections of [25]. Right: the kinematic coverage of the NC e^-p scattering pseudodata at the LHeC, where the blue (red) points indicate those bins for which DGLAP (saturation) predictions are available.

only in the kinematic region for $x \lesssim 10^{-4}$, rather than for all the bins indicated in red in Fig. 2.9. The reason for this choice is that PDF4LHC15 already includes HERA data down to $x \simeq 10^{-4}$ which is successfully described via the DGLAP framework, and therefore if we assume departures from DGLAP in the LHeC pseudodata this should only be done for smaller values of x.

Results and discussion

Using the analysis settings described above, we have carried out the profiling of PDF4LHC15 with the LHeC inclusive structure function pseudodata, which for $x \leq 10^{-4}$ ($x > 10^{-4}$) has been generated using the GBW saturation (DGLAP) calculations, and compare them with the results of the profiling where the pseudodata follows the DGLAP prediction. We have generated $N_{\rm exp} = 500$ independent sets LHeC pseudodata, each one characterised by different random fluctuations (determined by the experimental uncertainties) around the underlying central value.

To begin with, it is instructive to compare the data versus theory agreement, $\chi^2/n_{\rm dat}$, between the pre-fit and post-fit calculations, in order to assess the differences between the DGLAP and saturation cases. In the upper plots of Fig. 2.10 we show the distributions of pre-fit and post-fit values of $\chi^2/n_{\rm dat}$ for the $N_{\rm exp} = 500$ sets of generated LHeC pseudodata. We compare the results of the profiling of the LHeC pseudodata based on DGLAP calculations in the entire range of x with those where the pseudodata is based on the saturation model in the region $x < 10^{-4}$. Then in the bottom plot we compare of the post-fit χ^2 distributions between the two scenarios. Note that in these three plots the ranges in the x axes are different.

From this comparison we can observe that for the case where the pseudodata is generated using a consistent DGLAP framework (PDF4LHC15) as the one adopted for the theory calculations used in the fit, as expected the agreement is already good at the pre-fit level, and it is further improved at the post-fit level. However the situation is rather different in the case where a subset of the LHeC pseudodata is generated using a saturation model: at the pre-fit level the agreement between theory and pseudodata is poor, with $\chi^2/n_{\rm dat} \simeq 7$. The situation markedly improves at the post-fit level, where now the $\chi^2/n_{\rm dat}$ distributions peaks around 1.3. This result

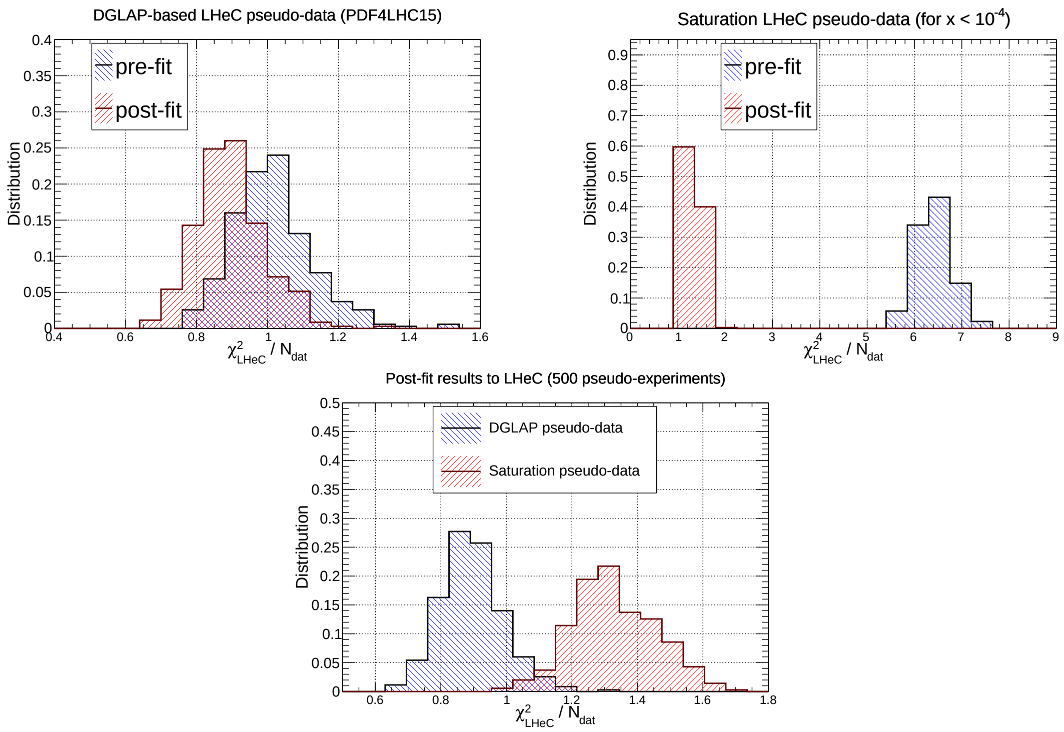

Figure 2.10: Upper plots: the distribution of pre-fit and post-fit values of $\chi^2/n_{\rm dat}$ for the $N_{\rm exp} = 500$ sets of generated LHeC pseudodata. We compare the results of the profiling of the LHeC pseudodata based on DGLAP calculations in the entire range of x (left) with those where the pseudodata is based on the saturation model in the region $x < 10^{-4}$ (right plot). Bottom plot: comparison of the post-fit $\chi^2/n_{\rm dat}$ distributions between these two scenarios for the pseudodata generation.

implies that the DGLAP fit manages to absorb most of the differences in theory present in the saturation pseudodata. This said, the DGLAP fit cannot entirely *fit away* the non-linear corrections: as shown in the lower plot of Fig. 2.10, even at the post-fit level one can still tell apart the $\chi^2/n_{\rm dat}$ distributions between the two cases, with the DGLAP (saturation) pseudodata peaking at around 0.9 (1.3). This comparison highlights that it is not possible for the DGLAP fit to completely absorb the saturation effects into a PDF redefinition.

In order to identify the origin of the worse agreement between theory predictions and LHeC pseudodata in the saturation case, it is illustrative to take a closer look at the pulls defined as

$$P(x, Q^2) = \frac{\mathcal{F}_{\rm fit}(x, Q^2) - \mathcal{F}_{\rm dat}(x, Q^2)}{\delta_{\rm exp}\mathcal{F}(x, Q^2)} \,, \tag{2.5}$$

where $\mathcal{F}_{\rm fit}$ is the central value of the profiled results for the observable $\mathcal{F}$ (in this case the reduced neutral current DIS cross section), $\mathcal{F}_{\rm dat}$ is the corresponding central value of the pseudodata, and $\delta_{\rm exp}\mathcal{F}$ represents the associated total experimental uncertainty. In Fig. 2.11 we display the pulls between the post-fit prediction and the central value of the LHeC pseudodata for different bins in Q^2. We compare the cases where the pseudodata has been generated using a consistent theory calculation (DGLAP) with that based on the GBW saturation model.

The comparisons in Fig. 2.11 show first of all that in the DGLAP case the pulls are $\mathcal{O}(1)$ in the entire kinematical range. This is of course expected, given that the LHeC pseudodata is generated using the same theory as the one subsequently used for the fit. In the case where the pseudodata has been partially generated with the saturation calculation, on the other hand, one finds a systematic tension between the theory used for the fit (DGLAP) and the one used

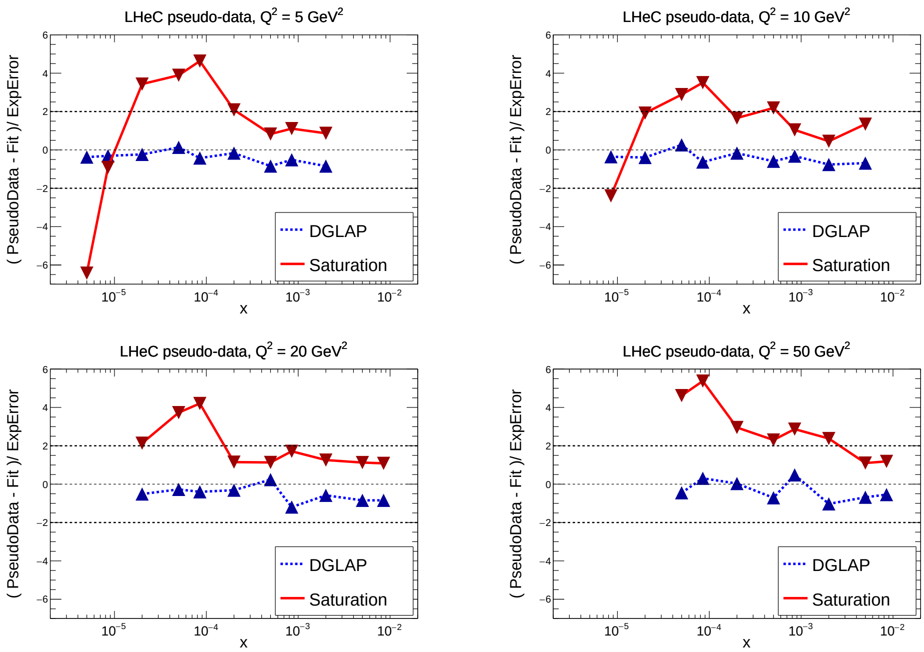

Figure 2.11: The pulls between the post-fit prediction and the central value of the LHeC pseudodata, Eq. (2.5), for four different bins in Q^2. We compare the results of the profiling where the LHeC pseudodata has been generated using a consistent DGLAP theory with that partially based on the saturation calculations.

to generate the pseudodata (saturation). Indeed, we find that at the smallest values of x the theory prediction undershoots the data by a significant amount, while at higher x the opposite behaviour takes place. One can also see that in the region $10^{-4} \lesssim x \lesssim 10^{-3}$ the fit overshoots the pseudodata by a large amount.

These comparisons highlight how a QCD fit to the saturation pseudodata is obtained as a compromise between opposite trends: the theory wants to overshoot the data at very small x and overshoot it at larger values of x. These tensions result in a distorted fit, explaining the larger $\chi^2/n_{\rm dat}$ values as compared to the DGLAP case. Such a behaviour can be partially traced back by the different scaling in Q^2 between DGLAP and GBW: while a different x dependence could eventually be absorbed into a change of the PDFs at the parameterisation scale Q_0, this is not possible with a Q^2 dependence.

The pull analysis of Fig. 2.11 highlights how in order to tell apart linear from non-linear QCD evolution effects at small-x it would be crucial to ensure a lever arm in Q^2 as large as possible in the perturbative region. This way it becomes possible to disentangle the different scaling in Q^2 for the two cases. The lack of a sufficiently large lever arm in Q^2 at HERA at small x could explain in part why both frameworks are able to describe the same structure function measurements at the qualitative level. Furthermore, we find that amplifying the significance of these subtle effects can be achieved by monitoring the χ^2 behaviour in the Q^2 bins more affected by the saturation corrections. The reason is that the total χ^2, such as that reported in Fig. 2.10, is somewhat less informative since the deviations at small-Q are washed out by the good agreement between theory and pseudodata in the rest of the kinematical range of the LHeC summarised in Fig. 2.9.

To conclude this analysis, in Fig. 2.12 we display the comparison between the PDF4LHC15 baseline with the results of the PDF profiling of the LHeC pseudodata for the gluon (left) and quark singlet (right) for $Q = 10\,\text{GeV}$. We show the cases where the pseudodata is generated using DGLAP calculations and where it is partially based on the GBW saturation model (for $x \lesssim 10^{-4}$). We find that the distortion induced by the mismatch between theory and pseudodata in the saturation case is typically larger than the PDF uncertainties expected once the LHeC constraints are taken into account. While of course in a realistic situation such a comparison would not be possible, the results of Fig. 2.12 show that saturation-induced effects are expected to be larger than the typical PDF errors in the LHeC era, and thus that it should be possible to tell them apart using for example tools such as the pull analysis of Fig. 2.11 or other statistical methods.

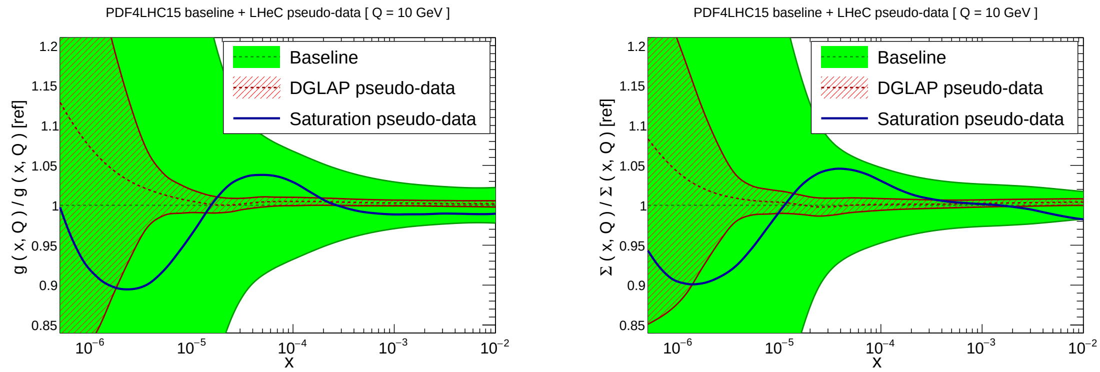

Figure 2.12: Comparison between the PDF4LHC15 baseline (green band) with the results of the profiling of the LHeC pseudodata for the gluon (left) and quark singlet (right) for $Q = 10\,\text{GeV}$. We show the cases where the pseudodata is generated using DGLAP calculations (red hatched band) and where it is partially based on the GBW saturation model (blue curve).

Summary

Here we have assessed the feasibility of disentangling DGLAP evolution from non-linear effects at the LHeC. By means of a QCD analysis where LHeC pseudodata is generated using a saturation model, we have demonstrated that the LHeC should be possible to identify non-linear effects with large statistical significance, provided their size is the one predicted by current calculations such as the that of [209] that have been tuned to HERA data. A more refined analysis would require to study whether or not small-x BFKL resummation effects can partially mask the impact of non-linear dynamics, though this is unlikely since the main difference arises in their Q^2 scaling. The discovery of non-linear dynamics would represent an important milestone for the physics program of the LHeC, demonstrating the onset of a new gluon-dominated regime of the strong interactions and paving the way for detailed studies of the properties of this new state of matter. Such discovery would have also implications outside nuclear and particle physics, for instance it would affect the theory predictions for the scattering of ultra-high energy neutrinos with matter [211].

2.2.3 Low x and the Longitudinal Structure Function F_L

DIS Cross Section and the Challenge to Access F_L

The inclusive, deep inelastic electron-proton scattering cross section at low $Q^2 \ll M_Z^2$,

$$\frac{Q^4 x}{2\pi\alpha^2 Y_+} \cdot \frac{d^2\sigma}{dxdQ^2} = \sigma_r \simeq F_2(x,Q^2) - f(y) \cdot F_L(x,Q^2) = F_2 \cdot \left(1 - f(y)\frac{R}{1+R}\right) \tag{2.6}$$

is defined by two proton structure functions, F_2 and F_L, with $y = Q^2/sx$, $Y_+ = 1 + (1-y)^2$ and $f(y) = y^2/Y_+$. The cross section may also be expressed [212] as a sum of two contributions, $\sigma_r \propto (\sigma_T + \epsilon\sigma_L)$, referring to the transverse and longitudinal polarisation state of the exchanged boson, with ϵ characterising the ratio of the longitudinal to the transverse polarisation. The ratio of the longitudinal to transverse cross sections is termed

$$R(x,Q^2) = \frac{\sigma_L}{\sigma_T} = \frac{F_L}{F_2 - F_L}, \tag{2.7}$$

which is related to F_2 and F_L as given above. Due to the positivity of the cross sections $\sigma_{L,T}$ one observes that $F_L \leq F_2$. The reduced cross section σ_r, Eq. (2.6), is therefore a direct measure of F_2, apart from a limited region of high y where a contribution of F_L may be sizeable. To leading order, for spin 1/2 particles, one expected $R = 0$. The initial measurements of R at SLAC [213, 214] showed that R was indeed small, $R \simeq 0.18$, which was taken as evidence for quarks to carry spin 1/2.

The task to measure F_L thus requires to precisely measure the inclusive DIS cross section near to $y = 1$ and to then disentangle the two structure functions by exploiting the $f(y) = y^2/Y_+$ variation which depends on x, Q^2 and s. By varying the centre-of-mass (cms) beam energy, s, one can disentangle F_2 and F_L obtaining independent measurements at each common, fixed point of x, Q^2. This is particularly challenging not only because the F_L part is small, calling for utmost precision, but also because it requires to measure at high y. The inelasticity $y = 1 - E'/E_e$, however, is large only for scattered electron energies E_e' much smaller than the electron beam energy E_e, for example $E_e' = 2.7\,\text{GeV}$ for $y = 0.9$ at HERA [4]. In the region where E' is a few GeV only, the electron identification becomes a major problem and the electromagnetic ($\pi^0 \to \gamma\gamma$) and hadronic backgrounds, mainly from unrecognised photoproduction, rise strongly.

The history and achievements on F_L, the role of HERA and the prospects as sketched in the CDR of the LHeC, were summarised in detail in [20]. The measurement of F_L at HERA [215] was given very limited time and it collected about 5.9 and $12.2\,\text{pb}^{-1}$ of data at reduced beam energies which were analysed together with about $100\,\text{pb}^{-1}$ at nominal HERA energies. The result may well be illustrated with the data obtained on the ratio $R(x,Q^2)$ shown in Fig. 2.13. To good approximation, $R(x,Q^2)$ is a constant which was determined as $R = 0.23 \pm 0.04$, in good agreement with the SLAC values of $R \simeq 0.18$ despite the hugely extended kinematic range. The rather small variation of R towards small x, at fixed $y = Q^2/sx$, may appear to be astonishing as one observed F_2 to strongly rise towards low x. A constant R of e.g. 0.25 means that $F_2 = (1+R)F_L/R$ is five times larger than F_L, and that they rise together, as they have a common origin, the rise of the gluon density. This can be understood in approximations to the DGLAP expression of the Q^2 derivative of F_2 and the so-called Altarelli-Martinelli relation

[4] The nominal electron beam energy E_e at the LHeC is doubled as compared to HERA. Ideally one would like to vary the proton beam energy in an F_L measurement at the LHeC, which yet would affect the hadron collider operation. In the present study it was therefore considered to lower E_e which may be done independently of the HL-LHC.

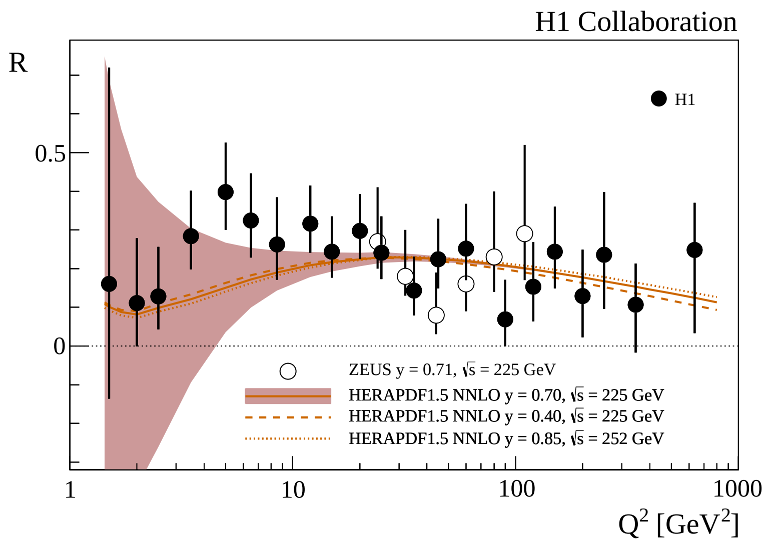

Figure 2.13: Measurement of the structure function ratio $R = F_L/(F_2 - F_L)$ by H1 (solid points) and ZEUS (open circles), from a variation of proton beam energy in the final half year of HERA operation. The curve represents an NNLO QCD fit analysis of the other HERA data. This becomes uncertain for Q^2 below $10\,\mathrm{GeV}^2$ where the Q^2 dependence of F_2 at HERA does not permit an accurate determination of the gluon density which dominates the prediction on F_L.

of F_L to the parton densities [216, 217], see the discussion in Ref. [20]. The resulting H1 value also obeyed the condition $R \leq 0.37$, which had been obtained in a rigorous attempt to derive the dipole model for inelastic DIS [218].

Parton Evolution at Low x

Parton distributions are to be extracted from experiment as their x dependence and flavour sharing are not predicted in QCD. They acquire a particular meaning through the theoretical prescription of their kinematic evolution. PDFs, as they are frequently used for LHC analyses, are predominantly defined through the now classic DGLAP formalism, in which the Q^2 dependence of parton distributions is regulated by splitting functions while the DIS cross section, determined by the structure functions, is calculable by folding the PDFs with coefficient functions. Deep inelastic scattering is known to be the most suited process to extract PDFs from the experiment, for which the HERA collider has so far delivered the most useful data. Through factorisation theorems the PDFs are considered to be universal such that PDFs extracted in ep DIS shall be suited to describe for example Drell-Yan scattering cross sections in pp at the LHC. This view has been formulated to third order pQCD already and been quite successful in the interpretation of LHC measurements, which by themselves also constrain PDFs in parton-parton scattering sub-processes.

As commented in Sec. 2.2.1, the question has long been posed about the universal validity of the DGLAP formalism, especially for the region of small Bjorken x where logarithms $\propto \ln(1/x)$ become very sizeable. This feature of the perturbation expansion is expected to significantly modify the splitting functions. This in turn changes the theory underlying the physics of parton distributions, and predictions for the LHC and its successor will correspondingly have to be altered. This mechanism, for an equivalent Q^2 of a few GeV^2, is illustrated in Fig. 2.14, taken from Ref. [201]. It shows the x dependence of the gluon-gluon and the quark-gluon splitting functions, P_{gg} and P_{qg}, calculated in DGLAP QCD. It is observed that at NNLO P_{gg} strongly decreases towards small x, becoming smaller than P_{qg} for x below 10^{-4}. Resummation of the large $\ln(1/x)$ terms, see Ref. [201], here performed to next-to-leading log x, restores the dominance of the gg splitting over the qg one. Consequently, the gluon distribution in the resummed theory exceeds the one derived in pure DGLAP. While this observation has been

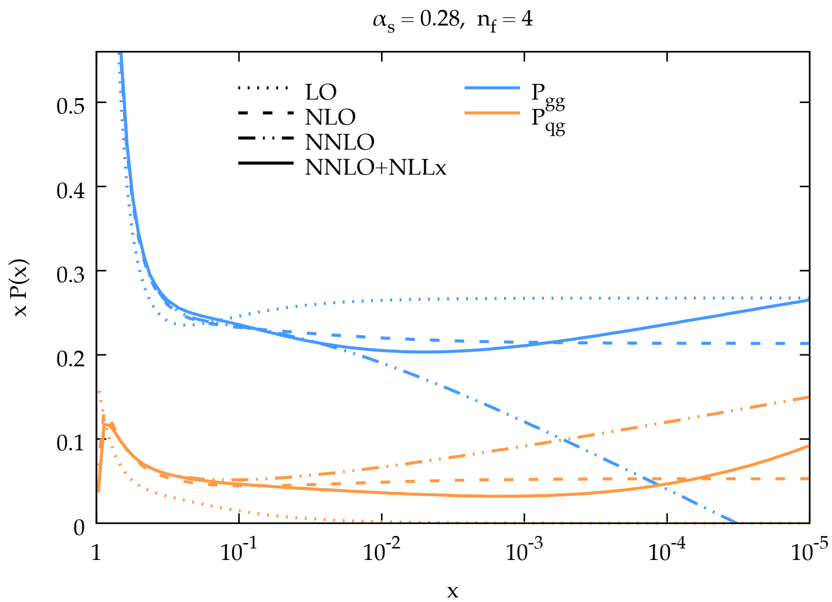

Figure 2.14: Calculation of splitting functions P_{gg} (top, blue) and P_{qg} (bottom, brown) in resummed NNLO (solid) as compared to non-resummed calculations at LO (dotted), NLO (dashed) and NNLO (dashed-dotted) as functions of x for $n_f = 4$ at a large value of α_s corresponding to a Q^2 of a few GeV^2, from Ref. [201]. The resummed calculation is seen to restore the dominance of P_{gg} over P_{qg} as x becomes small (towards the right side), which is violated at NNLO.

supported by the HERA data, it yet relies on limited kinematic coverage and precision. The LHeC will examine this in detail, at a hugely extended range and is thus expected to resolve the long known question about the validity of the BFKL evolution and the transition from DGLAP to BFKL as x decreases while Q^2 remains large enough for pQCD to apply.

Kinematics of Higgs Production at the HL-LHC

The clarification of the evolution and the accurate and complete determination of the parton distributions is of direct importance for the LHC. This can be illustrated with the kinematics of Higgs production at HL-LHC which is dominated by gluon-gluon fusion. With the luminosity upgrade, the detector acceptance is being extended into the forward region to pseudorapidity values of $|\eta| = 4$, where $\eta = \ln \tan \theta/2$ is a very good approximation of the rapidity. In Drell-Yan scattering of two partons with Bjorken x values of $x_{1,2}$ these are related to the rapidity via the relation $x_{1,2} = \exp(\pm\eta) \cdot M/\sqrt{s}$ where $\sqrt{s} = 2E_p$ is the cms energy and M the mass of the produced particle. It is interesting to see that $\eta = \pm 4$ corresponds to $x_1 = 0.5$ and $x = 0.00016$ for the SM Higgs boson of mass $M = 125\,\text{GeV}$. Consequently, Higgs physics at the HL-LHC will depend on understanding PDFs at high x, a challenge resolved by the LHeC too, and on clarifying the evolution at small x. At the FCC-hh, in its 100 TeV energy version, the small x value for $\eta = 4$ will be as low as $2 \cdot 10^{-5}$. Both the laws of QCD and the resulting phenomenology of particle production at the HL-LHC and its successor demand to clarify the evolution of the parton contents at small x as a function of the resolution scale Q^2. This concerns in particular the unambiguous, accurate determination of the gluon distribution, which dominates the small-x parton densities and as well the production of the Higgs boson in pp scattering.

Indications for Resummation in H1 F_L Data

The simultaneous measurement of the two structure functions F_2 and F_L is the cleanest way to establish new parton dynamics at low x. This holds because their independent constraints on the dominating gluon density at low x ought to lead to consistent results. In other words, one may constrain all partons with a complete PDF analysis of the inclusive cross section in the kinematic region where its F_L part is negligible and confront the F_L measurement with this result. A significant deviation from F_L data signals the necessity to introduce new, non-DGLAP physics in the theory of parton evolution, especially at small x. The salient value of the F_L structure function results from its inclusive character enabling a clean theoretical treatment as has early on been recognised [216, 217]. This procedure has recently been illustrated [201] using the H1 data on F_L [219] which are the only accurate data from HERA at smallest x. The

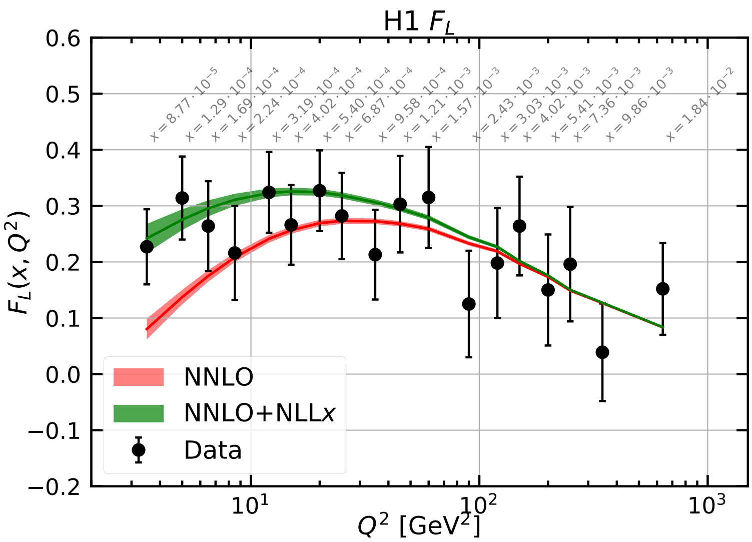

Figure 2.15: Measurement of the longitudinal structure function F_L, obtained as an average results over a number of x dependent points at fixed Q^2, plotted vs Q^2 with the corresponding x values indicated in grey. Red curve: NNLO fit to the H1 cross section data; green curve: NNLO fit including NLLx resummation, from Ref. [201].

result is shown in Fig. 2.15. One observes the trend described above: the resummed prediction is higher than the pure NNLO curve, and the description at smallest x, below $5 \cdot 10^{-4}$, appears to be improved. The difference between the two curves increases as x decreases. However, due to the peculiarity of the DIS kinematics, which relates x to Q^2/sy, one faces the difficulty of Q^2 decreasing with x at fixed s for large $y \geq 0.6$, which is the region of sensitivity to F_L. Thus one not only wishes to improve substantially the precision of the F_L data but also to increase substantially s in order to avoid the region of non-perturbative behaviour while testing theory at small x. This is the double and principal advantage which the LHeC offers - a much increased precision and more than a decade of extension of kinematic range.

The Longitudinal Structure Function at the LHeC

Following the method described above, inclusive cross section data have been simulated for $E_p = 7$ TeV and three electron beam energies E_e of $60, \sim 30$ and 20 GeV. The assumed integrated luminosity values are $10, \sim 1$ and $1\,\text{fb}^{-1}$, respectively. These are about a factor of a hundred larger than the corresponding H1 luminosities. At large y, the kinematics is best reconstructed using the scattered electron energy, E_e', and polar angle, θ_e. The experimental methods to calibrate the angular and energy measurements are described in [215]. For the present study similar results are assumed: for E_e' a scale uncertainty of 0.5 % at small y (compared to 0.2 % with H1) rising linearly to 1.2 %, in the range of $y = 0.4$ to 0.9. For the polar angle, given the superior quality of the anticipated LHeC Silicon tracker as compared to the H1 tracker, it is assumed that θ_e may be calibrated to 0.2 mrad, as compared to 0.5 mrad at H1. The residual photo-production background contamination is assumed to be 0.5 % at largest y, twice better than with H1. There is further an assumption made on the radiative corrections which are assumed to be uncertain to 1 % and treated as a correlated error. The main challenge is to reduce the uncorrelated uncertainty, which here was varied between 0.2 and 0.5 %. This is about ten to three times more accurate than the H1 result which may be a reasonable assumption: the hundred fold increase in statistics sets a totally different scale to the treatment of uncorrelated uncertainties, as from imperfect simulations, trigger efficiency or Monte Carlo statistics. It is very difficult to transport previous results to the modern and future conditions. It could, however, be an important fix point if one knows that the most precise measurement of Z boson production by ATLAS at the LHC had a total systematic error of just 0.5 % [220].

The method here used is that of a simple straight-line fit of $\sigma_r = F_2 - f(y)F_L$ (Eq. (2.6)), in which F_L is obtained as the slope of the $f(y)$ dependence [5]. The predictions for F_2 and F_L were obtained using LO formulae for the PDF set of MSTW 2008. In this method any common factor does not alter the absolute uncertainty of F_L. This also implies that the estimated absolute error on F_L is independent of whether F_L is larger or smaller than here assumed. For illustration, F_L was scaled by a factor of two. Since $f(y) \propto y^2$, the accuracy is optimised with a non-linear choice of lowered beam energies. The fit takes into account cross section uncertainties and their correlations, calculated numerically following [24], by considering each source separately and adding the results of the various correlated sources to one correlated systematic error which is added quadratically to the statistical and uncorrelated uncertainties to obtain one total error.

The result is illustrated in Fig. 2.16 presenting the x-dependent results, for some selected Q^2 values, of both H1, with their average over x, and the prospect LHeC results. It reflects the huge extension of kinematic range, towards low x and high Q^2 by the LHeC as compared to HERA. It also illustrates the striking improvement in precision which the LHeC promises to provide. The F_L measurement will cover an x range from $2 \cdot 10^{-6}$ to above $x = 0.01$. Surely, when comparing with Fig. 2.15, one can safely expect that any non-DGLAP parton evolution would be discovered with such data, in their combination with a very precise F_2 measurement.

A few comments are in order on the variation of the different error components with the kinematics, essentially Q^2 since the whole F_L sensitivity is restricted to high y which in turn for each Q^2 defines a not wide interval of x values covered. One observes in Fig. 2.16 that the precision is spoiled towards large $x \propto 1/y$, see e.g. the result for $Q^2 = 8.5\,\text{GeV}^2$. The assumptions on the integrated luminosity basically define a Q^2 range for the measurement. For example, the statistical uncertainty for $Q^2 = 4.5\,\text{GeV}^2$ and $x = 10^{-5}$, a medium x value at this Q^2 interval, is only 0.6 % (or 0.001 in absolute for $F_L = 0.22$). At $Q^2 = 2000\,\text{GeV}^2$ it rises to 21 % (or 0.012

[5]Better results were achieved by H1 using a χ^2 minimisation technique, see Ref. [221], which for the rough estimate on the projected F_L uncertainty at the LHeC has not been considered.

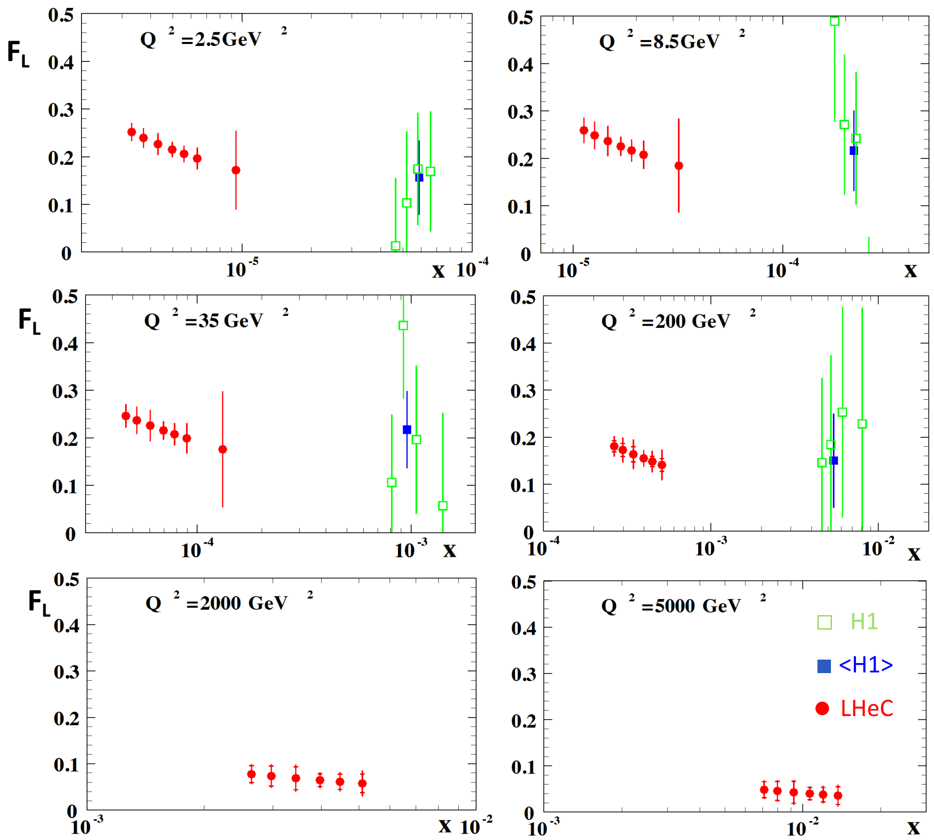

Figure 2.16: H1 measurement and LHeC simulation of data on the longitudinal structure function $F_L(x, Q^2)$. Green: Data by H1, for selected Q^2 intervals from Ref. [219]; Blue: Weighted average of the (green) data points at fixed Q^2; Red: Simulated data from an F_L measurement at the LHeC with varying beam energy, see text. The H1 error bars denote the total measurement uncertainty. The LHeC inner error bars represent the data statistics, visible only for $Q^2 \geq 200\,\text{GeV}^2$, while the outer error bars are the total uncertainty. Since the F_L measurement is sensitive only at high values of inelasticity, $y = Q^2/sx$, each Q^2 value is sensitive only to a certain limited interval of x values which increase with Q^2. Thus each panel has a different x axis. The covered x range similarly varies with s, i.e. H1 x values are roughly twenty times larger at a given Q^2. There are no H1 data for high Q^2, beyond $1000\,\text{GeV}^2$, see Ref. [219].

for $F_L = 0.064$). One thus can perform the F_L measurement at the LHeC, with a focus on only small x, with much less luminosity than the $1\,\text{fb}^{-1}$ here used. The relative size of the various systematic error sources also varies considerably, which is due to the kinematic relations between angles and energies and their dependence on x and Q^2. This is detailed in [24]. It implies, for example, that the 0.2 mrad polar angle scale uncertainty becomes the dominant error at small Q^2, which is the backward region where the electron is scattered near the beam axis in the direction of the electron beam. For large Q^2, however, the electron is more centrally scattered and the θ_e calibration requirement may be more relaxed. The E'_e scale uncertainty has a twice smaller effect than that due to the θ_e calibration at lowest Q^2 but becomes the dominant correlated systematic error source at high Q^2. The here used overall assumptions on scale uncertainties are therefore only rough first approximations and would be replaced by kinematics and detector dependent requirements when this measurement may be pursued. These could also exploit the cross calibration opportunities which result from the redundant determination of the inclusive DIS scattering kinematics through both the electron and the hadronic final state. This had been noted very early at HERA times, see Ref. [21,23,222] and was worked out in considerable detail by both H1 and ZEUS using independent and different methods. A feature used by H1 in their F_L measurement includes a number of decays such as $\pi^0 \to \gamma\gamma$ and $J/\psi \to e^+e^-$ for calibrating the low energy measurement or $K_s^0 \to \pi^+\pi^-$ and $\Lambda \to p\pi$ for the determination of tracker scales, see Ref. [215].

It is obvious that the prospect to measure F_L as presented here is striking. For nearly a decade, Guido Altarelli was a chief theory advisor to the development of the LHeC. In 2011, he publishes an article [221], in honour of Mario Greco, about *The Early Days of QCD (as seen from Rome)* in which he describes one of his main achievements [216], and persistent irritation, regarding the longitudinal structure function, F_L, and its measurement: ... *The present data, recently obtained by the H1 experiment at DESY, are in agreement with our [!this] LO QCD prediction but the accuracy of the test is still far from being satisfactory for such a basic quantity.* The LHeC developments had not been rapid enough to let Guido see results of much higher quality on F_L with which the existence of departures from the DGLAP evolution, to high orders pQCD, may be expected to most safely be discovered.

2.2.4 Relation to Ultrahigh Energy Neutrino and Astroparticle physics

The small-x region probed by the LHeC is also very important in the context of ultra-high energy neutrino physics and astroparticle physics. Highly energetic neutrinos provide a unique window into the Universe, due to their weak interaction with matter, for a review see for example [223]. They can travel long distances from distant sources, undeflected by the magnetic fields inside and in between galaxies, and thus provide complementary information to cosmic rays, gamma rays and gravitational wave signals. The IceCube observatory on Antarctica [224] is sensitive to neutrinos with energies from 100 GeV up (above 10 GeV with the use of their Deep Core detector). Knowledge about low-x physics becomes indispensable in two contexts: neutrino interactions and neutrino production. At energies beyond the TeV scale the dominant part of the cross section is due to the neutrino DIS CC and NC interaction with the hadronic targets [223].

In Fig. 2.17 we show the charged current neutrino cross section as a function of the neutrino energy for an isoscalar target (in the laboratory frame where the target is at rest), using a calculation [225] based on the resummed model in [181]. We see that at energies below ~ 50 TeV the cross section grows roughly linearly with energy, and in this region it is dominated by contributions from the large-x valence region. Beyond that energy the neutrino cross section grows slower, roughly as a power $\sim E_\nu^\lambda$ with $\lambda \simeq 0.3$. This high energy behaviour is totally controlled by the small-x behaviour of the parton distributions. The dominance of the sea contributions to the cross section is clearly seen in Fig. 2.17. To illustrate more precisely the contributing values of x and Q^2, in Fig. 2.18 we show the differential cross section for the CC interaction $xQ^2 d\sigma^{CC}/dxdQ^2$ for a neutrino energy $E_\nu = 10^{11}$ GeV (in the frame where the hadronic target is at rest). We see a clear peak of the cross section at roughly a value of $Q^2 = M_W^2$ and an x value

$$x \simeq \frac{M_W^2}{2ME_\nu} \,, \tag{2.8}$$

which in this case is about 3×10^{-8}. We note that IceCube extracted the DIS cross section from neutrino observations [226] in the region of neutrino energies $10 - 1000$ TeV. The extraction is consistent, within the large error bands, with the predictions based on the QCD, like those illustrated in Fig. 2.17. It is important to note that the IceCube extraction is limited to these energies by the statistics due to the steeply falling flux of neutrinos at high energy. We thus

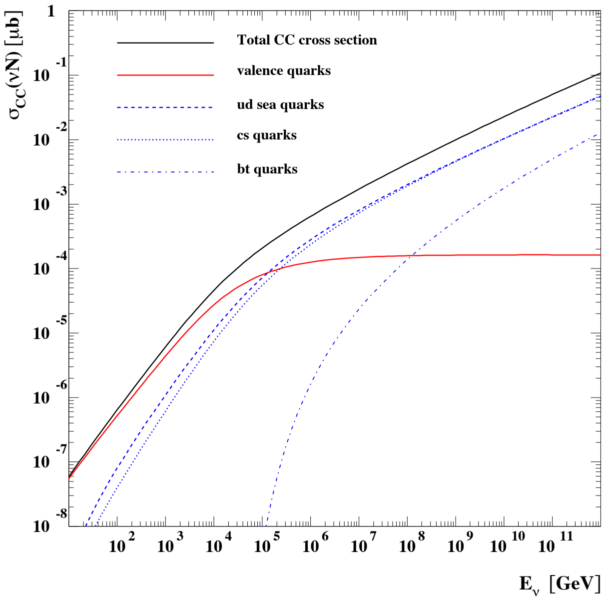

Figure 2.17: Charged current cross section for the neutrino - nucleon interaction on a isoscalar target as a function of neutrino energy. The total CC cross section is broken down into several contributions due to valence, up-down,strange-charm and bottom-top quarks. The calculation was based on Ref. [225].

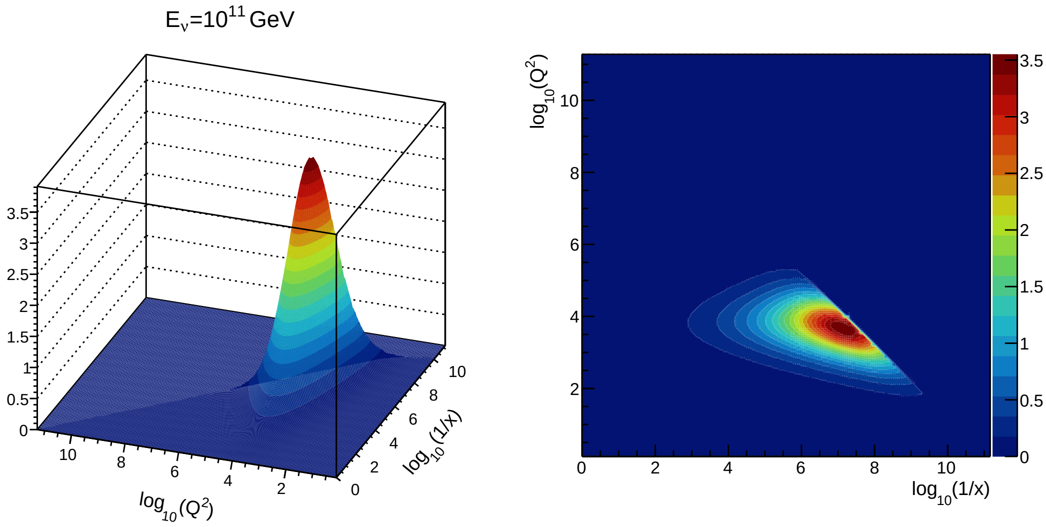

Figure 2.18: Differential charged current neutrino cross section $10^5 \cdot xQ^2 d\sigma^{CC}/dxdQ^2$ [nb] as a function of Q^2 and x for fixed neutrino energy $E_\nu = 10^{11}$ GeV. Left: surface plot; right: contour plot.

see that the neutrino interaction cross section at high energies is sensitive to a region which is currently completely unconstrained by existing precision DIS data.

Another instance where dynamics at low x are crucial for neutrino physics is in understanding the mechanisms of ultra-high energy neutrino production. The neutrinos are produced in interactions which involve hadrons, either in γp or in pp interactions. They emerge as decay products of pions, kaons and charmed mesons, and possibly beauty mesons if the energy is high enough [227]. For example, in the atmosphere neutrinos are produced in the interactions of the highly energetic cosmic rays with nitrogen and oxygen nuclei. The lower energy part of the atmospheric neutrino spectrum, up to about 100 TeV or so, is dominated by the decay of pions and kaons. This is called the conventional atmospheric neutrino flux. Above that energy the neutrino flux is dominated by the decay of the shorter-lived charmed mesons. Thus, this part of the neutrino flux is called the prompt-neutrino flux. The reason why the prompt-neutrino flux dominates at high energies is precisely related to the life-time of the intermediate mesons (and also baryons like Λ_c). The longer lived pions and kaons have a high probability of interacting before they decay, thus degrading their energy and leading to a steeply falling neutrino flux. The cross section for the production of charmed mesons is smaller than that for pions and kaons, but the charmed mesons $D^{\pm}, D^0, D_s$ and baryon Λ_c live shorter than pions and kaons, and thus decay prior to any interaction. Thus, at energies about 100 TeV the prompt neutrino flux will dominate over the conventional atmospheric neutrino flux. Therefore, the knowledge of this part of the spectrum is essential as it provides a background for the sought-after astrophysical neutrinos [228]. Charmed mesons in high energy hadron-hadron interactions are produced through gluon-gluon fusion into $c\bar{c}$ pairs, where one gluon carries rather large x and the other one carries very small x. Since the scales are small, of the order of the charm masses, the values of the longitudinal momentum fractions involved are also very small and thus the knowledge of the parton distributions in this region is essential [229]. The predictions for the prompt neutrino flux become extremely sensitive to the behaviour of the gluon distribution at low x (and low Q^2), where novel QCD phenomena like resummation as well as gluon saturation are likely to occur [230].

Finally, the low-x dynamics will become even more important at the HL-LHC and FCC hadron colliders. With increasing centre-of-mass energy, hadron colliders will probe values of x previously unconstrained by HERA data. It is evident that all the predictions in pp interactions at high energy will heavily rely on the PDF extrapolations to the small x region which carry large uncertainties. As discussed in detail in this Section, resummation will play an increasingly important role in the low x region of PDFs. A precision DIS machine is thus an indispensable tool for constraining the QCD dynamics at low x with great precision as well as for providing complementary information and independent measurements to hadronic colliders.

2.2.5 Impact of New Small-x Dynamics on Hadron Collider Physics

As discussed in Subsections 2.2.1 and 2.2.3, the presence of new dynamics at small x as claimed in Refs. [196, 200, 201] will have impact on hadronic observables. The impact is stronger for larger energies, therefore more important for the FCC-hh than for the LHC. But it may compete with other uncertainties and thus become crucial for precision studies even at LHC energies. Studies on the impact of non-linear dynamics at hadron colliders have been devoted mainly to photoproduction in UPCs, see e.g. [231–233] and Refs. therein for the case of gauge boson production. In this section we focus on the effect of resummation at small x.

While hadronic data like jet, Drell-Yan or top production at existing energies do not have much constraining power at low x [196] and thus need not be included in the extraction of PDFs using resummed theoretical predictions, this fact does not automatically mean that the impact of resummation is not visible at large scales for large energies. Indeed the PDFs obtained with small-x resummation may change at low energies in the region of x relevant for hadronic data, thereby giving an effect also at higher energies after evolving to those scales. A consistent inclusion of resummation effects on hadronic observables is thus crucial for achieving precision. The difficulty for implementing resummation on different observables lies in the fact that not only evolution equations should include it but also the computation of the relevant matrix elements for the observable must be performed with matching accuracy.

Until present, the only observable that has been examined in detail is Higgs production cross section through gluon fusion [234]. Other observables like Drell-Yan [235] or heavy quark [236] production are under study and they will become available in the near future.

For $gg \to H$, the LL resummation of the matrix elements matched to fixed order at N^{3}LO was done in Refs. [234, 237] and the results are shown in Figs. 2.19 and 2.20. Fig. 2.19 shows the increasing impact of resummation on the cross section with increasing energy. It also illustrates the fact that the main effect of resummation comes through the modification of the extraction of parton densities and their extrapolation, not through the modification of the matrix elements or the details of the matching.

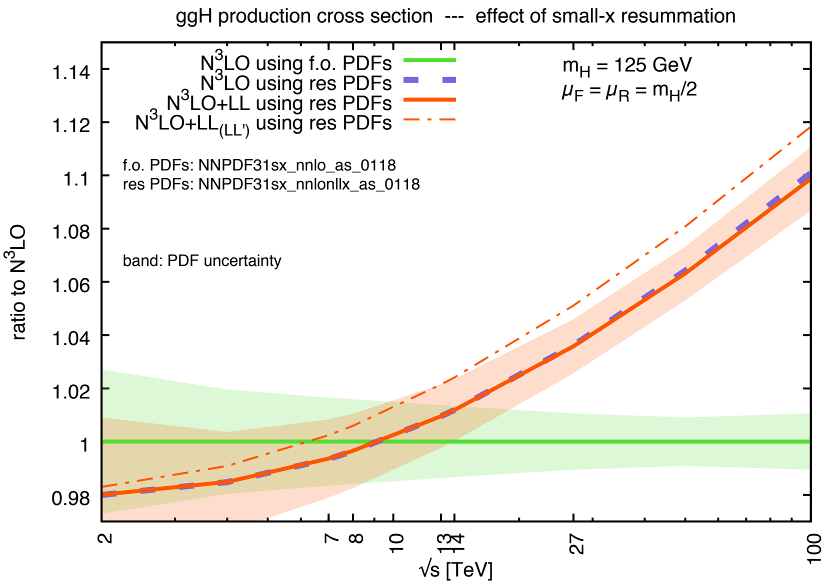

Figure 2.19: Ratio of the N^{3}LO Higgs cross section with and without resummation to the N^{3}LO fixed-order cross section, as a function of the collider centre-of-mass energy. "f.o." denotes fixed order, "res" denotes resummed and "LL′" a different anomalous dimension matching at leading logarithmic accuracy, see the legend on the plot and Ref. [234] for details. The PDFs used are from the global dataset of Ref. [200]. Figure taken from Ref. [234].

Fig. 2.20 indicates the size of the different uncertainties on the absolute values of the cross section with increasing accuracy of the perturbative expansion, at HL-LHC and FCC-hh energies. For N^{3}LO(+LL) it can be seen that while at the HL-LHC, the effect of resummation is of the same order as other uncertainties like those coming scale variations, PDFs and subleading logarithms, this is not the case for the FCC where it can be clearly seen that it will be the dominant one. Resummation should also strongly affect the rapidity distributions, a key need for extrapolation of observed to total cross sections. In particular, rapidity distributions are more directly sensitive to PDFs at given values of momentum fraction x, and therefore in regions where this momentum fraction is small (large rapidities) the effect of resummation may be sizeable also at lower collider energies. These facts underline the need of understanding the dynamics at small x for any kind of precision physics measurements at future hadronic colliders, with increasing importance for increasing energies.

Finally, it should be mentioned that a different kind of factorisation, called transverse momentum

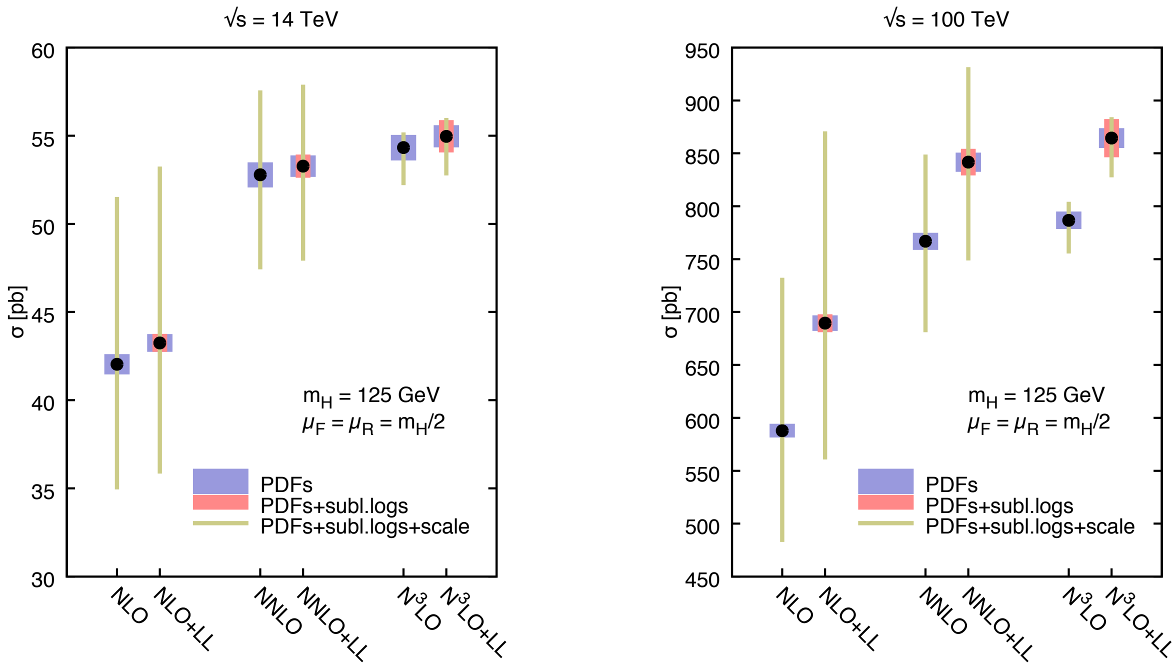

Figure 2.20: Perturbative progression of the Higgs cross section for two collider energies $\sqrt{s} = \{14, 100\}$ TeV. In each plot the NLO, NLO+LL, NNLO, NNLO+LL, N^{3}LO and N^{3}LO+LL results are shown. The results are supplemented by uncertainty bands from PDF, subleading logarithms and scale uncertainties. Figure taken from Ref. [234].

(TMD) factorisation [6, 238–242], may have an effect on large scale observables in hadronic colliders. The extension of the TMD evolution equations towards small x [243] and the relation of such factorisation with new dynamics at small x, either through high-energy factorisation [244–247] or with the CGC [248, 249], is under development [250].

2.3 Diffractive Deep Inelastic Scattering at the LHeC

2.3.1 Introduction and Formalism

An important discovery of HERA was the observation of a large ($\sim 10\,\%$) fraction of diffractive events in DIS [251, 252]. In these events the proton stays intact or dissociates into a state with the proton quantum numbers, despite undergoing a violent, highly energetic collision, and is separated from the rest of the produced particles by a large rapidity gap. In a series of ground-breaking papers (see Ref. [253] for a review), the HERA experiments determined the deep inelastic structure of the t-channel exchange in these events in the form of diffractive parton densities.

The precise measurement of diffraction in DIS is of great importance for our understanding of the strong interaction. First, the mechanism through which a composite strongly interacting object interacts perturbatively while keeping colour neutrality offers information about the confinement mechanism. Second, diffraction is known to be highly sensitive to the low-x partonic content of the proton and its evolution with energy and it therefore has considerable promise to reveal deviations from standard linear evolution through higher twist effects or, eventually, non-linear dynamics. Third, it allows checks of basic theory predictions such as the relation between diffraction in *ep* scattering and nuclear shadowing [254]. Finally, the accurate extraction of diffractive parton distribution functions facilitates tests of the range of validity of perturbative factorisation [255–257]. The potential studies of inclusive diffraction that would be possible at the LHeC are presented here (see Ref. [258] for further details). They substantially extend the kinematic coverage of the HERA analyses, leading to much more detailed tests of theoretical ideas than have been possible hitherto. Although we work here at NLO of QCD, it is worth noting that similar analyses in the HERA context have recently extended to NNLO [259].

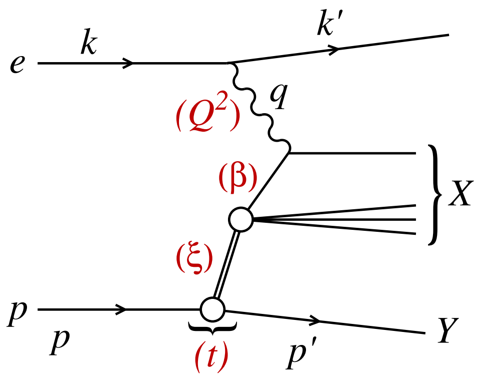

Figure 2.21: A diagram of a diffractive NC event in DIS together with the corresponding variables, in the one-photon exchange approximation. The large rapidity gap is between the system X and the scattered proton (or its low mass excitation) Y.

In Fig. 2.21 we show a diagram depicting a neutral current diffractive deep inelastic event. Charged currents could also be considered and were measured at HERA [260] but with large statistical uncertainties and in a very restricted region of phase space. Although they could be measured at both the LHeC and the FCC-eh with larger statistics and more extended kinematics, in this first study we limit ourselves to neutral currents. The incoming electron or positron, with four momentum k, scatters off the proton, with incoming four momentum p, and the interaction proceeds through the exchange of a virtual photon with four-momentum q. The kinematic variables for such an event include the standard deep inelastic variables

$$Q^2 = -q^2 \,, \qquad x = \frac{-q^2}{2p \cdot q} \,, \qquad y = \frac{p \cdot q}{p \cdot k} \,, \tag{2.9}$$

where Q^2 describes the photon virtuality, x is the Bjorken variable and y the inelasticity of the process. In addition, the variables

$$s = (k+p)^2 \,, \qquad W^2 = (q+p)^2 \,, \tag{2.10}$$

are the electron-proton centre-of-mass energy squared and the photon-proton centre-of-mass energy squared, respectively. A distinguishing feature of the diffractive event $ep \to eXY$ is the presence of the large rapidity gap between the diffractive system, characterised by the invariant mass M_X and the final proton (or its low-mass excitation) Y with four momentum p'. In addition to the standard DIS variables listed above, diffractive events are also characterised by an additional set of variables defined as

$$t = (p - p')^2 \,, \qquad \xi = \frac{Q^2 + M_X^2 - t}{Q^2 + W^2} \,, \qquad \beta = \frac{Q^2}{Q^2 + M_X^2 - t} \,. \tag{2.11}$$

In the above t is the squared four-momentum transfer at the proton vertex, ξ (alternatively denoted by x_{IP}) can be interpreted as the momentum fraction of the *diffractive exchange* with respect to the hadron, and β is the momentum fraction of the parton with respect to the diffractive exchange. The two momentum fractions combine to give Bjorken-x, $x = \beta\xi$.

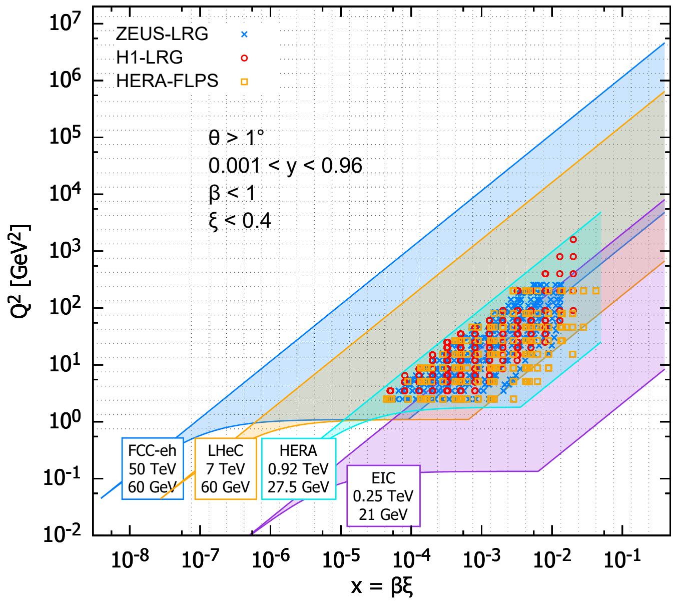

Figure 2.22: Kinematic phase space for inclusive diffraction in (x, Q^2) for the EIC (magenta region), the LHeC (orange region) and the FCC-eh (dark blue region) as compared with the HERA data (light blue region, ZEUS-LRG [261], H1-LRG [262], HERA-FLPS [263]). The acceptance limit for the electron in the detector design has been assumed to be $1°$, and we take $\xi < 0.4$.

The kinematic range in (β, Q^2, ξ) that we consider at the LHeC is restricted by the following cuts:

- $Q^2 \geq 1.8\,\text{GeV}^2$: due to the fact that the initial distribution for the DGLAP evolution is parameterised at $\mu_0^2 = 1.8\,\text{GeV}^2$. The renormalization and factorisation scales are taken to be equal to Q^2.
- $\xi < 0.4$: constrained by physical and experimental limitations. This rather high ξ value is an experimental challenge and physically enters the phase-space region where the Pomeron contribution should become negligible compared with sub-leading exchanges. Within the two-component model, see Eq. (2.16) below, at high ξ the cross section is dominated by the secondary Reggeon contribution, which is poorly fixed by the HERA data. We present this high ξ (> 0.1) region for illustrative purpose and for the sake of discussion of the fit results below.

In Fig. 2.22 the accessible kinematic range in (x, Q^2) is shown for three machines: HERA, LHeC and FCC-eh. For the LHeC design the range in x is increased by a factor ~ 20 over HERA and the maximum available Q^2 by a factor ~ 100. The FCC-eh machine would further increase this range with respect to LHeC by roughly one order of magnitude in both x and Q^2. We also show the EIC kinematic region for comparison. The three different machines are clearly complementary in their kinematic coverage, with LHeC and EIC adding sensitivity at lower and higher x than HERA, respectively.

In Fig. 2.23 the phase space in (β, Q^2) is shown for fixed ξ for the LHeC. The LHeC machine probes very small values of ξ, reaching 10^{-4} with a wide range of β. Of course, the ranges in β and ξ are correlated since $x = \beta\xi$. Therefore, for small values of ξ only large values of β are accessible while for large ξ the range in β extends to very small values.

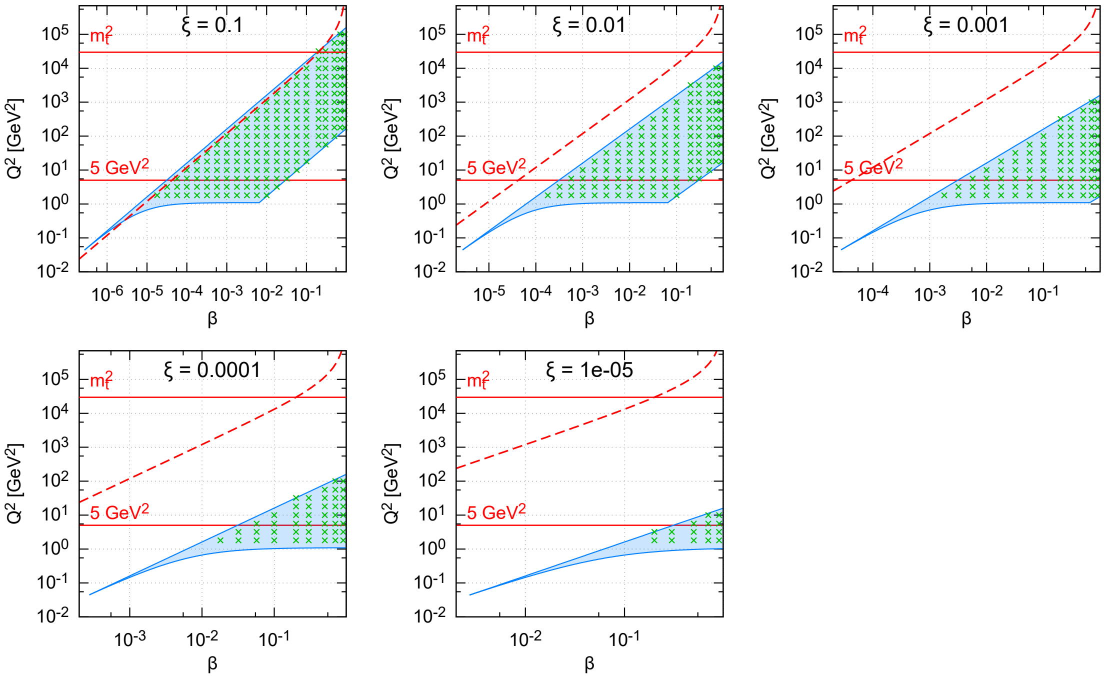

Figure 2.23: Kinematic phase space for inclusive diffraction in (β, Q^2) for fixed values of ξ for the LHeC design. The horizontal lines indicate correspondingly, $Q^2 = 5$ GeV^2, the lowest data value for the DGLAP fit performed in this study and m_t^2 the 6-flavour threshold. The dashed line marks the kinematic limit for $t\bar{t}$ production.

Diffractive cross sections in the neutral current case can be presented in the form of the reduced cross sections integrated over t [260]:

$$\frac{d^3\sigma^{\rm D}}{d\xi d\beta dQ^2} = \frac{2\pi\alpha_{\rm em}^2}{\beta Q^4}\, Y_+\, \sigma_{\rm red}^{\rm D(3)} \,, \tag{2.12}$$

where $Y_+ = 1+(1-y)^2$ and the reduced cross sections can be expressed in terms of two diffractive structure functions $F_2^{\rm D}$ and $F_{\rm L}^{\rm D}$. In the one-photon approximation, the relations are

$$\sigma_{\rm red}^{\rm D(3)} = F_2^{\rm D(3)}(\beta,\xi,Q^2) - \frac{y^2}{Y_+} F_{\rm L}^{\rm D(3)}(\beta,\xi,Q^2) \,. \tag{2.13}$$

In this analysis we neglect Z^0 exchange, though it should be included in future studies.

Both $\sigma_{\rm red}^{\rm D(3)}$ and $\sigma_{\rm red}^{\rm D(4)}$ have been measured at the HERA collider [251, 252, 260–262, 264–267] and used to obtain QCD-inspired parameterisations.

The standard perturbative QCD approach to diffractive cross sections is based on collinear factorisation [255–257]. It was demonstrated that, similarly to the inclusive DIS cross section, the diffractive cross section can be written, up to terms of order $\mathcal{O}(\Lambda^2/Q^2)$, where Λ is the hadronic scale, in a factorised form

$$d\sigma^{ep\to eXY}(\beta,\xi,Q^2,t) \;=\; \sum_i \int_\beta^1 dz\; d\hat{\sigma}^{ei}\left(\frac{\beta}{z},Q^2\right)\; f_i^{\rm D}(z,\xi,Q^2,t) \,, \tag{2.14}$$

where the sum is performed over all parton flavours (gluon, d-quark, u-quark, etc.). The hard scattering partonic cross section $d\hat{\sigma}^{ei}$ can be computed perturbatively in QCD and is the same as in the inclusive deep inelastic scattering case. The long distance part $f_i^{\rm D}$ corresponds to the diffractive parton distribution functions, which can be interpreted as conditional probabilities for partons in the proton, provided the proton is scattered into the final state system Y with specified 4-momentum p'. They are evolved using the DGLAP evolution equations [268–271] similarly to the inclusive case. The analogous formula for the t-integrated structure functions reads

$$F_{2/{\rm L}}^{{\rm D}(3)}(\beta,\xi,Q^2) = \sum_i \int_\beta^1 \frac{dz}{z}\, C_{2/{\rm L},i}\Big(\frac{\beta}{z}\Big)\, f_i^{{\rm D}(3)}(z,\xi,Q^2)\;, \tag{2.15}$$

where the coefficient functions $C_{2/{\rm L},i}$ are the same as in inclusive DIS.

Fits to the diffractive structure functions usually [260, 266] parameterise the diffractive PDFs in a two component model, which is a sum of two diffractive exchange contributions, $I\!\!P$ and $I\!\!R$:

$$f_i^{{\rm D}(4)}(z,\xi,Q^2,t) = f^p_{I\!\!P}(\xi,t)\, f_i^{I\!\!P}(z,Q^2) + f^p_{I\!\!R}(\xi,t)\, f_i^{I\!\!R}(z,Q^2)\;. \tag{2.16}$$

For both of these terms proton vertex factorisation is separately assumed, meaning that the diffractive exchange can be interpreted as colourless objects called a *Pomeron* or a *Reggeon* with parton distributions $f_i^{I\!\!P,I\!\!R}(\beta,Q^2)$. The flux factors $f^p_{I\!\!P,I\!\!R}(\xi,t)$ represent the probability that a Pomeron/Reggeon with given values ξ,t couples to the proton. They are parameterised using the form motivated by Regge theory,

$$f^p_{I\!\!P,I\!\!R}(\xi,t) = A_{I\!\!P,I\!\!R}\frac{e^{B_{I\!\!P,I\!\!R}t}}{\xi^{2\alpha_{I\!\!P,I\!\!R}(t)-1}}\;, \tag{2.17}$$

with a linear trajectory $\alpha_{I\!\!P,I\!\!R}(t) = \alpha_{I\!\!P,I\!\!R}(0) + \alpha'_{I\!\!P,I\!\!R}\,t$. The diffractive PDFs relevant to the t-integrated cross sections read

$$f_i^{{\rm D}(3)}(z,\xi,Q^2) = \phi^p_{I\!\!P}(\xi)\, f_i^{I\!\!P}(z,Q^2) + \phi^p_{I\!\!R}(\xi)\, f_i^{I\!\!R}(z,Q^2)\;, \tag{2.18}$$

with

$$\phi^p_{I\!\!P,I\!\!R}(\xi) = \int dt\; f^p_{I\!\!P,I\!\!R}(\xi,t)\;. \tag{2.19}$$

Note that, the notions of *Pomeron* and *Reggeon* used here to model hard diffraction in DIS are, in principle, different from those describing the soft hadron-hadron interactions; in particular, the parameters of the fluxes may be different.

The diffractive parton distributions of the Pomeron at the initial scale $\mu_0^2 = 1.8\,{\rm GeV}^2$ are parameterised as

$$z f_i^{I\!\!P}(z,\mu_0^2) = A_i z^{B_i}(1-z)^{C_i}\;, \tag{2.20}$$

where i is a gluon or a light quark and the momentum fraction $z=\beta$ in the case of quarks. In the diffractive parameterisations the contributions of all the light quarks (anti-quarks) are assumed to be equal. For the treatment of heavy flavours, a variable flavour number scheme (VFNS) is adopted, where the charm and bottom quark DPDFs are generated radiatively via DGLAP evolution, and no intrinsic heavy quark distributions are assumed. The structure functions are calculated in a General-Mass Variable Flavour Number scheme (GM-VFNS) [272, 273] which ensures a smooth transition of $F_{2,{\rm L}}$ across the flavour thresholds by including $\mathcal{O}(m_h^2/Q^2)$ corrections. The parton distributions for the Reggeon component are taken from a parameterisation which was obtained from fits to the pion structure function [274, 275].

In Eq. (2.16) the normalisation factors of fluxes, $A_{I\!\!P,I\!\!R}$ and of DPDFs, A_i enter in the product. To resolve the ambiguity we fix[6] $A_{I\!\!P}$ and use $f_i^{I\!\!R}(z,Q^2)$ normalised to the pion structure function, which results in A_i and $A_{I\!\!R}$ being well defined free fit parameters. For full details, see Ref. [258].

[6] Here, as in the HERA fits, $A_{I\!\!P}$ is fixed by normalizing $\phi^p_{I\!\!P}(0.003) = 1$.

2.3.2 Pseudodata for diffractive structure functions

The reduced cross sections are extrapolated using the ZEUS-SJ DPDFs. Following the scenario of the ZEUS fit [266] we work within the VFNS scheme at NLO accuracy. The transition scales for DGLAP evolution are fixed by the heavy quark masses, $\mu^2 = m_h^2$ and the structure functions are calculated in the Thorne–Roberts GM-VFNS [276]. The Reggeon PDFs are taken from the GRV pion set [275], the numerical parameters are taken from Tables 1 and 3 of Ref. [266], the heavy quark masses are $m_c = 1.35\,\mathrm{GeV}, m_b = 4.3\,\mathrm{GeV}$, and $\alpha_s(M_Z^2) = 0.118$.

The pseudodata were generated using the extrapolation of the fit to HERA data, which provides the central values, amended with a random Gaussian smearing with standard deviation corresponding to the relative error δ. An uncorrelated 5% systematic error was assumed giving a total uncertainty

$$\delta = \sqrt{\delta_{\mathrm{sys}}^2 + \delta_{\mathrm{stat}}^2}\,. \tag{2.21}$$

The statistical error was computed assuming a very modest integrated luminosity of $2\,\mathrm{fb}^{-1}$, see Ref. [277, 278]. For the binning adopted in this study, the statistical uncertainties have a very small effect on the uncertainties in the extracted DPDFs. Obviously, a much larger luminosity would allow a denser binning that would result in smaller DPDF uncertainties.

In Fig. 2.24 we show a subset of the simulated data for the diffractive reduced cross section $\xi\sigma_{\mathrm{red}}$ as a function of β in selected bins of ξ and Q^2 for the LHeC. For the most part the errors are very small, and are dominated by the systematics. The breaking of Regge factorisation evident at large ξ comes from the large Reggeon contribution in that region, whose validity could be further investigated at the LHeC.

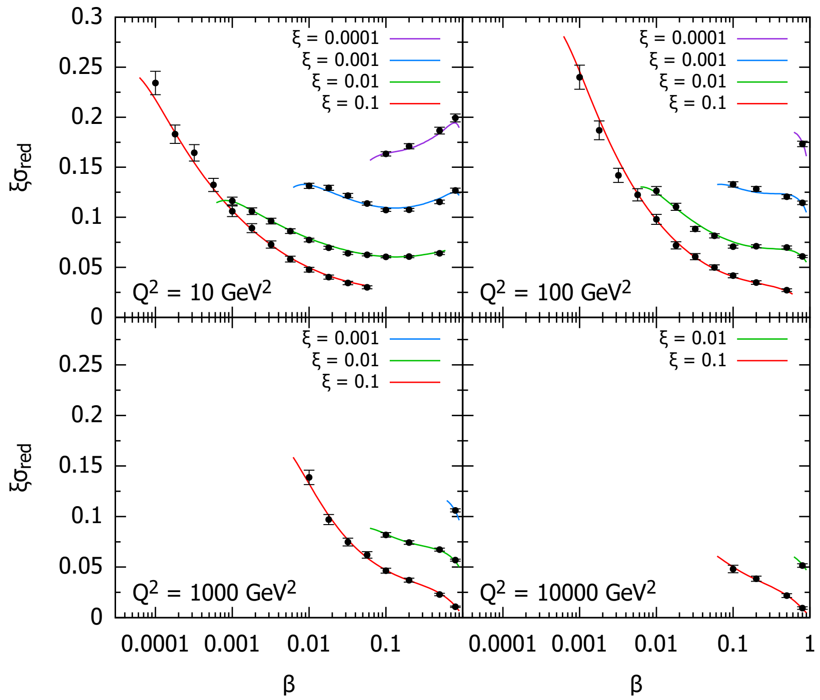

Figure 2.24: Selected subset of the simulated data for the diffractive reduced cross section as a function of β in bins of ξ and Q^2 for ep collisions at the LHeC. The curves for $\xi = 0.01, 0.001, 0.0001$ are shifted up by 0.04, 0.08, 0.12, respectively.

2.3.3 Potential for constraining diffractive PDFs at the LHeC and FCC-eh

With the aim of establishing the experimental precision with which DPDFs could be extracted when LHeC data become available, we generate the central values of the pseudodata using the central set of the ZEUS-SJ fit that are distributed according to a Gaussian with experimental width given by Eq. (2.21), that also provides the uncertainty in the pseudodata. We then include the pseudodata in a fit alongside the existing HERA data using the same functional form and, as expected, obtain a $\chi^2/\mathrm{ndf} \sim 1$, which demonstrates the consistency of the approach.

To evaluate the experimental precision with which the DPDFs can be determined, several pseudodata sets, corresponding to independent random error samples, were generated. Each pseudodata set was fitted separately. The minimal value of Q^2 for the data considered in the fits was set to $Q^2_{\mathrm{min}} = 5\,\mathrm{GeV}^2$. The reason for this cut-off is to show the feasibility of the fits including just the range in which standard twist-2 DGLAP evolution is expected to be trustable. At HERA, the Q^2_{min} values giving acceptable DGLAP (twist-2) fits were $8\,\mathrm{GeV}^2$ [260] and $5\,\mathrm{GeV}^2$ [261] for H1 and ZEUS, respectively. The maximum value of ξ was set by default to $\xi_{\mathrm{max}} = 0.1$, above which the cross section starts to be dominated by the Reggeon exchange. The binning adopted in this study corresponds roughly to 4 bins per order of magnitude in each of ξ, β, Q^2. For $Q^2_{\mathrm{min}} = 5\,\mathrm{GeV}^2$, $\xi_{\mathrm{max}} = 0.1$ and below the top threshold this results in 1229 and 1735 pseudodata points for the LHeC and FCC-eh, respectively. The top-quark region adds 17 points for the LHeC and 255 for FCC-eh. Lowering Q^2_{min} down to $1.8\,\mathrm{GeV}^2$ we get 1589 and 2171 pseudodata points, while increasing ξ up to 0.32 adds around 180 points for both proposed machines.

The potential for determination of the gluon DPDF was investigated by fitting the inclusive diffractive DIS pseudodata with two models with different numbers of parameters, named S and C (see Ref. [258]) with $\alpha_{IP,IR}(0)$ fixed, in order to focus on the shape of the Pomeron's PDFs. At HERA, both S and C fits provide equally good descriptions of the data with $\chi^2/\mathrm{ndf} = 1.19$ and 1.18, respectively, despite different gluon DPDF shapes. The LHeC pseudodata are much more sensitive to gluons, resulting in χ^2/ndf values of 1.05 and 1.4 for the S and C fits, respectively. This motivates the use of the larger number of parameters in the fit-S model, which we employ in the following studies. It also shows clearly the potential of the LHeC and the FCC-eh to better constrain the low-x gluon and, therefore, unravel eventual departures from standard linear evolution.

In Fig. 2.25 the diffractive gluon and quark distributions are shown for the LHeC and FCC-eh, respectively, as a function of momentum fraction z for fixed scales $\mu^2 = 6, 20, 60, 200\,\mathrm{GeV}^2$. The bands labelled A, B, C denote fits to three statistically independent pseudodata replicas, obtained from the same central values and statistical and systematic uncertainties. Hereafter the uncertainty bands shown correspond to $\Delta\chi^2 = 2.7$ (90 % CL). Also the extrapolated ZEUS-SJ DPDFs are shown with error bands marked by the '/' hatched area. Note that the depicted uncertainty bands come solely from experimental errors, neglecting theoretical sources, such as fixed input parameters and parameterisation biases. The extrapolation beyond the reach of LHeC/FCC-eh is marked in grey and the HERA kinematic limit is marked with the vertical dotted line. The stability of the results with respect to the independent pseudodata replicas used for the analysis is evident, so in the following only one will be employed. The low x DPDF determination accuracy improves with respect to HERA by a factor of 5–7 for the LHeC and 10–15 for the FCC-eh and completely new kinematic regimes are accessed.

For a better illustration of the precision, in Fig. 2.26 the relative uncertainties are shown for parton distributions at different scales. The different bands show the variation with the upper cut on the available ξ range, from 0.01 to 0.32. In the best constrained region of $z \simeq 0.1$,

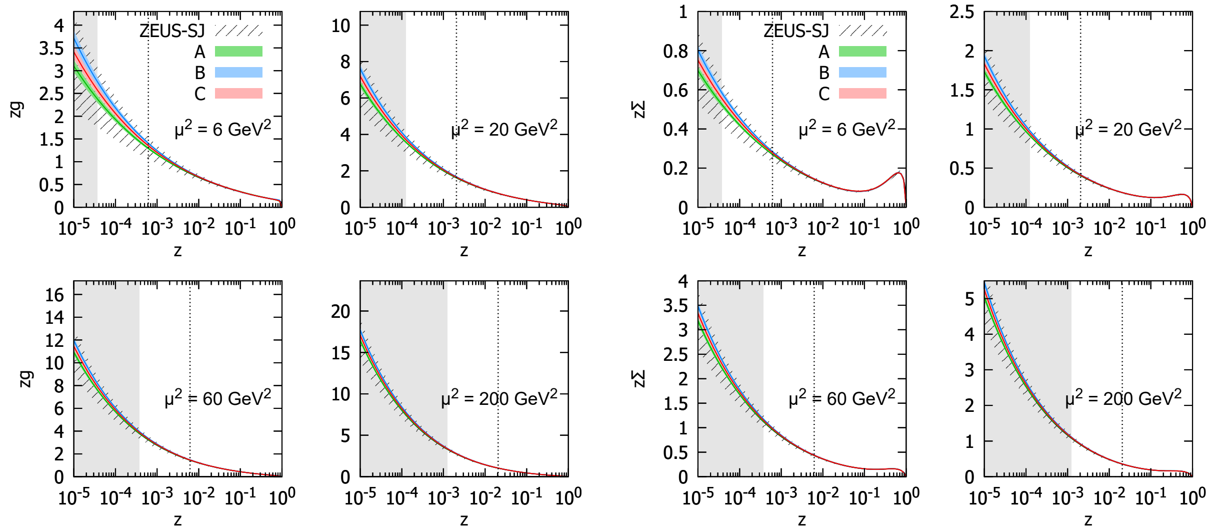

Figure 2.25: Diffractive PDFs for gluon and quark in the LHeC kinematics as a function of momentum fraction z for fixed values of scale μ^2. Results of fits to three (A,B,C) pseudodata replicas are shown together with the experimental error bands. For comparison, the extrapolated ZEUS-SJ fit is also shown (black) with error bands marked with the hatched pattern. The vertical dotted lines indicate the HERA kinematic limit. The bands indicate only the experimental uncertainties.

the precision reaches the 1% level. We observe only a modest improvement in the achievable accuracy of the extracted DPDFs with the change of ξ by an order of magnitude from 0.01 to 0.1. An almost negligible effect is observed when further extending the ξ range up to 0.32. This is encouraging, since the measurement for the very large values of ξ is challenging. It reflects the dominance of the secondary Reggeon in this region. We stress again that only experimental errors are included in our uncertainty bands. Neither theoretical uncertainties nor the parameterisation biases are considered. For a detailed discussion of this and other aspects of the fits, see Ref. [258].

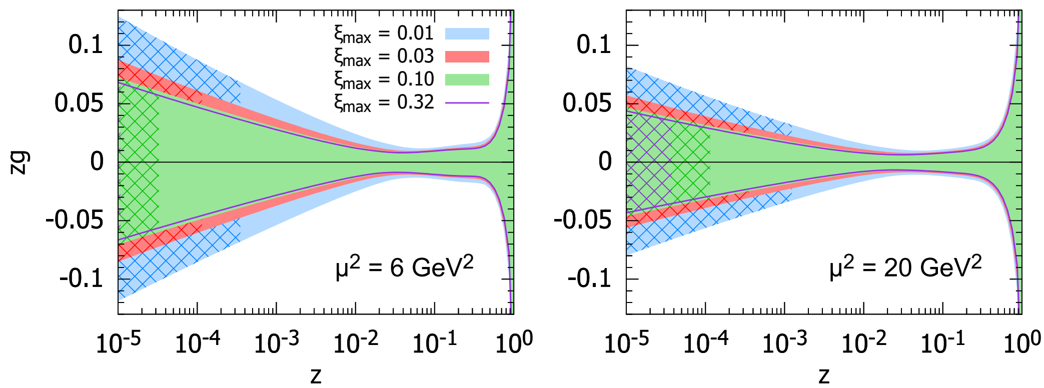

Figure 2.26: Relative uncertainties on the diffractive gluon PDFs for the LHeC kinematics. Two different choices of scales are considered $\mu^2 = 6$ and $\mu^2 = 20\,\mathrm{GeV}^2$. The blue, red, green bands and magenta line correspond to different maximal values of $\xi = 0.01, 0.03, 0.1, 0.32$, respectively. The cross-hatched areas show kinematically excluded regions. The bands indicate only the experimental uncertainties, see the text.

2.3.4 Factorisation tests using Hadronic Final States in Diffractive DIS

The factorisation properties of diffractive DIS were a major topic of study at HERA [253] and are highly relevant to the interpretation of diffractive processes at the LHC [279]. A general theoretical framework is provided by the proof [255] of a hard scattering collinear QCD factorisation theorem for semi-inclusive DIS scattering processes such as $ep \to epX$. This implies that the DPDFs extracted in fits to inclusive diffractive DIS may be used to predict perturbative cross sections for hadronic final state observables such as heavy flavour or jet production. Testing this factorisation pushes at the boundaries of applicability of perturbative QCD and will be a major topic of study at the LHeC.

Tests of diffractive factorisation at HERA are strongly limited by the kinematics. The mass of the dissociation system X is limited to approximately $M_X < 30\,\mathrm{GeV}$, which implies for example that jet transverse momenta cannot be larger than about 15 GeV and more generally leaves very little phase space for any studies at perturbative scales. As well as restricting the kinematic range of studies, this restriction also implied large hadronisation and scale uncertainties in theoretical predictions, which in turn limit the precision with which tests can be made.

The higher centre-of-mass energy of the LHeC opens up a completely new regime for diffractive hadronic final state observables in which masses and transverse momenta are larger and theoretical uncertainties are correspondingly reduced. For example, M_X values in excess of 250 GeV are accessible, whilst remaining in the region $\xi < 0.05$ where the leading diffractive (pomeron) exchange dominates. The precision of tests is also improved by the development of techniques for NNLO calculations for diffractive jets [280].

Fig. 2.27 shows a simulation of the expected diffractive jet cross section at the LHeC, assuming DPDFs extrapolated from H1 at HERA [260], using the NLOJET++ framework [281]. An integrated luminosity of $100\,\mathrm{fb}^{-1}$ is assumed and the kinematic range considered is $Q^2 > 2\,\mathrm{GeV}^2$, $0.1 < y < 0.7$ and scattered electron angles larger than 1°. Jets are reconstructed using the k_T algorithm with $R = 1$. The statistical precision remains excellent up to jet transverse momenta of almost 50 GeV and the theoretical scale uncertainties (shaded bands) are substantially reduced compared with HERA measurements. Comparing a measurement of this sort of quality with predictions refined using DPDFs from inclusive LHeC data would clearly provide an exacting test of diffractive factorisation.

Further interesting hadronic final state observables that were studied at HERA and could be extended at the LHeC include open charm production, thrust and other event shapes, charged particle multiplicities and energy flows. In addition, the LHeC opens up completely new channels, notably diffractive beauty, W and Z production, the latter giving complementary sensitivity to the quark densities to that offered by inclusive diffraction.

2.4 Theoretical Developments

2.4.1 Prospects for Higher Order pQCD in DIS

TO BE WRITTEN

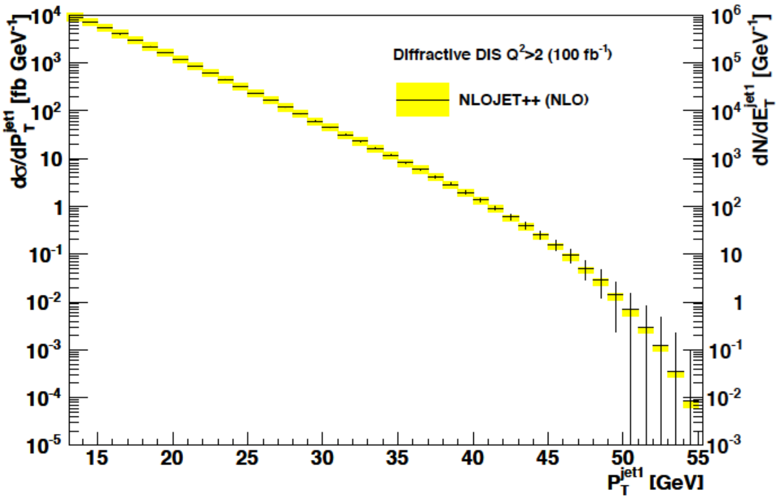

Figure 2.27: Simulated diffractive dijet cross section as a function of leading jet transverse momentum in the kinematic range $Q^2 > 2\,\mathrm{GeV}^2$ and $0.1 < y < 0.7$, with scattered electron angles in excess of 1°. The error bars indicate predicted statistical uncertainties for a luminosity of $100\,\mathrm{fb}^{-1}$. The coloured bands correspond to theoretical uncertainties when varying the renormalisation and factorisation scales by factors of 2.

2.4.2 Theoretical Concepts on the Light Cone

Intrinsic Heavy Quark Phenomena

One of the most interesting nonperturbative quantum field theoretic aspects of hadron light front wavefunctions in QCD are the intrinsic heavy-quark Fock states [282–284]. Consider a heavy-quark loop insertion to the proton's self-energy. The heavy-quark loop can be attached by gluons to just one valence quark. The cut of such diagrams yields the standard DGLAP gluon splitting contribution to the proton's heavy quark structure function. In this case, the heavy quarks are produced at very small x. However, the heavy quark loop can also be attached to two or more valence quarks in the proton self-energy. In the case of QED this is corresponds to the light-by-light lepton loop insertion in an atomic wavefunction. In the case of QCD, the heavy quark loop can be attached by three gluons to two or three valence quarks in the proton self-energy. This is a non-Abelian insertion to the hadron's self-energy. The cut of such diagrams gives the *intrinsic* heavy-quark contribution to the proton's light-front wavefunction. In the case of QCD, the probability for an intrinsic heavy $Q\bar{Q}$ pair scales as $\frac{1}{M_Q^2}$; this is in contrast to heavy $\ell\bar{\ell}$ lepton pairs in QED where the probability for heavy lepton pairs in an atomic wavefunction scales as $\frac{1}{M_\ell^4}$. This difference in heavy-particle scaling in mass distinguishes Abelian from non-Abelian theories.

A basic property of hadronic light-front wavefunctions is that they have strong fall-off with the invariant mass of the Fock state. For example, the Light-Front Wave Functions (LFWFs) of the colour-confining AdS/QCD models [285] $\mathcal{M}^2 = [\sum_i k_i^\mu]^2$ of the Fock state constituents. This means that the probability is maximised when the constituents have equal true rapidity, i.e. $x_i \propto (\vec{k}_{\perp i}^2 + m_i^2)^{1/2}$. Thus the heavy quarks carry most of the momentum in an intrinsic heavy quark Fock state. For example, the charm quark in the intrinsic charm Fock state $|uudc\bar{c}\rangle$ of a proton carries about 40 % of the proton's momentum: $x_c \sim 0.4$. After a high-energy collision, the co-moving constituents can then recombine to form the final state hadrons. along the proton. Thus, in a ep collision the comoving udc quarks from the $|uudc\bar{c}\rangle$ intrinsic 5-quark Fock state can recombine to a Λ_c, where $x_{\Lambda_c} = x_c + x_u + x_d \sim 0.5$. Similarly, the comoving dcc in the $|uudc\bar{c}c\bar{c}\rangle$ intrinsic 7-quark Fock state can recombine to a $\Xi(ccd)^+$, with $x_{\Xi(ccd)} = x_c + x_c + x_d \sim 0.9$.

Therefore, in the intrinsic heavy quark model the wavefunction of a hadron in QCD can be represented as a superposition of Fock state fluctuations, e.g. $|n_V\rangle$, $|n_V g\rangle$, $|n_V Q\overline{Q}\rangle$, ... components where $n_V \equiv dds$ for Σ^-, uud for proton, $\overline{u}d$ for π^- and $u\overline{d}$ for π^+. Charm hadrons can be produced by coalescence in the wavefunctions of the moving hadron. Doubly-charmed hadrons require fluctuations such as $|n_V c\bar{c}c\bar{c}\rangle$. The probability for these Fock state fluctuations to come on mass shell is inversely proportional to the square of the quark mass, $\mathcal{O}(m_Q^{-2n})$ where n is the number of $Q\overline{Q}$ pairs in the hadron. Thus the natural domain for heavy hadrons produced from heavy quark Fock states is $\vec{k}^2_{\perp Q} \sim m_Q^2$ and high light-front momentum fraction x_Q [282, 283, 283, 284]. For example, the rapidity regime for double-charm hadron production $y_{ccd} \sim 3$ at low energies is well within the kinematic experiment domain of a fixed target experiment such as SELEX at the Tevatron [286]. Note that the intrinsic heavy-quark mechanism can account for many previous observations of forward heavy hadron production single and double J/ψ production by pions observed at high $x_F > 0.4$ in the low energy fixed target NA3 experiment, the high x_F production of $pp \to \Lambda_c, +X$ and $pp \to \Lambda_b + X$ observed at the ISR; single and double $\Upsilon(b\bar{b})$ production, as well as *quadra-bottom* tetraquark $[bb\bar{b}\bar{b}]$ production observed recently by the AnDY experiment at RHIC [287]. In addition the EMC collaboration observed that the charm quark distribution in the proton at $x = 0.42$ and $Q^2 = 75\,\mathrm{GeV}^2$ is 30 times larger that expected from DGLAP evolution. All of these experimental observations are naturally explained by the intrinsic heavy quark mechanism. The SELEX observation [286] of double charm baryons at high x_F reflects production from double intrinsic heavy quark Fock states of the baryon projectile. Similarly, the high x_F domain – which would be accessible at forward high x_F – is the natural production domain for heavy hadron production at the LHeC.

The production of heavy hadrons based on intrinsic heavy quark Fock states is thus remarkable efficient and greatly extends the kinematic domain of the LHeC, e.g. for processes such as $\gamma^* b \to Z^0 b$. This is in contrast with the standard production cross sections based on gluon splitting, where only a small fraction of the incident momentum is effective in creating heavy hadrons.

Light-Front Holography and Superconformal Algebra

The LHeC has the potential of probing the high mass spectrum of QCD, such as the spectroscopy and structure of hadrons consisting of heavy quarks. Insights into this new domain of hadron physics can now be derived by new non-perturbative colour-confining methods based on light-front (LF) holography. A remarkable feature is universal Regge trajectories with universal slopes in both the principal quantum number n and internal orbital angular momentum L. A key feature is di-quark clustering and supersymmetric relations between the masses of meson, baryons, and tetraquarks. In addition the running coupling is determined at all scales, including the soft domain relevant to rescattering corrections to LHeC processes. The combination of lightfront holography with superconformal algebra leads to the novel prediction that hadron physics has supersymmetric properties in both spectroscopy and dynamics.

A. Light-front holography and recent theoretical advances

Five-dimensional AdS_5 space provides a geometrical representation of the conformal group. Remarkably, AdS_5 is holographically dual to $3+1$ spacetime at fixed LF time τ [288]. A colour-confining LF equation for mesons of arbitrary spin J can be derived from the holographic mapping of the *soft-wall model* modification of AdS_5 space for the specific dilaton profile $e^{+\kappa^2 z^2}$, where z is the fifth dimension variable of the five-dimensional AdS_5 space. A holographic dictionary maps the fifth dimension z to the LF radial variable ζ, with $\zeta^2 = b_\perp^2(1-x)$. The same physics transformation maps the AdS_5 and $(3+1)$ LF expressions for electromagnetic and gravitational form factors to each other [289].

A key tool is the remarkable dAFF principle [290] which shows how a mass scale can appear in a Hamiltonian and its equations of motion while retaining the conformal symmetry of the action. When applying it to LF holography, a mass scale κ appears which determines universal Regge slopes, and the hadron masses. The resulting *LF Schrödinger Equation* incorporates colour confinement and other essential spectroscopic and dynamical features of hadron physics, including Regge theory, the Veneziano formula [291], a massless pion for zero quark mass and linear Regge trajectories with the universal slope in the radial quantum number n and the internal orbital angular momentum L. The combination of LF dynamics, its holographic mapping to AdS_5 space, and the dAFF procedure provides new insight into the physics underlying colour confinement, the non-perturbative QCD coupling, and the QCD mass scale. The $q\bar{q}$ mesons and their valence LFWFs are the eigensolutions of the frame-independent a relativistic bound-state LF Schrödinger equation.

The mesonic $q\bar{q}$ bound-state eigenvalues for massless quarks are $M^2(n,L,S) = 4\kappa^2(n+L+S/2)$. This equation predicts that the pion eigenstate $n = L = S = 0$ is massless for zero quark mass. When quark masses are included in the LF kinetic energy $\sum_i \frac{k_{\perp i}^2 + m^2}{x_i}$, the spectroscopy of mesons are predicted correctly, with equal slope in the principal quantum number n and the internal orbital angular momentum L. A comprehensive review is given in Ref. [288].

B. The QCD Running Coupling at all Scales from Light-Front Holography

The QCD running coupling $\alpha_s(Q^2)$ sets the strength of the interactions of quarks and gluons as a function of the momentum transfer Q (see Sec. 2.1). The dependence of the coupling Q^2 is needed to describe hadronic interactions at both long and short distances [292]. It can be defined [293] at all momentum scales from a perturbatively calculable observable, such as the coupling $\alpha_s^{g_1}(Q^2)$, which is defined using the Bjorken sum rule [294], and determined from the sum rule prediction at high Q^2 and, below, from its measurements [295–297]. At high Q^2, such *effective charges* satisfy asymptotic freedom, obey the usual pQCD renormalisation group equations, and can be related to each other without scale ambiguity by commensurate scale relations [298].

The high Q^2 dependence of $\alpha_s^{g_1}(Q^2)$ is predicted by pQCD. In the small Q^2 domain its functional behaviour can be predicted by the dilaton $e^{+\kappa^2 z^2}$ soft-wall modification of the AdS_5 metric, together with LF holography [299], as $\alpha_s^{g_1}(Q^2) = \pi e^{-Q^2/4\kappa^2}$. The parameter κ determines the mass scale of hadrons and Regge slopes in the zero quark mass limit, and it was shown that it can be connected to the mass scale Λ_s, which controls the evolution of the pQCD coupling [299–301]. Measurements of $\alpha_s^{g_1}(Q^2)$ [302,303] are remarkably consistent with this predicted Gaussian form, and a fit gives $\kappa = 0.513 \pm 0.007\,\text{GeV}$, see Fig. 2.28.

The matching of the high and low Q^2 regimes of $\alpha_s^{g_1}(Q^2)$ determines a scale Q_0, which sets the interface between perturbative and non-perturbative hadron dynamics. This connection can be done for any choice of renormalisation scheme and one obtains an effective QCD coupling at all momenta. In the $\overline{\text{MS}}$ scheme one gets $Q_0 = 0.87 \pm 0.08\,\text{GeV}$ [304]. The corresponding value of

$\Lambda_{\overline{\rm MS}}$ agrees well with the measured world average value and its value allows to compute hadron masses using the AdS/QCD superconformal predictions for hadron spectroscopy. The value of Q_0 can further be used to set the factorization scale for DGLAP evolution [269–271] or the ERBL evolution of distribution amplitudes [305,306]. The use of the scale Q_0 to resolve the factorization scale uncertainty in structure functions and fragmentation functions, in combination with the scheme-independent *principle of maximum conformality* (PMC) [139] for setting renormalization scales, can greatly improve the precision of pQCD predictions for collider phenomenology at LHeC and HL-LHC.

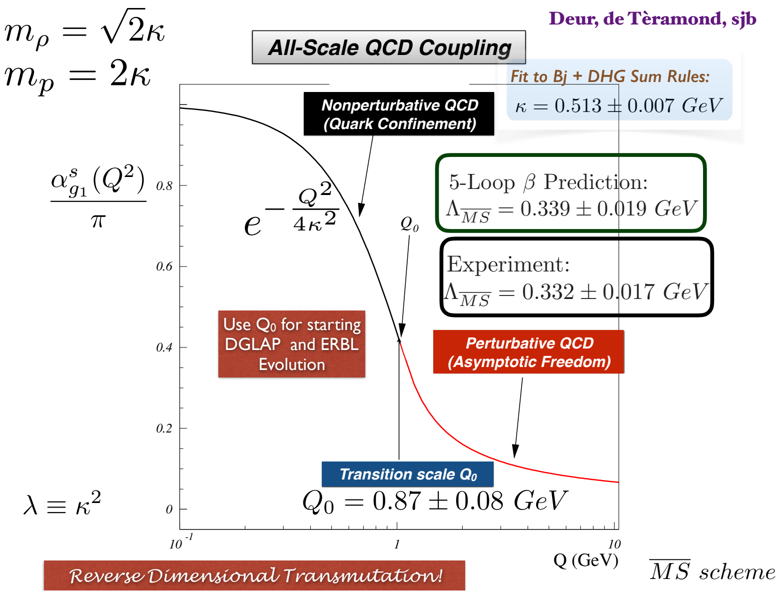

Figure 2.28: Prediction for the running coupling $\alpha_s^{g_1}(Q^2)$ at all scales. At lower Q^2 predictions are obtained from LF Holography and at higher Q^2 from perturbative QCD. The magnitude and derivative of the perturbative and non-perturbative coupling are matched at the scale Q_0. This matching connects the perturbative scale $\Lambda_{\overline{MS}}$ to the non-perturbative scale κ which underlies the hadron mass scale.

C: Superconformal Algebra and Hadron Physics with LHeC data

If one generalises LF holography using *superconformal algebra* the resulting LF eigensolutions yield a unified Regge spectroscopy of mesons, baryons and tetraquarks, including remarkable supersymmetric relations between the masses of mesons and baryons of the same parity [7] [307, 308]. This generalisation further predicts hadron dynamics, including vector meson electroproduction, hadronic LFWFs, distribution amplitudes, form factors, and valence structure functions [309, 310]. Applications to the deuteron elastic form factors and structure functions are given in Refs. [311,312]

The eigensolutions of superconformal algebra predict the Regge spectroscopy of mesons, baryons, and tetraquarks of the same parity and twist as equal-mass members of the same 4-plet representation with a universal Regge slope [313–315]. A comparison with experiment is shown in Fig. 2.29. The $q\bar{q}$ mesons with orbital angular momentum $L_M = L_B + 1$ have the same mass as their baryonic partners with orbital angular momentum L_B [313, 316].

[7] QCD is not supersymmetrical in the usual sense, since the QCD Lagrangian is based on quark and gluonic fields, not squarks or gluinos. However, its hadronic eigensolutions conform to a representation of superconformal algebra, reflecting the underlying conformal symmetry of chiral QCD and its Pauli matrix representation.

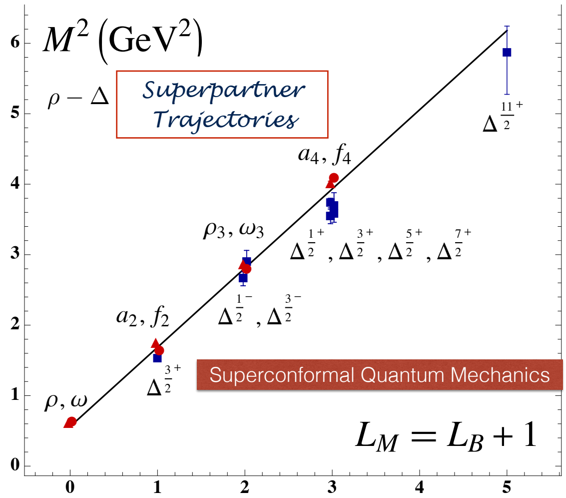

Figure 2.29: Comparison of the ρ/ω meson Regge trajectory with the $J = 3/2$ Δ baryon trajectory. Superconformal algebra predicts the mass degeneracy of the meson and baryon trajectories if one identifies a meson with internal orbital angular momentum L_M with its superpartner baryon with $L_M = L_B + 1$. See Refs. [313, 316].

2257 The predictions from LF holography and superconformal algebra can also be extended to mesons, baryons, and tetraquarks with strange, charm and bottom quarks. Although conformal symmetry is strongly broken by the heavy quark masses, the basic underlying supersymmetric mechanism, which transforms mesons to baryons (and baryons to tetraquarks), still holds and gives remarkable mass degeneracy across the entire spectrum of light, heavy-light and double-heavy hadrons.

2263 The 4-plet symmetry of quark-antiquark mesons, quark-diquark baryons, and diquark-antidiquark tetraquarks are important predictions by superconformal algebra [304, 307]. Recently the AnDY experiment at RHIC has reported the observation of a state at 18 GeV which can be identified with the $[bb][\bar{b}\bar{b}]$ tetraquark [287]. The states with heavy quarks such as the $[bb][\bar{b}\bar{b}]$ tetraquark can be produced at the LHeC, especially at high x_F along the proton beam direction. New measurements at the LHeC are therefore inevitable to manifest the superconformal nature of hadronic bound states.

Chapter 3

Electroweak and Top Quark Physics

Preface to EW and Top.

3.1 Electroweak Physics with Inclusive DIS data

With the discovery of the Standard Model (SM) Higgs boson at the CERN LHC experiments and subsequent measurements of its properties, all fundamental parameters of the SM have now been measured directly and with remarkable precision. To further establish the validity of the theory of electroweak interactions [317–321], validate the mechanism of electroweak symmetry breaking and the nature of the Higgs sector [322–324], new electroweak measurements have to be performed at highest precision. Such high-precision measurements can be considered as a portal to new physics, since non-SM contributions, as for instance loop-insertions, may cause significant deviations for some precisely measurable and calculable observables. At the LHeC, the greatly enlarged kinematic reach to higher mass scales in comparison to HERA [325–327] and the large targeted luminosity will enable electroweak measurements in ep scattering with higher precision than ever before.

3.1.1 Electroweak effects in inclusive NC and CC DIS cross sections

Electroweak NC interactions in inclusive $e^{\pm}p$ DIS are mediated by exchange of a virtual photon (γ) or a Z boson in the t-channel, while CC DIS is mediated exclusively by W-boson exchange as a purely *weak* process. Inclusive NC DIS cross sections are expressed in terms of generalised structure functions $\tilde{F}_2^{\pm}$, $x\tilde{F}_3^{\pm}$ and $\tilde{F}_{\rm L}^{\pm}$ at EW leading order (LO) as

$$\frac{d^2\sigma^{\rm NC}(e^{\pm}p)}{dxdQ^2} = \frac{2\pi\alpha^2}{xQ^4}\left[Y_+\tilde{F}_2^{\pm}(x,Q^2) \mp Y_- x\tilde{F}_3^{\pm}(x,Q^2) - y^2\tilde{F}_L^{\pm}(x,Q^2)\right] , \tag{3.1}$$

where α denotes the fine structure constant. The terms $Y_{\pm} = 1 \pm (1-y)^2$, with $y = Q^2/sx$, describe the helicity dependence of the process. The generalised structure functions are separated into contributions from pure γ- and Z-exchange and their interference [63, 99]:

$$\tilde{F}_2^{\pm} = F_2 - (g_V^e \pm P_e g_A^e)\varkappa_Z F_2^{\gamma Z} + [(g_V^e g_V^e + g_A^e g_A^e) \pm 2P_e g_V^e g_A^e]\,\varkappa_Z^2 F_2^Z , \tag{3.2}$$

$$\tilde{F}_3^{\pm} = -(g_A^e \pm P_e g_V^e)\varkappa_Z F_3^{\gamma Z} + [2g_V^e g_A^e \pm P_e(g_V^e g_V^e + g_A^e g_A^e)]\,\varkappa_Z^2 F_3^Z . \tag{3.3}$$

Similar expressions hold for $\tilde{F}_L$. In the naive quark-parton model, which corresponds to the LO QCD approximation, the structure functions are calculated as

$$\left[F_2, F_2^{\gamma Z}, F_2^Z\right] = x \sum_q \left[Q_q^2, 2Q_q g_V^q, g_V^q g_V^q + g_A^q g_A^q\right] \{q + \bar{q}\} \;, \tag{3.4}$$

$$x\left[F_3^{\gamma Z}, F_3^Z\right] = x \sum_q \left[2Q_q g_A^q, 2g_V^q g_A^q\right] \{q - \bar{q}\} \;, \tag{3.5}$$

representing two independent combinations of the quark and anti-quark momentum distributions, xq and $x\bar{q}$. In Eq. (3.3), the quantities g_V^f and g_A^f stand for the vector and axial-vector couplings of a fermion ($f = e$ or $f = q$ for electron or quark) to the Z boson, and the coefficient $\varkappa_Z$ accounts for the Z-boson propagator including the normalisation of the weak couplings. Both parameters are fully calculable from the electroweak theory. The (effective) coupling parameters depend on the electric charge, Q_f and the third component of the weak-isospin, $I^3_{\mathrm{L},f}$. Using $\sin^2\theta_{\mathrm{W}} = 1 - \frac{M_{\mathrm{W}}^2}{M_{\mathrm{Z}}^2}$, one can write

$$g_V^f = \sqrt{\rho_{\mathrm{NC},f}}\left(I^3_{\mathrm{L},f} - 2Q_f \kappa_{\mathrm{NC},f}\,\sin^2\theta_{\mathrm{W}}\right) \;, \quad \text{and} \tag{3.6}$$

$$g_A^f = \sqrt{\rho_{\mathrm{NC},f}}\, I^3_{\mathrm{L},f} \qquad \text{with } f = (e, u, d)\,. \tag{3.7}$$

The parameters $\rho_{\mathrm{NC},f}$ and $\kappa_{\mathrm{NC},f}$ are calculated as real parts of complex form factors which include the higher-order loop corrections [328–330]. They contain non-leading flavour-specific components.

Predictions for CC DIS are written in terms of the CC structure functions W_2, xW_3 and W_L and higher-order electroweak effects are collected in two form factors $\rho_{\mathrm{CC},eq}$ and $\rho_{\mathrm{CC},e\bar{q}}$ [331, 332].

In this study, the on-shell scheme is adopted for the calculation of higher-order corrections. This means that the independent parameters are chosen as the fine structure constant α and the masses of the weak bosons, the Higgs boson and the fermions. The weak mixing angle is then fixed and G_{F} is a prediction, whose higher-order corrections are included in the well-known correction factor Δr [333–335] (see discussion of further contributions in Ref. [99]).

The predicted single-differential inclusive NC and CC DIS cross sections for polarised e^-p scattering as a function of Q^2 are displayed in Fig. 3.1. For NC DIS and at higher Q^2, electroweak effects are important through γZ interference and pure Z-exchange terms and the polarisation of the LHeC electron beam of $P_e = \pm 0.8$ will considerably alter the cross sections. For CC DIS, the cross section scales linearly with P_e. Two different electron beam energies are displayed in Fig. 3.1, and albeit the impact of a reduction from $E_e = 60$ to 50 GeV appears to be small, a larger electron beam energy would yield higher precision for the measurement of electroweak parameters, since these are predominantly sensitive to the cross sections at highest scales, as will be shown in the following.

3.1.2 Methodology of a combined EW and QCD fit

A complete electroweak analysis of DIS data has to consider PDFs together with electroweak parameters [337]. In this study, the uncertainties of electroweak parameters are obtained in a combined fit of electroweak parameters and the PDFs, and the inclusive NC and CC DIS pseudodata (see Sec. 2.3.2) are explored as input data. The PDFs are parameterised with 13 parameters at a starting scale Q_0^2 and NNLO DGLAP evolution is applied [16, 17]. In this way, uncertainties from the PDFs are taken into account, which is very reasonable, since the

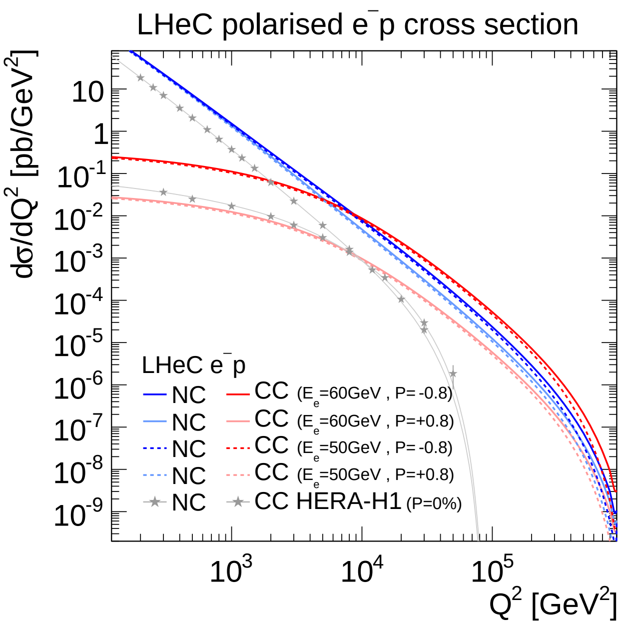

Figure 3.1: Single differential cross sections for polarised e^-p NC and CC DIS at LHeC for two different electron beam energies (E_e). Cross sections for longitudinal electron beam polarisations of $P_e = -0.8$ and $+0.8$ are displayed. For comparison also measurements at centre-of-mass energies of $\sqrt{s} = 920\,\text{GeV}$ by H1 at HERA for unpolarised ($P_e = 0\,\%$) electron beams are displayed [336].

PDFs will predominantly be determined from those LHeC data in the future. The details of the PDF fit are altogether fairly similar to the PDF fits outlined in Sec. **??**. Noteworthy differences are that additionally EW effects are included into the calculation by considering the full set of 1-loop electroweak corrections [338], and the χ^2 quantity [111], which is input to the minimisation and error propagation, is based on normal-distributed relative uncertainties. In this way, a dependence on the actual size of the simulated cross sections is avoided. The size of the pseudodata are therefore set equivalent to the predictions [339].

3.1.3 Weak boson masses M_W and M_Z

The expected uncertainties for a determination of the weak boson masses, M_W and M_Z, are determined in the PDF+EW-fit, where one of the masses is determined together with the PDFs, while the other mass parameter is taken as external input. The expected uncertainties for M_W are

$$\begin{aligned}\Delta M_\text{W}(\text{LHeC-60}) &= \pm 5_{(\text{exp})} \pm 8_{(\text{PDF})}\,\text{MeV} = 10_{(\text{tot})}\,\text{MeV} \quad \text{and} \\ \Delta M_\text{W}(\text{LHeC-50}) &= \pm 8_{(\text{exp})} \pm 9_{(\text{PDF})}\,\text{MeV} = 12_{(\text{tot})}\,\text{MeV}\end{aligned} \tag{3.8}$$

for LHeC with $E_e = 60\,\text{GeV}$ or $50\,\text{GeV}$, respectively. The breakdown into experimental and PDF uncertainties is obtained by repeating the fit with PDF parameters fixed. These uncertainties are displayed in Fig. 3.2 and compared to the values obtained by LEP2 [341], Tevatron [340], ATLAS [342] and the PDG value [142]. The LHeC measurement will become the most precise measurement from one single experiment and will greatly improve over the best measurement achieved by H1, which was $M_\text{W}(\text{H1}) = 80.520 \pm 0.115\,\text{GeV}$ [327]. If the dominating uncorrelated

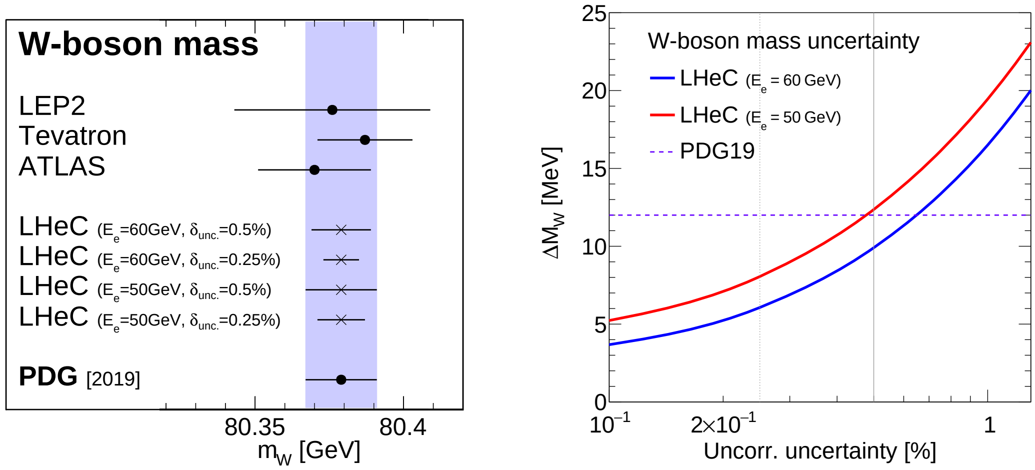

Figure 3.2: Left: Measurements of the W-boson mass assuming fixed values for the top-quark and Z-boson masses at the LHeC for different scenarios in comparison with today's measurements [340–342] and the world average value (PDG19) [142]. For LHeC, prospects for $E_e = 60\,\text{GeV}$ and $50\,\text{GeV}$ are displayed, as well as results for the two scenarios with 0.5 % or 0.25 % uncorrelated uncertainty (see text). Right: Comparison of the precision for M_W for different assumptions of the uncorrelated uncertainty of the pseudodata. The uncertainty of the world average value is displayed as horizontal line. The nominal (and alternative) size of the uncorrelated uncertainty of the inclusive NC/CC DIS pseudodata is indicated by the vertical line (see text).

uncertainties can be reduced from the prospected 0.5 % to 0.25 % [1], a precision for M_W of up to

$$\Delta M_\text{W}(\text{LHeC-60}) = \pm 3_{(\text{exp})} \pm 5_{(\text{PDF})}\,\text{MeV} = 6_{(\text{tot})}\,\text{MeV} \quad \text{and} \tag{3.9}$$
$$\Delta M_\text{W}(\text{LHeC-50}) = \pm 6_{(\text{exp})} \pm 6_{(\text{PDF})}\,\text{MeV} = 8_{(\text{tot})}\,\text{MeV}$$

for LHeC-60 and LHeC-50 may be achieved, respectively. A complete dependence of the expected total experimental uncertainty ΔM_W on the size of the uncorrelated uncertainty component is displayed in Fig. 3.2, and with a more optimistic scenario an uncertainty of up to $\Delta M_\text{W} \approx 5\,\text{MeV}$ can be achieved. In view of such a high accuracy, it will be important to study carefully theoretical uncertainties. For instance the parameteric uncertainty due to the dependence on the top-quark mass of 0.5 GeV will yield an additional error of $\Delta M_\text{W} = 2.5\,\text{MeV}$. Also higher-order corrections, at least the dominating 2-loop corrections will have to be studied and kept under control. Then, the prospected determination of the W-boson mass from LHeC data will be among the most precise determinations and significantly improve the world average value of M_W. It will also become competitive with its prediction from global EW fits with present uncertainties of about $\Delta M_\text{W} = 7\,\text{MeV}$ [142, 343, 344].

While the determination of M_W from LHeC data is competitive with other measurements, the experimental uncertainties of a determination of M_Z are estimated to be about 11 MeV and 13 MeV for LHeC-60 and LHeC-50, respectively. Therefore, the precision of the determination of M_Z at LHeC cannot compete with the precise measurements at the Z-pole by LEP+SLD and future e^+e^- colliders may even improve on that.

A simultaneous determination of M_W and M_Z is displayed in Fig. 3.3 (left). Although the precision of these two mass parameters is only moderate, a meaningful test of the high-energy

[1] Due to performance reasons, the pseudodata are generated for a rather coarse grid. With a binning which is closely related to the resolution of the LHeC detector, much finer grids in x and Q^2 are feasible. Already such a change would alter the uncertainties of the fit parameters. However, such an effect can be reflected by a changed uncorrelated uncertainty, and a value of 0.25 % appears like an optimistic, but achievable, alternative scenario.

behaviour of electroweak theory is obtained by using G_F as additional input: The high precision of the G_F measurement [345] yields a very shallow error ellipse and a precise test of the SM can be performed with only NC and CC DIS cross sections alone. Such a fit determines and simultaneously tests the high-energy behaviour of electroweak theory, while using only low-energy parameters α and G_F as input (plus values for masses like M_t and M_H needed for loop corrections).

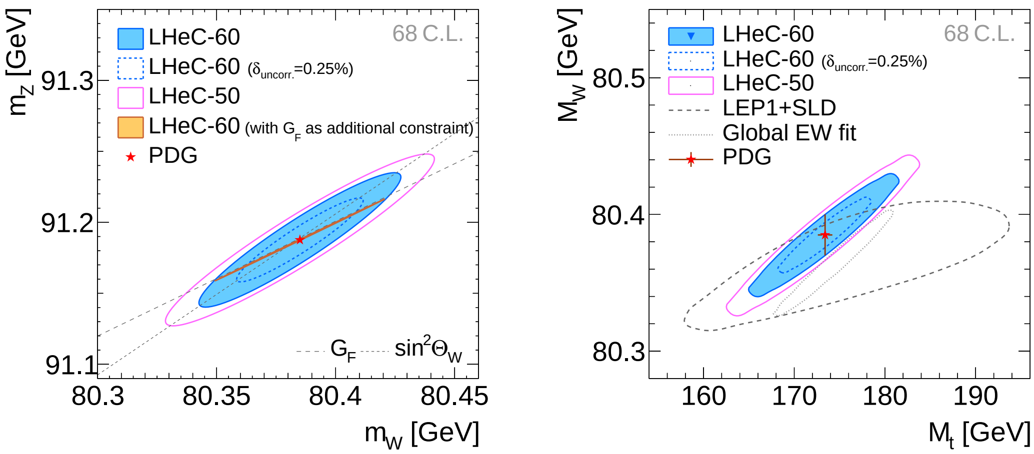

Figure 3.3: Simultaneous determination of the top-quark mass M_t and W-boson mass M_W from LHeC-60 or LHeC-50 data (left). Simultaneous determination of the W-boson and Z-boson masses from LHeC-60 or LHeC-50 data (right).

3.1.4 Further mass determinations

Inclusive DIS data are sensitive to the top-quark mass M_t indirectly through radiative corrections. M_t-dependent terms are dominantly due to corrections from the gauge boson self-energy corrections. They are contained in the ρ and κ parameters and in the correction factor Δr. The leading contributions are proportional to M_t^2. This allows for an indirect determination of the top-quark mass using LHeC inclusive DIS data, and a determination of M_t will yield an uncertainty of $\Delta M_t = 1.8\,\mathrm{GeV}$ to $2.2\,\mathrm{GeV}$. Assuming an uncorrelated uncertainty of the DIS data of 0.25 % the uncertainty of M_t becomes as small as

$$\Delta M_t = 1.1 \quad \text{to} \quad 1.4\,\mathrm{GeV} \tag{3.10}$$

for 60 and 50 GeV electron beams, respectively. This would represent a very precise indirect determination of the top-quark mass from purely electroweak corrections and thus being fully complementary to measurements based on real t-quark production, which often suffer from sizeable QCD corrections. The precision achievable in this way will be competitive with indirect determinations from global EW fits after the HL-LHC [346].

More generally, and to some extent depending on the choice of the renormalisation scheme, the leading self-energy corrections are proportional to $\frac{M_t^2}{M_\mathrm{W}^2}$ and thus a simultaneous determination of M_t and M_W is desirable. The prospects for a simultaneous determination of M_t and M_W is displayed in Fig. 3.3 (right). It is remarkable that the precision of the LHeC is superior to that of the LEP+SLD combination [347]. In an optimistic scenario an uncertainty similar to the global electroweak fit [344] can be achieved. In a fit without PDF parameters similar uncertainties are found (not shown), which illustrates that the determination of EW parameters is to a large extent independent of the QCD phenomenology and the PDFs.

The subleading contributions to self-energy corrections have a Higgs-boson mass dependence and are proportional to $\log \frac{M_H^2}{M_W^2}$. When fixing all other EW parameters the Higgs boson mass could be constrained indirectly through these loop corrections with an experimental uncertainty of $\Delta m_H = ^{+29}_{-23}$ to $^{+24}_{-20}$ GeV for different LHeC scenarios, which is again similar to the indirect constraints from a global electroweak fit [344], but not competitive with direct measurements.

3.1.5 Weak Neutral Current Couplings

The vector and axial-vector couplings of up-type and down-type quarks to the Z, g_V^q and g_A^q, see Eq. (3.7), are determined in a fit of the four coupling parameters together with the PDFs.

Coupling parameter	PDG value	Expected uncertainties LHeC-60	LHeC-60 ($\delta_{\text{uncor.}}$=0.25 %)	LHeC-50
g_A^u	$0.50\ ^{+0.04}_{-0.05}$	0.0022	0.0015	0.0035
g_A^d	$-0.514\ ^{+0.050}_{-0.029}$	0.0055	0.0034	0.0083
g_V^u	$0.18\ \pm 0.05$	0.0015	0.0010	0.0028
g_V^d	$-0.35\ ^{+0.05}_{-0.06}$	0.0046	0.0027	0.0067

Table 3.1: Light-quark weak NC couplings (g_A^u,g_A^d,g_V^u,g_V^d) and their currently most precise values from the PDG [142] compared with the prospected uncertainties for different LHeC scenarios. The LHeC prospects are obtained in a simultaneous fit of the PDF parameters and all four coupling parameters determined at a time.

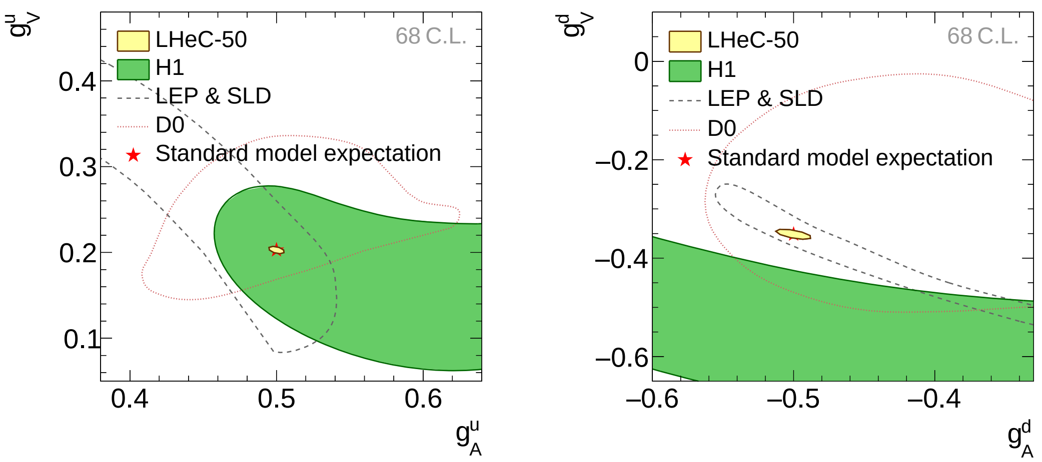

Figure 3.4: Weak NC vector and axial-vector couplings of u-type (left) and d-type quarks (right) at 68 % confidence level (C.L.) for simulated LHeC data with $E_e = 50$ GeV. The LHeC expectation is compared with results from the combined LEP+SLD experiments [347], a single measurement from D0 [348] and one from H1 [327]. The standard model expectations are diplayed by a red star, partially hidden by the LHeC prospects.

The resulting uncertainties are collected in Tab. 3.1. The two-dimensional uncertainty contours at 68 % confidence level obtained from LHeC data with $E_e = 50$ GeV are displayed in Fig. 3.4 for the two quark families and compared with available measurements. While all the current determinations from e^+e^-, ep or $p\bar{p}$ data have a similar precision, the future LHeC data will greatly improve the precision of the weak neutral-current couplings and expected uncertainties are an order of magnitude smaller than the currently most precise ones [142]. An increased electron beam energy of $E_e = 60\,\text{GeV}$ or improved experimental uncertainties would further improve this measurement.

The determination of the couplings of the electron to the Z boson, $g_V^e$and g_A^e, can be determined at the LHeC with uncertainties of up to $\Delta g_V^e = 0.0013$ and $\Delta g_A^e = \pm 0.0009$, which is similar to the results of a single LEP experiment and about a factor three larger than the LEP+SLD combination [347].

3.1.6 The neutral-current ρ_{NC} and κ_{NC} parameters

Beyond Born approximation, the weak couplings are subject to higher-order loop corrections. These corrections are commonly parameterised by quantities called ρ_{NC}, κ_{NC} and ρ_{CC}. They are sensitive to contributions beyond the SM and the structure of the Higgs sector. It is important to keep in mind that these effective coupling parameters depend on the momentum transfer and are, indeed, form factors rather than constants. It is particularly interesting to investigate the so-called effective weak mixing angle defined as $\sin^2\theta_{\text{W}}^{\text{eff}} = \kappa_{\text{NC}}\sin^2\theta_{\text{W}}$. At the Z-pole it is well accessible through asymmetry measurements in e^+e^- collisions. In DIS at the LHeC, the scale dependence of the effective weak mixing angle is not negligible. It can be determined only together with the ρ parameter due to the Q^2 dependence and the presence of the photon exchange terms. Therefore, we introduce (multiplicative) anomalous contributions to these factors, denoted as $\rho'_{\text{NC,CC}}$ and κ'_{NC}, and test their agreement with unity (for more details see Ref. [327]), and uncertainties of these parameters are obtained in a fit together with the PDFs. The two-dimensional uncertainty contours of the anomalous form factors $\rho'_{\text{NC},f}$ and $\kappa'_{\text{NC},f}$ are

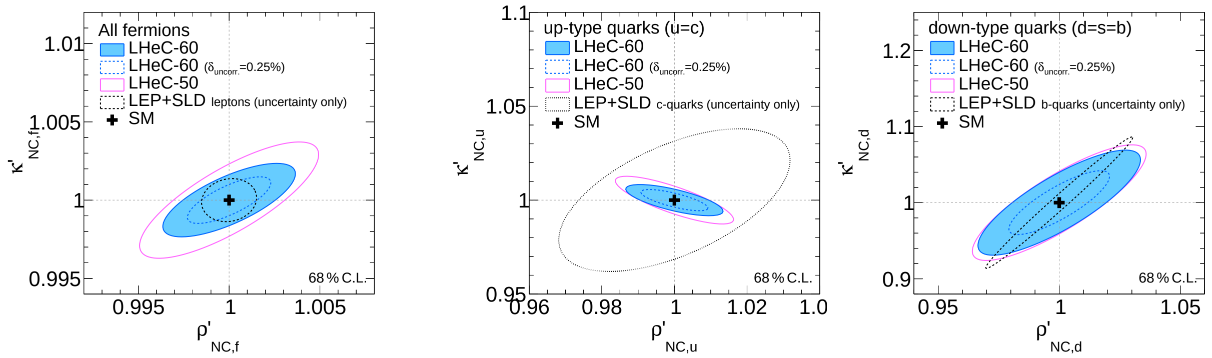

Figure 3.5: Expectations at 68 % confidence level for the determination of the ρ'_{NC} and κ'_{NC} parameters assuming a single anomalous factor equal for all fermions (left). The results for three different LHeC scenarios are compared with the achieved uncertainties from the LEP+SLD combination [347] for the determination the respective leptonic quantities. Right: uncertainties for the simultaneous determination of the anomalous form factors for u and d-type quarks, assuming known values for the electron parameters. The values are compared with uncertainties reported by LEP+SLD for the determination of the values $\rho_{\text{NC},(c,b)}$ and $\sin\theta_{\text{W}}^{\text{eff},(c,b)}$ for charm or bottom quarks, respectively.

displayed for three different LHeC scenarios in Fig. 3.5 (left), and compared with uncertainties from the LEP+SLD combination [2] [347]. It is found that these parameters can be determined

[2]Since in the LEP+SLD analysis the values of ρ_{NC} and $\kappa_{\text{NC}}\sin^2\theta_{\text{W}}$ are determined, we compare only the size of the uncertainties in these figures. Furthermore it shall be noted, that LEP is mainly sensitive to the

with very high experimental precision.

Assuming the couplings of the electron are given by the SM, the anomalous form factors for the two quark families can be determined and results are displayed in Fig. 3.5 (right). Since these measurements represent unique determinations of parameters sensitive to the light-quark couplings, we can compare only with nowadays measurements of the parameters for heavy-quarks of the same charge and it is found that the LHeC will provide high-precision determinations of the $\rho'_{\rm NC}$ and $\kappa'_{\rm NC}$ parameters.

A meaningful test of the SM can be performed by determining the effective coupling parameters as a function of the momentum transfer. In case of $\kappa'_{\rm NC}$, this is equivalent to measuring the running of the effective weak mixing angle, $\sin\theta_{\rm W}^{\rm eff}(\mu)$ (see also Sec. 3.1.7). However, DIS is quite complementary to other measurements since the process is mediated by space-like momentum transfer, i.e. $q^2 = -Q^2 < 0$ with q being the boson four-momentum. Prospects for a determination of $\rho'_{\rm NC}$ or $\kappa'_{\rm NC}$ at different Q^2 values are displayed in Fig. 3.6 and compared to results obtaind by H1. The value of $\kappa'_{\rm NC}(\mu)$ can be easily translated to a measurement of $\sin\theta_{\rm W}^{\rm eff}(\mu)$.

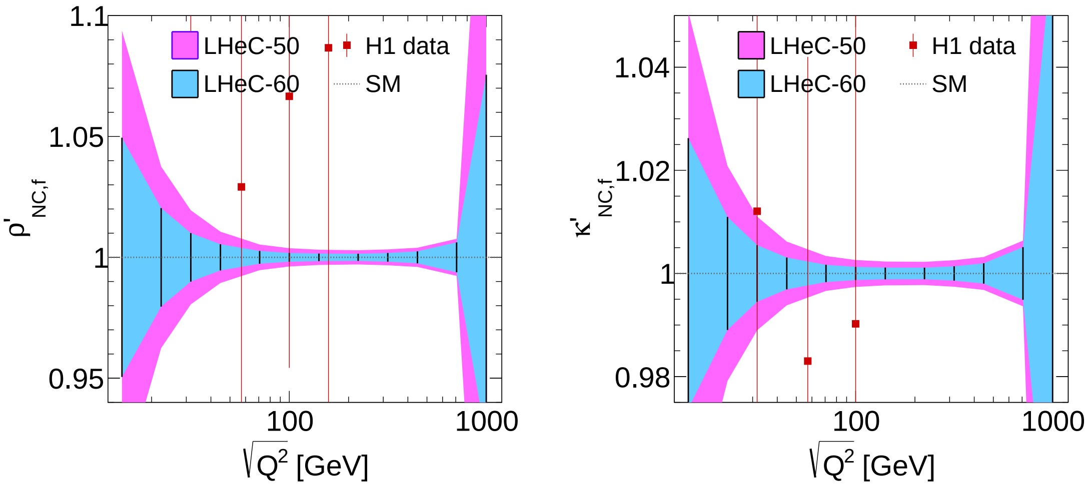

Figure 3.6: Test of the scale dependence of the anomalous ρ and κ parameters for two different LHeC scenarios. For the case of LHeC-60, i.e. $E_e = 60\,\text{GeV}$, we assume an uncorrelated uncertainty of 0.25 %. The uncertainties of the parameter $\kappa'_{\rm NC,f}$ can be interpreted as sensitivity to the scale-dependence of the weak mixing angle, $\sin\theta_{\rm W}^{\rm eff}(\mu)$.

From Fig. 3.6 one can conclude that this quantity can be determind with a precision of up to 0.1 % and better than 1 % over a wide kinematic range of about $25 < \sqrt{Q^2} < 700\,\text{GeV}$.

3.1.7 The effective weak mixing angle $\sin^2\theta_{\rm W}^{\rm eff,\ell}$

The leptonic effective weak mixing angle is defined as $\sin^2\theta_{\rm W}^{\rm eff,\ell}(\mu^2) = \kappa_{{\rm NC},\ell}(\mu^2)\sin^2\theta_{\rm W}$. Due to its high sensitivity to loop corrections it represents an ideal quantity for precision tests of the Standard Model. Its value is scheme dependent and it exhibits a scale dependence. Near the Z pole, $\mu^2 = M_{\rm Z}^2$, its value was precisely measured at LEP and at SLD. Those analyses were based on the measurement of asymmetries and their interpretation in terms of the leptonic weak mixing angle was simplified by the fact that many non-leptonic corrections and contributions

parameters of leptons or heavy quarks, while LHeC data is more sensitive to light quarks (u,d,s), and thus the LHeC measurements are highly complementary.

from box graphs cancel or can be taken into account by subtracting their SM predictions. The highest sensitivity to $\sin^2\theta_W^{\text{eff},\ell}(M_Z)$ to date arises from a measurement of $A_{\text{fb}}^{0,b}$ [347], where the non-universal flavour-specific corrections to the quark couplings are taken from the SM and consequently these measurements are interpreted to be sensitive only to the universal, i.e. flavour-independent [3], non-SM contributions to κ_{NC}. Applying this assumption also to the DIS cross sections, the determination of $\kappa'_{\text{NC},f}$ can directly be interpreted as a sensitivity study of the leptonic effective weak mixing angle $\sin^2\theta_W^{\text{eff},\ell}$.

Fit parameters	Parameter of interest	SM value	Expected uncertainties: LHeC-50 ($\delta_{\text{uncor.}} = 0.50\,\%$)	LHeC-60 ($\delta_{\text{uncor.}} = 0.50\,\%$)	LHeC-50 ($\delta_{\text{uncor.}} = 0.25\,\%$)	LHeC-60 ($\delta_{\text{uncor.}} = 0.25\,\%$)
$\kappa'_{\text{NC},f}$, PDFs	$\sin^2\theta_W^{\text{eff},\ell}(M_Z^2)$	0.23154	0.00033	0.00025	0.00022	0.00015
$\kappa'_{\text{NC},f}$, $\rho'_{\text{NC},f}$, PDFs	$\sin^2\theta_W^{\text{eff},\ell}(M_Z^2)$	0.23154	0.00071	0.00036	0.00056	0.00023
$\kappa'_{\text{NC},e}$, PDFs	$\sin^2\theta_W^{\text{eff},e}(M_Z^2)$	0.23154	0.00059	0.00047	0.00038	0.00028
$\kappa'_{\text{NC},e}$, $\kappa'_{\text{NC},u}$, $\kappa'_{\text{NC},d}$, PDFs	$\sin^2\theta_W^{\text{eff},e}(M_Z^2)$	0.23154	0.00111	0.00095	0.00069	0.00056
$\kappa'_{\text{NC},f}$	$\sin^2\theta_W^{\text{eff},\ell}(M_Z^2)$	0.23154	0.00028	0.00023	0.00017	0.00014

Table 3.2: Determination of $\sin^2\theta_W^{\text{eff},\ell}(M_Z^2)$ with inclusive DIS data at the LHeC for different scenarios. Since the value of the effective weak mixing angle at the Z pole cannot be determined directly in DIS, a fit of the $\kappa'_{\text{NC},f}$ parameter is performed instead and its uncertainty is translated to $\sin^2\theta_W^{\text{eff},\ell}(M_Z^2)$. Different assumptions on the fit parameters are studied, and results include uncertainties from the PDFs. Only the last line shows results where the PDF parameters are kept fixed. See text for more details.

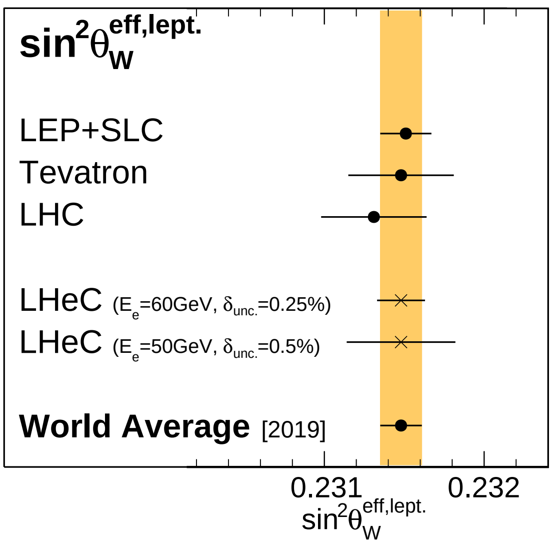

Figure 3.7: Comparison of the determination of $\sin^2\theta_W^{\text{eff},\ell}(M_Z^2)$ from LHeC inclusive DIS data with recent averaged values. Results from LEP+SLC [347], Tevatron [349], LHC [350–353] and the world average value [353] are all obtained from a combination of various separate measurements (not shown individually) (see also Ref. [354] for additional discussions). For LHeC, the experimental and PDF uncertainties are displayed.

The prospects for a determination of $\sin^2\theta_W^{\text{eff},\ell}$ are listed in Tab. 3.2. Two fits have been studied: one with a fixed parameter ρ'_{NC} and one where $\sin^2\theta_W^{\text{eff},\ell}$ is determined together with ρ'_{NC} (see

[3] Flavour-specific tests have been discussed to some extent in the previous Section.

Fig. 3.5 (left)). At the LHeC, it will be possible to determine the value of $\sin^2\theta_{\mathrm{W}}^{\mathrm{eff},\ell}(M_{\mathrm{Z}}^2)$ with an experimental uncertainty of up to

$$\Delta\sin^2\theta_{\mathrm{W}}^{\mathrm{eff},\ell} = \pm 0.00015\,, \tag{3.11}$$

where PDF uncertainties are already included. If the PDF parameters are artificially kept fixed, the uncertainties are of very similar size, which demonstrates that these measurements are fairly insensitive to the QCD effects and the PDFs. The uncertainties are compared [4] to recent average values in Fig. 3.7. One can see that the LHeC measurement has the potential to become the most precise single measurement in the future with a significant impact to the world average value. It is obvious that a conclusive interpretation of experimental results with such a high precision will require correspondingly precise theoretical predictions, and the investigation of two-loop corrections for DIS will become important.

This LHeC measurement will become competitive with measurements at the HL-LHC [146]. Since in pp collisions one of the dominant uncertainty is from the PDFs, future improvements can (only) be achieved with a common analysis of LHeC and HL-LHC data. Such a study will yield highest experimental precision and the challenging theoretical and experimental aspects for a complete understanding of such an analysis will deepen our understanding of the electroweak sector.

It may be further of interest, to determine the value of the effective weak mixing angle of the electron separately in order to compare with measurements in pp and test furthermore lepton-specific contributions to $\kappa_{\mathrm{NC,lept.}}$. Such fits are summarised in Table 3.2 and a reasonable precision is achieved with LHeC.

3.1.8 Electroweak effects in charged-current scattering

The charged-current sector of the SM can be uniquely measured at high scales over many orders of magnitude in Q^2 at the LHeC, due to the excellent tracking detectors, calorimetry, and high-bandwidth triggers. Similarly as in the NC case, the form factors of the effective couplings of the fermions to the W boson can be measured. In the SM formalism, only two of these form factors are present, $\rho_{\mathrm{CC},eq}$ and $\rho_{\mathrm{CC},e\bar{q}}$. We thus introduce two anomalous modifications to them, $\rho_{\mathrm{CC},(eq/e\bar{q})} \to \rho'_{\mathrm{CC},(eq/e\bar{q})}\rho_{\mathrm{CC},(eq/e\bar{q})}$ (see Ref. [327]). The prospects for the determination of these parameters are displayed in Fig. 3.8, and it is found, that with the LHeC these parameters can be determined with a precision up to 0.2–0.3 %. Also their Q^2 dependence can be uniquely studied with high precision up to $\sqrt{Q^2}$ values of about 400 GeV.

3.1.9 Direct W and Z production and Anomalous Triple Gauge Couplings

The direct production of single W and Z bosons as a crucial signal represents an important channel for EW precision measurements. The production of W bosons has been measured at $\sqrt{s} \simeq 320$ GeV at HERA [355–357]. With the full $e^{\pm}p$ data set collected by the H1 and ZEUS

[4] It shall be noted, that in order to compare the LHeC measurements with the Z-pole measurements at $\mu^2 = M_Z^2$ in a conclusive way, one has to assume the validity of the SM framework. In particular the scale-dependence of $\kappa_{\mathrm{NC},\ell}$ must be known in addition to the flavour-specific corrections. On the other hand, the scale dependence can be tested itself with the LHeC data which cover a large range of space-like Q^2. In this aspect, DIS provides a unique opportunity for precision measurements in the space-like regime ($\mu^2 < 0$) as has been discussed in the previous Section, see Fig. 3.6 (right).

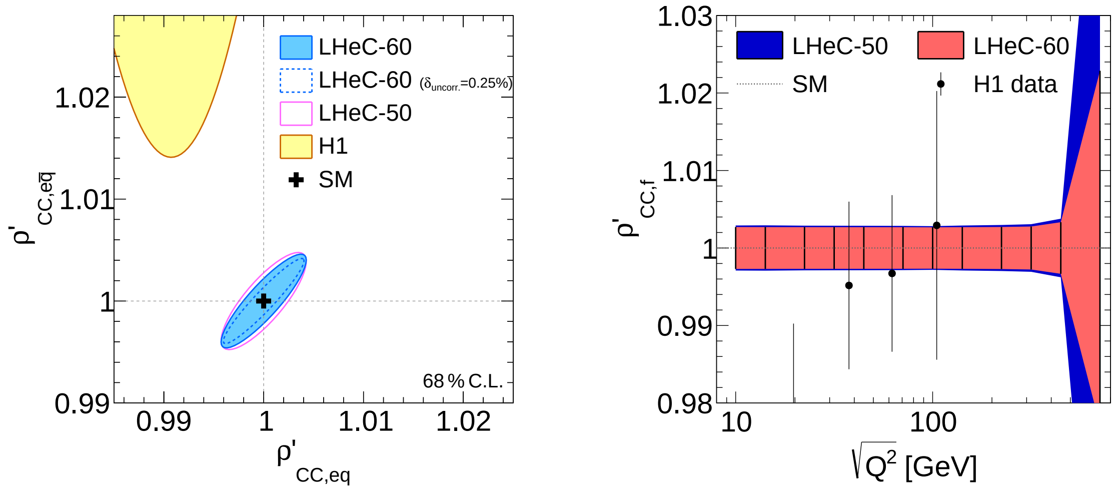

Figure 3.8: Left: anomalous modifications of the charged current form factors $\rho'_{\mathrm{CC},eq}$ and $\rho'_{\mathrm{CC},e\bar{q}}$ for different LHeC scenarios in comparison with the H1 measurement [327]. Right: scale dependent measurement of the anomalous modification of the charged current form factor $\rho'_{\mathrm{CC}}(Q^2)$, assuming $\rho'_{\mathrm{CC},eq} = \rho'_{\mathrm{CC},e\bar{q}} = \rho'_{\mathrm{CC}}$.

experiments together, corresponding to an integrated luminosity of about $\mathcal{L} \sim 1\,\mathrm{fb}^{-1}$, a few dozens of W boson event candidates have been identified in the e, μ or τ decay channel.

Detailed studies of direct W/Z production in ep collisions at higher centre-of-mass energies have been presented in the past, see Refs. [358–360]. These theoretical studies were performed for a proton beam energy of $E_p = 8\,\mathrm{TeV}$ and electron beam energies of $E_e = 55\,\mathrm{GeV}$ or $100\,\mathrm{GeV}$, which correspond to a very similar centre-of-mass energy as the LHeC. Measurements at the LHeC will benefit considerably from the large integrated luminosity, in comparison to earlier projections.

The W or Z direct production in e^-p collisions can be classified into five processes

$$\begin{aligned} &e^-p \to e^-W^+j, \quad e^-p \to e^-W^-j, \\ &e^-p \to \nu_e^- W^-j, \quad\ \ e^-p \to \nu_e^- Zj \end{aligned} \tag{3.12}$$

and

$$e^-p \to e^-Zj, \tag{3.13}$$

where j denotes the hadronic the final state (i.e. the *forward jet*). According to the above classification, the four processes in Eq. (3.12) can be used to study Tripe Gauge Couplings (TGCs), e.g. $WW\gamma$ and WWZ couplings, since some contributing diagrams represent Vector Boson Fusion (VBF) processes. The process shown in Eq. (3.13) does not contain any TGC vertex. The processes for positron-proton collisions can be easily derived from Eqs. (3.12) and (3.13), but are not discussed further here due to the small integrated luminosity of the LHeC e^+p data.

The MadGraph5_v2.4.2 program [361] is employed for matrix element calculation and event generation and the PDF NNPDF23_nlo_as_0119_qed [362] is used. Technical cuts on the transverse momentum of the outgoing scattered lepton, p_T^ℓ, of 10 GeV or alternatively 5 GeV, are imposed and other basic cuts are $p_T^j > 20\,\mathrm{GeV}$, $|\eta_{e,j}| < 5$ and $\Delta R_{ej} < 0.4$. The resulting Standard Model total cross sections of the above processes are listed in Tab. 3.3.

Process	$E_e = 50\,\text{GeV}$, $E_p = 7\,\text{TeV}$ $p_T^e > 10\,\text{GeV}$	$E_e = 60\,\text{GeV}$, $E_p = 7\,\text{TeV}$ $p_T^e > 10\,\text{GeV}$	$E_e = 60\,\text{GeV}$, $E_p = 7\,\text{TeV}$ $p_T^e > 5\,\text{GeV}$
e^-W^+j	1.00 pb	1.18 pb	1.60 pb
e^-W^-j	0.930 pb	1.11 pb	1.41 pb
$\nu_e^-W^-j$	0.796 pb	0.956 pb	0.956 pb
ν_e^-Zj	0.412 pb	0.502 pb	0.502 pb
e^-Zj	0.177 pb	0.204 pb	0.242 pb

Table 3.3: The SM predictions of direct W and Z production cross sections in e^-p collisions for different collider beam energy options, E_e, and final state forward electron transverse momentum cut, p_T^e. Two different electron beam energy options are considered, $E_e = 50\,\text{GeV}$ and $60\,\text{GeV}$.

The process with the largest production cross section in e^-p scattering is the single W^+ boson production. This will be the optimal channel of both the SM measurement and new physics probes in the EW sector. Also, this channel is experimentally preferred since the W^+ is produced in NC scattering, so the beam electron is measured in the detector, and the W-boson has opposite charge to the beam lepton and thus in a leptonic decay an opposite charge lepton and missing transverse momentum is observed. Altogether, it is expected that a few million of direct W-boson events are measured at LHeC.

Several 10^5 direct Z events are measured, which corresponds approximately to the size of the event sample of the SLD experiment [347], but at the LHeC these Z bosons are predominantly produced in VBF events.

All these total cross sections increase significantly with smaller transverse momentum of the outgoing scattered lepton. Therefore it will become important to decrease that threshold with dedicated electron taggers, see Chapter **??**.

The measurement of gauge boson production processes provides a precise measurement of the triple gauge boson vertex. The measurement is sensitive to new physics contributions in *anomalous* Tripe Gauge Couplings (aTGC). The LHeC has advantages of a higher centre-of-mass energy and easier kinematic analysis in the measurement of aTGCs.

In the effective field theory language, aTGCs in the Lagrangian are generally parameterised as

$$\begin{aligned}\mathcal{L}_{TGC}/g_{WWV} \;=\;& ig_{1,V}(W^+_{\mu\nu}W^-_\mu V_\nu - W^-_{\mu\nu}W^+_\mu V_\nu) + i\kappa_V W^+_\mu W^-_\nu V_{\mu\nu} + \frac{i\lambda_V}{M_W^2}W^+_{\mu\nu}W^-_{\nu\rho}V_{\rho\mu} \\ & + g_5^V \epsilon_{\mu\nu\rho\sigma}(W^+_\mu \overleftrightarrow{\partial}_\rho W^-_\nu)V_\sigma - g_4^V W^+_\mu W^-_\nu(\partial_\mu V_\nu + \partial_\nu V_\mu) \\ & + i\tilde{\kappa}_V W^+_\mu W^-_\nu \tilde{V}_{\mu\nu} + \frac{i\tilde{\lambda}_V}{M_W^2}W^+_{\lambda\mu}W^-_{\mu\nu}\tilde{V}_{\nu\lambda}, \end{aligned} \tag{3.14}$$

where $V = \gamma, Z$. The gauge couplings $g_{WW\gamma} = -e$, $g_{WWZ} = -e\cot\theta_W$ and the weak mixing angle θ_W are from the SM. $\tilde{V}_{\mu\nu}$ and $A\overleftrightarrow{\partial}_\mu B$ are defined as $\tilde{V}_{\mu\nu} = \frac{1}{2}\epsilon_{\mu\nu\rho\sigma}V_{\rho\sigma}$, $A\overleftrightarrow{\partial}_\mu B = A(\partial_\mu B) - (\partial_\mu A)B$, respectively. There are five aTGCs ($g_{1,Z}$, κ_V, and λ_V) conserving the C and CP condition with electromagnetic gauge symmetry requires $g_{1,\gamma} = 1$. Only three of them are independent because $\lambda_Z = \lambda_\gamma$ and $\Delta\kappa_Z = \Delta g_{1,Z} - \tan^2\theta_W \Delta\kappa_\gamma$ [363–365]. The LHeC can set future constraints on $\Delta\kappa_\gamma$ and λ_γ.

In the direct Z/γ production process, the anomalous WWZ and $WW\gamma$ couplings can be separately measured without being influenced by their interference [366, 367]. In the direct W production process, both the deviation in signal cross section and the kinematic distributions can effectively constrain the $WW\gamma$ aTGC, while anomalous WWZ contribution in this channel is insensitive as a result of the suppression from Z boson mass [368–370].

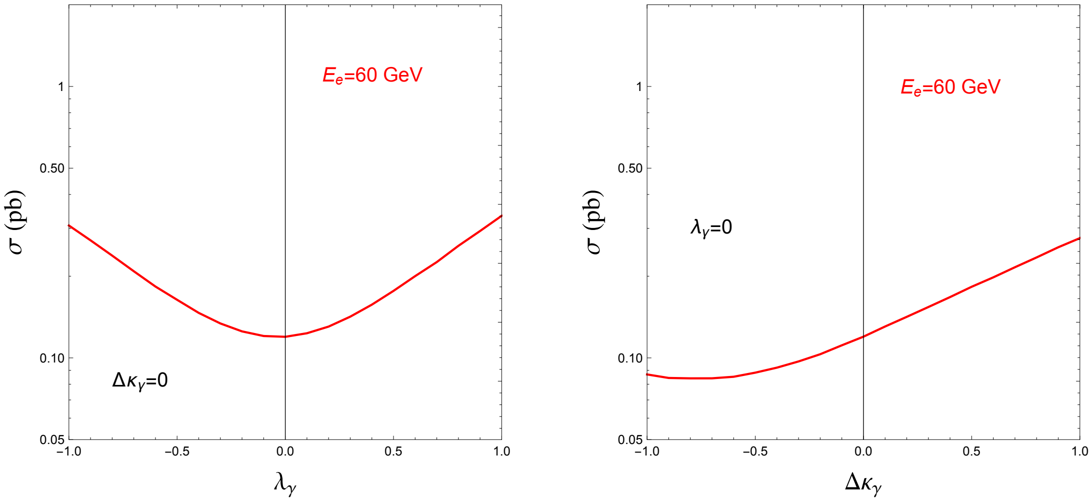

Figure 3.9: Total cross sections of the $e^-p \to e^-\mu^+\nu_\mu j$ process with varying λ_γ (left plot) and $\Delta\kappa_\gamma$ (right plot).

The W decay into muon channel is the expected optimal measurement for the anomalous $WW\gamma$ coupling because of the discrimination of final states and mistagging efficiencies [368]. Fig. 3.9 shows the cross section of single W^+ production process followed by $W^+ \to \mu^+\nu_\mu$ decay, with different λ_γ and $\Delta\kappa_\gamma$ values. Large anomalous coupling leads to measurable deviation to the SM prediction. The cross section increases monotonically with $\Delta\kappa_\gamma$ and the absolute value of λ_γ within the region of $-1.0 \leq \lambda_\gamma/\Delta\kappa_\gamma \leq 1.0$.

Kinematic analysis is necessary for the precise aTGC measurement. At LHeC, the $e^-p \to e^-W^\pm j$ process with leptonic W boson decay can be fully reconstructed because the undetected neutrino information is reconstructed either with energy-momentum conservation or the recoil mass method. This allows to use angular correlation observables, which are sensitive to the W boson polarization. Helicity amplitude calculation indicates that a non-SM value of λ_γ leads to a significant enhancement in the transverse polarization fraction of the W boson in the $e^-p \to e^-W^+j$ process, while a non-SM value of $\Delta\kappa_\gamma$ leads to enhancement in the longitudinal component fraction [358]. The angle $\theta_{\ell W}$ is defined as the angle between the decay product lepton ℓ in the W rest frame and W moving direction in the collision rest frame. Making use of the energetic final states in the forward direction, a second useful angle $\Delta\phi_{ej}$ is defined as the separation of final state jet and electron on the azimuthal plane. In an optimised analysis, assuming an integrated luminosity of $1\,\mathrm{ab}^{-1}$, the observable $\Delta\phi_{ej}$ can impose stringent constraints on both λ_γ and $\Delta\kappa_\gamma$, and uncertainties within $[-0.007, 0.0056]$ and $[-0.0043, 0.0054]$ are achieved, respectively. The $\cos\theta_{\mu W}$ observable is also sensitive to $\Delta\kappa_\gamma$ at the same order, but fails to constrain λ_γ. The analysis is described in detail in Ref. [368].

Fig. 3.10 shows the two-parameter aTGC constraint on the λ_γ–$\Delta\kappa_\gamma$ plane based on a χ^2 analysis of $\Delta\phi_{ej}$ at parton-level and assuming an electron beam energy of $E_e = 60\,\mathrm{GeV}$. When comparing with the current LHC (blue and green) and LEP (red) bounds, the LHeC has the potential to significantly improve the constraints, in particular on the $\Delta\kappa_\gamma$ parameter. The polarised electron beam is found to improve the aTGC measurement [367, 370]. In consideration of the *realistic* analysis at detector level, one expects 2-3 ab^{-1} integrated luminosity to achieve same results [368].

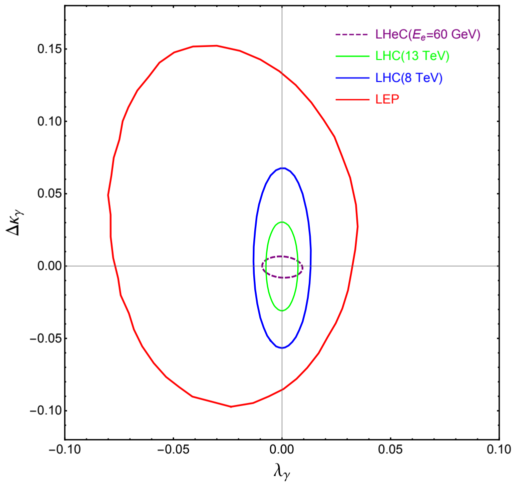

Figure 3.10: The 95% C.L. exclusion limit on the $\Delta\kappa_\gamma$-λ_γ plane. The purple dashed contour is the projected LHeC exclusion limit with $1\,\mathrm{ab}^{-1}$ integrated luminosity [368]. The blue, green and red contours are current bounds from LHC [371, 372] and LEP [373].

One uncertainty in the aTGC measurement at the (HL-)LHC comes from the PDF uncertainty. Future LHeC PDF measurement will improve the precision of aTGC measurement in the $x \simeq \mathcal{O}(10^{-2})$ region.

3.1.10 Radiation Amplitude Zero

The LHeC is ideal for testing a novel feature of the Standard Model: the *radiation amplitude zero* [374–377] of the amplitude $\gamma W^- \to c\bar{b}$ and related amplitudes, see Fig. 3.11. The Born amplitude is predicted to vanish and change sign at $\cos\theta_{CM} = \frac{e_{\bar{b}}}{e_{\bar{W}}} = -1/3$. This LHeC measurement tests W compositeness and its zero anomalous magnetic moment at leading order: $g_W = 2, \kappa_W = 1$, as well as $g_q = 2$ for quarks.. One can also test the radiation amplitude zero for the top quark from $\gamma b \to W^- t$.

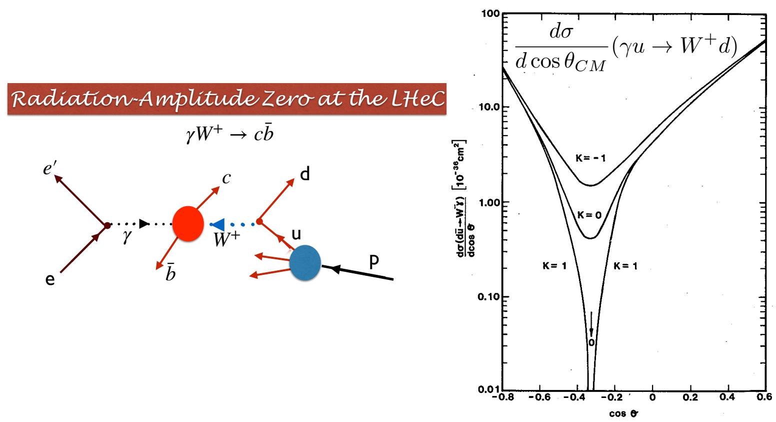

Figure 3.11: The radiation amplitude zero of the Standard Model in $\gamma W^+ \to c\bar{b}$ and $\gamma u \to W^+ d$. The prediction for the angular distribution $\frac{d\sigma}{dcos(\theta_{CM})}(\gamma u \to W^+ d)$ is from Ref. [377].

3.1.11 Conclusion

With LHeC inclusive NC and CC DIS data, unique measurements of electroweak parameters can be performed with highest precision. Since inclusive DIS is mediated through space-like momentum transfer (t-channel exchange) the results are often complementary to other experiments, such as pp or e^+e^- collider experiments, where measurements are performed in the time-like regime and most often at the Z peak. Among many other quantities, measurements of the weak couplings of the light quarks, u and d, or their anomalous form factors $\rho'_{\mathrm{NC},u/d}$ and $\kappa'_{\mathrm{NC},u/d}$, can be performed uniquely due to the important contributions of valence quarks in the initial state. Also scale dependent measurements of weak interactions can be performed over a large range in $\sqrt{Q^2}$, which provides an interesting portal to BSM physics. The W boson mass can be determined with very small experimental uncertainties, such that theoretical uncertainties are expected to become more important than experimental uncertainties. While the parameters of the PDFs are determined together with the EW parameters in the present study, it is found that the PDFs do not induce a limitation of the uncertainties. Considering the dominating top-quark mass dependence of higher-order electroweak effects, one can realise that the LHeC will be competitive with the global electroweak fit after the HL-LHC era [146, 346].

Besides proving its own remarkable prospect on high-precision electroweak physics, the LHeC will further significantly improve the electroweak measurements in pp collisions at the LHC by reducing the presently sizeable influence of PDF and α_s uncertainties. This is discussed in Sec. **??**.

3.2 Top Quark Physics

SM top quark production at a future ep collider is dominated by single top quark production, mainly via CC DIS production. An example graph is shown in Fig. 3.12 (left). The total cross section is 1.89 pb at the LHeC [378] and with an electron beam energy of 60 GeV, and an LHC proton beam of 7 TeV, leading to a centre-of-mass energy of 1.3 TeV, respectively. The other important top quark production mode is $t\bar{t}$ photoproduction with a total cross section of 0.05 pb at the LHeC [379]. An example graph is shown in Fig. 3.12 (right). This makes a future LHeC a top quark factory and an ideal tool to study top quarks with a high precision, and to analyse in particular their electroweak interaction. Selected highlights in top quark physics are summarised here.

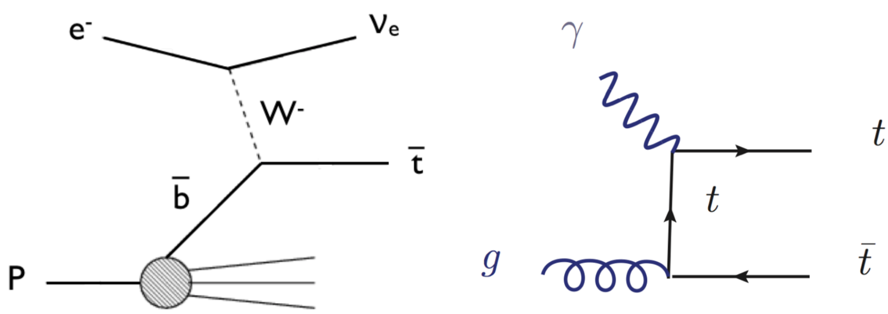

Figure 3.12: Example graphs for CC DIS top quark production (left) and top quark photoproduction (right).

3.2.1 Wtq Couplings

One flagship measurement is the direct measurement of the CKM matrix element $|V_{tb}|$, i.e. without making any model assumptions such as on the unitarity of the CKM matrix or the number of quark generations. An elaborate analysis of the single top quark CC DIS process at the LHeC including a detailed detector simulation using the DELPHES package [380] shows that already at $100\,\mathrm{fb}^{-1}$ of integrated luminosity an uncertainty of 1% can be expected. This compares to a total uncertainty of 4.1 % of the currently most accurate result at the LHC Run-I performed by the CMS experiment [381].

The same analysis [378] can also be used to search for anomalous left- and right-handed Wtb vector (f_1^L, f_1^R) and tensor (f_2^L, f_2^R couplings analyzing the following effective Lagrangian:

$$L = -\frac{g}{\sqrt{2}}\bar{b}\gamma^{\mu}V_{tb}(f_1^L P_L - f_1^R P_R)tW_{\mu}^{-} - \frac{g}{\sqrt{2}}\bar{b}\frac{i\sigma^{\mu\nu}q_{\nu}}{M_W}(f_2^L P_L - f_2^R P_R)tW_{\mu}^{-} + h.c. \tag{3.15}$$

In the SM $f_1^L = 1$ and $f_1^R = f_2^L = f_2^R = 0$. The effect of anomalous Wtb couplings is consistently evaluated in the production and the decay of the antitop quark, cf. Fig. 3.12 (left). Using hadronic top quark decays only, the expected accuracies in a measurement of these couplings as a function of the integrated luminosity are presented in Fig. 3.13 (upper left), derived from expected 95% C.L. limits on the cross section yields. The couplings can be measured with accuracies of 1 % for the SM f_1^L coupling determining $|V_{tb}|$ (as discussed above) and of 4 % for f_2^L, 9 % for f_2^R, and 14% for f_1^R at 1 ab^{-1}.

Similarly, the CKM matrix elements $|V_{tx}|$ ($x = d, s$) can be extracted using a parameterisation of deviations from their SM values with very high precision through W boson and bottom (light) quark associated production channels, where the W boson and b-jet (light jet $j = d, s$) final states can be produced via s-channel single top quark decay or t-channel top quark exchange as outlined in [382]. As an example, analysing the processes

Signal 1: $pe^- \to \nu_e\bar{t} \to \nu_e W^-\bar{b} \to \nu_e\ell^-\nu_\ell\bar{b}$

Signal 2: $pe^- \to \nu_e W^- b \to \nu_e\ell^-\nu_\ell b$

Signal 3: $pe^- \to \nu_e\bar{t} \to \nu_e W^- j \to \nu_e\ell^-\nu_\ell j$

in an elaborate analysis including a detailed detector simulation using the DELPHES package [380], the expected accuracies on $|V_{td}|$ and $|V_{ts}|$ at the 2σ confidence level (C.L.) are shown as a function of the integrated luminosity in Fig. 3.13 (upper right, middle left). At $1\,\mathrm{ab}^{-1}$ of integrated luminosity and an electron polarization of 80 %, the 2σ limits improve on existing limits from the LHC [383] (interpreted by [384]) by a factor of ≈ 3.5. Analyzing Signal 3 alone, and even more when combining Signals 1, 2 and 3, will allow for the first time to achieve an accuracy of the order of the actual SM value of $|V_{ts}^{\mathrm{SM}}| = 0.04108^{+0.0030}_{-0.0057}$ as derived from an indirect global CKM matrix fit [385], and will therefore represent a direct high precision measurement of this important top quark property. In these studies, upper limits at the 2σ level down to $|V_{ts}| < 0.06$, and $|V_{td}| < 0.06$ can be achieved.

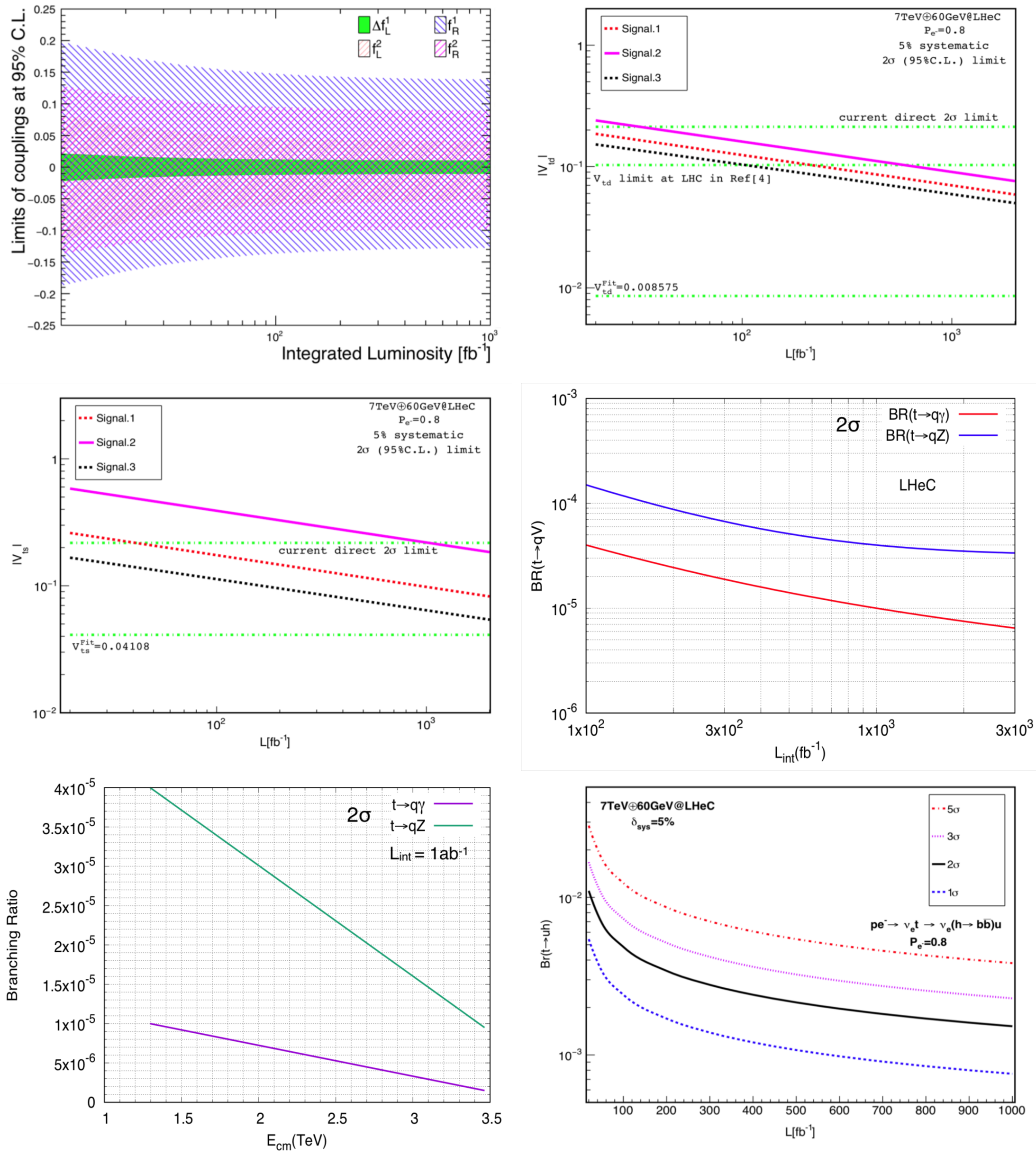

Figure 3.13: Expected sensitivities as a function of the integrated luminosity on the SM and anomalous Wtb couplings [378] (upper left), on $|V_{td}|$ (upper right) and $|V_{ts}|$ (middle left) [382], on FCNC $t \to qV$ branching ratios (middle right) [386, 387], and on FCNC $t \to uH$ branching ratios [388] (lower left). The expected upper limits on FCNC $t \to qV$ branching ratios are also shown as a function of the centre-of-mass-energy (lower right).

3.2.2 FCNC Top Quark Couplings

Single top quark NC DIS production can be used to search for flavour Changing Neutral Current (FCNC) $tu\gamma$, $tc\gamma$, tuZ, and tcZ couplings [386, 387] as represented by the Lagrangian

$$L = \sum_{q=u,c} \left(\frac{g_e}{2m_t} \bar{t}\sigma^{\mu\nu}(\lambda_q^L P_L + \lambda_q^R P_R) q A_{\mu\nu} + \frac{g_W}{4c_W m_Z} \bar{t}\sigma^{\mu\nu}(\kappa_q^L P_L + \kappa_q^R P_R) q Z_{\mu\nu} \right) + h.c. \,, \quad (3.16)$$

where g_e (g_W) is the electromagnetic (weak) coupling constant, c_W is the cosine of the weak mixing angle, $\lambda_q^{L,R}$ and $\kappa_q^{L,R}$ are the strengths of the anomalous top FCNC couplings (the values of these couplings vanish at the lowest order in the SM). In an elaborate analysis events including at least one electron and three jets (hadronic top quark decay) with high transverse momentum and within the pseudorapidity acceptance range of the detector are selected. The distributions of the invariant mass of two jets (reconstructed W boson mass) and an additional jet tagged as b-jet (reconstructed top quark mass) are used to further enhance signal over background events, mainly given by $W+$jets production. Signal and background interference effects are included. A detector simulation with DELPHES [380] is applied.

The expected limits on the branching ratios BR($t \to q\gamma$) and BR($t \to qZ$) as a function of the integrated luminosity at the 2σ C.L. are presented in Fig. 3.13 (middle right). Assuming an integrated luminosity of $1\,\text{a}b^{-1}$, limits of BR($t \to q\gamma$) $< 1 \cdot 10^{-5}$ and BR($t \to qZ$) $< 4 \cdot 10^{-5}$ are expected. This level of precision is close to actual predictions of concrete new phenomena models, such as SUSY, little Higgs, and technicolour, that have the potential to produce FCNC top quark couplings. This will improve on existing limits from the LHC by one order of magnitude [389]. Fig. 3.13 (lower left) shows how this sensitivity on BR($t \to q\gamma$) and BR($t \to qZ$) changes as a function of centre-of-mass energy. At a future FCC-ep [389] with, for example, an electron beam energy of 60 GeV, and a proton beam energy of 50 TeV, leading to a centre-of-mass energy of 3.5 TeV, the sensitivity on FCNC $tq\gamma$ couplings even exceed expected sensitivities from the High Luminosity-LHC (HL-LHC) with $300\,\text{fb}^{-1}$ at $\sqrt{s} = 14\,\text{TeV}$, and from the International Linear Collider (ILC) with $500\,\text{fb}^{-1}$ at $\sqrt{s} = 250\,\text{GeV}$ [390, 391].

Another example for a sensitive search for anomalous top quark couplings is the one for FCNC tHq couplings as defined in

$$L = \kappa_{tuH}\, \bar{t}uH + \kappa_{tcH}\, \bar{t}cH + h.c. \quad (3.17)$$

This can be studied in CC DIS production, where singly produced top anti-quarks could decay via such couplings into a light anti-quark and a Higgs boson decaying into a bottom quark-antiquark pair, $e^-p \to \nu_e\bar{t} \to \nu_e H\bar{q} \to \nu_e b\bar{b}\bar{q}$ [388]. Another signal involves the FCNC tHq coupling in the production vertex, i.e. a light quark from the proton interacts via t-channel top quark exchange with a W boson radiated from the initial electron producing a b quark and a Higgs boson decaying into a bottom quark-antiquark pair, $e^-p \to \nu_e Hb \to \nu_e b\bar{b}b$ [388]. This channel is superior in sensitivity to the previous one due to the clean experimental environment when requiring three identified b-jets. Largest backgrounds are given by $Z \to b\bar{b}$, SM $H \to b\bar{b}$, and single top quark production with hadronic top quark decays. A 5 % systematic uncertainty for the background yields is added. Furthermore, the analysis assumes parameterised resolutions for electrons, photons, muons, jets and unclustered energy using typical parameters taken from the ATLAS experiment. Furthermore, a b-tag rate of 60 %, a c-jet fake rate of 10%, and a light-jet fake rate of 1% is assumed. The selection is optimised for the different signal contributions separately. Fig. 3.13 (lower right), shows the expected upper limit on the branching ratio Br($t \to Hu$) with 1σ, 2σ, 3σ, and 5σ C.L. as a function of the integrated luminosity for the

$e^-p \to \nu_e Hb \to \nu_e b\bar{b}b$ signal process. For an integrated luminosity of $1\,\mathrm{ab}^{-1}$, upper limits of $\mathrm{Br}(t \to Hu) < 0.15 \cdot 10^{-3}$ are expected at the 2σ C.L.

In Fig. 3.14 the different expected limits on various flavour-changing neutral current (FCNC) top quark couplings from the LHeC are summarised, and compared to results from the LHC and the HL-LHC. This clearly shows the competitiveness of the LHeC results, and documents the complementarity of the results gained at different colliders.

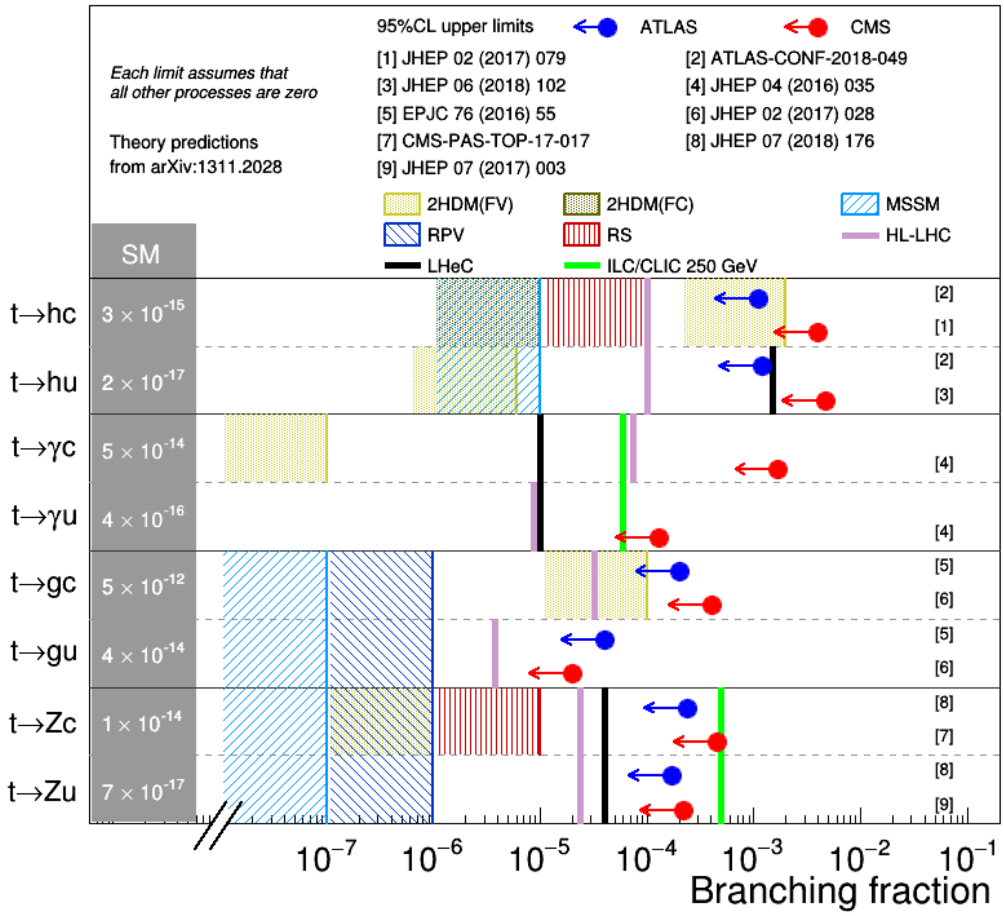

Figure 3.14: Comparison of top quark FCNC branching ratio limits at the LHC, HL-LHC, LHeC, and ILC/CLIC colliders.

3.2.3 Other Top Quark Property Measurements and Searches for New Physics

Other exciting results not presented here involve, for example, the study of the CP-nature in $t\bar{t}H$ production [392] (see Section **??**), searches for anomalous $t\bar{t}\gamma$ and $t\bar{t}Z$ chromoelectric and chromomagnetic dipole moments in $t\bar{t}$ production [379], the study of top quark spin and polarisation [393], and the investigation of the top quark structure function inside the proton [1, 8].

3.2.4 Summary Top Quark Physics

Top quark physics at the LHeC represents a very rich and diverse field of research involving high precision measurements of top quark properties, and sensitive searches for new physics. Only a few highlights involving Wtq and FCNC top quark couplings are presented here. One particular highlight is the expected direct measurement of the CKM matrix element $|V_{tb}|$ with a precision of less than 1 %. Furthermore, FCNC top quark couplings can be studied with a precision high enough to explore those couplings in a regime that might be affected by actual new phenomena models, such as SUSY, little Higgs, and technicolour.

It has been shown [389], that results from future e^+e^--colliders, eh-colliders, and hh-colliders deliver complimentary information and will therefore give us a more complete understanding of the properties of the heaviest elementary particle known to date, and of the top quark sector in general.

Bibliography [read the footnote] [999]

[1] LHeC Study Group, J. L. Abelleira *et al.*, *J. Phys.* G39 (2012) 075001, arXiv:1206.2913.

[2] E. D. Bloom *et al.*, *Phys. Rev. Lett.* 23 (1969) 930.

[3] M. Breidenbach, J. I. Friedman, H. W. Kendall, E. D. Bloom, D. H. Coward, H. C. DeStaebler, J. Drees, L. W. Mo and R. E. Taylor, *Phys. Rev. Lett.* 23 (1969) 935.

[4] R. P. Feynman, *Photon-hadron interactions*. Westview Press, Reading, MA, 1972.

[5] C. Quigg, *PoS* DIS2013 (2013) 034, arXiv:1308.6637.

[6] J. C. Collins, D. E. Soper and G. F. Sterman, *Factorization of Hard Processes in QCD*, vol. 5, pp. 1–91. 1989. arXiv:hep-ph/0409313.

[7] LHeC Study Group, J. L. Abelleira *et al.*, "On the Relation of the LHeC and the LHC," 2012. arXiv:1211.5102.

[8] G. R. Boroun, *Phys. Lett.* B744 (2015) 142–145, arXiv:1503.01590.

[9] T. J. Hobbs, J. T. Londergan, D. P. Murdock and A. W. Thomas, *Phys. Lett.* B698 (2011) 123, arXiv:1101.3923.

[10] M. Klein, "The structure of the proton and HERA," in *International Conference on the Structure and Interactions of the Photon and 18th International Workshop on Photon-Photon Collisions and International Workshop on High Energy Photon Linear Colliders*, 1 2010.

[11] M. Klein and R. Yoshida, *Prog. Part. Nucl. Phys.* 61 (2008) 343, arXiv:0805.3334.

[999] Note on bibliography:

- Put all *bibitems* into file *../lhec.bib.*
- Use 'inspirehep.net' bibtex entries whenever possible
- Check for duplicates in the bib file
- Use entry-type '`@article`' for regular articles (also `doi` and/or `arXiv` references are used). Use entry-type `@inproceedings` for other items (using at least: `author`. Specify then `Publisher` or `booktitle` where this article appeared (i.e. a talk, a chapter in a book, a technical note, a webpage, etc...), and provide `title`, `year`, `month`, `url`, `doi`, etc. if available.).
- Do not forget to commit the updated .bib file to the repository
- There will be only a single bibliography at the end of the CDR document. This bibliography section is only for editing purposes and disappears in the final document.

[12] H1 and ZEUS Collaborations, F. Aaron *et al.*, *JHEP* 1001 (2010) 109, arXiv:0911.0884.

[13] H1 and ZEUS Collaborations, H. Abramowicz *et al.*, *Eur. Phys. J.* C75 (2015) 580, arXiv:1506.06042.

[14] HERAFitter Group, S. Alekhin *et al.*, *Eur. Phys. J.* C75 (2015) 304, arXiv:1410.4412.

[15] H1 Collaboration, F. Aaron *et al.*, *Eur. Phys. J.* C64 (2009) 561, arXiv:0904.3513.

[16] M. Botje, *Comput. Phys. Commun.* 182 (2011) 490, arXiv:1005.1481.

[17] M. Botje, "Erratum for the time-like evolution in QCDNUM," 2016. arXiv:1602.08383.

[18] R. Thorne, *Phys.ReV. D* 73 (2006) 054019, arXiv:0601245.

[19] R. Thorne, *Phys.ReV. D* 86 (2012) 074017, arXiv:1201.6180.

[20] M. Klein, "Future Deep Inelastic Scattering with the LHeC," in *From My Vast Repertoire ...: Guido Altarelli's Legacy*, A. Levy, S. Forte and G. Ridolfi (eds.), p. 303. 2019. arXiv:1802.04317.

[21] S. Bentvelsen, J. Engelen and P. Kooijman, "Reconstruction of (x, Q**2) and extraction of structure functions in neutral current scattering at HERA," in *Workshop on Physics at HERA Hamburg, Germany, October 29-30, 1991*, 1992.

[22] U. Bassler and G. Bernardi, *Nucl. Instrum. Meth.* A361 (1995) 197–208, arXiv:hep-ex/9412004.

[23] U. Bassler and G. Bernardi, *Nucl. Instrum. Meth. A* 426 (1999) 583–598, arXiv:hep-ex/9801017.

[24] J. Blümlein and M. Klein, "Kinematics and resolution at future e p colliders," in *1990 DPF Summer Study on High-energy Physics: Research Directions for the Decade (Snowmass 90) Snowmass, Colorado, June 25-July 13, 1990*, 1990.

[25] R. Abdul Khalek, S. Bailey, J. Gao, L. Harland-Lang and J. Rojo, arXiv:1906.10127.

[26] S. J. Brodsky and G. R. Farrar, *Phys. Rev. Lett.* 31 (1973) 1153.

[27] S. J. Brodsky and G. R. Farrar, *Phys. Rev.* D11 (1975) 1309.

[28] V. A. Matveev, R. M. Muradian and A. N. Tavkhelidze, *Lett. Nuovo Cim.* 7 (1973) 719.

[29] ATLAS Collaboration, G. Aad *et al.*, *Eur. Phys. J. C* 79 (2019) 970, arXiv:1907.05120.

[30] H1 and ZEUS Collaborations, H. Abramowicz *et al.*, *Eur. Phys. J.* C78 (2018) 473, arXiv:1804.01019.

[31] J. Kuti and V. F. Weisskopf, *Phys. Rev. D* 4 (1971) 3418–3439.

[32] S. Dulat *et al.*, *Phys. Rev.* D93 (2016) 033006, arXiv:1506.07443.

[33] W. G. Seligman *et al.*, *Phys. Rev. Lett.* 79 (1997) 1213–1216, arXiv:hep-ex/9701017.

[34] NuTeV Collaboration, M. Tzanov *et al.*, *Phys. Rev.* D74 (2006) 012008, arXiv:hep-ex/0509010.

[35] CHORUS Collaboration, G. Onengut *et al.*, *Phys. Lett.* B632 (2006) 65–75.

[36] J. P. Berge *et al.*, *Z. Phys.* C49 (1991) 187–224.

[37] NOMAD Collaboration, O. Samoylov *et al.*, *Nucl. Phys.* B876 (2013) 339–375, arXiv:1308.4750.

[38] ATLAS Collaboration, G. Aad *et al.*, *Phys. Rev. Lett.* 109 (2012) 012001, arXiv:1203.4051.

[39] CMS Collaboration, S. Chatrchyan *et al.*, *JHEP* 02 (2014) 013, arXiv:1310.1138.

[40] ATLAS Collaboration, G. Aad *et al.*, *JHEP* 05 (2014) 068, arXiv:1402.6263.

[41] ATLAS Collaboration, M. Aaboud *et al.*, *Eur. Phys. J.* C77 (2017) 367, arXiv:1612.03016.

[42] S. Alekhin, J. Bluemlein and S. Moch, *Phys. Lett.* B777 (2018) 134–140, arXiv:1708.01067.

[43] A. M. Cooper-Sarkar and K. Wichmann, *Phys. Rev.* D98 (2018) 014027, arXiv:1803.00968.

[44] H. Abdolmaleki *et al.*, arXiv:1907.01014.

[45] O. Behnke, A. Geiser and M. Lisovyi, *Prog. Part. Nucl. Phys.* 84 (2015) 1–72, arXiv:1506.07519.

[46] O. Zenaiev, *Eur. Phys. J.* C77 (2017) 151, arXiv:1612.02371.

[47] M. A. G. Aivazis, F. I. Olness and W.-K. Tung, *Phys. Rev. Lett.* 65 (1990) 2339.

[48] M. A. G. Aivazis, F. I. Olness and W.-K. Tung, *Phys. Rev.* D50 (1994) 3085, arXiv:hep-ph/9312318.

[49] M. A. G. Aivazis, J. C. Collins, F. I. Olness and W.-K. Tung, *Phys. Rev.* D50 (1994) 3102, arXiv:hep-ph/9312319.

[50] R. S. Thorne and R. G. Roberts, *Eur. Phys. J.* C19 (2001) 339, arXiv:hep-ph/0010344.

[51] S. Alekhin, J. Blümlein and S. Moch, *Phys. Rev.* D86 (2012) 054009, arXiv:1202.2281.

[52] S. Alekhin, J. Blümlein and S. Moch, *Phys. Rev.* D89 (2014) 054028, arXiv:1310.3059.

[53] S. Alekhin, J. Blümlein, S. Klein and S. Moch, *Phys. Rev.* D81 (2010) 014032, arXiv:0908.2766.

[54] S. Forte, E. Laenen, P. Nason and J. Rojo, *Nucl. Phys.* B834 (2010) 116, arXiv:1001.2312.

[55] A. D. Martin, W. J. Stirling, R. S. Thorne and G. Watt, *Eur. Phys. J.* C70 (2010) 51, arXiv:1007.2624.

[56] R. D. Ball, V. Bertone, F. Cerutti, L. Del Debbio, S. Forte, A. Guffanti, J. I. Latorre, J. Rojo and M. Ubiali, *Nucl. Phys.* B849 (2011) 296, arXiv:1101.1300.

[57] R. D. Ball, M. Bonvini and L. Rottoli, *JHEP* 11 (2015) 122, arXiv:1510.02491.

[58] S. Alekhin, J. Bluemlein, S. Moch and R. Placakyte, *Phys. Rev. D* 96 (2017) 014011, arXiv:1701.05838.

[59] S. Moch, B. Ruijl, T. Ueda, J. A. M. Vermaseren and A. Vogt, *JHEP* 10 (2017) 041, arXiv:1707.08315.

[60] F. Herzog, S. Moch, B. Ruijl, T. Ueda, J. A. M. Vermaseren and A. Vogt, *Phys. Lett.* B790 (2019) 436–443, arXiv:1812.11818.

[61] G. Das, S.-O. Moch and A. Vogt, arXiv:1912.12920.

[62] R. D. Ball, *AIP Conf. Proc.* 1819 (2017) 030002, arXiv:1612.03790.

[63] M. Klein and T. Riemann, *Z. Phys.* C24 (1984) 151.

[64] A. Argento *et al.*, *Phys. Lett. B* 140 (1984) 142–144.

[65] S. Drell and T.-M. Yan, *Phys. Rev. Lett.* 25 (1970) 316–320. [Erratum: Phys.Rev.Lett. 25, 902 (1970)].

[66] J. Kubar, M. Le Bellac, J. Meunier and G. Plaut, *Nucl. Phys. B* 175 (1980) 251–275.

[67] T.-J. Hou *et al.*, arXiv:1912.10053.

[68] A. Accardi *et al.*, *Eur. Phys. J.* A52 (2016) 268, arXiv:1212.1701.

[69] A. V. Belitsky, X.-d. Ji and F. Yuan, *Phys. Rev.* D69 (2004) 074014, arXiv:hep-ph/0307383.

[70] N. N. Nikolaev and B. G. Zakharov, *Z. Phys.* C49 (1991) 607.

[71] N. Nikolaev and B. G. Zakharov, *Z. Phys.* C53 (1992) 331.

[72] N. N. Nikolaev and B. G. Zakharov, *J. Exp. Theor. Phys.* 78 (1994) 598. [Zh. Eksp. Teor. Fiz.105,1117(1994)].

[73] N. N. Nikolaev, B. G. Zakharov and V. R. Zoller, *Z. Phys.* A351 (1995) 435.

[74] A. H. Müller, *Nucl. Phys.* B415 (1994) 373.

[75] A. H. Müller and B. Patel, *Nucl. Phys.* B425 (1994) 471, arXiv:hep-ph/9403256.

[76] U. Amaldi and K. R. Schubert, *Nucl. Phys.* B166 (1980) 301.

[77] S. Munier, A. M. Stasto and A. H. Müller, *Nucl. Phys.* B603 (2001) 427, arXiv:hep-ph/0102291.

[78] N. Armesto and A. H. Rezaeian, *Phys. Rev.* D90 (2014) 054003, arXiv:1402.4831.

[79] H. Kowalski and D. Teaney, *Phys. Rev.* D68 (2003) 114005, arXiv:hep-ph/0304189.

[80] H. Kowalski, L. Motyka and G. Watt, *Phys. Rev.* D74 (2006) 074016, arXiv:hep-ph/0606272.

[81] G. Watt and H. Kowalski, *Phys. Rev.* D78 (2008) 014016, arXiv:0712.2670.

[82] L. N. Lipatov, *Sov. Phys. JETP* 63 (1986) 904. [Zh. Eksp. Teor. Fiz.90,1536(1986)].

[83] Y. Hatta, B.-W. Xiao and F. Yuan, *Phys. Rev. Lett.* 116 (2016) 202301, arXiv:1601.01585.

[84] T. Altinoluk, N. Armesto, G. Beuf and A. H. Rezaeian, *Phys. Lett.* B758 (2016) 373, arXiv:1511.07452.

[85] H. Mantysaari, N. Muller and B. Schenke, *Phys. Rev.* D99 (2019) 074004, arXiv:1902.05087.

[86] F. Salazar and B. Schenke, *Phys. Rev.* D100 (2019) 034007, arXiv:1905.03763.

[87] H. Mäntysaari and B. Schenke, *Phys. Rev. Lett.* 117 (2016) 052301, arXiv:1603.04349.

[88] H. Mäntysaari and B. Schenke, *Phys. Rev.* D94 (2016) 034042, arXiv:1607.01711.

[89] H. Mäntysaari and B. Schenke, *Phys. Lett.* B772 (2017) 832, arXiv:1703.09256.

[90] H. Mäntysaari and B. Schenke, *Phys. Rev.* D98 (2018) 034013, arXiv:1806.06783.

[91] J. Cepila, J. G. Contreras and J. D. Tapia Takaki, *Phys. Lett.* B766 (2017) 186, arXiv:1608.07559.

[92] D. Bendova, J. Cepila and J. G. Contreras, *Phys. Rev.* D99 (2019) 034025, arXiv:1811.06479.

[93] M. Krelina, V. P. Goncalves and J. Cepila, *Nucl. Phys.* A989 (2019) 187, arXiv:1905.06759.

[94] G. Zweig, "An SU(3) model for strong interaction symmetry and its breaking. Version 1," 1964.

[95] H. Fritzsch, M. Gell-Mann and H. Leutwyler, *Phys. Lett.* 47B (1973) 365–368.

[96] D. J. Gross and F. Wilczek, *Phys. Rev. Lett.* 30 (1973) 1343–1346.

[97] H. D. Politzer, *Phys. Rev. Lett.* 30 (1973) 1346–1349.

[98] G. Dissertori, *Adv. Ser. Direct. High Energy Phys.* 26 (2016) 113–128, arXiv:1506.05407.

[99] Particle Data Group, M. Tanabashi *et al.*, *Phys. Rev.* D98 (2018) 030001.

[100] D. d'Enterria *et al.*, *PoS* ALPHAS2019 (2019) 001, arXiv:1907.01435.

[101] K. H. Streng, T. F. Walsh and P. M. Zerwas, *Z. Phys.* C2 (1979) 237.

[102] H1 Collaboration, F. D. Aaron *et al.*, *Eur. Phys. J.* C67 (2010) 1, arXiv:0911.5678.

[103] S. D. Ellis and D. E. Soper, *Phys. Rev.* D48 (1993) 3160–3166, arXiv:hep-ph/9305266.

[104] H1 Collaboration, C. Adloff *et al.*, *Eur. Phys. J.* C13 (2000) 397, arXiv:hep-ex/9812024.

[105] H1 Collaboration, C. Adloff *et al.*, *Eur. Phys. J.* C19 (2001) 289, arXiv:hep-ex/0010054.

[106] H1 Collaboration, C. Adloff *et al.*, *Phys. Lett.* B542 (2002) 193, arXiv:hep-ex/0206029.

[107] H1 Collaboration, A. Aktas *et al.*, *Eur. Phys. J.* C33 (2004) 477, arXiv:hep-ex/0310019.

[108] H1 Collaboration, A. Aktas *et al.*, *Eur. Phys. J.* C37 (2004) 141, arXiv:hep-ex/0401010.

[109] H1 Collaboration, A. Aktas *et al.*, *Phys. Lett.* B653 (2007) 134, arXiv:0706.3722.

[110] H1 Collaboration, F. D. Aaron *et al.*, *Eur. Phys. J.* C65 (2010) 363, arXiv:0904.3870.

[111] H1 Collaboration, V. Andreev *et al.*, *Eur. Phys. J.* C75 (2015) 65, arXiv:1406.4709.

[112] H1 Collaboration, V. Andreev *et al.*, *Eur. Phys. J.* C77 (2017) 215, arXiv:1611.03421.

[113] ZEUS Collaboration, J. Breitweg *et al.*, *Phys. Lett.* B479 (2000) 37, arXiv:hep-ex/0002010.

[114] ZEUS Collaboration, S. Chekanov *et al.*, *Eur. Phys. J.* C23 (2002) 13, arXiv:hep-ex/0109029.

[115] ZEUS Collaboration, S. Chekanov *et al.*, *Phys. Lett.* B547 (2002) 164, arXiv:hep-ex/0208037.

[116] ZEUS Collaboration, S. Chekanov *et al.*, *Eur. Phys. J.* C35 (2004) 487, arXiv:hep-ex/0404033.

[117] ZEUS Collaboration, S. Chekanov *et al.*, *Nucl. Phys.* B765 (2007) 1, arXiv:hep-ex/0608048.

[118] ZEUS Collaboration, S. Chekanov *et al.*, *Phys. Lett.* B649 (2007) 12, arXiv:hep-ex/0701039.

[119] ZEUS Collaboration, H. Abramowicz *et al.*, *Eur. Phys. J.* C70 (2010) 965, arXiv:1010.6167.

[120] ZEUS Collaboration, H. Abramowicz *et al.*, *Phys. Lett.* B691 (2010) 127, arXiv:1003.2923.

[121] CMS Collaboration, V. Khachatryan *et al.*, *JHEP* 03 (2017) 156, arXiv:1609.05331.

[122] K. Rabbertz, *Springer Tracts Mod. Phys.* 268 (2017) 1.

[123] ATLAS Collaboration, M. Aaboud *et al.*, *JHEP* 09 (2017) 020, arXiv:1706.03192.

[124] ATLAS Collaboration, M. Aaboud *et al.*, *JHEP* 05 (2018) 195, arXiv:1711.02692.

[125] J. Currie, T. Gehrmann and J. Niehues, *Phys. Rev. Lett.* 117 (2016) 042001, arXiv:1606.03991.

[126] J. Currie, T. Gehrmann, A. Huss and J. Niehues, *JHEP* 07 (2017) 018, arXiv:1703.05977.

[127] T. Gehrmann *et al.*, *PoS* RADCOR2017 (2018) 074, arXiv:1801.06415.

[128] T. Kluge, K. Rabbertz and M. Wobisch, "FastNLO: Fast pQCD calculations for PDF fits," in *Proceedings, 14th International Workshop of deep inelastic scattering (DIS 2006), Tsukuba, Japan, April 20-24, 2006*, 2006. arXiv:hep-ph/0609285.

[129] D. Britzger, K. Rabbertz, F. Stober and M. Wobisch, "New features in version 2 of the fastNLO project," in *Proceedings, 20th International Workshop on Deep-Inelastic Scattering and Related Subjects (DIS 2012): Bonn, Germany, March 26-30, 2012*, 2012. arXiv:1208.3641.

[130] D. Britzger *et al.*, *Eur. Phys. J.* C79 (2019) 845, arXiv:1906.05303.

[131] H1 Collaboration, V. Andreev *et al.*, *Eur. Phys. J.* C77 (2017) 791, arXiv:1709.07251.

[132] R. Kogler, *Measurement of jet production in deep-inelastic e p scattering at HERA*. PhD thesis, Hamburg U., 2011.

[133] CMS Collaboration, V. Khachatryan *et al.*, *JINST* 12 (2017) P02014, arXiv:1607.03663.

[134] ATLAS Collaboration, M. Aaboud *et al.*, "Determination of jet calibration and energy resolution in proton-proton collisions at $\sqrt{s} = 8$ TeV using the ATLAS detector," 2019. arXiv:1910.04482.

[135] J. R. Ellis, E. Gardi, M. Karliner and M. A. Samuel, *Phys. Lett.* B366 (1996) 268, arXiv:hep-ph/9509312.

[136] S. J. Brodsky and X.-G. Wu, *Phys. Rev.* D85 (2012) 034038, arXiv:1111.6175. [Erratum: Phys. Rev.D86,079903(2012)].

[137] S. J. Brodsky and X.-G. Wu, *Phys. Rev. Lett.* 109 (2012) 042002, arXiv:1203.5312.

[138] S. J. Brodsky and L. Di Giustino, *Phys. Rev.* D86 (2012) 085026, arXiv:1107.0338.

[139] M. Mojaza, S. J. Brodsky and X.-G. Wu, *Phys. Rev. Lett.* 110 (2013) 192001, arXiv:1212.0049.

[140] S. J. Brodsky, M. Mojaza and X.-G. Wu, *Phys. Rev.* D89 (2014) 014027, arXiv:1304.4631.

[141] S.-Q. Wang, S. J. Brodsky, X.-G. Wu, J.-M. Shen and L. Di Giustino, *Phys. Rev.* D100 (2019) 094010, arXiv:1908.00060.

[142] Particle Data Group, M. Tanabashi *et al.*, "2019 Update of the Review of Particle Physics,". http://pdg.lbl.gov/2019/. unpublished.

[143] Flavour Lattice Averaging Group, S. Aoki *et al.*, arXiv:1902.08191.

[144] D. Boito, M. Golterman, K. Maltman, J. Osborne and S. Peris, *Phys. Rev.* D91 (2015) 034003, arXiv:1410.3528.

[145] Gfitter Group, M. Baak, J. Cúth, J. Haller, A. Hoecker, R. Kogler, K. Mönig, M. Schott and J. Stelzer, *Eur. Phys. J.* C74 (2014) 3046, arXiv:1407.3792.

[146] P. Azzi *et al.*, *CERN Yellow Rep. Monogr.* 7 (2019) 1–220, arXiv:1902.04070.

[147] I. Abt, A. M. Cooper-Sarkar, B. Foster, V. Myronenko, K. Wichmann and M. Wing, *Phys. Rev.* D96 (2017) 014001, arXiv:1704.03187. [Phys. Rev.D96,014001(2017)].

[148] M. Dasgupta and G. P. Salam, *J. Phys.* G30 (2004) R143, arXiv:hep-ph/0312283.

[149] H1 Collaboration, A. Aktas *et al.*, *Eur. Phys. J.* C46 (2006) 343–356, arXiv:hep-ex/0512014.

[150] ZEUS Collaboration, S. Chekanov *et al.*, *Nucl. Phys.* B767 (2007) 1–28, arXiv:hep-ex/0604032.

[151] D. Kang, C. Lee and I. W. Stewart, *Phys. Rev.* D88 (2013) 054004, arXiv:1303.6952.

[152] Z.-B. Kang, X. Liu and S. Mantry, *Phys. Rev.* D90 (2014) 014041, arXiv:1312.0301.

[153] D. Kang, C. Lee and I. W. Stewart, *PoS* DIS2015 (2015) 142.

[154] G. Abelof, R. Boughezal, X. Liu and F. Petriello, *Phys. Lett.* B763 (2016) 52–59, arXiv:1607.04921.

[155] S. Höche, S. Kuttimalai and Y. Li, *Phys. Rev.* D98 (2018) 114013, arXiv:1809.04192.

[156] J. Currie, T. Gehrmann, E. W. N. Glover, A. Huss, J. Niehues and A. Vogt, *JHEP* 05 (2018) 209, arXiv:1803.09973.

[157] T. Gehrmann, A. Huss, J. Mo and J. Niehues, arXiv:1909.02760.

[158] H1 Collaboration, C. Adloff *et al.*, *Eur. Phys. J.* C29 (2003) 497–513, arXiv:hep-ex/0302034.

[159] H1 Collaboration, A. Aktas *et al.*, *Phys. Lett.* B639 (2006) 21–31, arXiv:hep-ex/0603014.

[160] ZEUS Collaboration, S. Chekanov *et al.*, *Phys. Rev.* D76 (2007) 072011, arXiv:0706.3809.

[161] ZEUS Collaboration, H. Abramowicz *et al.*, *Nucl. Phys.* B864 (2012) 1–37, arXiv:1205.6153.

[162] M. Klasen, *Rev. Mod. Phys.* 74 (2002) 1221–1282, arXiv:hep-ph/0206169.

[163] M. Glück, E. Reya and A. Vogt, *Phys. Rev.* D46 (1992) 1973–1979.

[164] K. Sasaki, T. Ueda and T. Uematsu, *CERN Proc.* 1 (2018) 7.

[165] H1 and ZEUS Collaborations, H. Abramowicz *et al.*, *JHEP* 09 (2015) 149, arXiv:1503.06042.

[166] A. J. Larkoski, I. Moult and B. Nachman, arXiv:1709.04464.

[167] J. R. Andersen *et al.*, "Les Houches 2017: Physics at TeV Colliders Standard Model Working Group Report," 2018. arXiv:1803.07977.

[168] F. Ringer, *PoS* ALPHAS2019 (2019) 010.

[169] I. I. Balitsky and L. N. Lipatov, *Sov. J. Nucl. Phys.* 28 (1978) 822. [Yad. Fiz.28,1597(1978)].

[170] E. A. Kuraev, L. N. Lipatov and V. S. Fadin, *Sov. Phys. JETP* 45 (1977) 199. [Zh. Eksp. Teor. Fiz.72,377(1977)].

[171] V. S. Fadin and L. N. Lipatov, *Phys. Lett.* B429 (1998) 127, arXiv:hep-ph/9802290.

[172] M. Ciafaloni and G. Camici, *Phys. Lett.* B430 (1998) 349, arXiv:hep-ph/9803389.

[173] J. Blümlein and A. Vogt, *Phys. Rev.* D58 (1998) 014020, arXiv:hep-ph/9712546.

[174] D. A. Ross, *Phys. Lett.* B431 (1998) 161, arXiv:hep-ph/9804332.

[175] Y. V. Kovchegov and A. H. Müller, *Phys. Lett.* B439 (1998) 428, arXiv:hep-ph/9805208.

[176] E. Levin, *Nucl. Phys.* B545 (1999) 481, arXiv:hep-ph/9806228.

[177] N. Armesto, J. Bartels and M. A. Braun, *Phys. Lett.* B442 (1998) 459, arXiv:hep-ph/9808340.

[178] M. Ciafaloni, *Nucl. Phys.* B296 (1988) 49.

[179] B. Andersson, G. Gustafson and J. Samuelsson, *Nucl. Phys.* B467 (1996) 443.

[180] J. Kwiecinski, A. D. Martin and P. J. Sutton, *Z. Phys.* C71 (1996) 585, arXiv:hep-ph/9602320.

[181] J. Kwiecinski, A. D. Martin and A. M. Stasto, *Phys. Rev.* D56 (1997) 3991, arXiv:hep-ph/9703445.

[182] G. P. Salam, *JHEP* 07 (1998) 019, arXiv:hep-ph/9806482.

[183] M. Ciafaloni, D. Colferai and G. P. Salam, *JHEP* 10 (1999) 017, arXiv:hep-ph/9907409.

[184] M. Ciafaloni, D. Colferai and G. P. Salam, *Phys. Rev.* D60 (1999) 114036, arXiv:hep-ph/9905566.

[185] M. Ciafaloni, D. Colferai, D. Colferai, G. P. Salam and A. M. Stasto, *Phys. Lett.* B576 (2003) 143, arXiv:hep-ph/0305254.

[186] M. Ciafaloni, D. Colferai, G. P. Salam and A. M. Stasto, *Phys. Lett.* B587 (2004) 87, arXiv:hep-ph/0311325.

[187] M. Ciafaloni, D. Colferai, G. P. Salam and A. M. Stasto, *Phys. Rev.* D68 (2003) 114003, arXiv:hep-ph/0307188.

[188] M. Ciafaloni, D. Colferai, G. P. Salam and A. M. Stasto, *JHEP* 08 (2007) 046, arXiv:0707.1453.

[189] G. Altarelli, R. D. Ball and S. Forte, *Nucl. Phys.* B575 (2000) 313, arXiv:hep-ph/9911273.

[190] G. Altarelli, R. D. Ball and S. Forte, *Nucl. Phys.* B599 (2001) 383, arXiv:hep-ph/0011270.

[191] G. Altarelli, R. D. Ball and S. Forte, *Nucl. Phys.* B621 (2002) 359, arXiv:hep-ph/0109178.

[192] G. Altarelli, R. D. Ball and S. Forte, *Nucl. Phys.* B674 (2003) 459, arXiv:hep-ph/0306156.

[193] G. Altarelli, R. D. Ball and S. Forte, *Nucl. Phys.* B799 (2008) 199, arXiv:0802.0032.

[194] R. S. Thorne, *Phys. Rev.* D64 (2001) 074005, arXiv:hep-ph/0103210.

[195] A. Sabio Vera, *Nucl. Phys.* B722 (2005) 65, arXiv:hep-ph/0505128.

[196] M. Bonvini, S. Marzani and T. Peraro, *Eur. Phys. J.* C76 (2016) 597, arXiv:1607.02153.

[197] V. Bertone, S. Carrazza and J. Rojo, *Comput. Phys. Commun.* 185 (2014) 1647, arXiv:1310.1394.

[198] M. Bonvini, S. Marzani and C. Muselli, *JHEP* 12 (2017) 117, arXiv:1708.07510.

[199] A. H. Müller, *Nucl. Phys.* B335 (1990) 115.

[200] R. D. Ball, V. Bertone, M. Bonvini, S. Marzani, J. Rojo and L. Rottoli, *Eur. Phys. J.* C78 (2018) 321, arXiv:1710.05935.

[201] H. Abdolmaleki *et al.*, *Eur. Phys. J.* C78 (2018) 621, arXiv:1802.00064.

[202] J. Butterworth *et al.*, *J. Phys.* G43 (2016) 023001, arXiv:1510.03865.

[203] S. Carrazza, S. Forte, Z. Kassabov, J. I. Latorre and J. Rojo, *Eur. Phys. J.* C75 (2015) 369, arXiv:1505.06736.

[204] H. Paukkunen and P. Zurita, *JHEP* 12 (2014) 100, arXiv:1402.6623.

[205] J. Rojo and F. Caola, "Parton distributions and small-x QCD at the Large Hadron Electron Collider," in *17th International Workshop on Deep-Inelastic Scattering and*

Related Subjects (DIS 2009): Madrid, Spain, April 26-30, 2009, Berlin, Germany, 2009. arXiv:0906.2079.

[206] R. Abdul Khalek, S. Bailey, J. Gao, L. Harland-Lang and J. Rojo, *Eur. Phys. J.* C78 (2018) 962, arXiv:1810.03639.

[207] J. Bartels, K. J. Golec-Biernat and H. Kowalski, *Phys. Rev.* D66 (2002) 014001, arXiv:hep-ph/0203258.

[208] K. J. Golec-Biernat and S. Sapeta, *Phys. Rev.* D74 (2006) 054032, arXiv:hep-ph/0607276.

[209] K. Golec-Biernat and S. Sapeta, *JHEP* 03 (2018) 102, arXiv:1711.11360.

[210] J. Gao, L. Harland-Lang and J. Rojo, *Phys. Rept.* 742 (2018) 1, arXiv:1709.04922.

[211] V. Bertone, R. Gauld and J. Rojo, *JHEP* 01 (2019) 217, arXiv:1808.02034.

[212] L. N. Hand, D. G. Miller and R. Wilson, *Rev. Mod. Phys.* 35 (1963) 335.

[213] G. Miller *et al.*, *Phys. Rev.* D5 (1972) 528.

[214] E. M. Riordan, A. Bodek, M. Breidenbach, D. L. Dubin, J. E. Elias, J. I. Friedman, H. W. Kendall, J. S. Poucher, M. R. Sogard and D. H. Coward, *Phys. Rev. Lett.* 33 (1974) 561.

[215] H1 Collaboration, F. D. Aaron *et al.*, *Eur. Phys. J.* C71 (2011) 1579, arXiv:1012.4355.

[216] G. Altarelli and G. Martinelli, *Phys. Lett.* 76B (1978) 89.

[217] M. Glück, E. Hoffmann and E. Reya, *Z. Phys.* C13 (1982) 119.

[218] C. Ewerz and O. Nachtmann, *Annals Phys.* 322 (2007) 1670, arXiv:hep-ph/0604087.

[219] H1 Collaboration, V. Andreev *et al.*, *Eur. Phys. J.* C74 (2014) 2814, arXiv:1312.4821.

[220] ATLAS Collaboration, G. Aad *et al.*, *Phys. Rev.* D85 (2012) 072004, arXiv:1109.5141.

[221] G. Altarelli, *Nuovo Cim.* C035N1 (2012) 1, arXiv:1106.3189.

[222] J. Blümlein and M. Klein, *Nucl. Instrum. Meth.* A329 (1993) 112.

[223] R. Gandhi, C. Quigg, M. H. Reno and I. Sarcevic, *Phys. Rev.* D58 (1998) 093009, arXiv:hep-ph/9807264.

[224] IceCube Collaboration, M. G. Aartsen *et al.*, *JINST* 12 (2017) P03012, arXiv:1612.05093.

[225] J. Kwiecinski, A. D. Martin and A. M. Stasto, *Phys. Rev.* D59 (1999) 093002, arXiv:astro-ph/9812262.

[226] IceCube Collaboration, M. G. Aartsen *et al.*, *Nature* 551 (2017) 596, arXiv:1711.08119.

[227] T. K. Gaisser, *Cosmic rays and particle physics*. 1990. http://www.cambridge.org/uk/catalogue/catalogue.asp?isbn=0521326672.

[228] IceCube Collaboration, M. G. Aartsen *et al.*, *Phys. Rev. Lett.* 113 (2014) 101101, arXiv:1405.5303.

[229] G. Gelmini, P. Gondolo and G. Varieschi, *Phys. Rev.* D61 (2000) 056011, arXiv:hep-ph/9905377.

[230] A. Bhattacharya, R. Enberg, Y. S. Jeong, C. S. Kim, M. H. Reno, I. Sarcevic and A. Stasto, *JHEP* 11 (2016) 167, arXiv:1607.00193.

[231] C. Brenner Mariotto and M. Machado, *Phys. Rev. D* 86 (2012) 033009, arXiv:1208.5685.

[232] R. Coelho and V. Goncalves, arXiv:2002.10713.

[233] R. Coelho and V. Goncalves, *Nucl. Phys. B* 956 (2020) 115013.

[234] M. Bonvini, *Eur. Phys. J. C* 78 (2018) 834, arXiv:1805.08785.

[235] M. Bonvini, R. Gauld, T. Giani and S. Marzani in preparation.

[236] M. Bonvini and F. Silvetti in preparation.

[237] M. Bonvini and S. Marzani, *Phys. Rev. Lett.* 120 (2018) 202003, arXiv:1802.07758.

[238] J. C. Collins, D. E. Soper and G. F. Sterman, *Nucl. Phys. B* 250 (1985) 199–224.

[239] J. Collins, *Foundations of perturbative QCD*, vol. 32. Cambridge University Press, 11 2013.

[240] R. Angeles-Martinez *et al.*, *Acta Phys. Polon. B* 46 (2015) 2501–2534, arXiv:1507.05267.

[241] M. Diehl, *Eur. Phys. J. A* 52 (2016) 149, arXiv:1512.01328.

[242] T. C. Rogers, *Eur. Phys. J. A* 52 (2016) 153, arXiv:1509.04766.

[243] I. Balitsky and A. Tarasov, *JHEP* 06 (2016) 164, arXiv:1603.06548.

[244] S. Catani, M. Ciafaloni and F. Hautmann, *Phys. Lett. B* 242 (1990) 97–102.

[245] S. Catani, M. Ciafaloni and F. Hautmann, *Nucl. Phys. B* 366 (1991) 135–188.

[246] J. C. Collins and R. Ellis, *Nucl. Phys. B* 360 (1991) 3–30.

[247] E. Levin, M. Ryskin, Y. Shabelski and A. Shuvaev, *Sov. J. Nucl. Phys.* 53 (1991) 657.

[248] F. Gelis, E. Iancu, J. Jalilian-Marian and R. Venugopalan, *Ann. Rev. Nucl. Part. Sci.* 60 (2010) 463, arXiv:1002.0333.

[249] Y. V. Kovchegov and E. Levin, *Camb. Monogr. Part. Phys. Nucl. Phys. Cosmol.* 33 (2012) 1.

[250] T. Altinoluk and R. Boussarie, *JHEP* 10 (2019) 208, arXiv:1902.07930.

[251] H1 Collaboration, C. Adloff *et al.*, *Z. Phys.* C76 (1997) 613, arXiv:hep-ex/9708016.

[252] ZEUS Collaboration, J. Breitweg *et al.*, *Eur. Phys. J.* C1 (1998) 81, arXiv:hep-ex/9709021.

[253] P. Newman and M. Wing, *Rev. Mod. Phys.* 86 (2014) 1037, arXiv:1308.3368.

[254] V. N. Gribov, *Sov. Phys. JETP* 29 (1969) 483. [Zh. Eksp. Teor. Fiz.56,892(1969)].

[255] J. C. Collins, *Phys. Rev.* D57 (1998) 3051, arXiv:hep-ph/9709499. [Erratum: Phys. Rev.D61,019902(2000)].

[256] A. Berera and D. E. Soper, *Phys. Rev.* D53 (1996) 6162, arXiv:hep-ph/9509239.

[257] L. Trentadue and G. Veneziano, *Phys. Lett.* B323 (1994) 201.

[258] N. Armesto, P. R. Newman, W. Slominski and A. M. Stasto, *Phys. Rev.* D100 (2019) 074022, arXiv:1901.09076.

[259] H. Khanpour, *Phys. Rev.* D99 (2019) 054007, arXiv:1902.10734.

[260] H1 Collaboration Collaboration, A. Aktas *et al.*, *Eur.Phys.J.* C48 (2006) 715, arXiv:hep-ex/0606004.

[261] ZEUS Collaboration Collaboration, S. Chekanov *et al.*, *Nucl.Phys.* B816 (2009) 1, arXiv:0812.2003.

[262] H1 Collaboration Collaboration, F. Aaron *et al.*, *Eur.Phys.J.* C72 (2012) 2074, arXiv:1203.4495.

[263] H1 and ZEUS Collaborations, F. D. Aaron *et al.*, *Eur. Phys. J.* C72 (2012) 2175, arXiv:1207.4864.

[264] ZEUS Collaboration, S. Chekanov *et al.*, *Nucl. Phys.* B713 (2005) 3, arXiv:hep-ex/0501060.

[265] H1 Collaboration, A. Aktas *et al.*, *Eur. Phys. J.* C48 (2006) 749, arXiv:hep-ex/0606003.

[266] ZEUS Collaboration Collaboration, S. Chekanov *et al.*, *Nucl.Phys.* B831 (2010) 1, arXiv:0911.4119.

[267] H1 Collaboration, F. Aaron *et al.*, *Eur.Phys.J.* C71 (2011) 1578, arXiv:1010.1476.

[268] V. N. Gribov and L. N. Lipatov, *Sov. J. Nucl. Phys.* 15 (1972) 675. [Yad. Fiz.15,1218(1972)].

[269] V. N. Gribov and L. N. Lipatov, *Sov. J. Nucl. Phys.* 15 (1972) 438. [Yad. Fiz.15,781(1972)].

[270] G. Altarelli and G. Parisi, *Nucl. Phys.* B126 (1977) 298.

[271] Y. L. Dokshitzer, *Sov. Phys. JETP* 46 (1977) 641. [Zh. Eksp. Teor. Fiz.73,1216(1977)].

[272] J. C. Collins and W.-K. Tung, *Nucl. Phys.* B278 (1986) 934.

[273] R. S. Thorne and W. K. Tung, arXiv:0809.0714.

[274] J. F. Owens, *Phys. Rev.* D30 (1984) 943.

[275] M. Glück, E. Reya and A. Vogt, *Z. Phys.* C53 (1992) 651.

[276] R. S. Thorne and R. G. Roberts, *Phys. Rev.* D57 (1998) 6871, arXiv:hep-ph/9709442.

[277] F. Bordry *et al.*, "Machine Parameters and Projected Luminosity Performance of Proposed Future Colliders at CERN," 2018. arXiv:1810.13022.

[278] O. Bruening, J. Jowett, M. Klein, D. Pellegrini, D. Schulte and F. Zimmermann, "Future Circular Collider Study FCC-eh Baseline Parameters," 2017. CERN FCC-ACC-RPT-012.

[279] ATLAS Collaboration, G. Aad *et al.*, *Phys. Lett.* B754 (2016) 214–234, arXiv:1511.00502.

[280] D. Britzger, J. Currie, T. Gehrmann, A. Huss, J. Niehues and R. Žlebčík, *Eur. Phys. J.* C78 (2018) 538, arXiv:1804.05663.

[281] Z. Nagy, *Phys. Rev.* D68 (2003) 094002, arXiv:hep-ph/0307268.

[282] S. J. Brodsky, P. Hoyer, C. Peterson and N. Sakai, *Phys. Lett.* 93B (1980) 451.

[283] S. J. Brodsky, A. Kusina, F. Lyonnet, I. Schienbein, H. Spiesberger and R. Vogt, *Adv. High Energy Phys.* 2015 (2015) 231547, arXiv:1504.06287.

[284] S. J. Brodsky and S. Gardner, *Phys. Rev. Lett.* 116 (2016) 019101, arXiv:1504.00969.

[285] G. F. de Teramond and S. J. Brodsky, *Phys. Rev. Lett.* 102 (2009) 081601, arXiv:0809.4899.

[286] SELEX Collaboration, A. Ocherashvili *et al.*, *Phys. Lett.* B628 (2005) 18, arXiv:hep-ex/0406033.

[287] ANDY Collaboration, L. C. Bland *et al.*, arXiv:1909.03124.

[288] S. J. Brodsky, G. F. de Teramond, H. G. Dosch and J. Erlich, *Phys. Rept.* 584 (2015) 1, arXiv:1407.8131.

[289] G. F. de Teramond, H. G. Dosch and S. J. Brodsky, *Phys. Rev.* D87 (2013) 075005, arXiv:1301.1651.

[290] V. de Alfaro, S. Fubini and G. Furlan, *Nuovo Cim.* A34 (1976) 569.

[291] G. Veneziano, *Nuovo Cim.* A57 (1968) 190.

[292] A. Deur, S. J. Brodsky and G. F. de Teramond, *Prog. Part. Nucl. Phys.* 90 (2016) 1, arXiv:1604.08082.

[293] G. Grunberg, *Phys. Lett.* 95B (1980) 70. [Erratum: Phys. Lett.110B,501(1982)].

[294] J. D. Bjorken, *Phys. Rev.* 148 (1966) 1467.

[295] A. Deur *et al.*, *Phys. Rev. Lett.* 93 (2004) 212001, arXiv:hep-ex/0407007.

[296] A. Deur, Y. Prok, V. Burkert, D. Crabb, F. X. Girod, K. A. Griffioen, N. Guler, S. E. Kuhn and N. Kvaltine, *Phys. Rev.* D90 (2014) 012009, arXiv:1405.7854.

[297] A. Deur *et al.*, *Phys. Rev.* D78 (2008) 032001, arXiv:0802.3198.

[298] S. J. Brodsky and H. J. Lu, *Phys. Rev.* D51 (1995) 3652, arXiv:hep-ph/9405218.

[299] S. J. Brodsky, G. F. de Teramond and A. Deur, *Phys. Rev.* D81 (2010) 096010, arXiv:1002.3948.

[300] A. Deur, S. J. Brodsky and G. F. de Teramond, *Phys. Lett.* B750 (2015) 528, arXiv:1409.5488.

[301] S. J. Brodsky, G. F. de Téramond, A. Deur and H. G. Dosch, *Few Body Syst.* 56 (2015) 621, arXiv:1410.0425.

[302] A. Deur, V. Burkert, J.-P. Chen and W. Korsch, *Phys. Lett.* B650 (2007) 244, arXiv:hep-ph/0509113.

[303] A. Deur, V. Burkert, J. P. Chen and W. Korsch, *Phys. Lett.* B665 (2008) 349, arXiv:0803.4119.

[304] S. J. Brodsky, *J. Phys. Conf. Ser.* 1137 (2019) 012027.

[305] G. P. Lepage and S. J. Brodsky, *Phys. Lett.* 87B (1979) 359.

[306] A. V. Efremov and A. V. Radyushkin, *Phys. Lett.* 94B (1980) 245.

[307] S. J. Brodsky, G. F. De Téramond and H. G. Dosch, *Phys. Lett.* B729 (2014) 3, arXiv:1302.4105.

[308] S. J. Brodsky, *Few Body Syst.* 57 (2016) 703, arXiv:1601.06328.

[309] R. S. Sufian, G. F. de Téramond, S. J. Brodsky, A. Deur and H. G. Dosch, *Phys. Rev.* D95 (2017) 014011, arXiv:1609.06688.

[310] HLFHS Collaboration, G. F. de Teramond, T. Liu, R. S. Sufian, H. G. Dosch, S. J. Brodsky and A. Deur, *Phys. Rev. Lett.* 120 (2018) 182001, arXiv:1801.09154.

[311] T. Gutsche, V. E. Lyubovitskij, I. Schmidt and A. Vega, *Phys. Rev.* D91 (2015) 114001, arXiv:1501.02738.

[312] T. Gutsche, V. E. Lyubovitskij and I. Schmidt, *Phys. Rev.* D94 (2016) 116006, arXiv:1607.04124.

[313] H. G. Dosch, G. F. de Teramond and S. J. Brodsky, *Phys. Rev.* D91 (2015) 085016, arXiv:1501.00959.

[314] S. J. Brodsky, G. F. de Téramond, H. G. Dosch and C. Lorcé, *Int. J. Mod. Phys.* A31 (2016) 1630029, arXiv:1606.04638.

[315] M. Nielsen, S. J. Brodsky, G. F. de Téramond, H. G. Dosch, F. S. Navarra and L. Zou, *Phys. Rev.* D98 (2018) 034002, arXiv:1805.11567.

[316] G. F. de Teramond, H. G. Dosch and S. J. Brodsky, *Phys. Rev.* D91 (2015) 045040, arXiv:1411.5243.

[317] S. L. Glashow, *Nucl. Phys.* 22 (1961) 579.

[318] S. Weinberg, *Phys. Rev. Lett.* 19 (1967) 1264.

[319] S. Weinberg, *Phys. Rev. Lett.* 27 (1971) 1688.

[320] S. Weinberg, *Phys. Rev.* D5 (1972) 1412.

[321] A. Salam and J. C. Ward, *Phys. Lett.* 13 (1964) 168.

[322] P. W. Higgs, *Phys. Lett.* 12 (1964) 132.

[323] P. W. Higgs, *Phys. Rev. Lett.* 13 (1964) 508.

[324] F. Englert and R. Brout, *Phys. Rev. Lett.* 13 (1964) 321.

[325] H1 Collaboration, A. Aktas *et al.*, *Phys. Lett.* B632 (2006) 35, arXiv:hep-ex/0507080.

[326] ZEUS Collaboration, H. Abramowicz *et al.*, *Phys. Rev.* D93 (2016) 092002, arXiv:1603.09628.

[327] H1 Collaboration, V. Andreev *et al.*, *Eur. Phys. J.* C78 (2018) 777, arXiv:1806.01176.

[328] M. Böhm and H. Spiesberger, *Nucl. Phys.* B294 (1987) 1081.

[329] D. Yu. Bardin, C. Burdik, P. C. Khristova and T. Riemann, *Z. Phys.* C42 (1989) 679.

[330] W. Hollik, D. Yu. Bardin, J. Blümlein, B. A. Kniehl, T. Riemann and H. Spiesberger, "Electroweak parameters at HERA: Theoretical aspects," in *Workshop on physics at HERA Hamburg, Germany, October 29-30, 1991*, 1992.

[331] M. Böhm and H. Spiesberger, *Nucl. Phys.* B304 (1988) 749.

[332] D. Yu. Bardin, K. C. Burdik, P. K. Khristova and T. Riemann, *Z. Phys.* C44 (1989) 149.

[333] A. Sirlin, *Phys. Rev.* D22 (1980) 971.

[334] M. Bohm, H. Spiesberger and W. Hollik, *Fortsch. Phys.* 34 (1986) 687.

[335] W. F. L. Hollik, *Fortsch. Phys.* 38 (1990) 165.

[336] H1 Collaboration, F. D. Aaron *et al.*, *JHEP* 09 (2012) 061, arXiv:1206.7007.

[337] D. Britzger and M. Klein, *PoS* DIS2017 (2018) 105.

[338] H. Spiesberger, "EPRC: A program package for electroweak physics at HERA," in *Future physics at HERA. Proceedings, Workshop, Hamburg, Germany, September 25, 1995-May 31, 1996. Vol. 1, 2*, 1995.

[339] G. Cowan, K. Cranmer, E. Gross and O. Vitells, *Eur. Phys. J.* C71 (2011) 1554, arXiv:1007.1727. [Erratum: Eur. Phys. J. C73 (2013) 2501].

[340] CDF and D0 Collaborations, arXiv:1204.0042.

[341] ALEPH, DELPHI, L3, OPAL, LEP Electroweak Collaboration, S. Schael *et al.*, *Phys. Rept.* 532 (2013) 119, arXiv:1302.3415.

[342] ATLAS Collaboration, M. Aaboud *et al.*, *Eur. Phys. J.* C78 (2018) 110, arXiv:1701.07240. [Erratum: Eur. Phys. J.C78,no.11,898(2018)].

[343] J. de Blas, M. Ciuchini, E. Franco, S. Mishima, M. Pierini, L. Reina and L. Silvestrini, *JHEP* 12 (2016) 135, arXiv:1608.01509.

[344] J. Haller, A. Hoecker, R. Kogler, K. Mönig, T. Peiffer and J. Stelzer, *Eur. Phys. J.* C78 (2018) 675, arXiv:1803.01853.

[345] MuLan Collaboration, V. Tishchenko *et al.*, *Phys. Rev.* D87 (2013) 052003, arXiv:1211.0960.

[346] M. Schott, "Global EW fits: experimental and theoretical issues," Talk presented at the Ultimate Precision at Hadron Colliders, Sarclay, France, 2019.

[347] ALEPH, DELPHI, L3, OPAL, SLD Collaborations, LEP Electroweak Working Group, SLD Electroweak Heavy Flavour Groups, S. Schael *et al.*, *Phys. Rept.* 427 (2006) 257, arXiv:hep-ex/0509008.

[348] D0 Collaboration, V. M. Abazov *et al.*, *Phys. Rev.* D84 (2011) 012007, arXiv:1104.4590.

[349] CDF and D0 Collaborations, T. A. Aaltonen *et al.*, *Phys. Rev.* D97 (2018) 112007, arXiv:1801.06283.

[350] LHCb Collaboration, R. Aaij *et al.*, *JHEP* 11 (2015) 190, arXiv:1509.07645.

[351] ATLAS Collaboration, T. A. collaboration, .

[352] CMS Collaboration, A. M. Sirunyan *et al.*, *Eur. Phys. J.* C78 (2018) 701, arXiv:1806.00863.

[353] J. Erler, "Global fits of the SM parameters," in *7th Large Hadron Collider Physics Conference (LHCP 2019) Puebla, Puebla, Mexico, May 20-25, 2019*, 2019. arXiv:1908.07327.

[354] J. Erler and M. Schott, *Prog. Part. Nucl. Phys.* 106 (2019) 68, arXiv:1902.05142.

[355] ZEUS Collaboration, S. Chekanov *et al.*, *Phys. Lett.* B672 (2009) 106, arXiv:0807.0589.

[356] H1 Collaboration, F. D. Aaron *et al.*, *Eur. Phys. J.* C64 (2009) 251, arXiv:0901.0488.

[357] H1 and ZEUS Collaborations, F. D. Aaron *et al.*, *JHEP* 03 (2010) 035, arXiv:0911.0858.

[358] U. Baur and D. Zeppenfeld, *Nucl. Phys.* B325 (1989) 253.

[359] U. Baur, B. A. Kniehl, J. A. M. Vermaseren and D. Zeppenfeld, "Single W and Z production at LEP / LHC," in *ECFA Large Hadron Collider Workshop, Aachen, Germany, 4-9 Oct 1990: Proceedings.2.*, 1990.

[360] U. Baur, J. A. M. Vermaseren and D. Zeppenfeld, *Nucl. Phys.* B375 (1992) 3.

[361] J. Alwall, R. Frederix, S. Frixione, V. Hirschi, F. Maltoni, O. Mattelaer, H. S. Shao, T. Stelzer, P. Torrielli and M. Zaro, *JHEP* 07 (2014) 079, arXiv:1405.0301.

[362] NNPDF Collaboration, R. D. Ball, V. Bertone, S. Carrazza, L. Del Debbio, S. Forte, A. Guffanti, N. P. Hartland and J. Rojo, *Nucl. Phys.* B877 (2013) 290, arXiv:1308.0598.

[363] K. Hagiwara, S. Ishihara, R. Szalapski and D. Zeppenfeld, *Phys. Rev.* D48 (1993) 2182.

[364] K. Hagiwara, S. Ishihara, R. Szalapski and D. Zeppenfeld, *Phys. Lett.* B283 (1992) 353.

[365] A. De Rujula, M. B. Gavela, P. Hernandez and E. Masso, *Nucl. Phys.* B384 (1992) 3.

[366] S. S. Biswal, M. Patra and S. Raychaudhuri, arXiv:1405.6056.

[367] I. T. Cakir, O. Cakir, A. Senol and A. T. Tasci, *Acta Phys. Polon.* B45 (2014) 1947, arXiv:1406.7696.

[368] R. Li, X.-M. Shen, K. Wang, T. Xu, L. Zhang and G. Zhu, *Phys. Rev.* D97 (2018) 075043, arXiv:1711.05607.

[369] M. Köksal, A. A. Billur, A. Gutiérrez-Rodríguez and M. A. Hernández-Ruíz, arXiv:1910.06747.

[370] A. Gutiérrez-Rodríguez, M. Köksal, A. A. Billur and M. A. Hernández-Ruíz, arXiv:1910.02307.

[371] CMS Collaboration, A. M. Sirunyan *et al.*, *Phys. Lett.* B772 (2017) 21, arXiv:1703.06095.

[372] CMS Collaboration, A. M. Sirunyan *et al.*, arXiv:1907.08354.

[373] S. Villa, *Nucl. Phys. Proc. Suppl.* 142 (2005) 391, arXiv:hep-ph/0410208.

[374] K. O. Mikaelian, M. A. Samuel and D. Sahdev, *Phys. Rev. Lett.* 43 (1979) 746.

[375] S. J. Brodsky and R. W. Brown, *Phys. Rev. Lett.* 49 (1982) 966.

[376] R. W. Brown, K. L. Kowalski and S. J. Brodsky, *Phys. Rev.* D28 (1983) 624. [Addendum: Phys. Rev.D29,2100(1984)].

[377] M. A. Samuel and J. H. Reid, *Prog. Theor. Phys.* 76 (1986) 184.

[378] S. Dutta, A. Goyal, M. Kumar and B. Mellado, *Eur. Phys. J.* C75 (2015) 577, arXiv:1307.1688.

[379] A. O. Bouzas and F. Larios, *Phys. Rev.* D88 (2013) 094007, arXiv:1308.5634.

[380] S. Ovyn, X. Rouby and V. Lemaitre, "DELPHES, a framework for fast simulation of a generic collider experiment," 2009. arXiv:0903.2225.

[381] CMS Collaboration, V. Khachatryan *et al.*, *JHEP* 06 (2014) 090, arXiv:1403.7366.

[382] H. Sun, *PoS* DIS2018 (2018) 167.

[383] CMS Collaboration, V. Khachatryan *et al.*, *Phys. Lett.* B736 (2014) 33–57, arXiv:1404.2292.

[384] J. A. Aguilar-Saavedra, *Acta Phys. Polon.* B35 (2004) 2695–2710, arXiv:hep-ph/0409342.

[385] J. Charles *et al.*, *Phys. Rev.* D91 (2015) 073007, arXiv:1501.05013.

[386] I. Turk Cakir, A. Yilmaz, H. Denizli, A. Senol, H. Karadeniz and O. Cakir, *Adv. High Energy Phys.* 2017 (2017) 1572053, arXiv:1705.05419.

[387] O. Cakir, A. Yilmaz, I. Turk Cakir, A. Senol and H. Denizli, *Nucl. Phys.* B944 (2019) 114640, arXiv:1809.01923.

[388] H. Sun and X. Wang, *Eur. Phys. J.* C78 (2018) 281, arXiv:1602.04670.

[389] FCC Collaboration, A. Abada *et al.*, *Eur. Phys. J.* C79 (2019) 474.

[390] J. A. Aguilar-Saavedra and T. Riemann, "Probing top flavor changing neutral couplings at TESLA," in *5th Workshop of the 2nd ECFA, Obernai, France, October 16-19, 1999*, 2001. arXiv:hep-ph/0102197.

[391] Top Quark Working Group, K. Agashe *et al.*, "Working Group Report: Top Quark," in *Community Summer Study on the Future of U.S. Particle Physics: Minneapolis, MN, USA, July 29-August 6, 2013*, 2013. arXiv:1311.2028.

[392] B. Coleppa, M. Kumar, S. Kumar and B. Mellado, *Phys. Lett.* B770 (2017) 335–341, arXiv:1702.03426.

[393] S. Atag and B. Sahin, *Phys. Rev.* D73 (2006) 074001.